Hybrid carbon based devices : functionalization of nanotube and graphene devices with active molecules

Yani Chen

UNIVERSITÉ DE GRENOBLE

THÈSE

Pour obtenir le grade de

DOCTEUR DE L'UNIVERSITÉ DE GRENOBLE

Spécialité : **Nanophysique**

Arrêté ministériel : 7 août 2006

Présentée par

Yani CHEN

Thèse dirigée par **Vincent BOUCHIAT** et
codirigée par **Laëtitia MARTY et Nedjma BENDIAB**

préparée au sein du **Département Nanosciences de l'Institut Néel**
dans **l'École Doctorale de Physique**

Hybrid carbon based devices: functionalization of nanotube and graphene devices with active molecules

Dispositifs hybrides à base de carbone: fonctionnalisation de nanotubes et de graphène avec des molécules actives

Thèse soutenue publiquement le **20 Janvier 2016**
devant le jury composé de :

Dr. Vincent DERYCKE Directeur de Laboratoire, NIMBE, CEA Saclay, Paris	Rapporteur.
Dr. Pascal PUECH Maître de Conférences Hors Classe, CEMES, Toulouse	Rapporteur.
Dr. Benjamin GREVIN Chargé de Recherches, CEA-INAC, Grenoble	Examinateur.
Dr. Jean Sébastien LAURET Professeur, Laboratoire Aimé Cotton, Orsay	Examinateur.
Dr. Alain PENICAUD Directeur de Recherches, CRPP, Bordeaux	Examinateur.
Dr. Michel MERMOUX Directeur de Recherches, LEPMI, Grenoble	Examinateur.
Dr. Laëtitia MARTY Chargée de Recherches, Institut Néel, Grenoble	Invitée, Co-Directrice de thèse.
Dr. Nedjma BENDIAB Maîtresse de Conférences, Institut Néel, UGA	Co-Directrice de thèse.
Dr. Vincent BOUCHIAT Directeur de Recherches, Institut Néel, Grenoble,	Directeur de thèse.

RESUME

Dans le cadre de la recherche sur les dispositifs post-CMOS, l'électronique moléculaire bénéficie de la polyvalence de la chimie organique, qui offre de nouvelles fonctions alliant spécificités optiques et électroniques, tout en accédant au régime de confinement quantique intrinsèque aux petites molécules. Conducteurs 1D, les nanotubes de carbone font le lien entre l'électronique des petites molécules émergente et la technologie des semi-conducteurs, tout en tirant parti de la chimie organique. Au-delà de la miniaturisation, ils offrent la possibilité de concevoir de nouveaux dispositifs pour des capteurs, l'optoélectronique et l'électronique quantique. Cependant, la plupart des études se concentrent sur leurs applications aux capteurs ou pour le photovoltaïque qui impliquent un ensemble macroscopique de nanotubes. Dans ce cas, les transferts d'excitation sont moyennés sur un ensemble statistique, ce qui empêche l'accès à leurs mécanismes fondamentaux. Il est donc nécessaire de concevoir des dispositifs fonctionnels à base de nanotubes de carbone individuels. Pour cela, les nanotubes double paroi ont de nombreux avantages sur les monoparois. En général, ils présentent une stabilité plus élevée, qui peut être d'une aide substantielle dans des expériences à haute intensité et à fort champ. Ils réalisent un système cœur-coquille: leur structure concentrique suggère leur utilisation pour réaliser indépendamment un dopage ou une fonctionnalisation des tubes intérieur et extérieur. Dans ce projet de thèse, nous étudions des transistors à effet de champ basés sur des systèmes hybrides nanotubes individuels double paroi/chromophore. Nous présentons d'abord le procédé de fabrication de transistors à effet de champ de nanotubes de carbone à paroi individuels (DWFET), qui sont ensuite caractérisés à la fois par des techniques optiques et électriques. Nous avons notamment étudié le couplage électron-phonon par spectroscopie Raman sous dopage électrostatique. Le tube métallique interne apparaît également affecté par la grille électrostatique et montre des changements significatifs de la signature Raman. Nous avons ensuite fonctionnalisé les DWFET de façon non covalente avec deux types de molécules optiquement sensibles (terpyridine d'osmium et complexe de zinc (II) métalloporphyrine). Les hybrides sont caractérisés à la fois en optique et en transport électronique. Il apparaît un transfert de charge entre les molécules et le DWNT qui joue le rôle d'une grille chimique détectable par spectroscopie Raman et transport électrique, ce qui indique que les DWFETs peuvent être utilisés pour la détection de molécules. L'excitation lumineuse des molécules conduit à un dopage des hybrides et permet de plus de révéler le couplage entre les parois des nanotubes.

De plus, nous avons réalisé des expériences de grille optique à longueur d'onde variable sur les dispositifs hybrides, couplant à la fois la spectroscopie Raman et des mesures de transport électrique de la température ambiante jusqu'à la température de l'hélium. Le contrôle optique du comportement électronique des hybrides est expliqué en termes de transfert de charge photo-induit entre les molécules greffées et le DWNT. Par conséquent, nos FET hybrides peuvent être utilisés comme mémoire à commande optique jusqu'au régime de transfert d'électrons uniques.

ABSTRACT

In the frame of the intense research on electronics beyond CMOS, molecular electronics offers the versatility of organic chemistry in order to tailor new functions combining optical and electronic specifications, while accessing the quantum confined regime intrinsic to small molecules. As 1D conductors, carbon nanotubes bridge the gap between small molecules electronics and semiconductor technology with great promises while being a playground for organic chemistry. Beyond miniaturization, they offer the opportunity to design new devices from accurate sensors to optoelectronic and quantum devices. However most studies focus on sensor or photovoltaic applications and thus involve a macroscopic assembly of nanotubes. This averages the excitation transfers, which prevents access to their fundamental mechanisms. This requires the design of individual carbon nanotube based functional devices. For this issue double wall carbon nanotubes have many advantages over simple SWNTs. In general, they exhibit higher stability, which can be a substantial help in high-current and high-field experiments. They realize a core-shell system: their concentric structure suggests its use for independent doping or functionalization of inner and outer tubes. In this PhD project, we demonstrate field effect transistors based on hybrid systems of individual double wall carbon nanotubes and optically sensitive molecule. We first introduce the method for making individual double wall carbon nanotube field effect transistors (DWNT FETs), which are then characterized both optically and electrically. We also studied the electron phonon coupling in the DWNT system by Raman spectroscopy with electrostatic gating. The inner metallic tube is also affected by the electrostatic gate and shows dramatic changes of the overall Raman signature. We then functionalized non covalently two kinds of optically sensitive molecules to DWNT and graphene FETs (Terpyridine Osmium complex and Zinc(II) metalloporphyrin). The hybrids are characterized both optically and electrically. Charge transfer between DWNTs and molecules plays as a chemical gating which can be detected by Raman spectroscopy as well as electrical transport measurements, which indicates that the DWNT FETs can be utilized for molecular sensing. Light excitation of the molecules leads to doping of the hybrids and reveals the coupling between the nanotube walls.

Moreover, we realized wavelength dependent optical gating on the hybrid device, detected by both Raman spectroscopy and electrical transport measurements at both room temperature and helium temperature. The optical control of the hybrids' electronic behavior will be elucidated in terms of photo-induced charge transfer between the grafted molecules and the DWNT component. As a consequence,

this hybrid FETs can be used as an optically controlled memory down to single electron transfers at low temperature.

不积跬步，无以至千里；不积小流，无以成江海。

------ 荀子 《劝学篇》

A journey of thousands of miles may not be achieved through accumulation of each single step, just as the enormous ocean may not be formed gathering every brook or stream.

—Xun Zi, Advice on Studying

ACKNOWLEDGEMENTS

At first, I want to thank China Scholarship Council who support me to do my PhD in this lovely country-France. During the past three years, I enjoyed very much not only the wonderful French culture, but also the fabulous research activities here in Grenoble. Here I would like to thank all the people who have helped me with this thesis.

I wish to thank my supervisors Dr. Laëtitia Marty, Dr. Nedjma Bendiab and Dr. Vincent Bouchiat. They not only gave me a lot of help in their research field, but also gave me meticulous care in daily life. They are always patient in teaching me and always helpful at needs. I really enjoyed the time I worked with them.

Many thanks to my group members: Johann Coraux, Laurence Magaud, Julien Renard, who help me a lot and give me lots of precious advices during my PhD thesis.

I wish to give my appreciation to Amina Kimouche, Antoine Reserbat-plantey, Alexandre Artaud, Cornelia Schwarz, Dipankar Kalita, Fabien Jean, Farida Veliev, Hadi Arjmandi-Tash, John Landers, Sergio Vlaic, Shashank Mathur, Simone Lisi, Sudipta Dubey. They are wonderful team mates, I was lucky to be able to work with them.

A lot of thanks to our collaborators, they are Emmanuel Flahaut, Frédéric Lafollet, Guy Royal, Saioa Cobo.

And thanks to Sébastien Pairis, Simon Le-Denmat, Valérie Reita, for their technical help. Also thanks to the NanoFab team: Bruno Fernandez, Gwénaëlle Julié, Jean-François Motte, Thierry Crozes, Sébastien Dufresnes, Thierry Fournier. Without their help I could not have carried out a single experiment.

At the end, I would like to thank my family and my fiancé Dr. Wu Li for their love and supports.

CONTENTS

MOTIVATION OF THIS WORK

Carbon nanotubes offer the opportunity to design new devices from accurate sensors to optoelectronic and quantum devices. However most studies focus on sensor or photovoltaic applications and thus involve a macroscopic assembly of nanotubes. This averages the excitation transfers, which prevents access to their fundamental mechanisms. This requires the design of an individual carbon nanotube based functional devices. In this thesis we adress the issue of optical stimulus detection with nanotube/chromophore hybrids. We investigate single nanotube hybrids in order to tackle the fundamental mechanisms involved in the light excitation and detection since the most reported functionalized devices are made from DWNT bundles which brings the difficulties to interpret the physical processes.

We give a brief introduction to graphene and carbon nanotubes, including the geometry, synthesis methods, the electronic band structure and phonon dispersion.

We mainly use a non covalent method to functionalize graphene or isolated DWNT transistors with optically sensitive molecules, the vibrational and electronic properties of the hybrids will be discussed by combining Raman spectroscopy and electrical transport measurements. For this issue double wall carbon nanotubes have many advantages over simple SWNTs. In general, they exhibit higher stability, which can be a substantial help in high-current and high-field experiments. They realize a core-shell system: their concentric structure suggests its use for independent doping or functionalization of inner and outer tubes is possible. The inter-tube interaction plays an important role in the electrical and vibrational properties of DWNTs. But there are only a few studies focusing on individual DWNTs. In this thesis, we mainly focus on isolated DWNT functionalized transistors which will be the subject of Chapter 2. The charge transfer between the doping molecule and the DWNTs is an important issue in the functionalized devices. We used electrostatics doping and optical phonons to demonstrate the doping effect on both walls of a DWNT, which reflects inter-tube charge transfer.

The charge transfer between the chromophore and each wall of the DWNTs will be investigated by resonant Raman spectroscopy and electrical transport measurement at room temperature in Chapter 3. Both the influence of the grafting of the molecule and of the light stimulus will be investigated. We will present different kind of molecules with significant different behaviours: a redox and a conformational switching molecule.

In the fourth chapter we focus more on the optical excitation of the hybrid devices. Through optical gating experiment down to low temperature, we will address issues about the reversibility of the process and its dynamics.

Most of our work is devoted to non covalent grafting of the chromophores. Preliminary results on covalent grafting will be discussed in the last chapter in terms of perspectives for nanotube optoelectronics.

1 INTRODUCTION

This chapter aims to give a brief introduction to graphene and carbon nanotubes, including their structure, synthesis and characterisation methods, moreover, we will focus on their electronic band structure, phonon dispersion and finally their application, which provides the background of this thesis. Besides, we will also introduce the main motivation and the structure of this thesis.

1.1 STRUCTURE AND SYNTHESIS OF GRAPHENE AND CARBON NANOTUBES

Since it was first discovered by Geim and Novoselov in 2004, graphene was intensely studied by scientists all over the world [1]. Graphene is the latest discovered carbon allotrope after fullerene and carbon nanotubes. Since then, the carbon paradigm from zero dimension to three dimensions has completed, including 0D fullerene (e.g. C_{60}), 1D carbon nanotube, 2D graphene, 3D graphite and diamond *et al.*

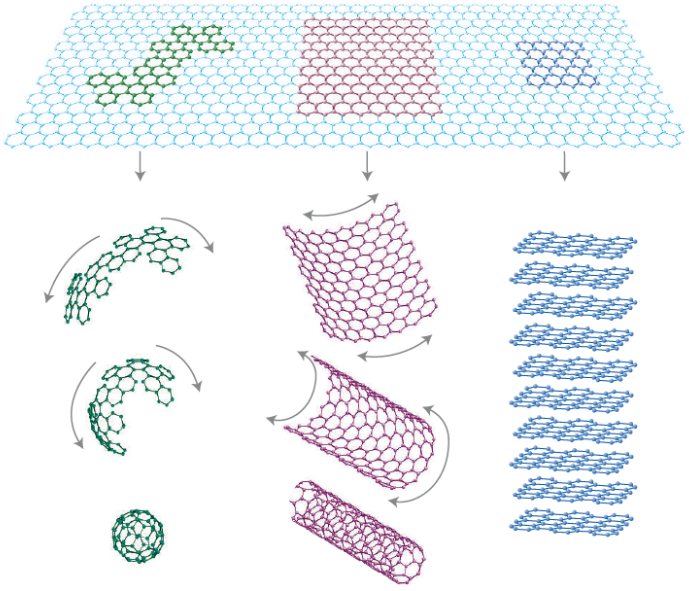

Figure 1: Mother of all graphitic forms. Graphene is a 2D building material for carbon materials of all other dimensionalities. It can be wrapped up into 0D buckyballs, rolled into 1D nanotubes or stacked into 3D graphite. Picture taken from [2].

Graphene and carbon nanotubes are both important materials in the sp^2 carbon family. Since carbon nanotubes were discovered before

graphene, many methods used to study graphene, for example, its electrical properties and optical properties, are borrowed from those for studying carbon nanotubes. They share many similarities, but also many differences.

1.1.1 *Structure of graphene and carbon nanotubes*

Graphene is a one-atom thick honeycomb-like sheet of carbon, and is thus a two-dimensional material. Carbon atoms are periodically arranged in the form of planar hexatomic rings. Each carbon atom is connected with three adjacent carbon atoms by σ bond. S, P_x and P_y hybridized orbitals form strong covalent bonds, which compose its sp^2 hybrid structure, and confer graphene very good mechanical properties. The estimated in-plane Young's modulus values of single- and bi-layer graphene are 2.4 ± 0.4 TPa and 2.0 ± 0.5 TPa, respectively [3]. The remaining P_z orbit forms a π orbit in the direction perpendicular to the plane. These π electrons can move freely in the graphene crystal plane, making a 2D free electron gas with outstanding mobility of $275,000$ cm^2 V^{-1} s^{-1} [4].

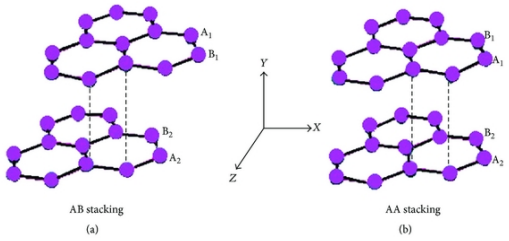

Figure 2: Sketch of the AB and AA stacking of bilayer graphene [5].

According to the number of layers, graphene can be classified into monolayer, bilayer and multilayer graphene, among which, though monolayer remains the case study material, bilayer graphene has also been widely studied in the recent years [6, 7, 8, 9, 10, 11]. Bilayer graphene can exist in the AB or AA form (Figure 2) or twisted with certain angles. It was predicted that a tunable bandgap can be introduced if an electric displacement field is applied to the two layers. The up left figure in Figure 3 presents the structure of bilayer graphene. The mismatch of the two layers form a twist angle and also a large periodic lattice (so called superlattice), which gives rise to a moiré pattern visible in STM and a Raman fingerprint.

Infinite single-wall nanotubes are hollow cylinders with carbon atoms organized in a honeycomb lattice. It can be considered as rolled monolayer graphene (for a review, see ref. [14]). Depending on the direction in which the graphene is rolled up, the resulting single wall carbon nanotube has different chiralities. Each SWNT is specified by the chiral vector C_h, defined as the vector corresponding to the

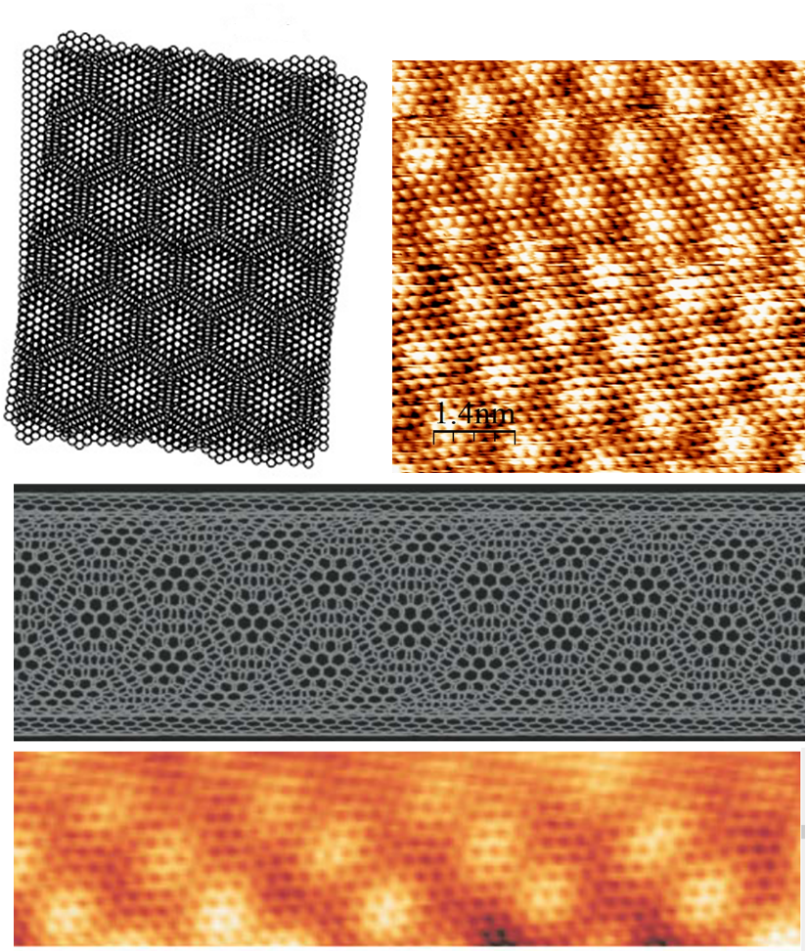

Figure 3: Sketches and atomically resolved STM images of bilayer graphene and DWNT, top: graphene, bottom: DWNT adapted from [12, 13].

circumference of the nanotube: $\mathbf{a}_1$ and $\mathbf{a}_2$ are two lattice vectors of graphene with 120 deg. between them, as shown in Figure 4.

$$\mathbf{C}_h = n \times \mathbf{a}_1 + m \times \mathbf{a}_2. \tag{1}$$

With this definition in the figure, $\mathbf{a}_1$ and $\mathbf{a}_2$ can be expressed using the Cartesian coordinate (x, y), $\mathbf{a_1} = (\frac{3}{2}a_{cc}, \frac{\sqrt{3}}{2}a_{cc})$ and $\mathbf{a_2} = (\frac{3}{2}a_{cc}, -\frac{\sqrt{3}}{2}a_{cc})$, where a_{cc} is the bond length of carbon atoms. For graphite $a_{cc} = 1.42$Å. The same value is often used for nanotubes. However, probably, $a_{cc} = 1.44$Å is a better approximation for nanotubes. Nevertheless, it depends on the curvature of the tube. A slightly larger value for higher curvature is required.

Hence, the combination of integers (n, m) characterizes the chirality of carbon nanotube. Chiral angle θ is defined as the angle between C_h and $\mathbf{a}_1$. The nanotube diameter can be calculated as

$$d = C_h/\pi = \sqrt{\frac{3}{2}}a_{CC}(m^2 + mn + n^2)/\pi, \tag{2}$$

and

$$\theta = \tan^{-1}[\sqrt{3}m/(m+2n)]. \quad (3)$$

The chirality (n,m) define the nanotube structure and also their electronic nature (Figure 4).

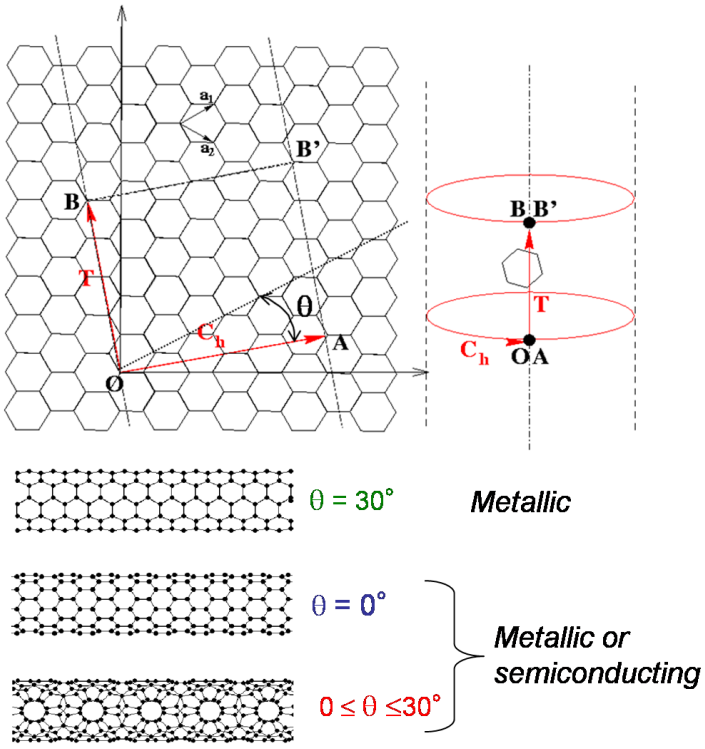

Figure 4: Structure of single wall carbon nanotubes [14].

1.1.2 *Synthesis of graphene and carbon nanotubes*

There are many methods for the synthesis of graphene and carbon nanotubes. The first monolayer graphene sample was made from the exfoliation of graphite using scotch tape [15], which is widely used for making high quality graphene in the lab. The graphene samples obtained in this way has a very high mobility (200,000 $cm^2.V^{-1}.s^{-1}$ at room temperature) [16]. However, it is not a scalable technique, as the flakes that can be obtained are in the micron range. Another method widely used by chemists is the chemical reduction of graphite to yield few-layer graphite oxide. Though reversible, this method induces a lot of defects and breaks the C=C bond. This type of graphene samples can be used for the functionalization for chemistry or biology purposes [17, 18]. Multilayer graphene has also been synthesized by thermal decomposition on the (0001) surface of 6H-SiC [19, 20].

The graphene used for this thesis was grown by chemical vapor deposition (CVD) on copper. In the recent few years, the CVD method

has become the most efficient way to make high quality, large size and uniform graphene [21, 22, 23]. By using copper as the catalytic substrate for the growth, it is possible to grow monolayer graphene over macroscopic surfaces [24]. In our research group, Z. Han et al. developed a pulsed CVD method to avoid any multilayer patches and make large scale homogeneous monolayer graphene (see Figure 5) [25]. The graphene made by this method has homogeneous optical and electronic properties. The mobility can reach as high as 200 000 $cm^2.V^{-1}.s^{-1}$.

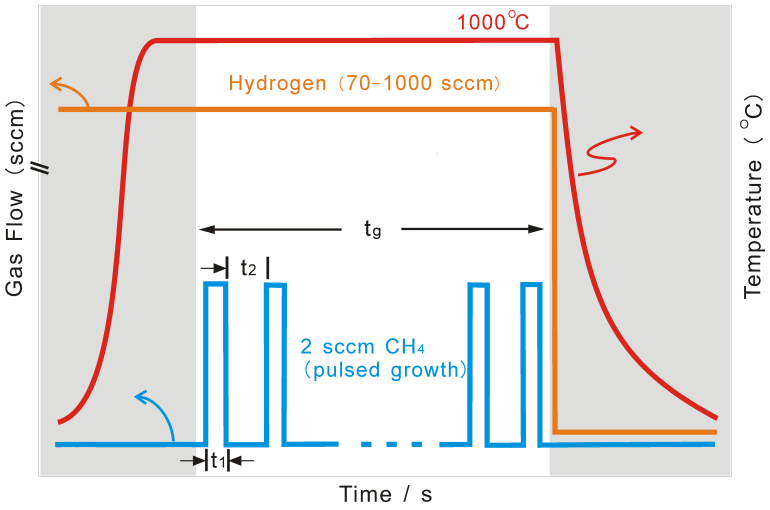

Figure 5: Sketch of work flow of standard and pulsed-CVD [25].

Many methods used to grow graphene are also applicable to carbon nanotubes. For example, the CVD method is also an important method for the carbon nanotube synthesis. Laser ablation [26] and arc discharge [27] are the other two methods that are mainly used for CNTs. Both of them need to make graphite sublimation. In order to reach the required high temperature, we can either create the arc discharge between two carbon electrodes or focus a laser onto graphite. The catalyst is also necessary. Normally, the transition metals (Fe, Co, Ni...) are used as the catalysts. They are put into the carbon electrode or the graphite rod. After a cooling down process, the carbon nanotube network or powder can be collected in the chamber. By controlling the catalyst, the reaction atmosphere and the pressure in the experiment chamber, the number of layers, the diameter and the purity can be controlled to a certain degree. Compared to laser ablation and arc discharge, the CVD method has many advantages.

Firstly, the experiment process is more controllable. There exist several parameters that can be used to tune the length, diameter and quality of carbon nanotubes:

1. The reaction gas, which is used as the carbon precursor. Many kinds of gas can be chosen from, for example, CH_2, C_2H_2, CH_4, CO et al.

2. The pressure and reaction time.

3. The type and size of catalyst particles.

Secondly, CVD is an efficient method for the mass production of carbon nanotubes. Last but not least, by using CVD, carbon nanotubes can be directly grown onto the silicon surface, metal electrodes or other substrates. This property makes more likely the control of the position and orientation of carbon nanotubes, which can directly self-assemble. This technique has many applications as well, for example, the field effect transistor, suspended carbon nanotube resonator and so on.

In this thesis, we mainly focus on the study of double wall carbon nanoutbes. Extending the CVD methods to synthesis of a high yield of double wall carbon nanotubes was achieved by controlling the thickness of the Fe catalyst thin film. T. Yamada *et al.* achieved an 85 percent yield of DWNTs [28]. M. Endo *et al.* developed a CVD method with a two-step purification process to fabricate high purity (more than 95%) DWNTs [29]. Another synthesis method used specifically for DWNTs or MWNTs is the so called "peapod" method. Peapods are fullerene filled SWNTs, which were first demonstrated in 1998 by Smith *et al.* [30]. Since the first example by Smith *et al.*,[31] the peapods have been used as precursors to prepare DWNTs by annealing in vacuum or inert gas. In this thesis, we have been using DWNTs from E. Flahaut *et al.* (CIRIMAT, Toulouse), which are fabricated by a catalytic chemical vapour deposition (CCVD) method. The carbon precusor is H_2-CH_4 mixture, and the heating and cooling rate is 5 °C.min^{-1} with a maximum temperature of 1000 °C. The catalyst is a $Mg_{1-x}Co_xO$ solid solution containing additions of Mo oxide; this MgO-based catalyst can be easily removed. This results in a dense mat of composite powder, which was treated with a concentrated aqueous HCl solution to separate the CNTs, leading to gram-scale amounts of clean carbon nanotubes [32].

To sum up, in this section, the structure and synthesis methods of graphene and carbon nanotubes has been introduced. The structure determines the electronic band structure and the phonon dispersion, and consequently the physical properties of DWNT. The next section will be dedicated to electronic band structure of graphene and CNTs.

1.2 ELECTRONIC STRUCTURE OF SP^2 CARBON

1.2.1 *Electronic band structure of monolayer graphene and single wall carbon nanotubes*

As discussed in the last section, graphene consists of a hexagonally organized carbon honeycomb lattice. The unit cell of monolayer graphene is shown in Figure 6. It contains two carbon atoms which were labeled as A and B. The distance between two atoms is $a = 0.142nm$, which

is an average of a single (C-C) and double (C=C) covalent σ bonds, as in the case of benzene.

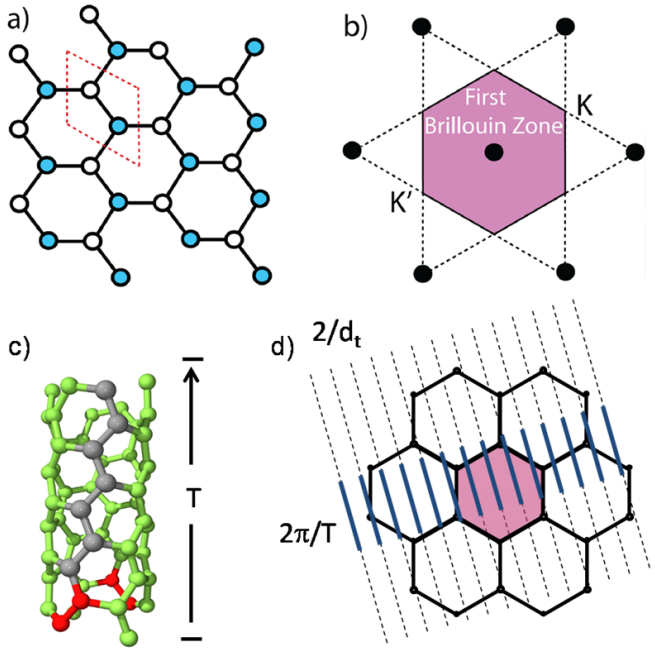

Figure 6: Schematics of graphene and carbon nanotube unit cells: (a) and (b) are the graphene lattice in real (a) and reciprocal space (b), (c) and (d) are the unit cell and first Brillouin zone of SWNT (figure adapted from Z. Han and R.Saito).

The band structure of graphene can be calculated from the tight-binding model [33]. The details of calculation can be easily found in the literature [34, 35, 36]. In this model, the electrons are not fixed on the lattice points, but in interaction with their neighbors. For this simple calculation, only the π electrons with interaction up to the first nearest neighbors (this interaction is characterized by the hopping parameter $\gamma_0 \simeq 3$ eV) is considered. Solving the Schrödinger equation in periodic lattice, the eigenvalue of the Bloch wave follows the energy dispersion relation:

$$E(\vec{k}) = \pm\gamma_0 \sqrt{1 + 4\cos\left(\frac{\sqrt{3}k_x a_{cc}}{2}\right)\cos\left(\frac{k_y a}{2}\right) + 4\cos^2\left(\frac{k_y a}{2}\right)} \quad (4)$$

The resulting band structure is presented in Figure 7. The valence and conduction bands can be distinguished. They meet at 6 points of the first Brillouin zone (noted as K and K′ points) with zero band gap.

Since a SWNT is a rolled up graphene sheet, the band structure can be obtained from the one of graphene. Figure 6 c) shows the unit cell of SWNT in real space. Because of the 1D quantum confinement, the Brillouin Zone (BZ) of a SWNT corresponds to a set of equidistant lines (also called cutting-lines or 1D BZs) in the BZ of 2D graphene (Figure 7). The direction and spacing of cutting lines are determined by C_h, as shown in Figure 6 d). If the cutting lines pass the **K** or

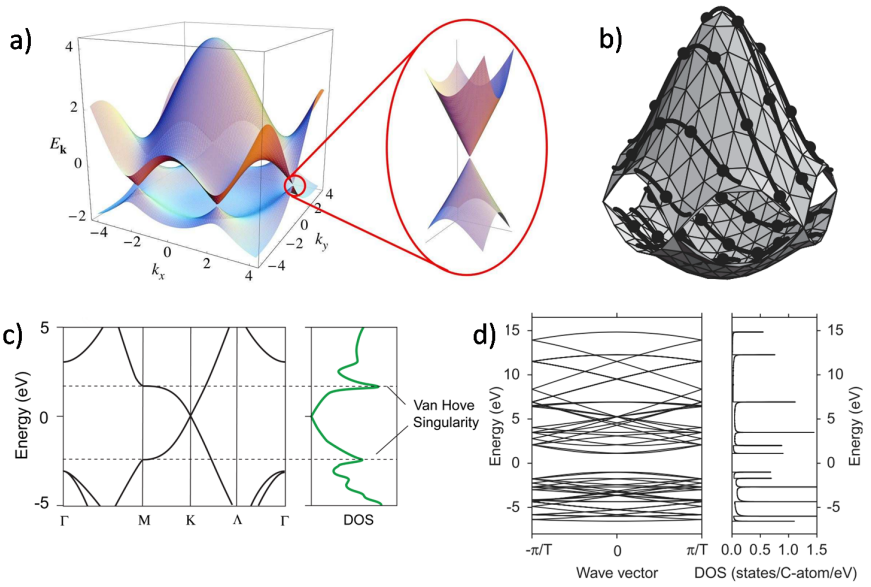

Figure 7: a) First Brillouin zone of graphene, b) calculated constant energy contours for the conduction an valence bands of graphene, the solid curves show the cutting line for the (4,2) nanotube. c) Band structure and DOS of graphene plotted as a cut of the 3D picture. d) Energy band diagram and DOS of the (4,2) carbon nanotube. Figure reproduced from [14, 36, 37, 38].

K'points, then the nanotube is metallic. Otherwise the nanotube is semiconducting. Therefore, the SWNTs are metals in case $(n - m)/3$ is an integer, and semiconductors (up to 2 eV bandgap) in other cases. Furthermore the density of states of SWNTs exhibits van Hove singularities (vHSs) depending on the chirality (Figure 7). Besides the chirality, curvature also plays a role in the electronic structure of SWNTs. For small diameter SWNTs, because the π electron states highly hybridize with the σ electron states, the tight binding model is not suitable anymore. The smaller the diameter, the greater the downward shift of the π states. Li *et al.* measured the absorption spectra of 4 Å single walled carbon nanotube, the results agreed well with the *ab initio* calculations of band structure based on the local density functional approximation [39], indicating that the strong hybridization is caused by the curvature.

1.2.2 *Electronic structure of double wall carbon nanotubes*

A DWNT is made of two SWNTs, but the electronic structure of DWNT cannot be simply considered as the sum of the two individual SWNTs. In 1993, Saito *et al.* studied commensurate metallic-metallic and also incommensurate metallic-semiconducting DWNTs, and found that the inner and outer tubules are coupled by interwall interaction. [40]. The interwall interaction should be considered when calculating the electronic structure of DWNTs.

By using tight binding method, Liang *et al.* found that there is a relation between interwall coupling strength and the diameter of DWNTs. Increasing interwall coupling and DWNT diameter causes the S@S tubes to become metallic. Many agree that the interwall interaction reduces the band gap or even drives the systems from semiconducting to metallic [41, 42, 40].

The interwall interaction also depends on the wall to wall distance. For example, Song *et al.* calculated the electronic structure of zigzag (7,0)@(15,0), (7,0)@(18,0) ,(8,0)@(16,0) and (4,2)@(10,5) DWNTs from DFT with the local density approximation [43]. Figure 8 shows their calculated band structure of (7,0), (15,0) SWNTs and (7,0)@(15,0) DWNT. Both of the π and π^* bands of the inner (7,0) SWNT have a larger downshift than those of the outer (15,0) SWNT. The downshifts caused by the interwall interaction. When the interwall distance becomes smaller, the downshifts becomes larger. For instance, for the larger inner (8,0) tube, the downshift is smaller and does not lead to a metallic state.

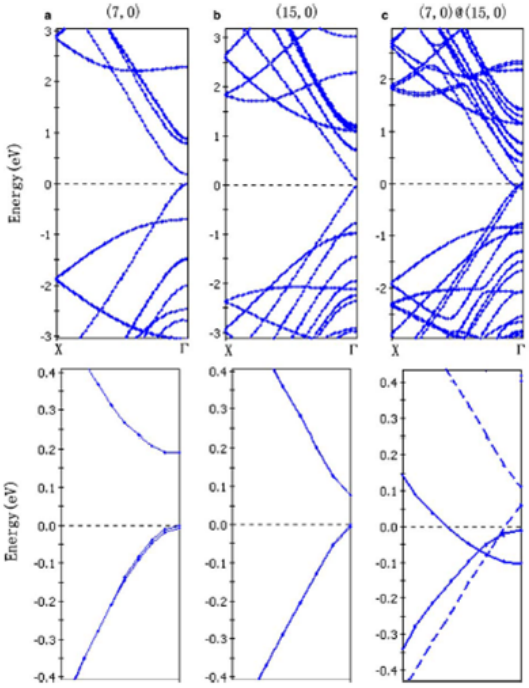

Figure 8: calculated electronic structure of (7,0),(15,0) SWNT, and (7,0)@(15,0) DWNT, figure taken from [43].

There are several other works related to the calculation of the electronic structure of DWNTs [44, 42, 43]. Because DWNT is a core-shell system, the inner tube and the outer tube have different chiralities. The unit cell of DWNT can then end up very big. The earlier calculations based on DFT or tight binding method only handled some special tube pairs, for example, both of which are armchair or zigzag tubes. The calculation of the electronic structure of DWNTs still have limitations. As mentioned, the DFT calculation can only apply to small unit cell DWNTs. In other cases, the parameters used

for the calculation still need to be chosen with great care in order to match experiments better.

From the experimental point of view, many different techniques have been used to investigate the electronic structures. Most experiments involve two or three techniques for unambiguous determination of the chirality and the electrical or optical properties. The experimental works also indicate that the interwall interaction has a strong influence on the electronic structure of DWNT. For example, Giusca *et al.* [45] used transmission electron microscopy (TEM) to get the distribution of the inner and outer tube diameters. They found that the inner diameters of their samples range from 0.9 to 1.9 nm, and the outer ones range from 1.9 to 2.6 nm, with the wall to wall distance ranging from 0.30 to 0.54 nm. Then they dispersed DWNTs onto Au substrate and obtained their structure by Scanning Tunneling Spectroscopy (STS) of a single DWNT. By comparing with DWNT density of state calculation, they deduced that the chirality of the outer tube is (18,10). Although the outer tube has semiconducting-like chirality, it shows finite DOS at the Fermi level (Figure 9 a)). Then inner tube chirality can be determined by comparing with the calculations (Figure 9 b)). However, this tube exhibits several additional Van Hove singularities, which are due to band structure modification by the interwall interaction.

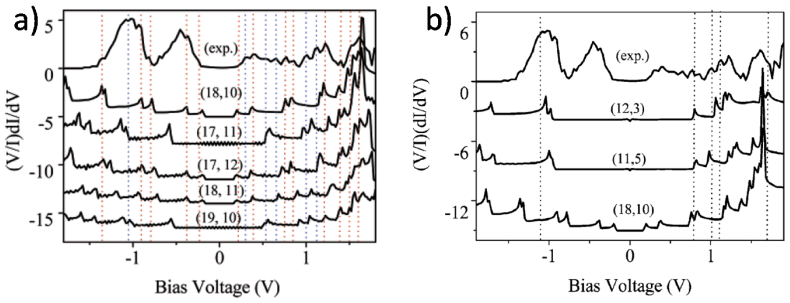

Figure 9: Scanning tunneling spectroscopy of a DWNT, (a) from the comparison with the calculation of SWNT DOS, the outer wall chirality is determined, (b) additional peaks come from the inter-tube interation [45].

These results show that the interaction between the outer wall and the inner wall cannot be ignored. The intertube interaction has interesting consequences on the electronic properties, as well as on vibrational properties probed by Raman spectroscopy, which we will discuss in the next section.

In this section, we introduced the electronic structures of graphene, SWNTs and DWNTs. In graphene, electrons behave like massless Dirac Fermions that appear in the electronic band structure as gapless excitations with a linear dispersion-the "Dirac cone". The electronic band structure of SWNTs can be obtained by superimposing the 1D cutting lines on the 2D graphene BZ. For DWNTs, the electronic structure cannot be considered as the sum of two individual SWNTs' ones, because of the interwall interaction. The current theoretical and ex-

perimental works studying the influence of the interwall interaction have limitations. Since the electronic properties rely on the electronic structures, it is very important to find new ways to study the influence of interwall interaction in a more accurate and straightforward manner.

The interwall interaction can also influence the vibrational properties of DWNTs, which will modify the Raman spectra of DWNTs. Moreover, because of band structure modification in the DWNT induced by the interwall interaction, the resonance Raman spectra will be influenced, which we will discuss in the next section.

1.3 VIBRATIONAL PROPERTIES OF GRAPHENE AND NANOTUBES

1.3.1 *Raman spectroscopy: a brief introduction*

When a substance is illuminated, part of the energy passes through it (transmission). The other part of energy is absorbed, reflected and scattered by the substance. Raman scattering is an inelastic scattering of light, that is, the frequency of the scattered light is different from the incident light. Raman scattering has two inelastically scattered components with frequency $\omega - \omega_0$ (Stokes) and $\omega + \omega_0$ (anti-Stokes). Feynman diagrams of the Stokes and anti-Stokes processes are shown in Figure 10. In experiments, most Raman spectra are Stokes measurements (as phonon absorption is a more probable event than phonon emission), Raman spectra show intensity of scattered light vs. the difference between incident and scattered photon energy, the so called "Raman shift" in cm^{-1} units.

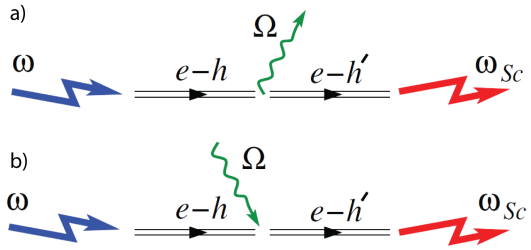

Figure 10: Feynman diagram of (a) Stokes scattering, (b) anti-Stokes scattering, picture adapted from [46].

In a scattering event, (1) an electron is excited from the valence energy band to a virtual band or a real electronic conduction energy band (resonance Raman scattering) by absorbing a photon, (2) the excited electron is scattered by emitting (or absorbing) phonons, and (3) the electron relaxes to a virtual valence band or another real electronic band (resonance Raman scattering) by emitting a photon. In Stokes measurements, the scattered photons whose energy is smaller than the incident photon are collected. By measuring the intensity of scattered light as a function of frequency downshift (losing energy)

of incident light, phonon frequencies of the probed material can be obtained Figure 11.

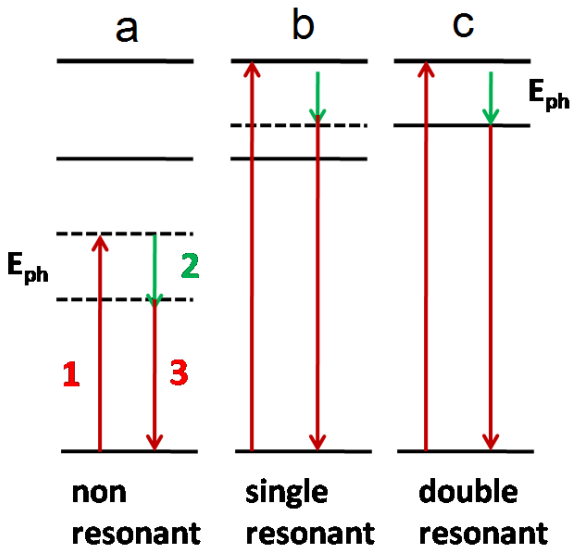

Figure 11: Scheme of Raman scattering process, (a) non resonant, (b) single resonant (incoming resonance), (c) double resonant (incoming and outcoming resonance), figure taken from [47]

The incident photons have energy E_i and momentum k_i. After scattering, the photon energy and momentum change to E_d and k_d, respectively. The scattering process obeys the conservation laws:

$$E_d = E_i + E_{ph} \tag{5}$$

$$\mathbf{k}_d = \mathbf{k}_i + \mathbf{q} \tag{6}$$

E_{ph} and $\mathbf{q}$ are phonon energy and momentum, respectively. Based on the Fermi golden rule, the Raman intensity I_{Raman} is related to 1) electron-radiation matrix element M_{e-r} for the incident or scattered light; 2) electron-phonon coupling matrix element M_{e-ph}; 3) energy E_μ corresponding to a certain transition state:

$$I(E_{ph}, E_i) = (n+1)\left|\frac{M_{e-r}M_{e-ph}M_{e-r}}{\Delta E(\Delta E - E_{ph})}\right|. \tag{7}$$

$\Delta E = E_i - E_\mu - i\gamma$, and E_μ is the energy difference between the ground electronic state and the intermediate state. γ is a damping parameter characterizing the life time of the excited electronic intermediate state, which determines the resonance window and inversely proportional to the electronic transition relaxation time τ,

$$\gamma = \frac{\hbar}{\tau} \tag{8}$$

The width of Raman peak (Γ) contains information about the anharmonic effect and/or anything else that disturbs the phonon life time, for example, the electron-phonon coupling.

The simplified expression of the Raman intensity shows two resonant laser energy

$$\begin{aligned} E_i &= E_\mu \qquad \text{incoming resonance} \\ E_i &= E_\mu + E_{ph} \qquad \text{outcoming resonance,} \end{aligned} \tag{9}$$

where the Raman signal reaches maximum. If one of these conditions is met, the process is a single resonance Raman process (see Figure 11). If both conditions are met, the process is a double resonance Raman process. The resonance phenomenon is important in the cases of carbon nanotubes and graphene. Both single and double resonances are observed in carbon nanotubes, but they have distinct features and yield different kinds of physical insight into nanotubes. The principle of resonant Raman scattering is responsible for the explanation of several observations.

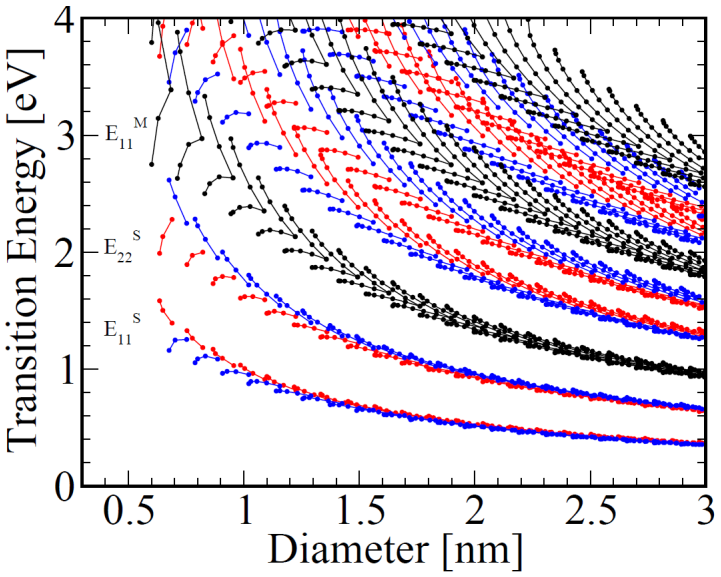

Figure 12: The Kataura plot for bundled SWNTs with medium diameter of about 1.4 nm. [48, 49, 50]

In practice, the carbon nanotube exhibits molecular-like behavior, with well defined electronic energy levels at van Hove singularities. A resonant Raman process occurs when the laser excitation energy is equal to the energy spacing between vHSs in the valence and conduction bands that are restricted to the selection rules required for optically allowed electronic transitions. When Raman spectra are measured, only the carbon nanotube with E_{ii} in resonance with the laser energy will contribute strongly to the spectrum, where E_{ii} [48, 49, 50] represents an optically allowed electronic transition energy. Kataura plot [48, 49, 50] shows the energy E_{ii} versus the nanotube diameter Figure 12. Each data point represents E_{ii} for a given (n, m) SWNT.

Kataura plots are very useful for Raman and PL characterization of carbon nanotubes.

1.3.2 *Optical phonons of graphene and carbon nanotubes*

Phonons are quanta of lattice vibrations in normal modes, which affect many processes in crystals. Phonons are carriers of thermal energy. The phonon dispersion of SWNTs can be deduced from the phonon dispersion of 2D graphene, as done for electronic band structure. Figure 13 shows the phonon dispersion of graphene and SWNTs.

1. For graphene: Graphene has three optical phonon modes, i.e. longitudinal optical (LO), in-plane transverse optical (iTO) and out-of-plane transverse optical (oTO) modes and three acoustic phonon modes (LA,iTA,oTA) [Figure 13 (a)].

2. For SWNTs: The phonon dispersion can be derived from that for graphene, as we discussed in the electronic structure session. Their unit cell comprises more atoms than graphene, and thus SWNTs have more phonon modes. Note that the LO and TO phonon modes of graphene are no longer degenerate in the case of nanotubes because of the curvature effect, showing two differentiable bands G^- and G^+ (Figure 14). Moreover, there is an additional mode only present in nanotubes, the radial breathing mode, in which the atoms vibrate along a radial direction of the tube.

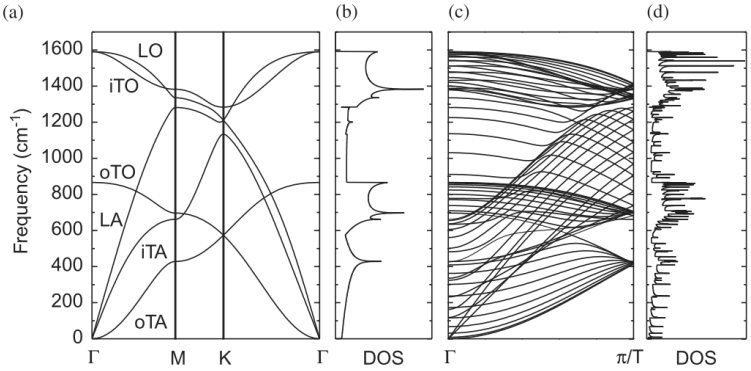

Figure 13: Phonon dispersion of graphene and CNTs, (a) phonon dispersion of graphene, (b) the phonon density of states of graphene, (c) the calculated phonon dispersion of (10,10) carbon nanotube, (d) phonon density of state of the (10,10) carbon nanotube (figure taken from [14])

Raman spectra from different types of sp^2 nanocarbons are shown in Figure 14. The graphene-related structures are labeled next to their respective spectra. The detailed analysis of the frequency, line shape, and intensity for these features gives a great deal of information about each respective sp^2 carbon structure.

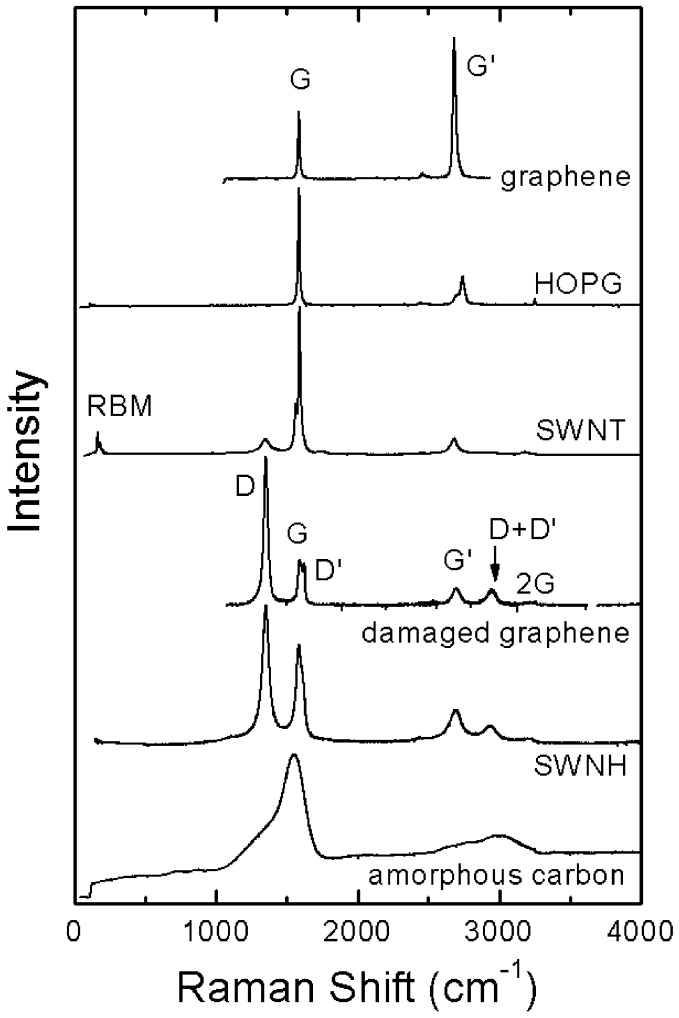

Figure 14: Raman spectra from different types of sp^2 nanocarbons. The graphene-related structures are labeled next to their respective spectra (figure taken from [51].)

Graphene has two atoms per unit cell, thus six normal modes (3 degrees of freedom for each atom, but actually two of the modes are doubly degenerate) at the Brillouin zone centre Γ (Figure 15).

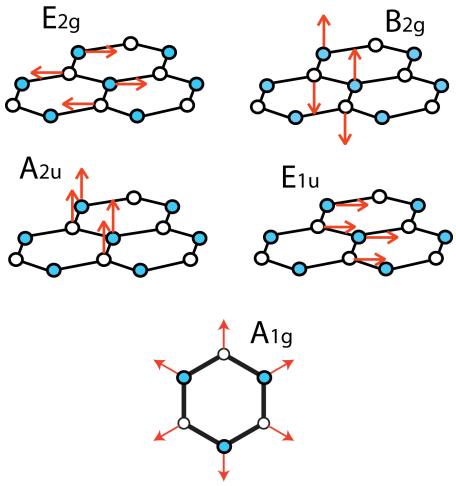

Figure 15: Lattice vibrating modes of graphene.

The G band (~ 1582 cm^{-1}, for laser excitation at 2.41 eV) can be found in all sp^2 carbon allotropes, whose energy is insensitive to incident laser, but can be influenced by factors that can affect the C-C bond, such as strain, doping, or temperature. Moreover, G band intensity is proportional to the number of graphene layers (up to about 10 layers). The G band is associated with the doubly degenerate (iTO and LO) phonon mode (E_{2g} symmetry) at the Brillouin zone center, which is the only band coming from a normal first order Raman scattering process in graphene systems.

When introducing defects, some modes are thus visible, this is the case of D band (~ 1350 cm^{-1}, for laser excitation at 2.41 eV). The associated vibrational mode D is the breath of aromatic rings. It comes from iTO phonons around the Brillouin zone corner K (A_{1g} symmetry). It requires a defect to activate it and it is a double resonance process, which is strongly dispersive with excitation energy. The D band phonon at K point is related to defects in graphitic materials. This peak was firstly assigned by Tuinstra *et al.* in 1970 [52], they show the presence of mode around 1355 cm^{-1} observed in disorderly or non crystalline graphite samples.

The 2D band is an intense band in graphitic systems, between 2650 and 2800 cm^{-1}, this 2D band is always present in sp^2 carbon (graphite, nanotubes, graphene). The 2D band is related to a double resonant process leading to the most intense Raman peak in the case of graphene. The double resonance process means that all the involved states in this process are real electronic states of the system. In general, the 2D band is generated by four steps where (a) an incoming photon excites an electron with wave vector **k**, (b) the electron is scattered from **k** to **k+q** by emitting a phonon with wavevector **q**, (c) the electron is backscattered from **k+q** to **k** by emitting a second phonon with wavevector **-q**, and (d) the electron recombines with a hole at **k**. Moreover, intensity and frequency of 2D band are extremely sensitive to the environment. In the graphene system, the 2D peak is also used widely to analyze the number of layers.

The D′ band is located near the right shoulder of G band (~ 1610 cm^{-1}, for laser excitation at 2.41 eV), and is due to double resonance of an intra-valley process connecting two points of the same Dirac cone (**K** or **K′**).

As a member of sp^2 carbon family, many peaks in graphene also exist in carbon nanotubes. In the following paragraphs, we will mainly discuss the G mode and the RBM mode in carbon nanotubes.

Lim *et al.* [53] used a macroscopic ensemble of highly (6,5) enriched single wall carbon nanotubes and observed vibrational modes in large spectral range (10-3000 cm^{-1}). A total of 14 modes were clearly resolved and identified, including fundamental modes of A, E_1,and E_2 symmetries and their combinational modes involving two and three phonons (Figure 16).

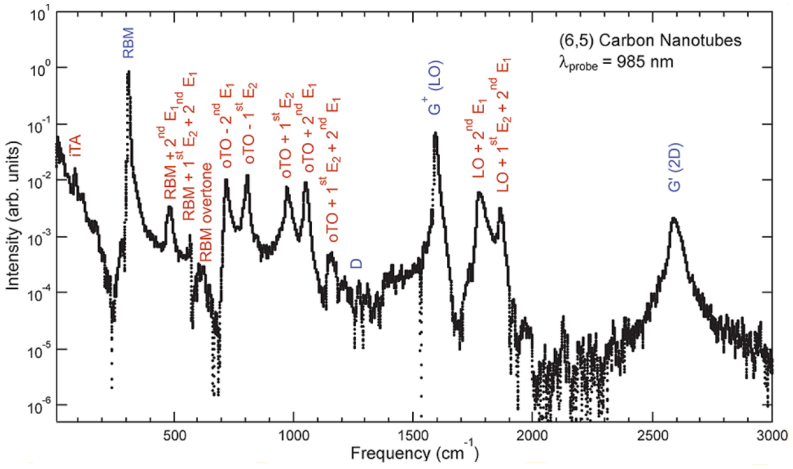

Figure 16: Fundamental and combinational mode in highly (6,5) enriched SWNT, the intensity is plotted in logarithm scale (figure taken from [53]).

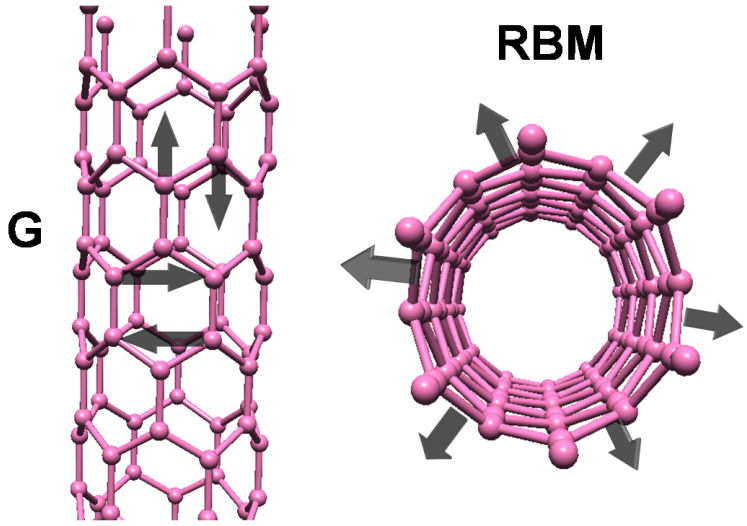

Figure 17: Scheme of the atomic vibration for the G (left) and the RBM (right) mode

The radial-breathing mode (RBM) is an important mode for characterization and identification of carbon nanotubes, in particular of their chirality. The RBM Raman feature of carbon nanotubes corresponds to atomic vibration of C atoms in the radial direction, as shown in Figure 17. The importance of radial-breathing mode for single wall carbon nanotube characterization comes from its frequency dependance with the tube diameter, $\omega_{RBM} = A/d_t + B$, where A and B are determined experimentally. In the case of double-walled nanotubes, the radial-breathing like modes (RBLMs) are the eigenmodes of the inner and outer tubes combine into in phase and out-of-phase modes, and their coupling is described by the graphite inter layer coupling strength. Popov and Henrard showed using a valence-force field model that the coupled radial modes both increase in frequency compared to the same tube in single walled form (see Figure 19). Experimentally, the exact assignment of double-walled tube modes have not been conclusively identified. In this thesis, we will call the RBLM

mode for DWNT instead of RBM mode because of the interwall interaction.

As mentioned above, the RBLM is a resonant Raman feature. The Raman intensity is enhanced by some orders of magnitude if the energy of the incident or scattered light matches the energy of an electronic transition. A single resonance profile is rendered by recording the Raman intensity as a function of excitation energy.

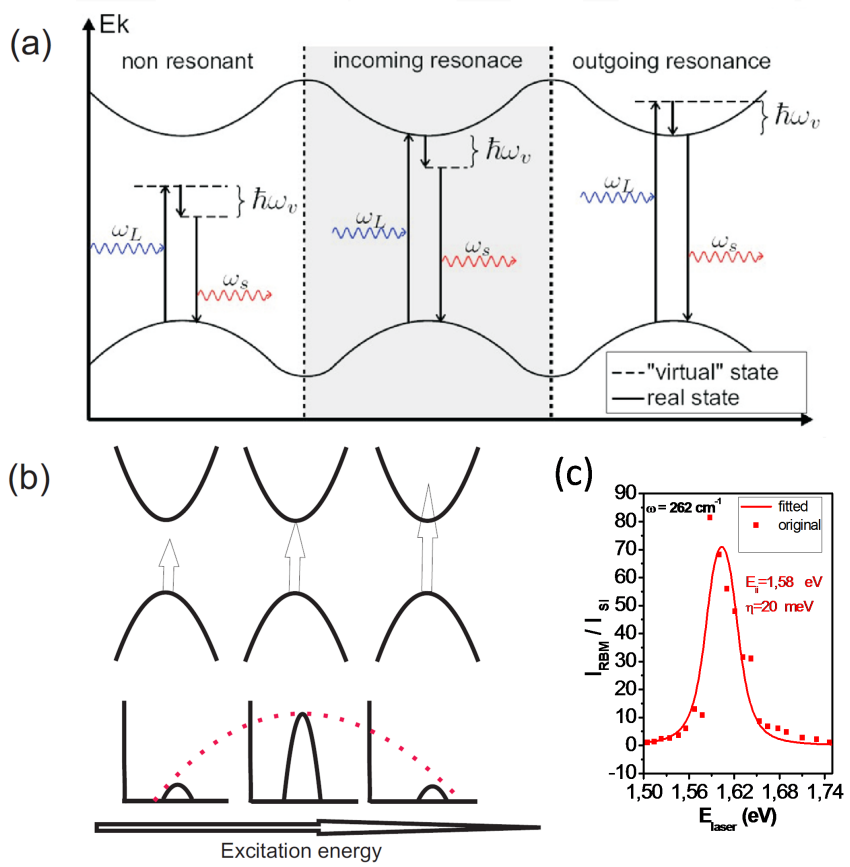

Figure 18: Schematic representation of the non resonance, incoming resonance and the outgoing resonance process (a), the resonance condition and the resonance window (b) (adapted from [54, 55]), (c) our data of tunable Raman spectra, fitted by Equation 10.

In this thesis, to quantify the strength of the measured Raman scattered signal (mainly the RBLM peaks), we use the differential Raman scattering cross-section

$$\frac{d\sigma(E_l, E_{ph}, \theta)}{d\Omega} = A\frac{(E_l - E_{ph})^2}{E_{ph}^2 E_l^2}\left|\frac{1}{\sqrt{E_l \mp E_{ph} - E_{ii} - i\eta}} - \frac{1}{\sqrt{E_l - E_{ii} - i\eta}}\right|^2 \tag{10}$$

[56, 57]. Where, $A = CN_{ph}\left|M_{e-ph}\right|^2$. C is a tube dependent constant which includes the photon energy independent parts of the optical matrix elements. E_l is the excitation photon energy, E_{ph} is the phonon energy, η is the broadening factor and related to elec-

tronic transition relaxation time, M_{e-ph} is the e-ph transition element (here we suppose that the electron phonon coupling contribution to the RBLM modes did not change with the laser energy), $N_{ph} = (n_{ph} + 1)$ for Stokes scattering and $N_{ph} = n_{ph}$ for anti-Stokes scattering, $n_{ph} = 1/(e^{E_{ph}/kT} - 1)$ is the phonon number.

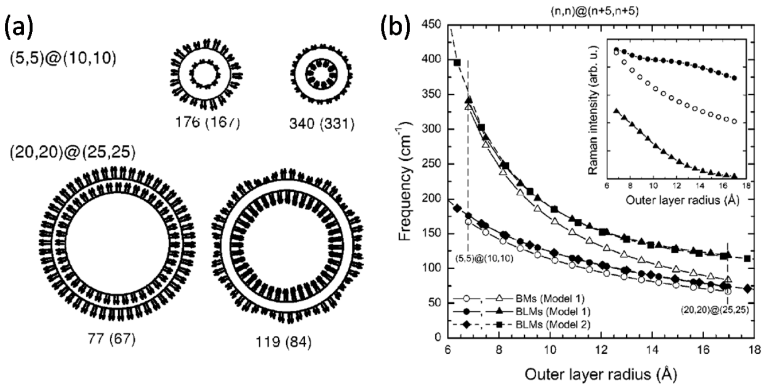

Figure 19: (a) Displacement of the unit cell atoms and frequencies for RBLM of two kinds of DWNTs with considering the inter-tube interaction. (b) Frequencies of coupled radial-breathing modes in double-walled nanotubes. Open symbols belong to uncoupled tubes of the same diameter, solid symbols to double-walled nanotubes. The coupled frequencies are always higher than the uncoupled ones. Figure taken from [58]

The G bands in carbon nanotubes are different from graphene: In contrast to the graphite Raman G band, which exhibits one single Lorentzian peak at 1582 cm^{-1} related to the tangential mode vibrations of carbon atoms, the SWNT G band split into G^- and the G^+ bands, due to the phonon wave vector confinement along the SWNT circumferential direction and due to symmetry-breaking effects associated with SWNT curvature which softens the tangential vibration in the circumferential direction (see Figure 17) [14]. In many cases the G^- band shows an asymmetric (Breit-Wigner-Fano) (BWF) shape. This BWF line is also observed in many graphite-like materials with metallic character, such as n-doped graphite intercalated compounds, n-doped fullerenes. The BWF feature is a signature of metallic tube, but not all the metallic tube shows a BWF feature. The G^- mode has also diameter dependence. Figure 20 shows the frequency vs. $1/d_t$ for the two most intense G band features (ω_{G^+} and ω_{G^-}) from isolated SWNTs. ω_{G^+} is practically independent of tube diameter, ω_{G^+} decreases when decreasing d_t, and this decrease becomes larger as the curvature of the sheet increases.

1.3.3 *Charge transfer influence on optical phonons*

Raman spectroscopy can non-invasively probe graphene and carbon nanotubes. It is also a useful tool to understand the electron phonon coupling in the sp^2 carbon system. It contains profound information by measuring a single spectrum. For example, doping or strain can

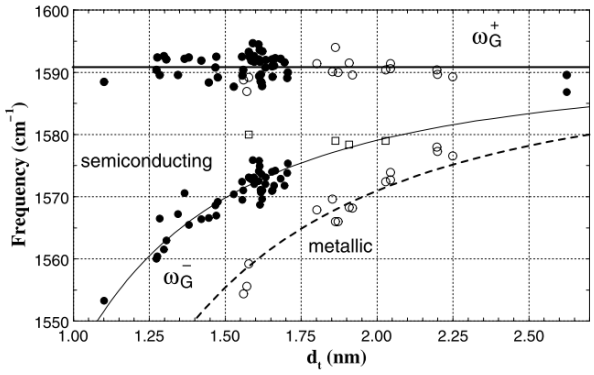

Figure 20: Diameter dependence for ω_{G^+} and ω_{G^-} for several isolated semiconducting and metallic SWNTs [59]

affect the full-width half maximum, peak area, peak position of G and 2D band. In the following paragraphs, we will mainly discuss the doping effect, since in the CNT and molecule hybrids, doping effect is the most important issue for the modification of Raman spectra.

As early as 1997, Rao *et al.* [60] studied the charge transfer from small molecules to carbon nanotubes by Raman spectroscopy. They doped carbon nanotubes with different kinds of molecules (electron donor and acceptor) and studied the G peak and the RBLM peak shifts for each doping conditions.

Carbon nanotube or graphene transistors have high mobility and are very sensitive to the environment change since all their atoms are exposed to it. Transfer of charges or the change of dipolar environment can be induced by deposition of molecules on the surface of nanotubes or graphene; or due to an electrical field applied by a back gate or top gate. One ultimate interest of such sensitivity to doping is to modulate the electronic properties of the transistors based on sp^2 nano carbon materials to induce superconductivity, such as the carbon nanotubes doped with boron or nitrogen [61]. Variation of the density of electric charges in graphene or metallic nanotubes strongly affects certain phonon modes due to the electron phonon coupling as explained below.

To test the effect of charge, the Fermi level is modulated by i) a back gate, ii) a top gate or side gate, iii) an ionic liquid gate. Figure 21 presents a summary about the study of the graphene or carbon nanotube G peak change while changing the Fermi level modulated by electrostatic doping.

It is found that the variation of the Fermi level leads to a softening of the phonon mode associated with the G band of graphene and nanotubes (LO mode). The work of Caudal *et al.* [71] in 2007 (nanotubes), Piscanec *et al.* [72] (graphite and nanotube) and Pisana *et al.* [65] in 2007 (graphene) lead to establish a model explaining the sensitivity of the G mode to the position of the Fermi level. In summary,

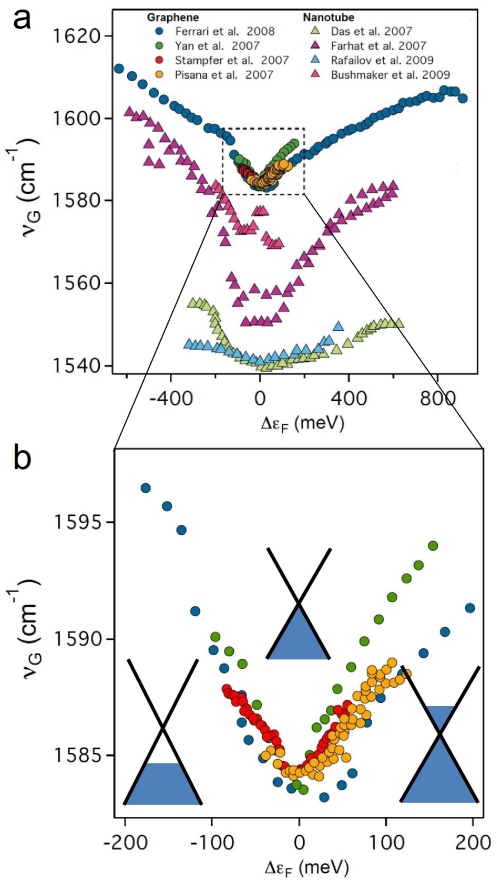

Figure 21: The Raman G peak dependence on the electronic doping; a, frequency of the G peak according to the Fermi level for graphene and metallic nanotubes; b, details for the graphene with low values of doping and sketch of the Fermi level shift, data taken from [62, 63, 64, 65, 66, 67, 68, 69], figure adapted from [70].

the dynamic matrix, which decides the frequency of phonon modes, contains an electron-phonon coupling term involving two kinds of interaction. One is the inter band (electron transition between the valence and conduction bands), and the other one is intra-band (electronic transition within the same band). For low values of doping (Δ E_F < upper band), electronic inter-band transitions dominate according to the transition diagram shown in Figure 21. By varying the position of the Fermi level around the Dirac point, the system reaches a regime where the electronic transition by phonon absorption turns possible or not. This change occurs when the Fermi level is shifted by an amount equal to half of the involved phonon energy.

The phonon spectrum has a singularity in the dispersion of the LO mode at $q = 0$. This singularity is called Kohn anomaly, and it is also observed for $q = K$ (D and 2D modes) [73]. Here we must emphasize that to describe the Kohn anomaly, it is necessary to consider the dynamic effects of ions compared to electrons. Meaning that adiabatic approximation Born-Oppenheimer is no longer valid [72]. The electron system cannot remain in the ground state and the the electron system is shaken up by an atomic vibration while keeping their

electronic ground state. The model should then describe the energy variation of G (LO) phonon with $q = 0$ (G band) as a function of displacement u associated with this mode along with the consequent variation of the Fermi level depending on the position of the ions since it is outside the framework of the adiabatic Born-Oppenheimer approximation:

$$\Delta\omega_G = \frac{1}{2m\omega_G^0}\frac{d^2\Delta E_F(u)}{du^2} \tag{11}$$

To sum up, any induced charge or dipolar environment change can affect the Raman spectra of graphene and CNTs through the electron-electron interaction or electron-phonon interaction. The charge can be injected into the system by molecular doping or electrostatic doping through a top or back gate, then the charge induced Raman spectra change can be studied systematically. We will now focus more specifically on the Raman spectroscopy of DWNTs.

1.3.4 *Optical phonons of DWNTs*

The first Raman spectroscopy experiments have been performed on DWNT bundles because nanosized carbon nanotubes have a high tendency toward self-aggregation due to strong van der Waals forces. Samples used, were synthesised by CVD method [74, 75] or peapod method [76, 77]. Figure 22 shows the Raman spectra of SWNTs, peapods and final product–DWNT bundles.

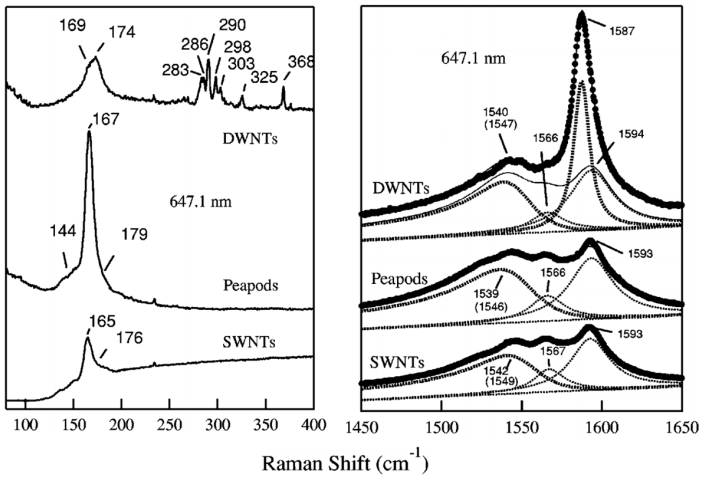

Figure 22: Raman spectra of SWNTs, peapods and DWNT bundles (figure adapted from [76])

The RBLM band is very interesting since responses of inner tube and outer tube are well separated since RBLM frequency is inversely proportional to tube diameter. From the Raman spectra, we can clearly see that peaks come out after 250 cm^{-1} which stand for the evolution from peapod to DWNT bundles. The Raman spectra of RBLM modes

of DWNTs show a much larger number of inner tubes RBLMs than geometrically possible [78]. It was certified by comparing the DWNT Raman map (contour plots of the RBLM intensity vs. frequency and excitation energy) to the SWNTs one [79](Figure 23). For example, the (6,5) and (6,4) tube show more than one RBM frequencies and form to cluster in the map. Pfeiffer *et al.* claimed that the clusters originate from the same inner-tube type accommodated in several different outer tubes. The inter tube interaction depends on the chirality difference of the two tubes. The stronger the interaction, the further the inner tube RBLM shifts to higher frequencies.

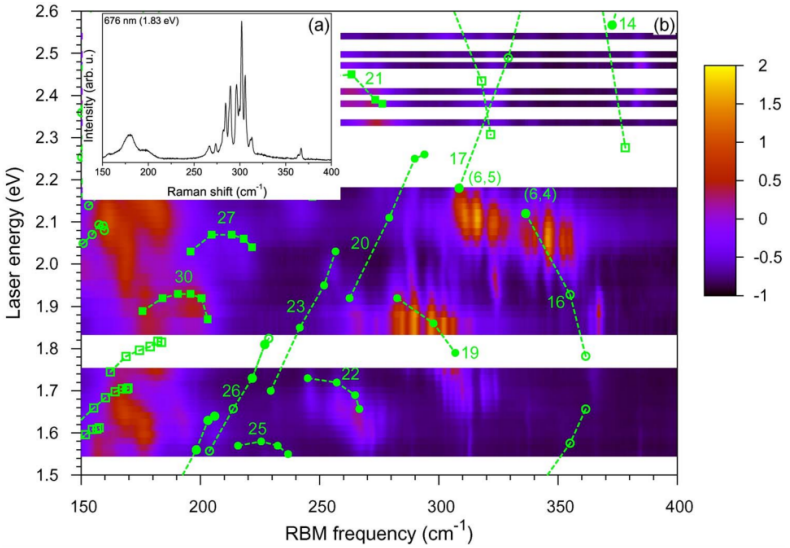

Figure 23: Fine structures of RBLM mode of DWNT bundles. The green lines are measured RBLM frenquencies and transition energies of sodium dodecyl sulfate wrapped HiPCo tubes. (figure adapted from [79])

Only a few groups measured the Raman spectra on individual DWNTs [80, 81]. Some experiments were performed on either isolated DWNTs lying on substrates or suspended DWNTs combined with Rayleigh scattering or TEM measurement. The experiments performed on suspended DWNTs could avoid the influence of the environment and reveal the intrinsic properties of DWNTs, especially the inner wall coupling between the outer and inner shells of DWNTs. For example, D.Levshov *et.al* performed Raman scattering experiment on chirality determined individual suspended DWNTs. They showed that the Raman features obtained at different excitation energies on the (12,8)@ (16,14) DWCNT can only be understood in a coherent way by considering the coupling between the two concentric layers. Because both of the RBLM frequency and intensity have mismatch to single wall carbon nanotube [82]. More recently, Levshov *et al.* investigated the intertube distance dependence of G-modes of individual index-identified DWNTs composed of two semiconducting SWNTs [81]. The results are: (1) when the interlayer distance is larger than the nominal van der Waals distance (close to 0.34 nm), a downshift of the inner-layer G-modes with respect to the G-modes in the equiva-

lent SWNTs is measured, (2) the amplitude of the downshift depends on the interlayer distance, or in other words, on the negative pressure felt by the inner layer in DWNT, (3) no shift is observed for an intertube distance close to 0.34 nm. This investigation indicates that not every DWNT has strong interlayer interation, it really depends on tube diameter and these relationship is still unclear.

Liu *et al.* combined simultaneous structral (TEM), electronic (Rayleigh scattering) and vibrational (Raman scattering) to investigate the coupled RBLM oscillations. From the modeling of the RBLMs frequencies measured on 12 individual free-standing index-identified DWNTs, they have been able to evaluate the coupling force constant, k_c, between the inner and outer tubes and by the following, to derive the average unit-area force constant owing to tube?tube van der Waals interaction for different interlayer distances. A comparison of these average force constants with high-pressure graphite measurements propose a relationship between the interlayer distance and an internal effective pressure. Furthermore, they also show that in many cases, both coupled RBM oscillations will be resonantly excited if an electronic transition of either wall matches the excitation photon energy, which can be explained by strong quantum interference between Raman scattering from inner and outer wall excitation pathways. Actually, from the differential Raman scattering cross section (Equation (9)), we can find that electronic transition can influence the resonance feature. The results of Levshov's and Liu's experiments lead us to consider the strain induced electronic transition energy change, which was studied by Souza Filho *et al.* and showed the evidence of strain induced quantum interference by applying forces on individual SWNT tube by AFM tips [83]. They also discussed that the electron-phonon matrix element can also affect Raman differential cross-section, in order to observe quantum interference, CNTs with low chiral angles should to be chosen because they will have large values for electron-phonon matrix elements [83]. The interaction between the walls also depends on the chirality of nanotubes.

The TEM data obtained by Levshov and Liu *et al.* are based on the nanotubes with big diameter, actually, the inter wall coupling also depend on the tube diameter, as it shown in Figure 19, the smaller the diameter, the higher shift of the RBLM frequency of the inner tube.

To sum up, in this section, we introduced the Raman spectra of graphene and carbon nanotubes. Raman spectroscopy is a versatile tool to investigate the vibrational properties of graphene and nanotubes. The Raman spectra of graphene and carbon nanotube are also sensitive to the charges around them. It is very useful for studying the charge transfer in the hybrid system. In addition, we also discussed the Raman spectra of DWNTs, many works have been done to study the intertube interaction from the shift of Raman profiles. The interactions depend on the interlayer distance. We will pursue the presen-

tation of the influence of the electronic properties by presenting the features of sp^2 nanocarbon-based devices.

1.4 CARBON NANOTUBE BASED DEVICES

Though single-atom thick materials, graphene and nanotubes have been the first real low dimension electrical conductors. They provide textbook systems to test electron transport at low dimensions.

1.4.1 *Carbon nanotube field effect transistors*

A field effect transistor (FET) is a transistor that uses an electric field to control the conductivity of a channel of one type of charge carrier in a semiconductor material. FETs can be majority-charge-carrier devices, in which current is carried predominantly by majority carriers, or minority-charge-carrier devices, in which current is mainly due to minority carriers. FETs consist of an active channel through which charge carriers flow from the source to the drain. Source and drain terminal conductors are normally (in bulk FETs at least) connected to the semiconductor through ohmic contacts. The FETs' terminals are: drain and source, which are connected to the "conduction channel" of the FET (through which current flows) and the gate, which is the terminal that modulates the channel's conductivity. By applying a gate voltage, one can control the current which flows from source to drain (I_{DS}). The flow of charges through the channel is controlled by affecting the size and shape of the conductive channel created and influenced by voltage applied across the gate and source terminals. A FET has different states. In the depletion state, the corresponding charges are kept away from the conduction channel, so that the "Off" state of the device is reached (the current passing through the channel is small compared to the "On" state). The voltage at which the FET is turned off is referred to as the threshold voltage (V_{th}) of the FET. When the back gate is swept to values which exceed V_{th}) (in positive or negative values depending on the type of carrier), the FET is in its active region ("on state"), which at first has a linear dependence with V_g, and then reaches a saturation point (current does not grow further with a higher V_g). Depending on whether the substrate of the transistor is p or n doped, the "on state" will correspond to negative or positive values of V_g.

A carbon nanotube field-effect transistor (CNTFET) refers to a field-effect transistor that uses a single carbon nanotube or an array of carbon nanotubes as the channel material instead of bulk silicon in the traditional MOSFET structure. Inspired by the unusual electronic properties of carbon nanotubes, the first single carbon nanotube transistor appeared in 1998 [84, 85]. There are many types of CNTFET de-

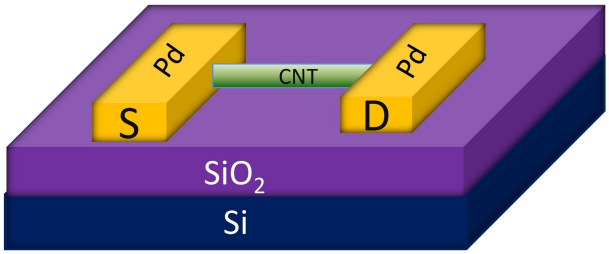

Figure 24: Sketch of the CNTFET, source and drain electrodes are patterned onto the nanotube while the silicon substrate is used as a back-gate.

vices, Figure 24 presents the sketch of a back gated individual CNT transistor which is used in this thesis. The CNTs (most of the time DWNTs in this thesis) were dispersed onto the SiO_2/Si substrate and connected with two palladium (Pd) electrodes.

The three main sources of resistance that limit carrier transport in CNTs are 1) quantized contact resistance arising from the mismatch in the number of states between bulk contacts and 1D nanotube [86]; 2) elastic and inelastic scattering mechanisms; 3) Schottky barriers and possible additional contact resistance. When the channel length is less than the mean free path of the scatters and the contact barriers are transparent, then the ballistic transport can be observed in CNTs transistors [86]. Here, we want to discuss more about the existence of Schottky barriers at the contact. A lot of works have shown that carbon nanotube transistors operate as Schottky barrier transistors (SBFETs) [87], in which the gate controls the Schottky barrier and the inject ion of the carriers.

Figure 25 shows the scheme of a Schottky barrier. When two materials with a different Fermi levels are put into contact, their charges are redistributed, so as to equalize the chemical energies at both sides of the interface. The larger the difference in Fermi energy, the more important this redistribution will be. In the case of a metal/semiconductor contact, consider that $q\phi_m$ is the work function of the metal (the energy which is necessary for an electron of charge q to escape from the Fermi level into vacuum and $q\chi$ is the energy which an electron needs to go from the conductance band of the semiconductor into vacuum ("electron affinity"). When the two materials come into contact, the Fermi energy of the semiconductors matches the one of the metal; if $q\chi > q\phi_m$, the concentration of holes increases at the surface and the energy bands of the semiconductor are bent towards positive energy values. If, on the contrary,$q\chi < q\phi_m$, a higher concentration of electrons at the interface causes the energy bands to bend towards more negative values at the interface, while remaining constant in the bulk of the semiconductor. Therefore, for both

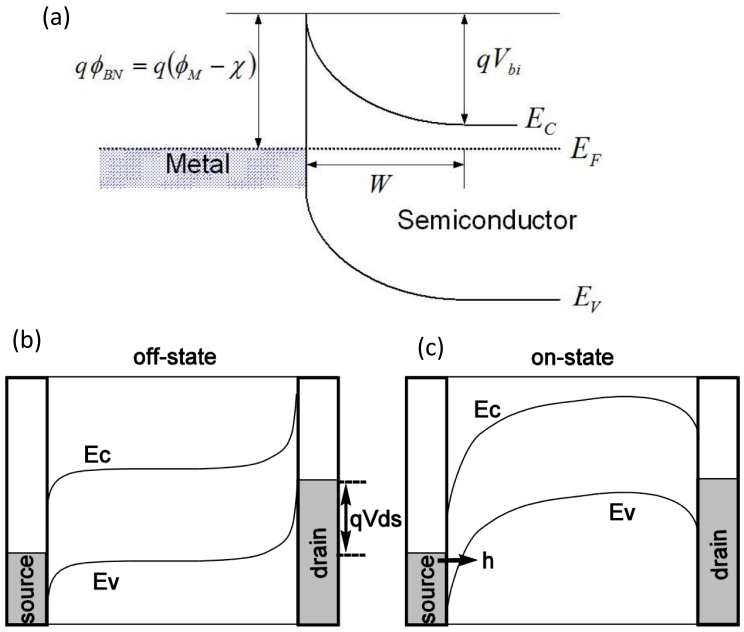

Figure 25: (a)Schematic representation of a Schottky barrier between a metal and a semiconductor; Schematic representation of the off state (b) and on state (p side) (c) of the field effect transistor.

electrons and holes a barrier is built: the barrier seen by electrons corresponds to $q\phi_{BN} = q(\phi_M - \chi)$ and the one seen by holes is $q\phi_{BP} = E_G - q(\phi_M - \chi)$. This means that the sum of the barrier seen by electrons and the one seen by holes is equivalent to the energy gap of the semiconductor.

In the case of CNTs, special characteristics arise due to the fact that they are one-dimensional systems: in doped CNTs, in fact, the length of charge depletion (W) is very sensitive to doping and to an applied back gate voltage (V_g), and the barrier profile is linear which makes it even more sensitive. In this way, the width of the barrier can be tuned changing V_g, and the amount of electrons which can tunnel through the potential barrier is controlled. The capability of electrons of passing through the Schottky barrier also depends on temperature: "hotter" electrons will see a lower barrier, and will therefore be able to go through it with a tunnel effect. In Figure 25 the working principle of a Schottky barrier field effect transistor (SBFET) is illustrated: when V_g is smaller than the threshold voltage (V_{TH}), the barriers at the contacts do not allow electrons to pass, whereas when $V_g > V_{TH}$ the barrier is thin enough and electrons or holes can tunnel through it. If the Fermi level aligns midgap with the CNT, both types of carriers can be injected from opposite contacts,then the device is an ambipolar device, as shown in Figure 45

When the finite size of a crystal is taken into account, the wavefunctions of electrons are altered and states that are forbidden within the bulk semiconductor gap are allowed at the surface. Similarly, at a metal-semiconductor interface, the wave function of an electron in

the semiconductor must match that of an electron in the metal at the interface. Since the Fermi levels of the two materials must match at the interface, there exists gap states that decay deeper into the semiconductor. This can pin the Fermi level of the semiconductor to a position in the bulk gap. These states (the so-called "Metal-induced gap states") decay exponentially with the distance from the interface, and after a certain distance the Fermi level is no longer pinned. Therefore, the choice of the metal used for the contacts is crucial to reduce the barrier height as much as possible and approach the ballistic conduction in the CNTs. Palladium has become the metal of choice for the contact with CNTs. Palladium's work function, known to be 5.12 eV, is among the highest in commonly available metals, so the Fermi level approximately aligns with the valence band edge, allowing for holes to tunnel easily into the conduction channel. As shown in Figure 26, comparing to Ti and Al contacts, the Pd contact achieve the highest on state current. The result in the experiments is consistent with the expected dependence of metal contacts.

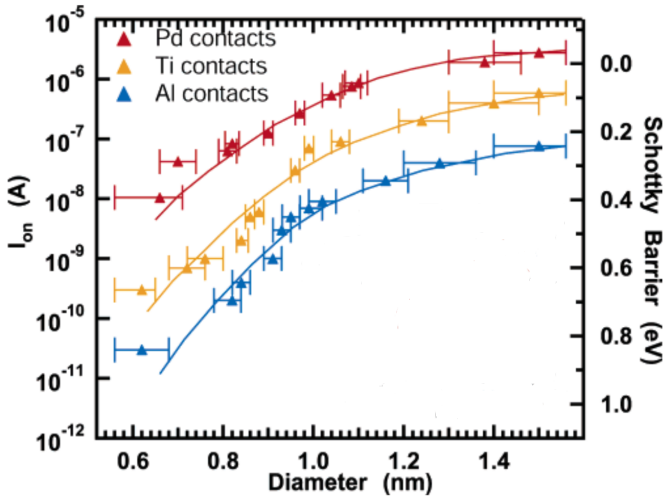

Figure 26: Plot of CNFETs I_{on} as a function of nanotube diameter, d, for Pd, Ti, and Al metal contacts. Figure taken from [88]

Many devices have been made based on CNTFETs, for example, T. Rueckes *et al.* made carbon nanotube-based nonvolatile random access memory [89]; in 2013, the CNT based computer has been made by M. Shulaker *et al.* in Stanford university [90]. Recently, IBM reports carbon nanotube transistor breakthrough for making CNTFETs with tiny (9nm) contacts that exhibit low, size-independent resistance [91]. This overcomes a huge hurdle in shrinking transistor size beyond current limits for post-CMOS applications. Moreover, plenty of works have pursued molecular electronic devices based on CNT-based field effect transistors. For example, X. Guo *et al.* covalently bridge a gap in a single wall carbon nanotube with an electrically functional molecule. The molecular bridge can perform the dual task of carrying electrical current and sensing (light, PH, gas, DNA...) / recognition of biology signals [92]. Recently, S. Sorgenfrei *et al.* realised the detection of DNA hybridization at the single-molecule level using a carbon nan-

otube field effect transistor [93]. Carbon nanotubes are very suitable for making hybrid devices with functional molecules as they offer the versatility of carbon-based chemistry. Carbon nanotube hybrids can be used to make single electron devices, for example, L. Marty *et al.* made single electron memories based on the hybrids of CNTFET and gold nano particles [94]. In the next section, we will introduce the principle of the single electron transistor.

1.4.2 *Coulomb blockade and single electron box*

The single electron transistor (SET) is a type of switching device that uses controlled electron tunneling and electrostatic repulsion to control current. It is the simplest device where the effect of Coulomb blockade can be observed [95]. A SET is composed of two tunnel junctions. The tunnelling of a single electron between two metal electrodes through an intermediate island can be blocked by the electrostatic energy of a single excess electron trapped on the central island. In the case of non-symmetric tunnelling barriers (e.g. tunnelling junction on the left and ideal (infinite resistance) capacitor on the right), this device model describes a 'single-electron box'.

There are two basic requirements for single electron tunneling to occur [96]. Firstly, the energy uncertainty ΔE associated with the lifetime due to tunneling when adding an extra charge, $\tau_r = R_t C$, needs to be much smaller than the charging energy $E_c = e^2/C$ which is required to add a charge carrier to the island:

$$E_c \tau_r = (e^2/C) R_t C \gg \Delta E \tau_r \sim \hbar. \tag{12}$$

So the tunneling resistance R_t must far exceed the quantum resistance $R_K = \hbar/e^2 \simeq 25.8 K\Omega$, namely,

$$R_t \gg R_K. \tag{13}$$

Secondly, the energy E_c should far exceeds the thermal fluctuation energy,

$$E_c \gg k_B T. \tag{14}$$

Figure 27 (b) shows a capacitive model for the single electron box [99]. The total capacitance is the sum of the capacitances between the dot and the source C_s, the drain C_d, and the gate C_g: $C = C_s + C_d + C_g$. The total energy U(N) of a dot with N electrons in the ground state, with voltages V_s, V_d, and V_g applied to the source, drain, and gate, respectively, is given by:

$$U(N) = \frac{(-e|N - N_0|^2 + C_s V_s + C_d V_d + C_g V_g)^2}{2C}, \tag{15}$$

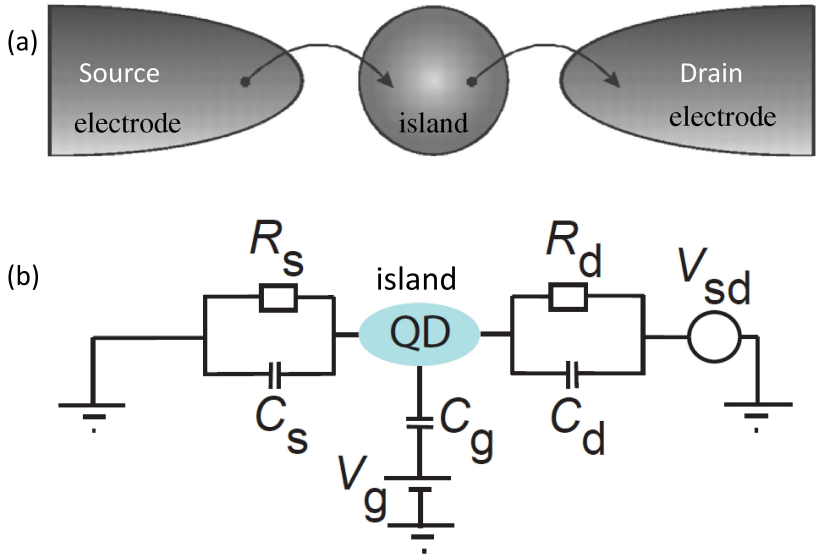

Figure 27: Sketch and capacitive model of single electron transistor, adapted from [97, 98]

where $-|e|$ is the electron charge, $N_0|e|$ is the charge in the dot compensating the positive background charge that originates from the donors in the heterostructure. The terms C_sV_s, C_dV_d and C_gV_g can be changed continuously, and represent an effective induced charge that changes the electrostatic potential on the dot. The electrochemical potential $\mu(N)$ of the dot is defined as:

$$\begin{aligned} \mu(N) &= U(N) - U(N-1) \\ \mu(N) &= (N - N_0 - \frac{1}{2}E_c) - \frac{E_c}{e}(C_sV_s + C_dV_d + C_gV_g). \end{aligned} \tag{16}$$

Energy conservation needs to be satisfied during the charge transport process. Therefore, the electrochemical potential (μ) of the island should lie between the electrochemical potentials of the source and the drain, that is,

$$\mu_s \geqslant \mu \geqslant \mu_d. \tag{17}$$

$\mu_s - \mu_d = -e \mid V_{sd} \mid$, with V_{sd} being the source-drain voltage.

Apparently, Coulomb blockade can be modified by changing V_{sd}. This changes the bias window as well as the electrochemical potential of the dot, due to the capacitive coupling to the source. A current flows only when μ falls within the bias window. By increasing V_{sd} until both the ground state and an excited state transition fall within the bias window, an electron can choose to tunnel not only through the ground state, but also through an excited state of the N-electron dot. This is reflected in the change of the total current.

The Coulomb blockade can also be lifted by changing V_g and consequently shifting the whole ladder of electrochemical potential

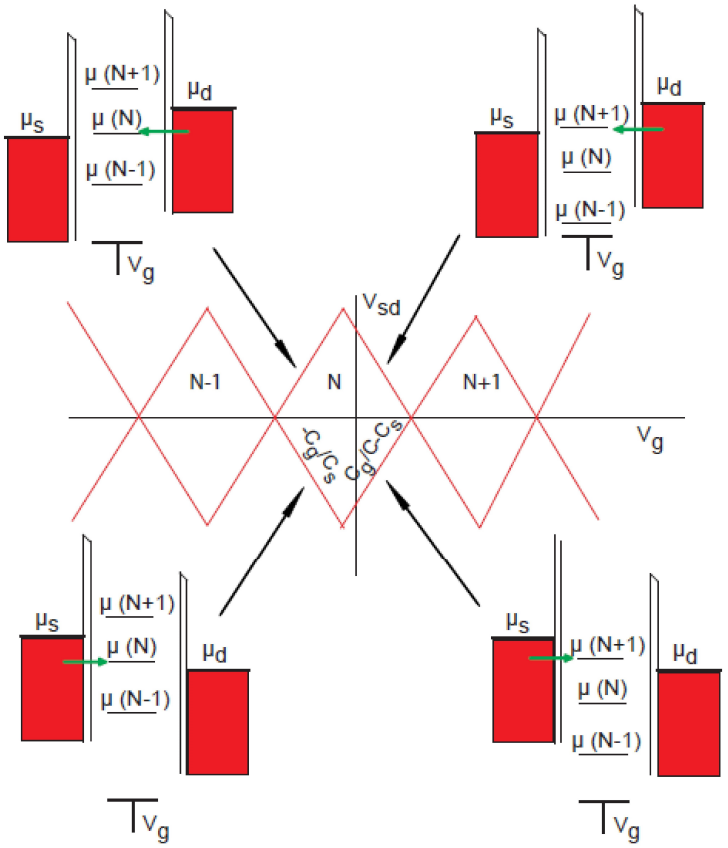

Figure 28: Scheme of Coulomb diamonds (or stability diagram of the island), adapted from [98].

levels up or down. When a level falls within the bias window, a current passes through the device.

Overall, the charging energy may be overcome by changing the source-drain voltage as well as by changing the gate voltage. In this way we draw the so called stability diagram of single electron transistor, which is shown as the Coulomb diamonds as presented in Figure 28. Within the diamonds, Coulomb blockade is established, while outside, a current flows between source and drain.

It was indeed demonstrated that nanotubes are quantum conductors allowing discrete charge transfers in the Coulomb blockade regime. In the case of graphene, one needs to design small size islands on graphene to allow confining charges and observe this Coulomb blockade. Beyond Coulomb interaction, we will now present charge/energy transfer to nanotubes driven by light.

1.5 FUNCTIONALIZATION OF GRAPHENE AND NANOTUBES FOR OPTOELECTRONICS

1.5.1 *Functionalization methods*

Functionalization of graphene and/or carbon nanotubes involves attaching molecular groups to the wall of the nanotube so as to modify their properties, especially their affinity with different chemical or biological environments and species. By choosing specific functional groups, it is possible to improve the properties of the devices (nanosensors, nanoprobes). Recent work has also demonstrated the operation of nanosensors based on functionalized graphene and carbon nanotubes. For example, by using the DNA strands to make an odor detector, or using an enzyme, for measuring real time biological activity. Over the past fifteen years, the functionalization of carbon nanotubes and graphene have been greatly developed. Variety of molecular groups with different types of chemical bonds were studied. The functionalization can be distinguished into covalent and non-covalent methods [100].

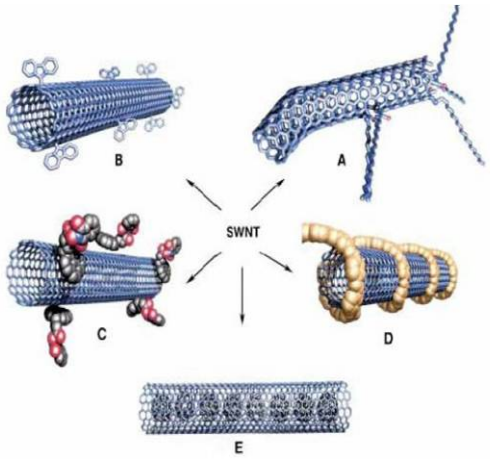

Figure 29: Covalent (A and B) and non covalent (C, D and E) functionalization of SWNTs [100]

.

Non-covalent methods are based on the Van der Waals interaction or π stacking. This method is particularly well suited to attach DNA, polymers and surfactants onto nanotubes. This category also includes encapsulation of small molecules inside the nanotubes. The non-covalent functionalization has the advantage that it provides weak interaction with the nanotube and can preserve the electrical or optical properties of it. But also because of the interaction with the nanotube or graphene is not strong, it can easily be affected by the surrounding environment. On the other hand, covalent methods involve the covalent bond to the carbon nanotube or graphene when adding the molecular groups. This type of functionalization is not easy to achieve, because the structure of carbon nanotube is stable and needs specific conditions to react with other chemical groups. Many addi-

tion reactions are limited to attack only already vulnerable sites on carbon nanotubes, such as the defects and the nanotube ends. So acid treated carbon nanotubes, which have carboxylic (-COOH) groups, are more reactive. Covalent methods allow a stronger coupling between the grafts and the carbon nanotubes, and is recognized for its stability, reproducibility and selectivity thanks to the good control of the chemical reaction bonds. However, this method also has disadvantages: the covalent bonds can highly affect the electronic structure of the carbon nanotube and can significantly destroy the electrical and optical properties of carbon nanotubes.

1.5.2 *Carbon nanotube and graphene-molecule hybrids for optoelectronics*

The functional carbon nanotubes and graphene with optically active molecules are quite promising for applications of nanometre-scale light sources [101], photodetectors [102] and photovoltaic devices [103]. In the recent years, there are many reports related to the

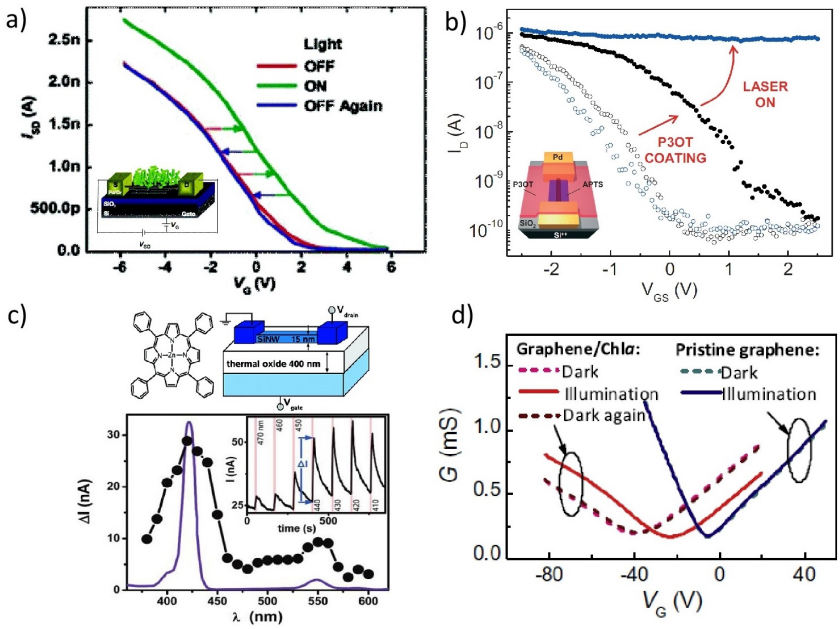

Figure 30: Hybrid optoelectronic devices: (a) zinc(II) metalloporphyrin/SWNT hybrid optical switch; (b) polymer functionalized CNTs for optoelectronic switch and memory devices; (c) porphyrin coated silicon nanowire for optical switch and photo detector; (d) graphene-chlorophyll phototransistors, figure adapted from [104, 105, 106, 107].

carbon nanotube and the optical active molecule hybrids, for example, Hecht *et al.* [104] used field-effect transistors to directly monitor the interactions between a zinc(II) metalloporphyrin/SWNT system upon irradiation with visible light, and emphasized that the hybrid nano-FETs have an extremely large possible range of optoelectronic applications, from spectrally resolved artificial eyes to photovoltaic cells (Figure 30 (a)); Borghetti *et al.* functionalised CNTFETs with op-

tical sensitive polymer and they demonstrated that depending on the applied gate bias, the device can be optimized as a memory element or as an optical switch [105] (Figure 30 (b)); Chen *et al.* reported graphene-chlophyll phototransistors with high gain (Figure 30 (d)). All of these studies indicate that carbon nanotube or graphene functionalised by chromophore or other kind photo sensitive molecule are strong candidates for optoelectronic applications.

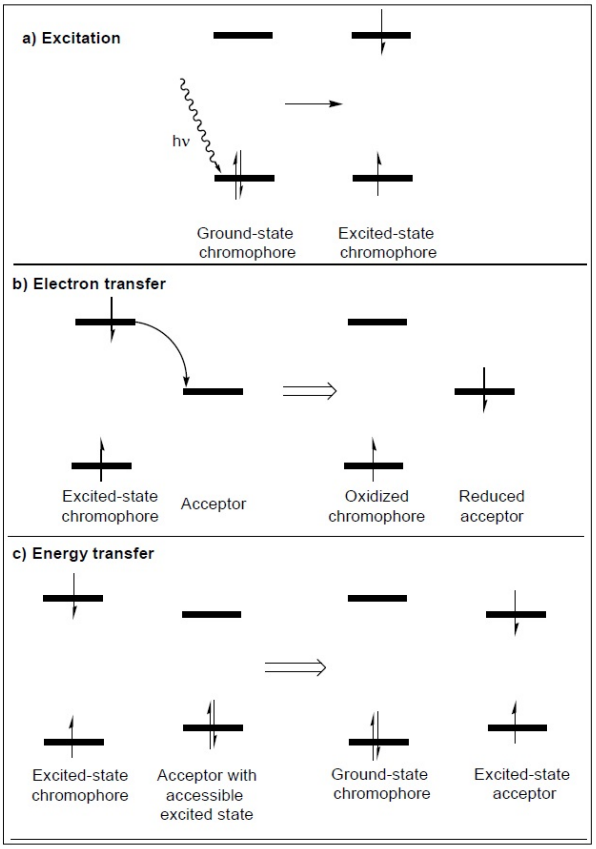

Figure 31: Schematic representation: excitation of chromophore (a); electron (b) and energy transfer (c) from chromophore to acceptor, figure adapted from [108]

.

Owing to the importance and complexity of carbon based hybrid optoelectronics, the basic principles of photo-induced electron and energy transfer are required. Figure 31 presents the sketch for explaining photo induced electron and energy transfer process. A molecule in the excited state can relax to the ground state either by fluorescence, non radiative decay *et al.* or by electron/energy transfer to another molecule. In an electron transfer reaction, upon photoexcitation, the electron donor transfer an electron to a electron acceptor, making the chromophore oxidized and the acceptor reduced (Figure 31 (b)). In the case of energy transfer, the excited state energy of the donor is transferred to the acceptor, which excites the acceptor molecule, thus leaving the donor molecule in the ground state and the acceptor molecule in the excited state. This absorbed energy will be efficiently converted into electrical or thermal energy or the energy

for chemical reaction (*e.g.* photosynthesis in plants), thus leads to the initial ground states of the donor-acceptor species (Figure 31 (c)).

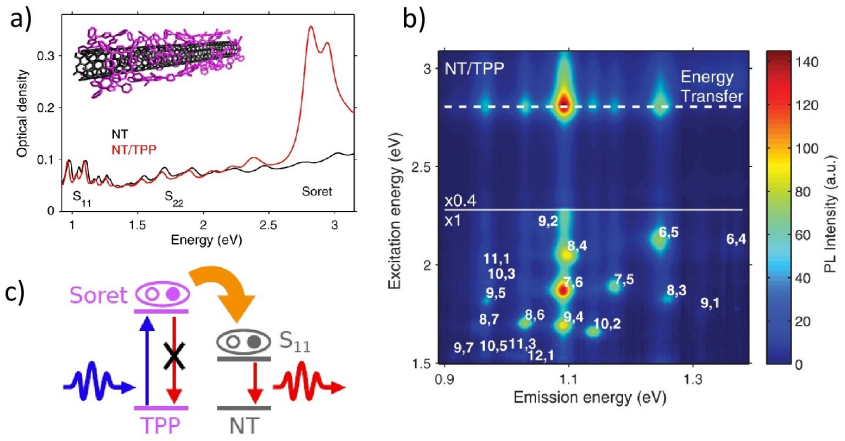

Figure 32: Energy transfer in SWNT/H_2TPP hybrids, (a) absorption spectra of SWNTs and SWNT/TPP compounds in micellar solutions; (b) PL map of SWNT/TPP compounds suspension; (c) schematic representation of energy transfer in SWNT/H_2TPP hybrids, figure adapted from [109]

.

For the carbon nanotube-molecule hybrids, the energy transfer from the excited molecule to carbon nanotube can be observed in photoluminescence experiment [110, 109]. We can observe from Figure 32 that when excitation energy corresponds to the molecule absorption Soret band, the emission of nanotube is enhanced. This brings evidence for EET from the porphyrin to the nanotube: when photons are absorbed by porphyrin molecules, the luminescence of the nanotube is enhanced.

However, the charge transfer process can not be observed through photoluminescence experiments. In the following paragraph, we will introduce how the charge transfer can be observed through electron transfer characterised curve of CNT-molecule hybrid transistors.

As we mentioned before, there are a lot of works describing the response of SWNT or graphene field effect transistors to various molecules. Those molecules noncovalently attached to the surface of SWNT or graphene are expected to have two effects that can change the conductivity. First, there is a charge transfer between the molecule and the nanotube, changing the carrier concentration; second, the molecule may act as a randomly distributed scattering potential, change the mobility of the charge carrier. A measurement of the conductivity alone can not distinguish between a change in the carrier concentration and a change in the mobility of the electrons. Extensive experiment has proved that the change of carrier concentration lead to shifts of the threshold voltage, which is the voltage where the device first turns on, as shown in Figure 30 (a) and (b) [104, 105]. In fact the change of carrier concentration leads to the shift of Fermi energy, which can be observed through the shift of Fermi

neutral point in the transfer characteristic curve [104, 105, 107]. From the shift of threshold voltage, the change of carrier concentration can be extracted. More details will be discussed in chapter 3 and chapter 4.

From this chapter, we know that both of Raman spectroscopy and electrical transport measurements are sensitive to the change of charge carrier concentration in sp^2 carbon hybrid system. In this thesis, we will discuss light induced charge transfer by crossing studying the vibrational and electron properties of several kinds of sp^2 carbon hybrid systems. Moreover, because in most of reported experiments, the nanotube bundles instead of individual nanotubes were used in this experiment, which prevents access to their fundamental mechanisms. In this thesis, we will introduce the carbon nanotube/-molecule hybrids based on individual nanotube and few molecules. On the other hand, in the recent years, Bouilly *et al.* [111] covalently functionalized individual double wall carbon nanotubes transistors by diazonium salt, which pave a way for covalently grafting optical active molecule onto DWNT transistors. We will firstly discuss the interaction, charge transfer and optical effect between the DWNT and the chromophores in the non covalently functionalized hybrid transisors, and will also show the preliminary results of covalently functionalized DWNT transistors.

2

GRAPHENE AND ISOLATED DWNT FETS–FROM FABRICATION TO ELECTRON PHONON COUPLING

In this chapter, we introduce the fabrication methods and process of graphene and individual DWNT field effect transistors. We also introduce the characterization methods of the pristine material and the transistors, such as scanning electron microscopy (SEM), high-resolution transmission electron microscopy (HRTEM), Raman spectroscopy and electrical transport measurement in ambient condition. In particular, we will detail how coupling Raman spectroscopy and transport measurements on a metallic carbon nanotubes, allow us to observe a Kohn anomaly which can be explained by an electron-phonon coupling process.

2.1 SYNTHESIS AND CHARACTERIZATION

2.1.1 *CCVD of DWNT*

The DWNTs that we used in this thesis is synthesised by the CCVD method which is described in chapter 1 [32]. In order to know the quality of the as grown DWNTs, we did Raman spectroscopy measurement.

2.1.1.1 *Brief introduction to the Raman spectrometers*

Two Raman spectrometers are available in NEEL institute. One is a commercial Witec Alpha 500 confocal micro Raman spectrometer, as it shown in Figure 33. A confocal microscope allows to determine with good approximation the desired spot (500 nm), while a mechanical stage is used to position the sample in all three directions in order to adjust the sample's position to the incoming laser spot (and so as to focus correctly), and a piezoelectric element can perform much more precise movements (resolution: about 10 nm) to perform Raman imaging. Scattered light is collected by a large numerical aperture objective and enters a fiber which carries the light to the spectrometer where it will be dispersed by a grating and analyzed by a CCD camera. The CCD camera collects the wavelength dispersed photons; a cooling system has to bring the CCD camera to a low temperature (in the case of the Witec alpha 500 Raman spectrometer, -62 °C by Peltier cooling). A sample holder with electrical

connection can be installed on the piezo stage (Figure 33), which can be used for the in situ Raman spectroscopy during the electrical transport measurement of the DWNT or hybrid transistors. There are two laser wavelengths available for this Witec spectrometer in the lab (532 and 633 nm).

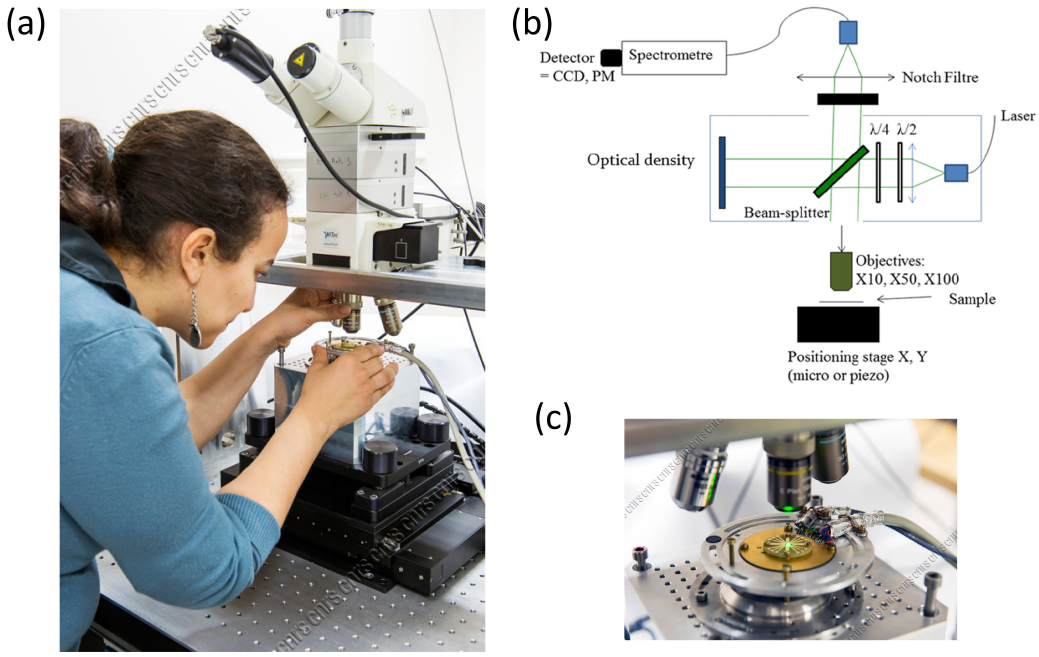

Figure 33: Witec Alpha 500 micro Raman spectrometer (a) photo of the confocal microscope and stages, (b) scheme of the Raman spectrometer, (c) in situ Raman spectroscopy on the back gated devices [CNRS Photothèque].

The other Raman spectrometer that we used is a commercial Jobin-Yvon T64000 spectrometer. It allows choice of single and triple monochromator stage spectrometer operation modes (Figure 34). The advantage of this spectrometer is that it has large spectral range and very high spectral resolution down to 0.15 cm^{-1}. Furthermore, a continuous tunable laser can be adapted to the system, which brings facilities for the resonance Raman spectroscopy study of the nanotube system. In this thesis, Raman spectra excited at 514 nm and 488 nm were taken by using an Ar/Kr laser lines. A Ti : sapphire laser was used for the continuous tunable laser wavelength between 740 to 850 nm.

Tunability is a very crucial aspect, since the DWNTs have different chiralities, and in our case, most of our samples are individual DWNTs. In order to get the signal of the Raman spectroscopy, suitable excitation laser wavelength needs to be chosen to make the sample resonant.

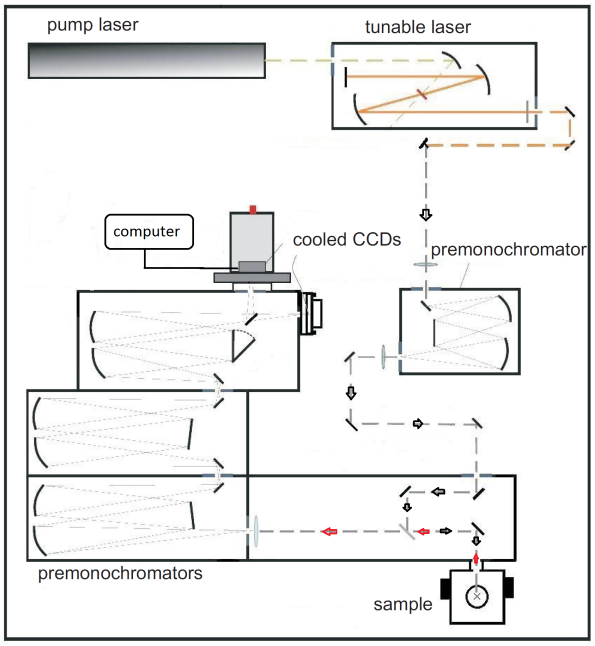

Figure 34: Optical setup of the tunable Raman spectroscopy.(Adapted from [54, 55])

2.1.1.2 *SEM and Raman spectra of as grown DWNTs*

The original as grown DWNT sample is black powder. But through the SEM, the sample looks quite different. Figure 35 (left) shows the SEM image of as grown DWNTs. We can see from the image that the carbon nanotubes are very long and get entangled and intertwined with each other. In this kind of samples, DWNT organize in bundles.

Figure 35 (right) shows the Raman spectra of the DWNT bundles. The used laser wavelength is 532 nm. The laser spot is around 500 nm. This kind of sample is very sensitive to the laser power, because it can absorb a lot of heat and the laser might burn the sample (nanotubes in air can burn at 400 °C), so we always use a low power (lower than 0.5 mW) to protect the sample. For the Raman spectra, the G mode and 2D mode can be clearly observed (see Chapter 1 for details about Raman spectroscopy). The G^+ mode is at 1593 cm^{-1} and the 2D mode components of the inner and outer tubes are at 2626, 2674 cm^{-1}. The D mode ($1200 - 1400 cm^{-1}$) is hardly observed. As we discussed in chapter 1, the appearance of D peak is due to the defects in the sample. The D peak absence here indicates that defects are few in the sample, or in other words, our pristine DWNTs have good structural quality. The G band exhibits both semiconducting and metallic components as expected on a bundle of NT. DWNT have different configurations, which are S@S, S@M, M@S, M@M, respectively. The DWNT bundle sample is a mixture of all the configurations. In the range of radial breathing like modes, it can be observed that two groups, corresponding to the breathing signals from the outer tubes and the inner tubes. Peaks around 160 and 191 cm^{-1}, corresponding

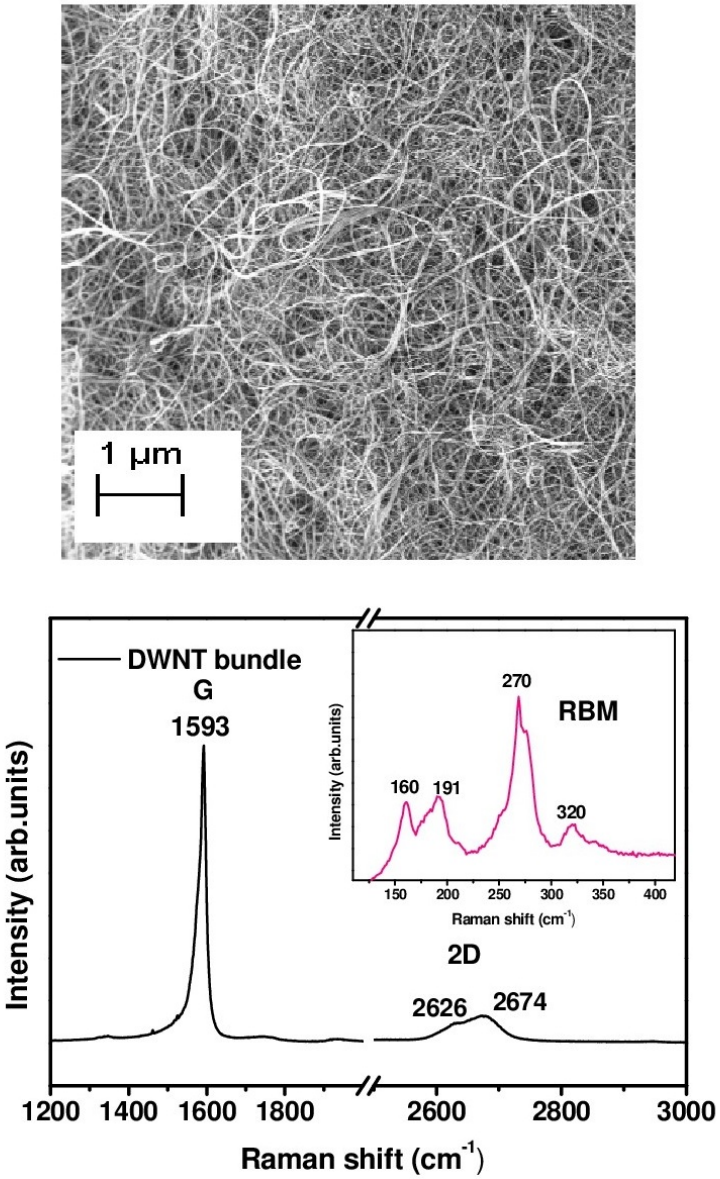

Figure 35: Up: SEM images of as grown DWNT powder, they are entangled and form as bundles. Bottom: Raman spectra of DWNT bundle(laser wavelength: 532 nm)

to the tube diameter from 1.51 and 1.25 nm, are from the contribution of outer walls. The peaks around 270 and 320 cm^{-1}, corresponding to tube diameter from 0.86 to 0.71 nm, are from the inner walls. Here, we used the function $\omega_{RBM} = 218.8/d_t + 15.9\ cm^{-1}$ to calculate the diameter [112, 113]. In the literature, there are other equations for calculating the diameters of DWNTs. For instance, in ref. [114], there are other equations which was proposed, for the inner tubes,

$$\omega_{inner} = \frac{225}{d_{inner}} + 20.6 d_{inner} - 2.4 \tag{18}$$

, and for the outer tubes,

$$\omega_{inner} = \frac{-88.76}{d_{inner}^2} + \frac{324.1}{d_{inner}} - 14.7 \tag{19}$$

If we use these equations, for the outer tubes, the diameters are from 1.22 to 1.53 nm, and for the inner tubes, the diameters are from 0.73 to 0.89 nm. The results are similar to the calculation from the other equations [114]. In DWNT bundles, the diameter distribution is bimodal and we expect a 2D band with two main features that correspond to the inner $2D_1$ and outer $2D_2$ tubes. We can deduce that the peaks around 2626cm^{-1} are from the inner tubes, 2674 cm^{-1} are from the outer tubes.

Raman can be interstingly complemented by HRTEM because of the unknown Kataura plot for DWNTs.

2.1.1.3 *HRTEM of as grown DWNTs*

The HRTEM can be used to get high resolution images of the individual DWNTs and do the statistic of the diameter of the DWNTs. Figure 36 (left) shows the HRTEM image of a DWNT bundle [32]. HRTEM was performed by E. Flahaut *et al.* at CIRIMAT. From this image, we can easily distinguish single wall from double wall carbon nanotubes. The diameter of the carbon nanotubes can be directly measured on the HRTEM image. The statistics of the diameter of both the inner and the outer tubes have been done on these samples. The inner and outer diameters range from 0.53 to 2.53 nm and from 1.23 to 3.23 nm, respectively. The median inner diameter is 1.35 nm and the median outer diameter is 2.05 nm. (Figure 36 (right)).

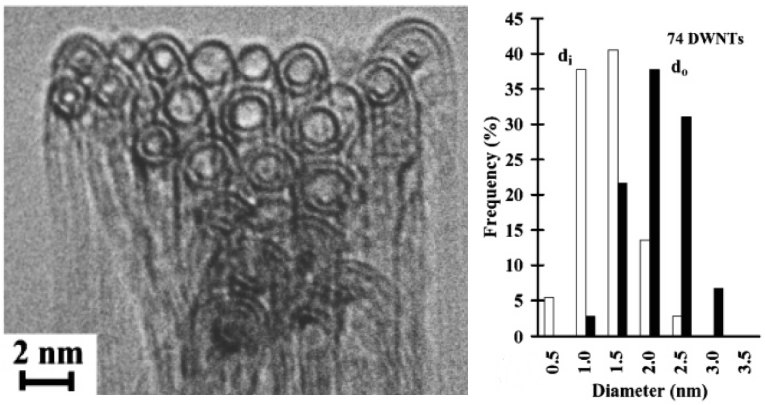

Figure 36: Left: The HRTEM image of as grown DWNT bundles, right: statistics of the diameter distribution of the inner (d_i) and outer tubes (d_0) (figure adapted from [32])

2.1.2 *CVD on copper of graphene*

Graphene was synthesised by the CVD method on copper foil (99.8% purity from Alfa-Aesar company), a home-built CVD reactor with a 4-inches diameter quartz tube and effective heating length of about 30 cm is used. All components are automated by a home-built program, which enables real time control of flow rate, injection time of reacting gases as well as the reaction temperature. A standard CVD process is used for this experiment (Figure 37). There are three steps in the synthesis process. The first one is the pre-growth stage, where the temperature is ramped up and the copper foil is annealed. The second one is the growth stage, CH_4 (carbon precusor), H_2 and Ar are injected to the furnace. After a certain growth time, the system is cooled down, which is the last step of the synthesis. Graphene used in this thesis is synthesised by Dipankar Kalita (PhD student, hybrid group).

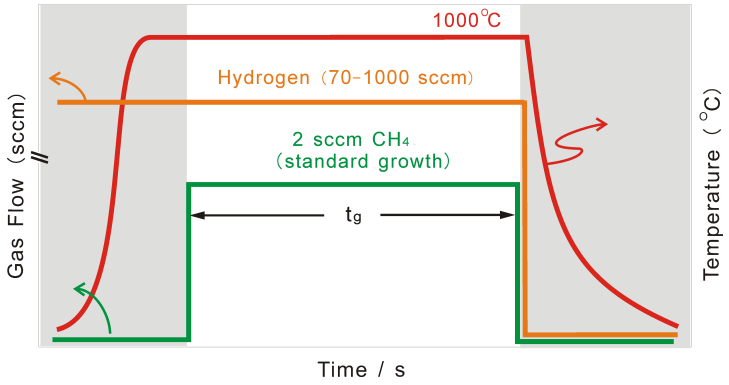

Figure 37: The process flow for the standard CVD growth (from Zheng Han [25]).

Then the graphene is transferred to a silicon substrate [25] by a polymer-assisted wet transfer technique [21]. Figure 38 shows the scheme of polymer assisted wet transfer technique. The principle of this technique is to cover graphene with a polymer supporting layer, PMMA (PolyMethylMetAcrylate) in our case, and then chemically etch the copper foil which is underneath the graphene layer. This method has been widely used for the transfer of graphene and other 2D materials [115, 116, 117, 118]. The ammonium persulfate $(NH_4)_2S_2O_8$ was chosen to disolve the copper in order to reduce defect formation [25].

In this section, we mainly introduce the synthesis and the characterization of pristine DWNTs and graphene. For the next step, we need to connect them to the electrodes and make field effect transistors, the methods of which will be discussed in the next section.

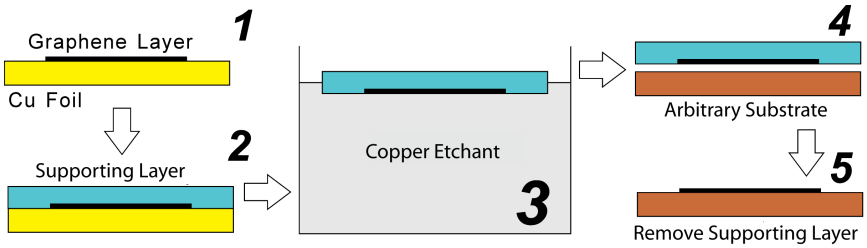

Figure 38: The process of polymer assisted wet transfer technique (adapted from [21]).

2.2 FABRICATION OF INDIVIDUAL DWNT FIELD EFFECT TRANSISTORS

Making the DWNT field effect transistors is the first task of the whole experiment. We are interested in both the optical and electrical properties of individual carbon nanotubes. For the electrical transport measurement, we need metal electrodes to make the contacts for the measurement. For Raman spectroscopy, we also need markers to locate the position of individual nanotubes. In the following text, we will present various techniques to completely introduce the fabrication process. To ensure the quality of the sample, the fabrication work was carried out in the Nanofab clean room of Néel institute and with the help of its technical support team.

The first step is cleaning of the silicon wafer. In all experiments, we used a highly p doped silicon wafer with a 285 nm thick silicon-oxide layer on top. The wafer was cleaned by firstly dipping into acetone, and then washing by deionized water and 2-isopropanol. The drying process is done with a nitrogen gun. At last, the wafer was put in the plasma chamber to do an oxygen plasma treatment to make sure the silicon wafer was totally cleaned.

2.2.1 *Substrate patterning*

After cleaning the silicon wafer, we then use a deep-UV lithography process to deposit the patterned macroscopic gold electrodes. The gold electrodes can be used as markers for the next electron beam lithography step. They were used to locate the position of carbon nantoubes and also to do the alignment in the electron beam lithography process. Attention is paid to create electrodes and markers which are parallel to the silicon grain boundaries for subsequent cleaving of the wafer.

The principle of UV or deep UV lithography is using light to transfer a geometric pattern from a photo mask to a light-sensitive chemical "photoresist", or simply "resist" on the substrate. A series of chemical treatments then either engraves the exposure pattern into, or

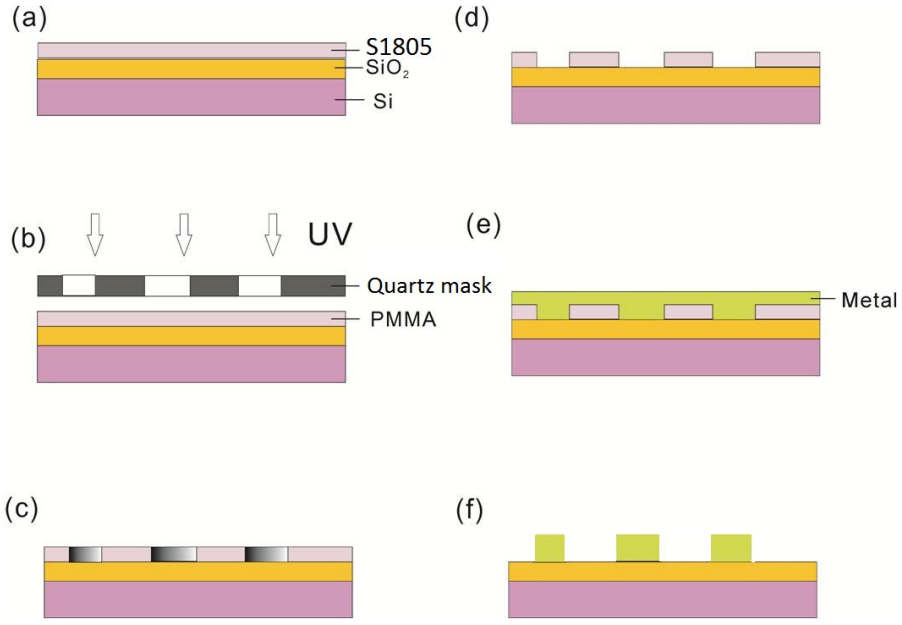

Figure 39: Scheme of the photo lithography process (a) S1085 coating, (b) exposure, (c) before development, (d) after development, (e) metal deposition, (f) after lift off.

enables deposition of a new material in the desired pattern upon, the material underneath the photo resist. The equipment that we used is a Karl Süss deep UV aligner in NEEL/Nanofab. This aligner is equipped with a 500 W pressurized Cd/Xe lamp which emits in Deep UV (240 nm). The resist that we chose is the S1805. At first, S1805 was spin coated on the silicon wafer (a). After that, the wafer was baked at 180 °C for drying S1850. Then a patterned quartz mask was used to make shadows where we want to block the UV light (b). The pattern is shown in figure Figure 40. After the alignment of the mask and the wafer, the sample was exposed to the deep UV light for 30 seconds (c). After a chemical development process, the S1805 at the patterned and exposured place was removed (d). Then the sample can be transferred to an evaporator system to deposit 10 nm Ti and 100 nm Au (e). At last, the sample was put into acetone solution to do the lift off and wash away the redundant resist and metal (f).

2.2.2 *Deposition of double wall carbon nanotubes*

The double wall carbon nanotubes fabricated by CCVD method usually twist into bundles. There are methods which have been developed to separate the bundles by dispersing the carbon nanotubes into chemicals. The most popular method consists in using surfactant to wrap onto the single nanotube surface and a following DGU process to separate them. But this method is not suitable for our purpose, since (1) this process needs very strong sonication which might bring defects on the nanotubes, (2) the surfactant is difficult to be

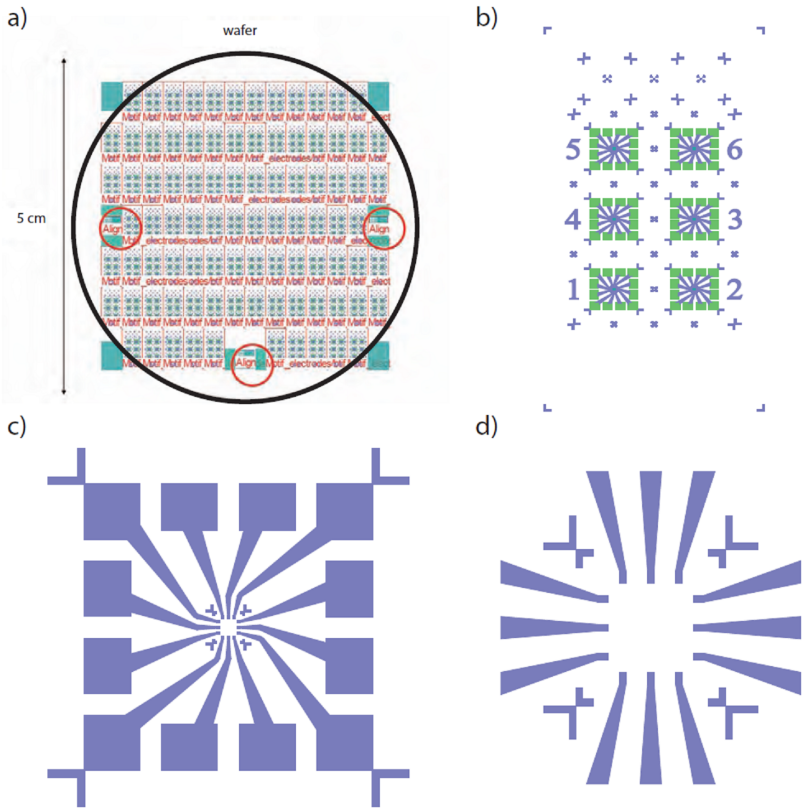

Figure 40: a) The patterned gold electrodes. b) Zoom of each grid with 6 patterns with alignment marks, c) Zoom of b),d) Zoom view of c) (50×50 μm^2), this is the writing field of e beam lithography, also the place of interest to connect the carbon nantoubes.

totally washed away which causes contamination of the nanotube. Both of the two factors can affect the optical and electrical properties of carbon nanotubes. So, we used a mild sonication process here. A few flakes of carbon nanotubes were put into a dichloroethane (DCE) solution. The bottle is then suspended in the ultrasonic bath for 3 minutes. The power was set at 40 percent. After the sonication, the solution was settled down for about 1 hour, and the supernatant was collected. One or two drops of the nanotube solution are spin-coated on the wafer. The concentration of the solution and the number of droplets need to be adjusted to make a better separation. After 15 seconds, wafer is washed with ethanol and dried with nitrogen. The above process need to be repeated several times in order to get a appropriate tube density (about 1 tube per μm^2) on the wafer for the fabrication of isolated DWNT, which can be checked under the AFM or SEM.

2.2.3 *Electrode design*

Electron-beam lithography (e-beam lithography) is the practice of scanning a focused beam of electrons to draw custom shapes on a surface covered with an electron-sensitive film called a resist ("expo-

sure"). Here, we want to draw electrodes to connect the carbon nanotubes to the already made bigger gold electrode patterns. So the first step of the e-beam lithography process is locate the carbon nanotubes. The position of a nanotube is determined with respect to the gold electrodes. We use SEM (ZEISS ultra+ FESEM) to get the image of the nanotube with the already designed markers. This imaging technique relies on the fact that the nanotubes are conducting, and the substrate on which they are lying is insulating which provides a good contrast down to the isolated nanotubes. The SEM images by scanning a high energy beam of electrons over the sample. For protecting the carbon nanotube sample from being damaged by the beam, typical accelerating voltage for imaging was 500-800 V and capture was performed in a few seconds. Several SEM images are stitched together so as to place all the CNTs present in the working area to avoid shortcuts and permit the most convenient design of the circuits. The software Klayout was used to design the electrodes on top of the SEM pictures. Figure 41 shows the stitched SEM images and the designed electrodes. The carbon nanotubes need to be separated very well, so the long, straight and thin tubes were selected for our design.

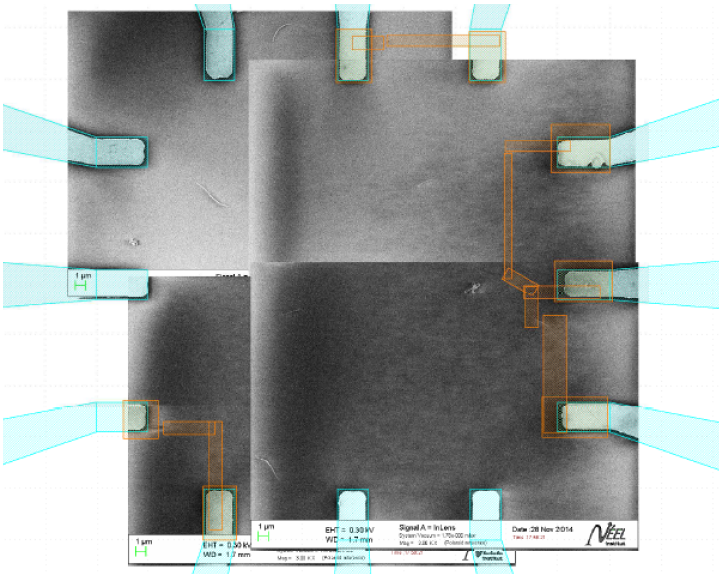

Figure 41: The SEM images and the design electrodes,we choose the long, thin and well isolated nanotubes to make the dessign.

The resist that we choose for the e-beam lithography is PMMA. The deposition of resist is done with the spin-coating method (acceleration: 4000-6000 $\mathrm{rotation/min^2}$, velocity: 4000 $\mathrm{rotation/min}$, time: 60 seconds). By using these parameters, about 2 µm PMMA can be deposited. After the deposition, the wafer was heated to 180 °C for 3 minutes to evaporate the solvent. Then we used optical microscopy to check the deposition. The PMMA should be uniform on the silicon surface. If there are bubbles or other contaminations, the wafer should be washed in acetone and the deposition process should be repeated.

Electronic lithography is carried out inside a Scanning Electron Microscope (SEM, model : Jeol LEO 1530). The process is controlled by the Elphy plus software. After the wafer is loaded into the chamber, one needs firstly to optimize different parameters of the SEM, in order to get it well focused on the wafer surface. Then the alignement procedure to locate the nanotube must be done. Knowing the relative positions of alignment marks with respect to the reference point, we need to zoom the view-field into the area with the alignment marks. Another alignment process is done to locate several special alignment marks serving as reference points for small structures. The exposure is done at 20 keV with a dose of 270 $\mu C/cm^2$ (To get a better quality of the sample, the dose test is necessary before the lithography process). The next step is using a mixed solution of Methylisobutylketone (MIBK) and 2-Isopropanol (IPA) to develop the exposed resist. The solution is made with one volume of MIBK and three volume of IPA. The wafer needs to be washed in the solution for 60 seconds, then transferred to the solution of IPA for more than 30 seconds to stop the developing.

After the development the desired metal is evaporated onto the wafer. Different metals can be used, with Pd affording the best contacts. The evaporation is done by using the electron gun evaporator (PLASSYS) system in NEEL/Nanofab. The process has been done in high-vacuum (10^{-7} mbar) by heating the material through Joule Effect. Before the evaporation of Pd, a degassing process is necessary to improve the vacuum, which can be done by heating Ti for 10 seconds in vacuum. The typical thickness of Pd is 50 nm.

After the evaporation, the wafer is completely covered by a metallic layer. To lift the undesired metal layer, one needs to leave the wafer in acetone for several hours. A syringe is used to eject acetone onto the wafer surface to help the removal of the metal layer. The wafer is then cleaned in 2-isopropanol. After lift-off, the device is ready.

The e-beam lithography is not used for making graphene transistor in this thesis because the graphene that we synthesised is in millimeter range. They were made by directly evaporating gold electrodes through a metal shadow mask with etched two parallel trenches. The gap between the trenches is 3 mm. The techniques that were used to characterise DWNT FETs can also be used to characterise graphene and graphene FETs.

In summary, in this section, we introduced the methods and the procedures for making the individual DWNT transistors. There are several steps, including using deep UV lithography to make the gold markers, seperation and deposition of the DWNTs and electron beam lithography to connect the individual DWNT to the gold markers. In the next section, several characterization methods will be introduced to characterise the DWNT transistors.

2.3 ELECTRON-PHONON COUPLING IN AN ISOLATED DWNT FET

Many techniques for the study of nano-materials can be used to characterise the as grown DWNTs. In this section, I will present the transfer characteristics of DWNT FETs at room temperature, and also the spatially resolved Raman spectroscopy for probing the individual DWNT.

2.3.1 *Electronic characteristics of graphene and isolated DWNT transistors*

2.3.1.1 *Introduction to the equipments for the electrical transport measurements*

During the PhD thesis, we used three kinds of equipments to do the electrical transport measurement for the transistors, including the individual DWNT, monolayer graphene and the DWNT or graphene/-molecule hybrid transistors. The first equipment is an ambient probe station with two tungsten probes at room temperature (Figure 42 (a)). Transfer characteristics can be acquired using a Keithley's Series 2400 Source Measure Unit. The transistor characteristics of device were measured by applying a V_{ds} = 2 mV DC bias between the source and drain electrodes while sweeping the gate voltage (V_g) between $\pm$ 30 V with a Yokogawa voltage source. The advantage of this probe station is the ease of operation. The transfer characteristic curves can be acquired in 2 minutes. One of the disadvantage is that there is no vacuum chamber, so the sample can be only measured in ambient condition. The other one is that there is a lot of noise because of the exposure to the air. This probe station is used for testing the connection of the nanotube to the electrodes. Depending on different purpose of the experiment, the metallic or semiconducting DWNTs need to be screened.

The second one is a vacuum Desert Cryogenics probe station with four beryllium-copper probes (Figure 42 (b)). One of the probe could be replaced by an optical fiber which can be used for measuring the sample under light illumination. Transfer characteristics $dV/dI - V_g$ curves are acquired in a current-biased lock-in configuration using a Stanford Research lock-in amplifier SR830 with a polarization resistance of 980 MOhms. The transistor characteristics of the device were measured by applying a 50 nA drain-source current while sweeping the gate voltage with a Keithley 6430. The use of lock-in amplifier reduced the noise. By using this probe station, the sample can be measured in vacuum and also at low temperature. One drawback is that we need to contact the probe to the sample manually, the vibration of the probe could affect the contact or damage the sample.

See Figure 42	(a)	(b)	(c)
contact mode	probe	probe	micro bond
Vacuum	no	yes	yes
Low T	no	1 K	4.2 K
Optical window	no	yes	compatible with microscopy

Table 1: Summary of the three equipments for the electrical transport measurements.

The last one is a Janis helium-flow cryostat (Figure 42 (c)). The sample should be micro bonded to a PCB or wired sample holder which contains several electrode that can be connected to the external circuit for the measurement. Adwin Pro system is used for applying the back gate voltage, bias voltage and measure the bias current. The Adwin Pro system can be controlled with Java script which is developed in NEEL Institute (Nano QT group: E. Bonet, C. Thirion) that can provide more facilities for the experiment. The advantage of this set up is that the sample can be well connected and protected in the cryostat. But the sample could be destroyed by the electrical static charge before or during the micro bonding or mounting of the sample to the cryostat.

Each of these three equipments have their own advantages and disadvantages. We have to select the appropriate equipment according to needs of the experiment. Janis was used when optics was really needed.

2.3.1.2 *Typical transfer characteristic curves of individual DWNT and graphene transistors*

In our experiment, the drain-source current (I_{ds}) is measured as a function of the gate voltage (V_g) at a constant drain-source potential (V_{ds}). This allows to distinguish the metallic and semiconducting nanotubes. For the metallic nanotubes, the density of states remains constant over a wide range of chemical potential and the current remains substantially constant as a function of the gate voltage. For semiconductors, the presence of an energy gap in the density of states results in several orders of magnitude modulation of the current. Figure 43 is the transfer characteristic of a typical metallic and a semiconducting double wall carbon nanotube. As we discussed in the last section, the gold and palladium electrodes were used to mark the position of the nanotubes. By using this method, we can compare the transfer characteristics to the Raman spectra in order to get more information. Moreover, as we discussed in chapter 1, the DWNTs have four kinds of metallic and semiconducting configurations, which are M@M, M@S, S@M, S@S tubes. Theoretically, the proportion of these four kinds of tubes are $\frac{1}{9}$, $\frac{2}{9}$, $\frac{2}{9}$ and $\frac{4}{9}$, respectively. Figure 44 shows the statistic of on/off current ratio (I_{on}/I_{off}) of 25 pristine isolated

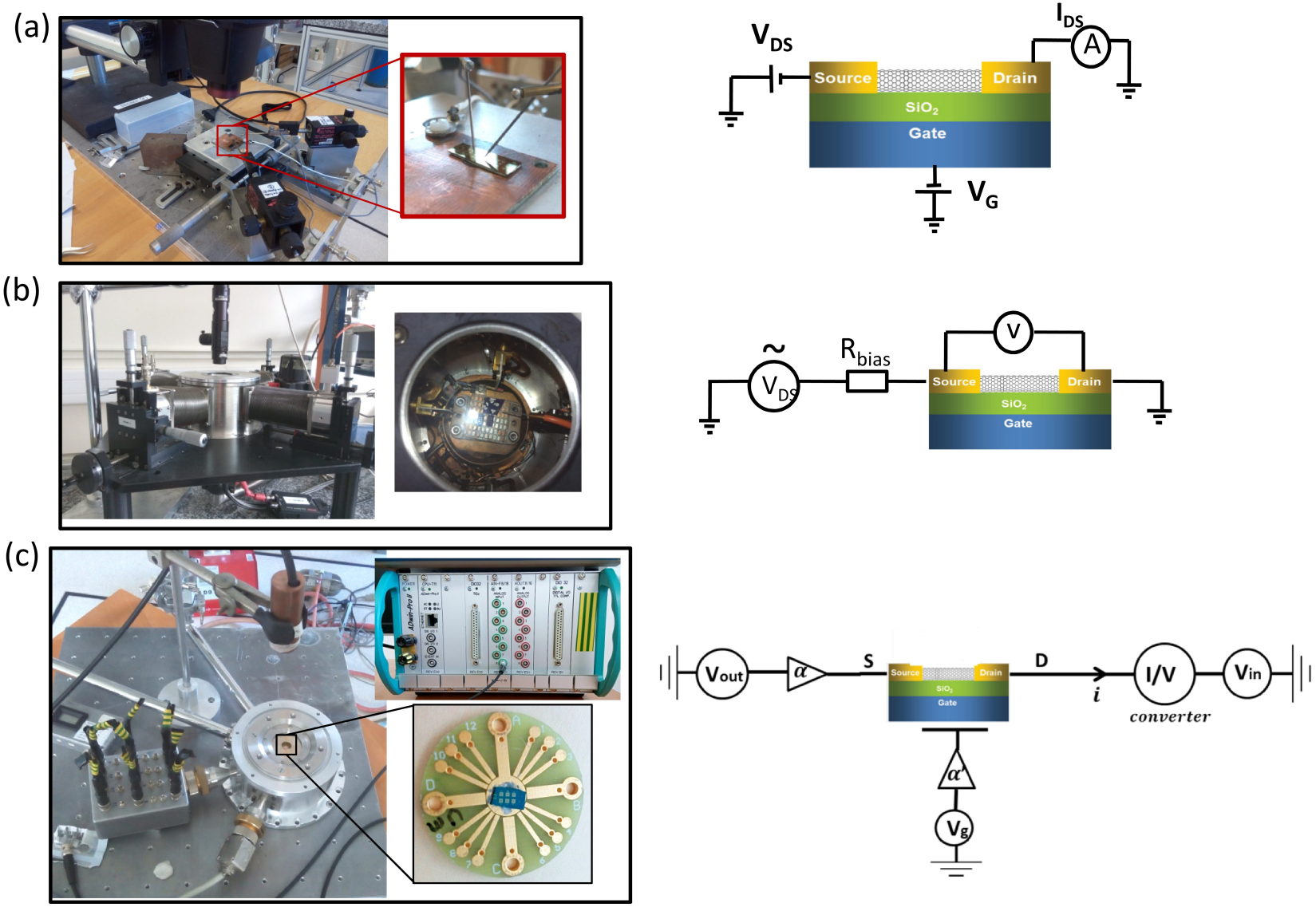

Figure 42: Equipments for the electrical transport measurement, (a) probe station in ambient condition, (b) probe station with cryogenic chamber, (c) Janis cryostat and Adwin pro system, the right panels show the electrical circuit for the corresponding equipments.

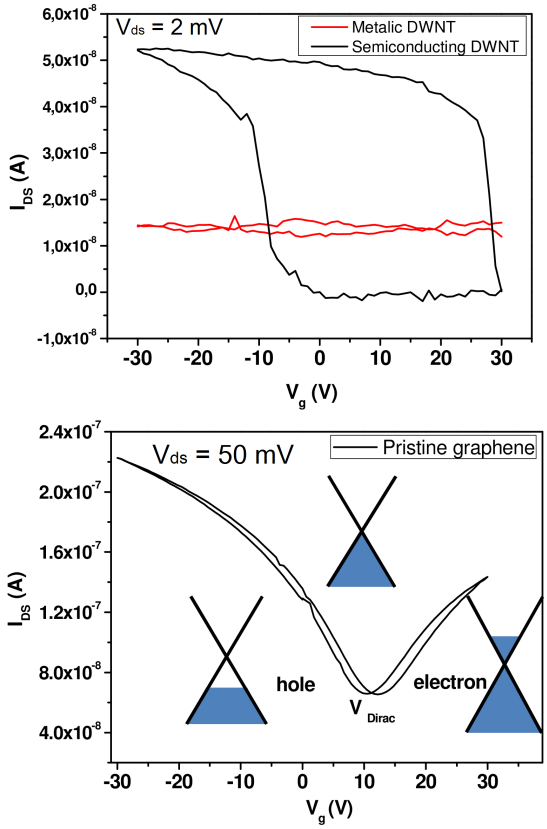

Figure 43: Typical transfer characteristic curves of individual DWNT (up) and graphene FETs (down).

DWNT FETs, among which, we found that 3 tubes have $I_{on}/I_{off} = 1$, which means these 3 tubes have M@M configuration. Similarly, for the $I_{on}/I_{off} > 30$, there are 8 tubes, the proportion of which satisfied the distribution of S@S tubes. The I_{on}/I_{off} of the rest of tubes are between 1 and 5, which may have M@S or M@S configuration. From Figure 44, we can observe that the distribution correlated well with the theory, therefore, we can roughly estimate that in our experiment, if $I_{on}/I_{off} > 30$, the DWNT has S@S configuration; if $1 < I_{on}/I_{off} < 30$, the DWNT is a M@S or S@M tube; if $I_{on}/I_{off} = 1$, then the DWNT is a M@M tube.

Recently, Ghedjatti et al. studied the structure and inter wall coupling of CVD synthesised DWNTs by HRTEM. By investigating huge amount of samples and Monte Carlo simulations, they found that many incommensurate DWNTs does exist (Ghedjatti PhD thesis 2016). We want to note that the statistical tool that we mentioned above only can be used to roughly estimate the metallic and semiconducting configurations of DWNT. In the experiment, we need to combine different methods to determine the configurations, for example, the Raman spectrosocpy which will be discussed in the next section.

Carbon nanotubes are ambipolar conductors, the transport carriers are either dominated by the holes or electrons depending on

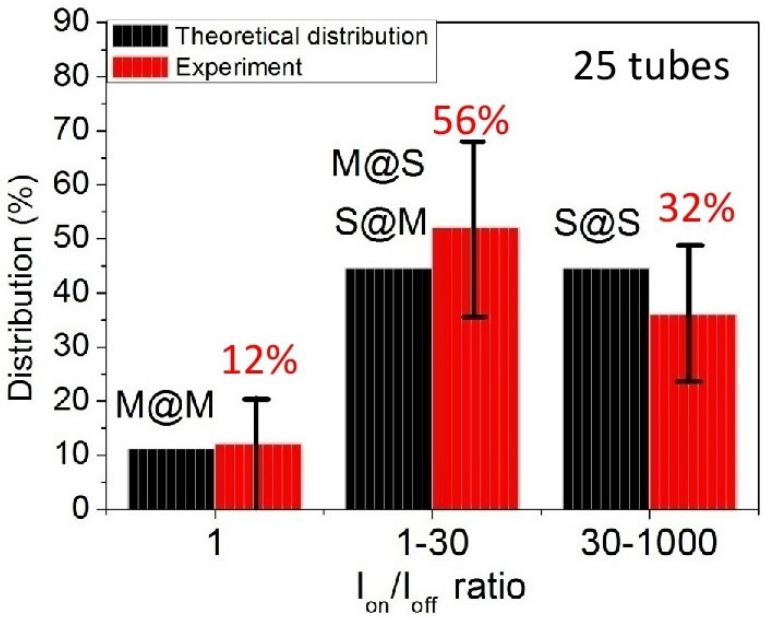

Figure 44: Distribution of the on/off current ratio for the pristine isolated DWNT FETs.

the doping level. The semiconductor transfer characteristic has three branches: the p branch where the majority carriers are holes (V_g<0), the n branch where the majority carriers are electrons (V_g>0) and the off branch where the conductance is minimum ($V_g \sim 0$). The current in the off state can be very low depending on the width of the band gap. Figure 45 (c) and (d) show a FET have ambipolar behavior and unipolar behavior, respectively.

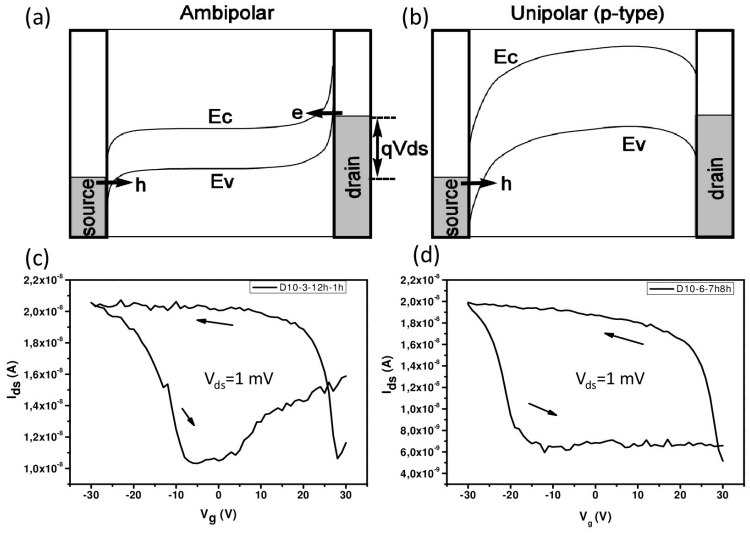

Figure 45: Schematic representation and the typical transfer characteristic of the ambipolar ((a),(c)) and unipolar FET ((b),(d)), nanotubes and graphene are always ambipolar, but if the barrier is too asymmetric then it turns difficult to reach the n side (but it exist).

The transfer characteristics should be corrected for the gate leakage. It is important to note that the transfer characteristics presents a

significant hysteresis which is mainly caused by the trapping charges on the substrate and also depend on the sweeping speed. To ensure they have comparable characteristics of a measurement to the other, we sweep the voltage at a constant speed and make several cycles to make sure of the stability of the systems. Normally, we compare the data from the second cycle to be sure to have reached stability.

After discussing the transfer characteristics of CNTFETs, in the next paragraphs, we will discuss the graphene FETs (GFETs). Large-area graphene is a semimetal with zero bandgap. Its valence and conduction bands are cone-shaped and meet at the K points of the Brillouin zone. This makes GFET the first atomically thin 2D ambipolar field effect transistors. The same as the nanotube transistor, the transport carriers are either dominated by the holes or electrons depending on the doping level Figure 43. From the equation,

$$E_F(n) = -sgn(n)\hbar v_F\sqrt{(\pi|n|)} \tag{20}$$

(n: charge carrier density, V_F: Fermi velosity). It is clear that by changing the charge carrier density, the Fermi level of graphene is tuned towards a certain energy, so the conductivity of the graphene FETs is also tuned. When the Fermi level is at the Dirac point, then the conductivity is tuned into minimum, so as the charge carrier density Figure 43. This point in field effect curve is often referred to as the Dirac point V_{Dirac} or the charge neutrality point V_{NP}. In our case, the charge carrier density is tuned by applying a back gate voltage. In our experiments, the graphene is transferred on top of a thick dielectric layer (285 nm SiO_2). By capacitive coupling $Q = CV_g$, the induced charge carrier density per unit area, per unit Volt, is

$$n = \frac{\epsilon\epsilon_0}{de} \sim 7.56 \times 10^{10} cm^{-2}V^{-1} \tag{21}$$

Normally, the dV/dI (V_g) curves of graphene transistors show the V shape behaviour related to the Dirac point. The gate-voltage dependent conductance shows hysteresis depending on the gate sweeping rate/range, which is mainly caused by the adsorbates on the graphene surface. In order to monitor the shift of the curves after functionalization, we keep the same sweeping rate and only compare the curve when sweeping the back gate from positive to the negative value. The shift of V_{Dirac} can be used to evaluate the shift of doping level (electrostatic doping or chemical doping), it also can be used in CNTFETs. We will discuss in detail in the next chapters.

Although many information, such as the resistance, the intrinsic doping level can be extracted from the transfer characteristic curve, other techniques are also needed for studying optical and vibrational properties of DWNT and graphene. In the following subsection, the Raman spectroscopy of graphene and DWNT FETs will be introduced.

2.3.2 *Vibrational features for monolayer graphene and isolated DWNT*

2.3.2.1 *Raman spectroscopy of isolated DWNT transistors*

In order to get the Raman spectra of individual DWNTs, a spatially resolved Raman mapping technic was used. It was performed with a commercial Witec Alpha 500 spectrometer set up with a dual axis X-Y piezo stage in a backscattering/reflection configuration. The grating had 1800 lines per mm. Two laser excitation wavelengths are available in our lab: 532 nm and 633 nm.

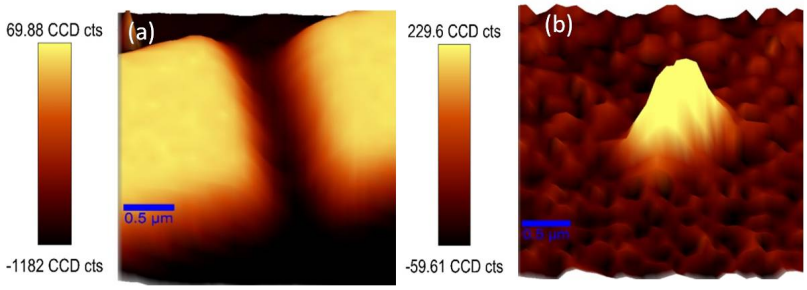

Figure 46: Spatial resolved Raman images of a DWNT transistor. (a) Sum of the mode of SiO_2,(b) sum of G peaks.

Figure 46 shows typical Raman images of an isolated DWNT transistor. The intensity is plotted in different colors. (a) is the mapping of the SiO_2, the electrode and substrate can be easily distinguished from this mapping figure. (b) is the sum of G peaks, that is the mapping of the carbon nanotube, we can clearly see that the position of the carbon nanotube is between two electrodes. In practical, using this method can help us to find the accurate position of the nanotube and focus the laser exactly on the tube that we want to measure. As soon as we get the best focus, the single spectra with better resolution and higher signal to noise ratio are recorded.

Figure 47 shows an example of single spectrum of the isolated DWNT. One is a metallic sample, the other is a semiconducting one. The corresponding transfer characteristic was present in the last section figure Figure 43. Two excitation laser wavelength were used for the measurement: 633 nm ((a), (b) and (c)) and 532 nm ((d), (e) and (f)). The red lines represent the signal of the metallic tube and the black lines are the signal from the semiconducting one. As we discussed in the first chapter, the Raman response for metallic and semiconducting tubes can be quite different, especially in the G band region. Due to the electron-phonon coupling, the G band could show an assymetric Breit-Wigner-Fano (BWF) like line shape and thus its FWHM is broader than for the semiconducting tubes. Here, we did a simple analysis of the data by using the software provided by the Witec system. We used a Lorentzien filter to fit the G peak with the Lorentzian function. At the excitation wavelength of 633 nm, for the metallic tube, a BMF line shape can be clearly observed in the G band region (figure (b)); for the semiconducting one, two sharp peaks at 1585 cm^{-1}

and 1561 cm^{-1} appeared, which can be easily assigned to the G^+ and the G^- peaks. The G peaks of the metallic tube are 2 to 6 cm^{-1} wider than the semiconducting tube. We have a similar result when the excitation laser wavelength changed to 532 nm, as shown in figure (e). For the metallic tube, the G peak at 1588 cm^{-1} has a FWHM of 22 cm^{-1} which is larger than the one of the semiconducting tube (6 cm^{-1}).

At 633 nm, the metallic tube achieves a good resonant condition, the RBLM peaks can be observed. We can observe from Figure 47 that except the peak at 302 cm^{-1} which is the signature of silicon substrate, two other peaks appear. We assign the peak around 146 cm^{-1} to the contribution from the outer wall and the 210 cm^{-1} to the inner wall. Because we are measuring isolated DWNTs with mixed chiralities, it is very difficult to find the resonant tubes like the metallic tube that we show here. We study only the tubes which are resonant in those wavelengths as far as the imaging is mandatory to check the nanotubes transistors. For this semiconducting tube, the RBM peaks are not observed.

Raman spectroscopy not only can get the M and S configurations of the isolated DWNTs, but also can give the information of the interwall coupling. In all the resonance samples that we have measured, two kinds of spectra can be observed. For most of the cases, only one RBM is resonant at a certain excitation wavelength (Figure 48 (b)), but sometimes, two RBM peaks from the inner and the outer wall can be observed at the same time, as shown in Figure 48 (a), and one peak is much higher than the other one. Moreover, even we change the excitation wavelength, the two peaks still can be observed spontaneously. In this case, the two walls have strong coupling, either mechanically [82, 81] or electrically [119]. In a word, from the observation of the RBM peaks of DWNTs, strong or weak interwall coupling could be determined.

2.3.2.2 *Raman spectroscopy of monolayer graphene*

The spatially resolved Raman spectroscopy also can be used to characterise graphene. Figure 49 (a) and (b) show the Raman mapping of graphene G band and 2D band respectively. The black part shows the position of SiO_2 which is not covered by graphene, because there is no graphene signal. The orange part shows the position of graphene. The graphene edge and the wrinkle can be easily distinguished. Figure 49 (c) shows several Raman spectra extracted from the Raman map at different positions. Single-Lorentzian profiles of G and 2D peaks unambiguously show a monolayer graphene feature. No noticeable D band can be found neither in the plain nor in the wrinkle parts, suggesting good quality of this graphene. Furthermore, comparing to the blue curve, the G peak of the green curve has a slight

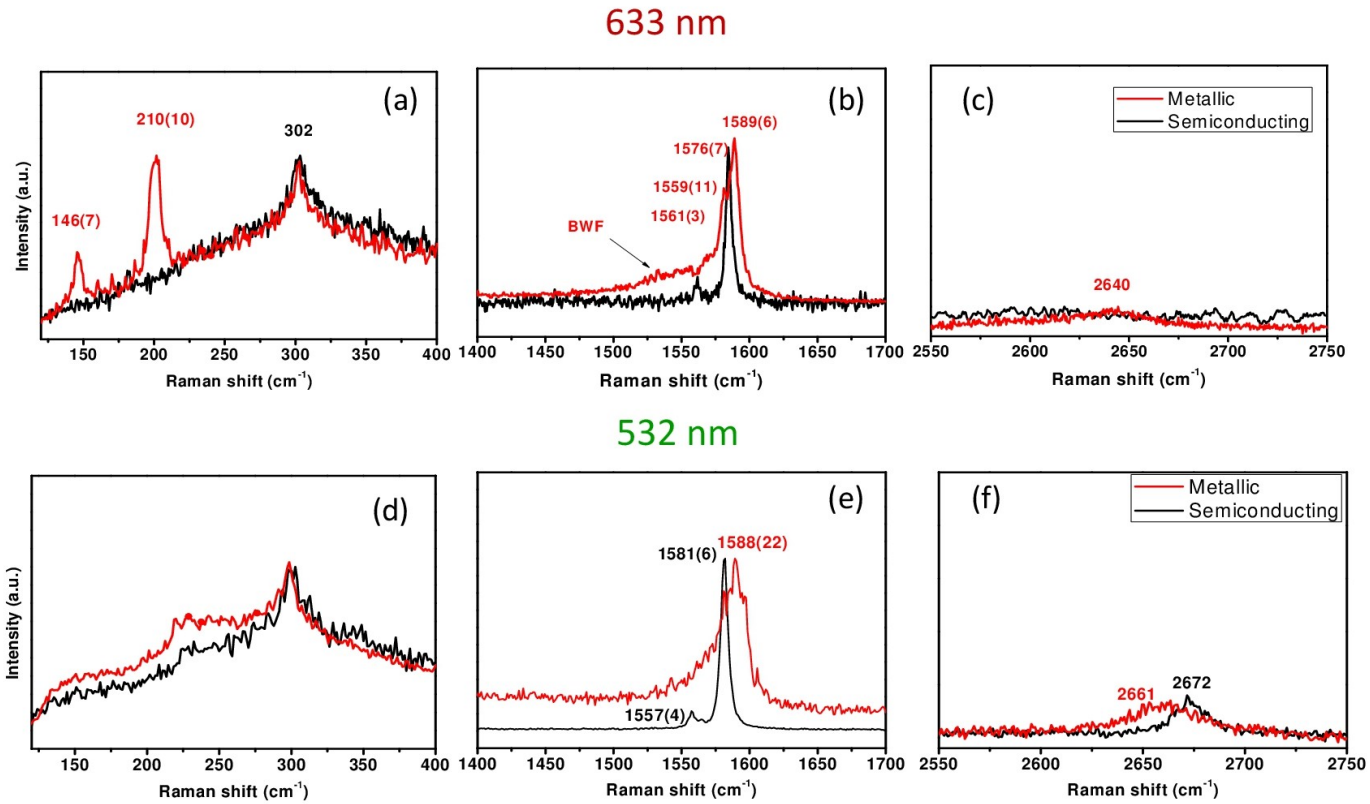

Figure 47: Raman spectra of a metallic (red) and a semiconducting (black) DWNTs with two excitation wavelengths: 633 nm ((a), (b) and (c)) and 532 nm ((d),(e) and (f)). Signals are observed in three regions: RBLM band: (a) and (d), G band: (b) and (e) , 2D band: (c) and (f).

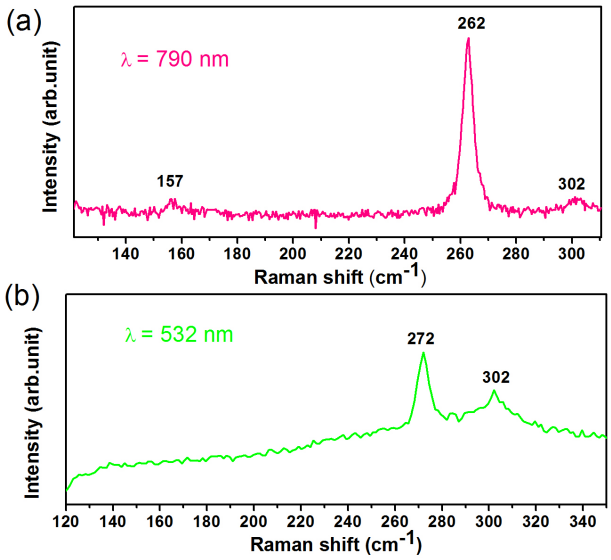

Figure 48: RBM peaks of two kinds of DWNT, (a) strong interwall coupling, (b) weak interwall coupling.

down shift (2 cm^{-1}), which was attribute to the strain induced by the wrinkle [120].

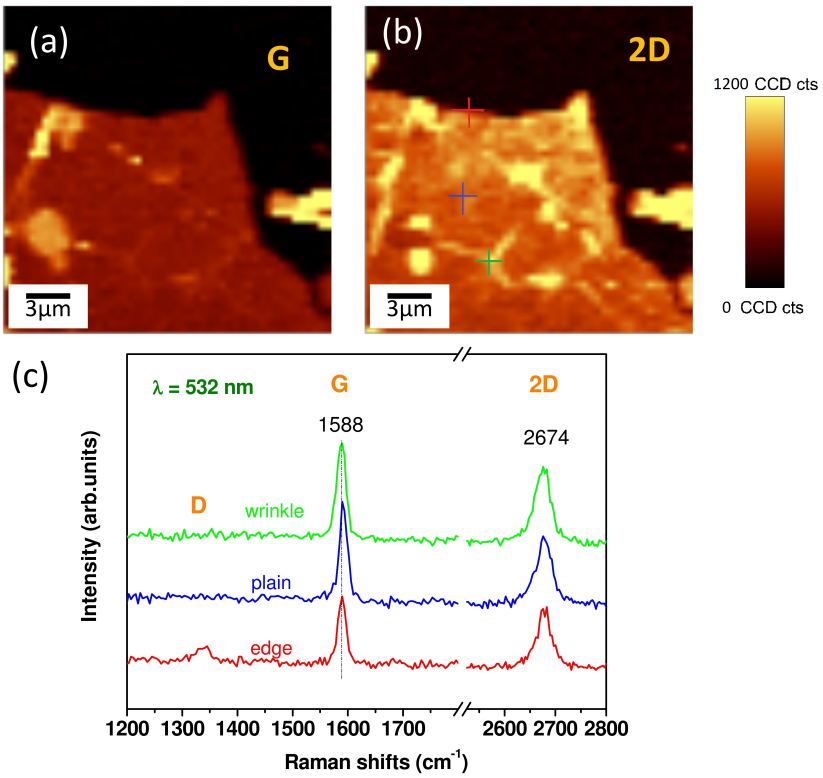

Figure 49: Spatially resolved Raman spectra of graphene on SiO_2 substrate, (a) (b) mapping of G band and 2D band, (c) spectra at different position extracted from the map (spectra correspond to the crosses on image b), grating: 1800/mm.

Overall, some information can be obtained from the spatially resolved Raman spectroscopy. For example, the position and the shape

of graphene, the number of layers, the quality and the defects ... It is the most used and performing tool to study the properties of graphene.

By combining the Raman spectra with the transfer characteristics of the DWNT, we can distinguish the metallic and semiconducting DWNT, and in some cases their configurations. Moreover, this technique also can be used to study graphene. It is one of the main technique that we used in this thesis to study the properties of isolated DWNT and graphene FETs. Raman spectroscopy also allows to investigate specific fundamental issues in sp^2 carbon systems, such as electron-phonon coupling, which we will discuss in the next section.

2.3.3 *Kohn anomaly and electron-phonon coupling*

Many researchers claim that the BWF line shape of the metallic nanotube G mode is caused by the so called Kohn anomally [121]. A Kohn anomaly is an anomaly in the dispersion relation of a phonon branch in a metal. For a specific wavevector, the frequency and thus the energy of the associated phonon is considerably lowered, and there is a discontinuity in its derivative. They have been first proposed by Walter Kohn in 1955 [122]. Metallic nanotubes are predicted to be one dimensional quantum wires with ballistic electron transport. However, high field electrical transport measurements show that the electron-phonon scattering by optical phonons at K breaks down the ballistic behavior [123]. Electron phonon coupling (EPC) is thus the fundamental bottleneck for ballistic transport. Recent experimental and theoretical studies on single wall nanotubes (SWNTs) have reported significant electron-phonon (e^--ph) interactions in electrical transport [124, 125], electron tunneling [126], and optical transitions [127, 128]. An investigation of the e^--p coupling mechanisms in metallic nanotubes is therefore fundamental to understanding 1D conduction in these materials. The frequency and the intensity of the Raman modes are determined by the EPC matrix elements. There are already many researchers studied the EPC in metallic SWNTs [67, 129, 130, 131, 132] and graphene [62, 63] by *in situ* Raman spectroscopy. In this thesis, we used this method to study individual DWNTs. As we discussed in chapter 1, for DWNT, there is inter-layer interaction as it in double layer graphene. We try to understand how the inter layer interaction can affect the electron phonon coupling in the double wall system.

2.3.3.1 *Experimental setup*

Figure 50 shows the scheme of the experimental setup. At first, we mounted the DWNT transitors to a cryostat which has optical access (Janis). The cryostat was mounted onto the Witec Raman stage, the

stage can move in X, Y and Z direction, therefore we can locate the position and focus the laser onto the DWNT. The objective used in a Mitutoyo 100× with a NA of 0.70 and corrected for the optical window. The Raman measurments were performed in a backscattering configuration with 532 nm and 633 nm laser excitation. The laser spot size is around 500 nm and the power was kept below 1 mW. The gate was applied by the Adwin-Pro system with a 20× voltage amplifier (A400D, FLC electronic).

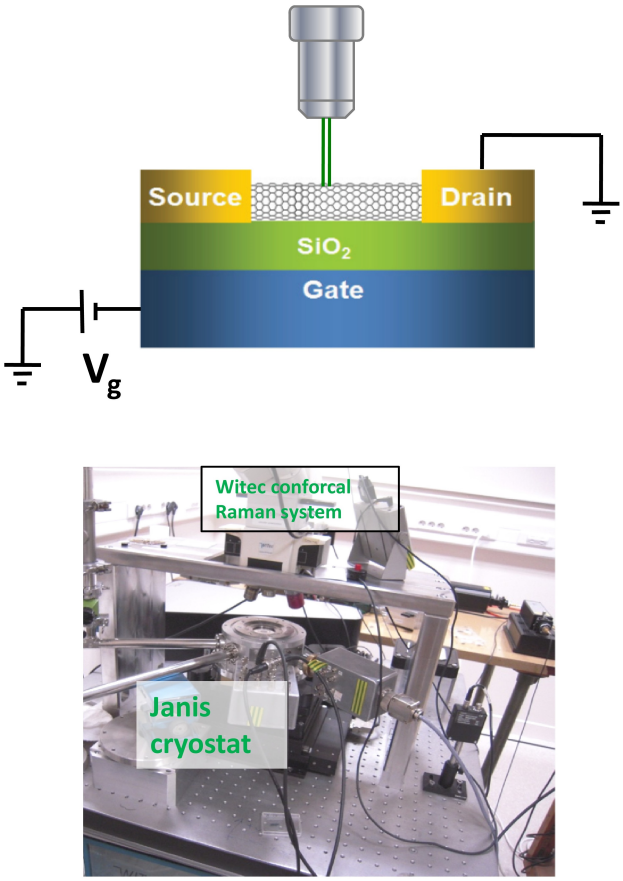

Figure 50: Schematic representation of the experimental set up for the in situ Raman measurement(up); experimental setup in the lab(down)

2.3.3.2 *Results and discussion*

Figure 51 shows the transfer characteristic of the measured DWNT. The applied bias voltage is adjusted according to the sample resistance so as to have a certain current in the device (high enough for the signal to noise ratio, small enough to prevent Joule heating and damage). In this case, the bias voltage is 1 mV. We can observe from the figure that the transfer characteristic shows a slight field effect with the on state and off state current ratio $I_{on}/I_{off} = 2.16$. The resistance of this DWNT is around 50 kΩ which is lower than a typical semiconducting CNT. Therefore, we assign this DWNT is a mixture of a metallic and a semiconducting tube as described in last section.

This can be confirmed by the Raman spectra of this DWNT, as shown in Figure 52.

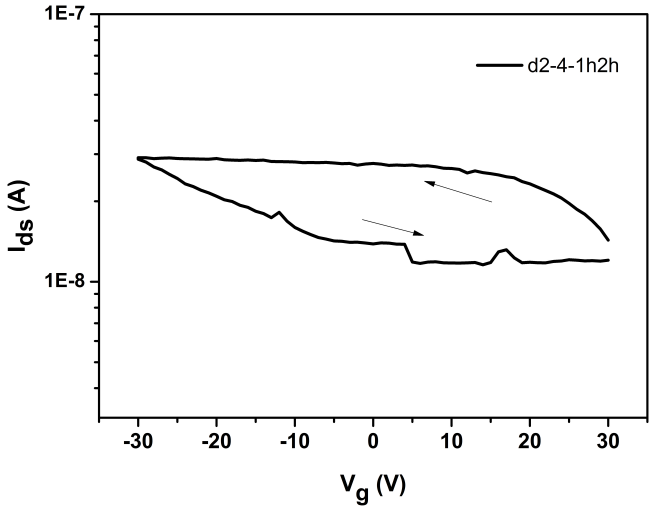

Figure 51: Transfer characteristic of the sample, the bias voltage is 1 mV, the back gate is swept from 30 V to -30 V and then from -30 V to 30 V.

In Figure 52, the RBM mode, G mode and 2D is presented. One RBM peak at 254 cm^{-1} can be observed. Here we can use the Kataura plot to estimate the metallic or semiconducting configuration of the DWNT, because from the Raman spectrum, only one RBM mode is observed, which means the mechanical coupling of the two walls is not very strong or we are not at the right wavelength (see chapter 3), other wise, two correlated RBM modes should be observed simultaneously [80, 82]. By using the Kataura plot, the transition energy falls into the first transition for metallic nanotubes (E_{11}^{M}), so this tube is metallic. By comparing the peak position to the DWNT bundles, we assign this peak to the inner tube. We did not have an efficient resonant condition for the outer tube to observe its breathing mode. But from the peaks in the G mode region, we still can get a lot of information. Nevertheless, as we discussed in chapter 1, The G peak of the DWNT should have 4 components, the highest two should come from the G^+ mode of the two tubes. And the two lowest ones are from the G^- mode. In the 2D mode region, we assign the peak at 2652 cm^{-1} to the contribute of the inner wall and 2684 cm^{-1} to the outer wall [133]. A asymmetric component can be observed from the G peak region, which is the so called BWF peak and the signature of metallic tube. Comparing our data to the literature [133], we claim that this DWNT has a M@S configuration, which is in consistent with the probe test measurements.

The *in situ* Raman spectra of this sample was measured at the laser excitation wavelength 532 nm with the gate tuning from 15 V to 65 V. The data are normalized by the intensity of G^+ peak. During the experimental process we tuned the back gate from 15 V to 65 V by step of 5 V. The high frequency mode corresponding to the G^+

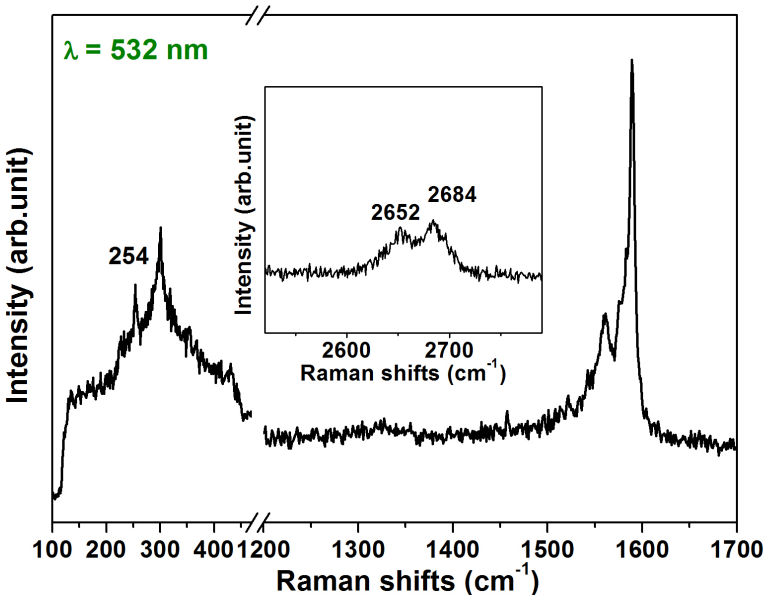

Figure 52: Raman spectrum of sample measured with the laser excitation wavelength 532 nm

ω_{G1} cm^{-1}	Γ_{G1} cm^{-1}	ω_{G} cm^{-1}	Γ_{G2} cm^{-1}	ω_{G3} cm^{-1}	Γ_{G3} cm^{-1}	ω_{GFano} cm^{-1}	Γ_{GFano} cm^{-1}
1594.7	7.4	1591.3	5.6	1582.1	11.6	1550.3	71.5

Table 2: Summary of the fitting of peaks when the applied back gate is 25 V.

mode and the low ones corresponding to the G^- mode. Before fitting the curves, several changes can already be observed easily when changing the back gate. At first, the intensity of the G^- Fano peak increasing when tuning the back gate. Second, comparing the data of Raman spectra at 65 V to that of 25 V, the G^- peak looks much wider. To see the changes more clearly, we fitted the data into four peaks. We call them G_1, G_2, G_3 and Fano peak, respectively. The peaks of G_1, G_2, G_3 were fitted by the Lorentzien function, and for the asymmetric peak at the lower frequency, the following Breit-Wigner-Fano function was used:

$$I(\omega) = I_0 \frac{[1 + (\omega - \omega_{Fano})/q\Gamma]^2}{1 + [(\omega - \omega_{Fano})/\Gamma]^2} \tag{22}$$

The function was used to fit the BWF lineshape, in which $1/q$ represents the asymmetry of the shape, (it represents the electron-phonon interaction), ω_{Fano}, I_0 and Γ are fitting parameters of the central frequency, the intensity and the broadening factor, respectively. As we discussed above, this nanotube is a mixture of a semiconducting outer tube and a metallic inner tube, this BWF peak shows another evidence of metallic tube existence in the sample.

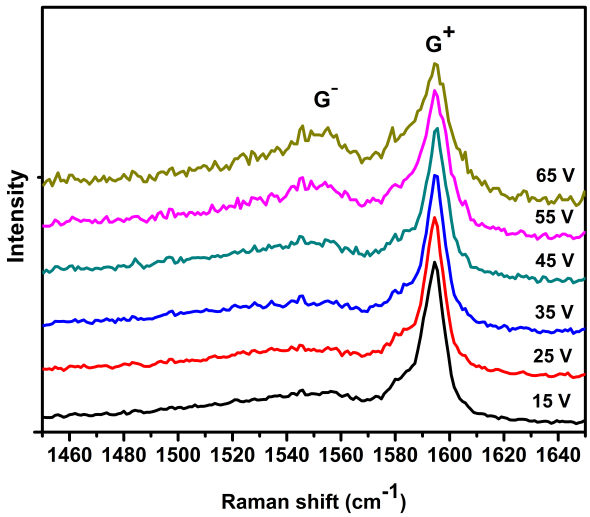

Figure 53: The *in situ* Raman spectra of the sample measure at the laser excitation wavelength 532 nm with the gate tuning from 15 V to 65 V

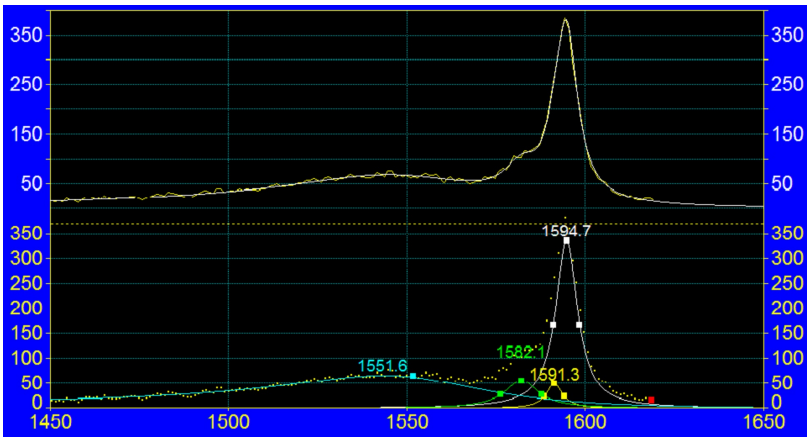

Figure 54: The fitting of G band of sample D2-4-1h2h with an applied 25 V back gate.

Table 2 shows the fitting results for the sample when applied a 25 V back gate. $\omega_{G_1}, \omega_{G_2}, \omega_{G_3}, \omega_{Fano}$ are 1594.7, 1591.3, 1582.1, 1551.6 $cm^{-}1$, respectively. Based on the method discussed in [134], we assign the two higher frequency peaks G_1 and G_2 to the G^+ peaks of the outer wall and the inner wall, and the lower frequency peaks G_3 and G_{Fano} to the G^- peaks of the two walls. The EPC determines an important broadening of the LO mode of metallic tubes [66]. This explains the large width of the G_{Fano} (71.5 cm^{-1}) lines. The sharpness of the G_1 and G_2 line (7.4 and 5.6 cm^{-1}) is explained by considering that the semiconducting LO and the metallic TO modes are not broadened by EPC and that their frequencies are almost independent from diameter. In the case of semiconducting tubes, the phonon is not coupled to electron since there is a gap, so the Raman process is not affected by the conduction electrons. In the case of the metallic tube, the TO is independent from the electron phonon coupling due to the selection rules.

In order to compare the position and FWHM change of the four peaks at different applied back gate voltage, the figures of back gate voltage (V_g VS.ω_G and Γ_G have been made. (Figure 55)

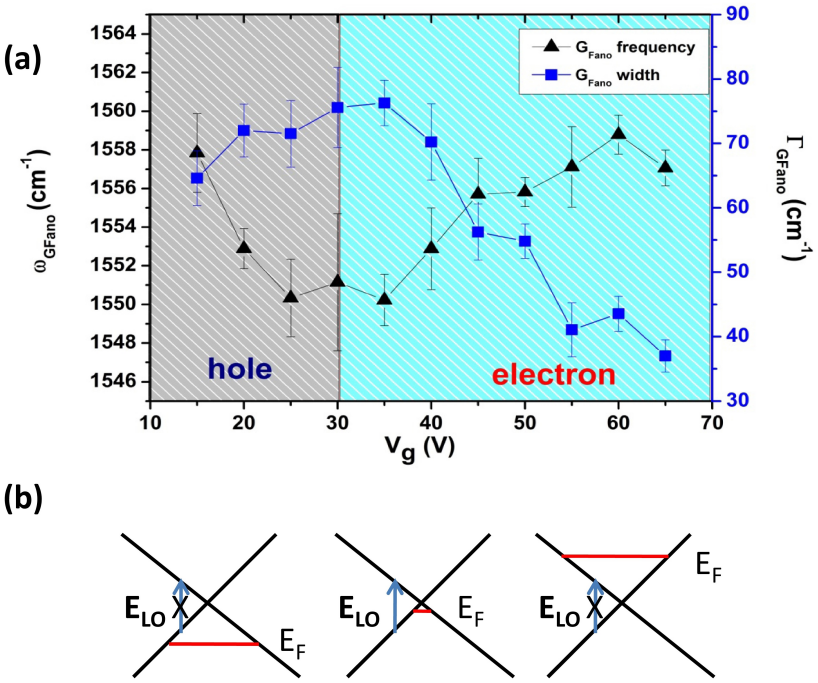

Figure 55: (a) The back gate dependence of the G_{Fano} peak frequency (triangle) and fitted width (squares). The left axis is the fitted frequency of the G_{Fano} peak, the right axis is the width. The triangle and square represent the frequency and width respectively; (b) The three diagrams show the modulation of the Fermi level relative to the Fermi neutral point. The arrows represent the possibility for an electron to produce an interband transition depending on the position of the Fermi level. The length of the arrows is equal to the energy of the phonon match (about 195 meV for the LO mode).

The back gate dependence of the G_{Fano} peak frequency and width are shown in Figure 55 (a). It is clear that both of the frequency and the width of the Fano peak have remarkable change while changing the back gate. For the frequency, before $30V \pm 2V$, it is decreasing while increasing the back gate, and after $30V \pm 2V$, it is increasing while the back gate increase. In the meanwhile, the width of the Fano peak shows the reverse behavior. These results are consistent with the result in [132] for the isolated metallic SWNT, and also the result in [63] for monolayer graphene. These behaviors can be explained by the electron phonon coupling process as shown in Figure 55 (b). As we mentioned in chapter 1, the electron or hole carriers were injected by the electrostatic charge which can be controlled by the back gate [132]. The symmetric changes of $\omega_{G_{Fano}}(V_g)$ and $\Gamma_{G_{Fano}(Vg)}$ relative to the value of $V_g \sim 30V$ linked to the symmetry of the electronic band structure that occurs at the Fermi neutral point. From the probe test, we stoppped at 30V to prevent the back gate leakage, so we know

$V_{Dirac} \geqslant 30V$, it is a proof here that $V_{Dirac} = 30V$, it is consistent with p doping we usually see in our devices. $\omega_{G_{Fano}(V_g)}$ has minimum near the Fermi neutral point, revealing that increases in charge density of either side result in stiffening of the G mode. On the other hand, $\Gamma_{G_{Fano}}$ sharply decreases as $|V_g - V_{Dirac}|$ ($V_{Dirac} = 30 \pm 2V$)increases, showing that longer phonon lifetimes are linked to higher particle/hole density. The largest effect is the frequency increase of the G_{Fano} line by 9 (8) cm^{-1} on electron (hole), which are smaller than the reported frequency increase of the doping SWNT by the liquid gate (10 to 15 cm^{-1}) [67]. This may be because the applied liquid gate in ref. [67] can push the Fermi level higher than the back gate that we used for this experiment. The substantial decrease of G_{Fano} line width is remarkable (over than 40 cm^{-1}). Both effects are due to the dependence of the EPC on V_g in the metallic inner tube. Phonon decay processes are real transitions that conserve energy and momentum. The small wavevector G phonon can only decay into particle-hole pairs represented by vertical transitions that have vanishingly small wavevector transfer. The coupling is allowed only when $|E_F| < E_{LO}$ (Figure 55 (b)). For evaluating the strength of the electron phonon coupling, we plotted $-1/q$ of the G_{Fano} peak as a function of V_g (Figure 56(a)). The value of $-1/q$ varies from 0.2 to 0.45 with the change of the back gate voltage, which means the electron phonon coupling strength is modified by the change of back gate voltage.

Figure 56 (b) shows the intensity ratio of the G_{Fano} and G_1 as a function of V_g. The intensity change may be mostly due to the resonant profile change when the Fermi level shift. [67, 132].

Moreover, the same analysis on G_1,G_2 and G_3, as presented in Figure 57. It can be observed from Figure 57 (a) that ω_{G_1} has no obvious change with the back gate. Only the Γ_{G_1} increases as the back gate increases after the $30 \pm 2V$ (Fermi neutral point). As we discussed above, the G_1 peak mostly comes from the contribution of the G^+ mode of the outer semiconducting tube, which can be assigned to the LO mode of the outer tube [72]. The behavior of the G_1 line at high doping is mostly due to semiconducting tubes. The width shift of the G_1 line is correlated to the trend of I_{DS} current which should also increase when increasing the electron doping level, indicating that the G_1 shift is due to the change of the electron (hole) populations in the conduction (valence) bands of semiconducting tube. The similar effect also observed by Das *et al.* [66] and Yuan *et al.* [135] for SWNT bundle and individual semiconducting DWNT.

Figure 57 (b) and (c) show that there is no obvious dependence of V_g for the frequency and width of G_2 and G_3, which consistent with the results of Das *et al.* [66]. The results shown in Figure 57 and Figure 55 indicate that even if there is no mechanical coupling between the inner wall and the outer wall of this double wall carbon nanotube, metallic inner tubes accept charge carriers even from the

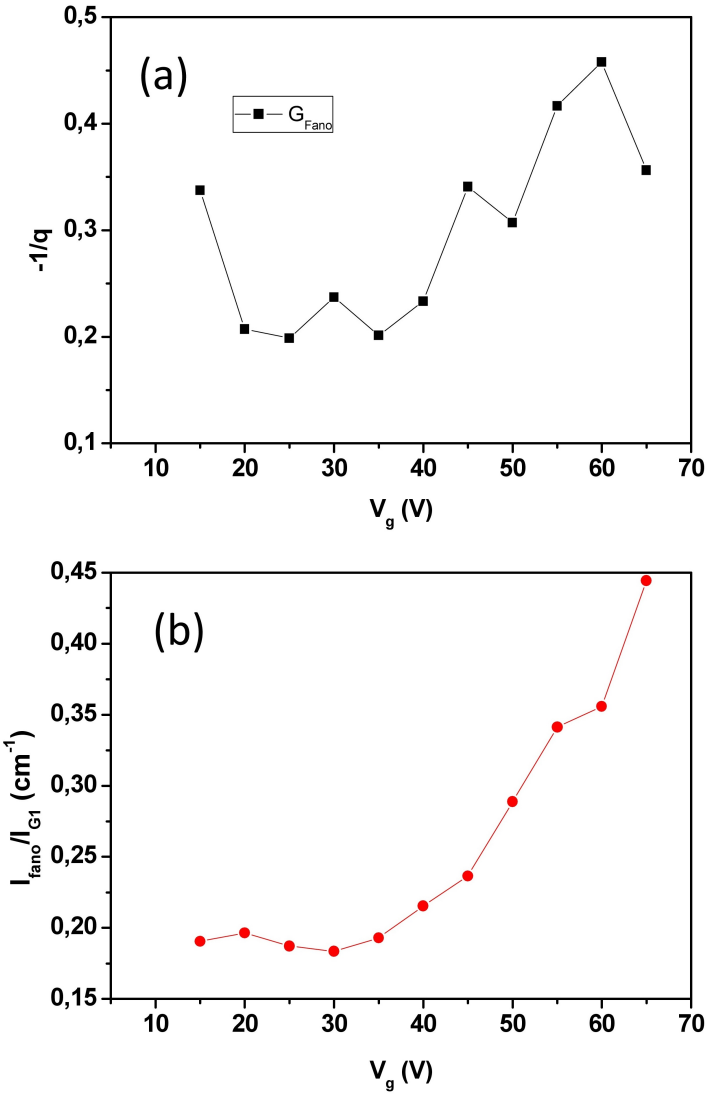

Figure 56: (a)$-1/q$ of the G_{Fano} peak as a function of V_g (b) The intensity ratio of the G_{Fano} and G_1 as a function of V_g.

semiconducting outer tube. Inner metallic tube still exhibits the similar electron phonon coupling behavior of a single metallic single wall carbon nanotube when applying the back gate.

In summary, we studied the electron phonon coupling in one individual DWNT. The sample that we measured have an inner metallic and outer semiconducting tube. The M@S configuration was determined by combining the spacially resolved Raman spectroscopy and the transport measurement on the same tube. The evolution of LO mode of the inner metallic tube while applying the back gate was carefully studied. The frequency, width, and the asymmetric factor -1/q of the LO peak of the inner wall shows the same dependence on the back gate voltage (Fermi level), and can be explained by the electron phonon coupling due to the Kohn anomaly. To the best of our knowledge, this is the first report of an experimental work for

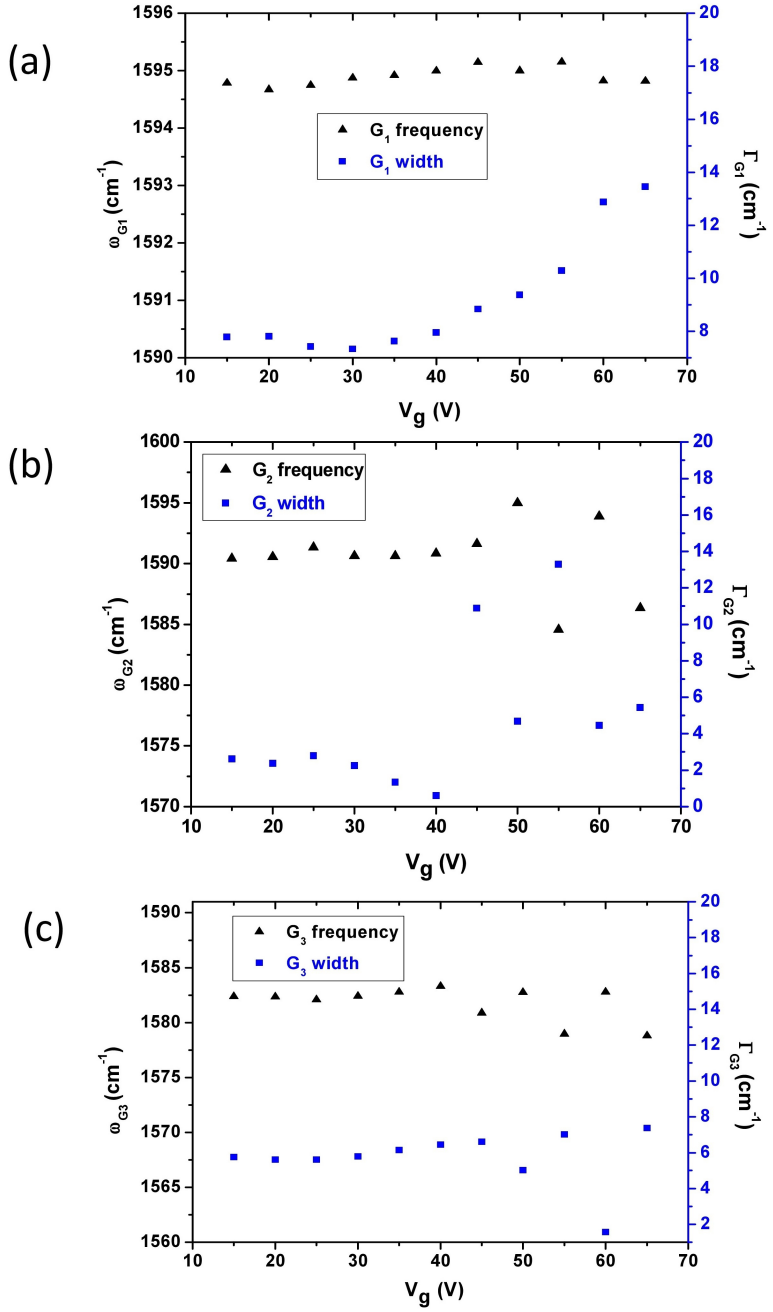

Figure 57: The frequency (black triangles) and width (blue squares) of G_1 (a), G_2 (b), G_3 (c) as a function of V_g. The left axis is the fitted frequency of the G_{Fano} peak, the right axis is the width. The triangle and square represent the frequency and width respectively.

studying the electron phonon coupling in double wall carbon nanotube. And because of the complex structure of DWNT, there is not many calculations studying the electron phonon coupling performed on this system. We are currently performing more experiments on different samples, for example, the samples with different configurations or different diameters. Our current results on the response of the asymmetric LO phonon mode of the inner tube under gating provide the guidance for assigning peaks in the double wall carbon

nanotube system and may create opportunities for studying the inter layer coupling in the double wall tube system, for instance, the S@M configuration would be interesting to see how much screening of the charges by the M tube affects the inner tube and M@M tubes are interesting to see the influence of the EPC on interwall coupling.

2.3.4 *Summary of the section*

By combining optical phonons measurements and electrical transport measurement, the electronic configuration (S@S, S@M, M@S, M@M) of the the DWNT could be determined. Moreover, we observe two families of DWNT: a strong interwall coupling family where the mechanical coupling is strong enough that the RBLM are correlated and simultaneously resonant whereas the second family of DWNTs behave like two embedded SWNTs.

By tuning the gate voltage on a FET configuration, we demonstrate that it is possible to tune the electronic properties of an inner metallic tube. In fact, the outer one has a semiconducting behaviour as a tranparent material. Once again, the strong coupling between optical phonons and electrons allows us to tune inner wall electronic properties. As we discussed in chapter 1, there are several ways to induce doping in the sp^2 system. In this section, we used the back gate electrostatic doping. In fact, molecules can also have doping effect which is comparable to the back gate doping effect. In order to study the molecule induced doping effect, especially study how doping can effect the inner tube, at first, we need to functionalise the nanotubes. In the following section, we will discuss the functionalization methods that are used in this thesis.

2.4 FUNCTIONALIZATION OF GRAPHENE AND ISOLATED DWNT TRANSISTORS

As we discussed in chapter 1, there are two methods to functionalize graphene and CNT transistors. One is the non covalent method, the other is the covalent method. In this thesis, we mainly use the non covalent way to functionalize graphene and DWNT transisors with the optical sensitive molecules. We also graft diazonium salt covalently to the outer wall of DWNT transistors to study the electrical and optical properties change with the effect of covalent grafting. For the non covalent functionalization experiment, we use the drop-cast method. At first, the molecules were dissolved in the solvent (Tetrahydrofuran (THF), Acetonitrile (ACN), Dichloromethane (CH_2Cl_2) et al.), the solution was then drop-casted onto the silicon substrate with the graphene or DWNT transistors. After that, the substrate was rinsed in the solvent to wash out extra molecules. In order

molecule	solvent	concentration ($mol.L^{-1}$)
TPyOs	ACN	2.64×10^{-4}
TPPZn	THF	5.89×10^{-4}
H_2TPP	THF	3.25×10^{-5}
DHP	ACN	2.4×10^{-5}

Table 3: List of molecules which was used to non covalently functionalize graphene and DWNT transistors.

to protect the transistors away from the damage caused by the capillary force, the substrate was then put into IPA. At last, a nitrogen gun was used to dry the substrate. The proper solvent and deposition time need to be chosen for different molecule. Table 3 shows the list of molecules that we used to non covalently functionalize graphene and DWNT transistors. The corresponding solvent, concentration of solution are presented.

2.5 CONCLUSION

Thanks to micro fabrication techniques, isolated DWNT transistors have been achieved. By combining optical phonons and electrical transport measurements, the electronic configuration (S@S, S@M, M@S, M@M) of the DWNT could be determined. Finally, the electron phonon coupling in individual DWNT is investigated. We observed a dependency of the metallic LO mode with an electrical gating, indicating, for the first time, a strong EPC in the complex DWNT system.

3

THE ROLE OF INTER-WALL INTERACTION IN THE HYBRID'S OPTICAL RESPONSE

Carbon nanotube transistors can, by themselves, emit or detect photons at wavelengths defined by the nanotube chirality [136, 137, 138, 139, 140, 141, 142]. To extend their capabilities in optoelectronics, one way is to couple them with molecules of various band gap, in order to broaden the detected light wavelength [143]. Among them, terpyridine transition metal complex [144, 145, 146] have been proven to be good photo-sensitizer due to their photo-activated redox states and can efficiently transfer charges to fullerene [147, 148], graphene [149, 150] or SWNTs [151] whereas molecular dipoles, like dimethyldihydropyrene molecules (DHP), can induce electric field similar to the one at play in CNFETs [152, 153, 154]. On the other hand, as we discussed previously (see chapter 1), the core-shell configuration of DWNTs is an important advantage to realize operating functionalized electronic devices compared to SWNTs based ones.

In this chapter, we will present combined optical phonons and electon transport measurements performed on functionalized DWNTs by two different photo-active molecules: terpyridine osmium complex which is a redox molecule and DHP chromophores which could have conformational change. We will try to emphasize similarities and differences on the grafting effect observed on DWNT based transistors and also on optoelectronics properties under illumination. Thus we will discuss these two kinds of devices both in the framework of electron-phonon coupling and interwall interaction with and without illumination.

3.1 NON COVALENT SP^2 CARBON / REDOX CHROMOPHORE BASED TRANSISTORS

3.1.1 *Introduction to structural and electronic properties of terpyridine complexes*

Terpyridine complexes, like other polypyridine complexes, exhibit optical characteristic and electrochemical properties like metal-to-ligand charge transfer (transfer of electrons from molecular orbital with metal-like character to those with ligand-like character) in the visible region, reversible reduction and oxidation, and fairly intense luminescence [155]. This terpyridin is a simple ring structure derived from pyridine

Figure 58 which is mainly used as a ligand and forms complexes with most transition metal.

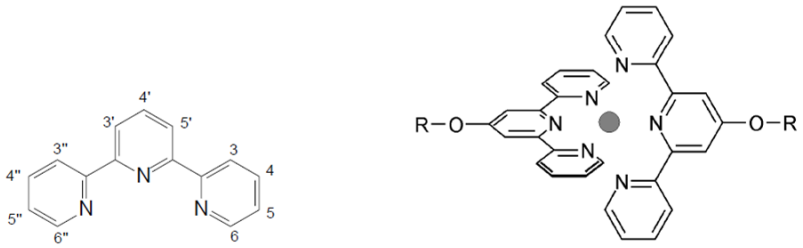

Figure 58: Left: Structure formula of the terpyridine group, right: symmetric bis-terpyridine metal complex

By using terpyridine complexes with different lengths, it is possible to access two different electronic transport regimes for quantum transport through a single molecule: the low transparency quantum dot regime for long chains and intermediate transparency quantum dot (so called Kondo effect regime). Actually, Park and Pasupathy *et al.* reported the introduction of thiol-functionalised bis-terpyridine complexes into a gap of a 200 nm. The inter-electrode gap arises from electromigration of metal of an electrode by ramping to large voltages at cryogenic temperatures [156]. During this process, some of the complexes, which were first bound to the gold wire before breakage, get into the 1-2 nm gap. Moreover, by using complexes with different thiol-to-thiol lengths, they show different physical effects at the molecular level: for "longer" complex, a single-electron molecular transistor behaviour has been observed whereas for "shorter" complex, a stronger coupling between the ion and the electrons leads to Kondo-assisted tunnelling, which can be described as the formation of a bound state between a local spin in the cobalt(II) centre and the conduction electrons in the electrodes, which drives to a conductance enhancement at low biases. Thus choosing the terpyridine metal complex length (but also anchors) allows to engineer the molecular device conductance.

Moreover, the terpyridine transition metal complexes feature very interesting photo-physical properties [157]. They have strong light absorption in the visible light range and are also luminescent at room temperature, making them ideal candidates for solar energy conversion, for example, in photo-voltaic devices, molecular opto-eclectrical switches and light emitting electrochemical cells [158, 159, 160, 161, 162]. Recently, the enhancement of photoinduced electron transfer in self-assembled polymer films using mixed metal-terpyridine complexes has been proven [163, 164]. Thus, the interaction between non bonding electrons of the three nitrogen atoms in terpyrine (Tpy) and the p-electrons of carbon nanotubes could induce electron transfer between the Tpy and carbon nanotubes through non covalent functionalization process [165].
In order to check this statement, we non covalently grafted terpyridine osmium complexes (TPyOs) onto double wall carbon nanotube

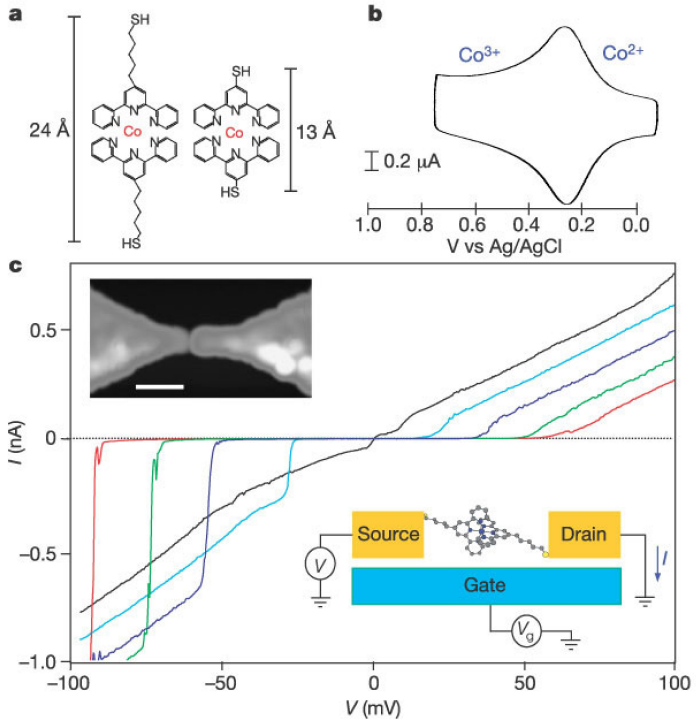

Figure 59: (a), Structure of the terpyridine Co complex, the scale bars show the lengths of the molecules as calculated by energy minimization. (b), Cyclic voltammogram showing the Co^{2+}/Co^{3+} redox peak. (c), I-V curves of a $[Co(tpy\text{-}(CH_2)_5\text{-}SH)_2]_2^+$ single-electron transistor at different gate voltages (V_g) from -0.4 V (red) to -1.0 V (black) with Δ V_g approximately -0.15 V. Upper inset, a topographic atomic force microscope image of the electrodes with a gap (scale bar, 100 nm). Lower inset, a schematic diagram of the device. (Figure reproduced from [156])

transistors. TPyOs is provided by G. Royal *et al.* (Département de Chimie Moléculaire, UJF, St Martin d'Hères) The absorption spectrum and the structural formula are presented in Figure 60. The absorption spectrum shows as expected a strong peak in the UV light region (315 nm) and two absorption peaks in the visible light range, 490 nm and 675 nm. The Raman spectra of TPyOs measured at two different excitation laser wavelength shows in Figure 61 . At both 633 nm and 532 nm, the Raman profile of TPyOs can be obtained. From Figure 61, several peaks can be observed. Peak at 1469 and 1605 cm^{-1} can be assigned to bipyridine ring stretch. And peak at 1350 cm^{-1} is from C-C inter ring stretch [166].

We will now focus on the charge and/or energy transfer mechanism between the terpyridine complex and the double wall nanotube as well as the exchange of this transfered excitation and/or charge between the outer and the inner walls of the double wall carbon nanotubes structure.

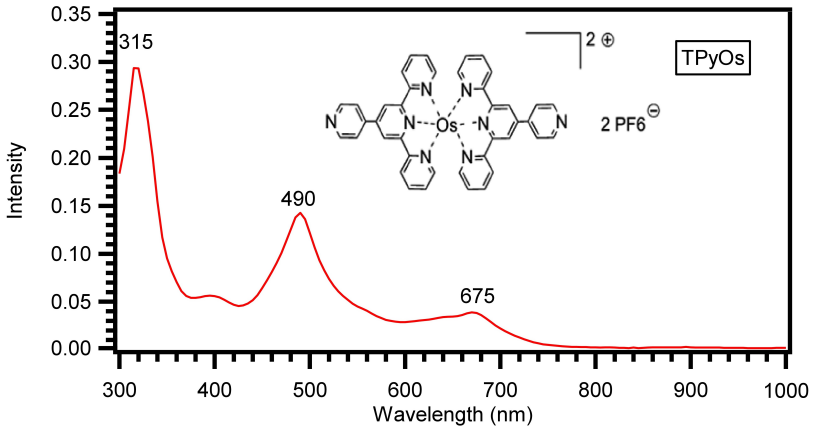

Figure 60: Absorption spectrum of TPyOs, the inset is the structural formula of TPyOs.

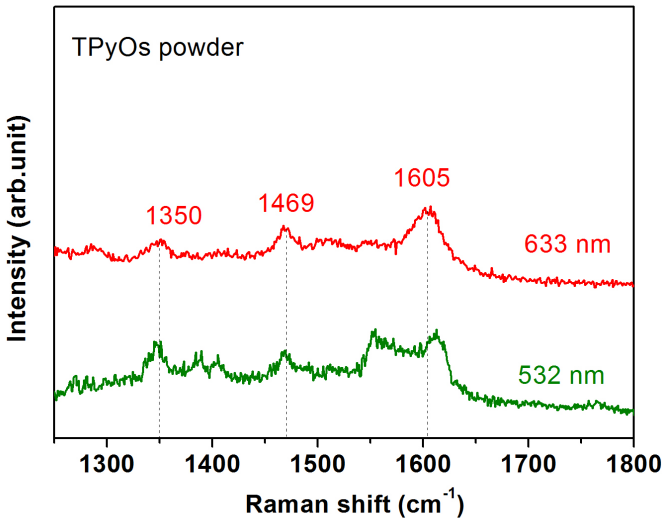

Figure 61: Raman spectra of TPyOs powders measured by the laser of 532 nm and 633 nm

3.1.2 *Graphene-Osmium terpyridine hybrid : the 2D case*

Graphene was first used as a reference system to evaluate the effect of grafting TPyOs on sp^2 carbon system. We expected charge transfer from the grafted molecules and a possible chemical enhancement effect. We will use this hybrid system to fixe experimental protocol and applied to DWNT. Let us first introduce the experiment method for making graphene/TPyOs hybrids.

For grafting TPyOs onto the graphene surface, 2.46×10^{-4} Mol.L^{-1} TPyOs in Acetonitrile (ACN) solution was drop-casted onto graphene sample which was then rinsed in ACN solvent; at last the sample was washed by IPA and blow dried by nitrogen. This method has

been proven efficient for non covalently grafting SMM molecules on the graphene surface [167]. The sample was characterized by optical microscopy, SEM and Raman spectroscopy.

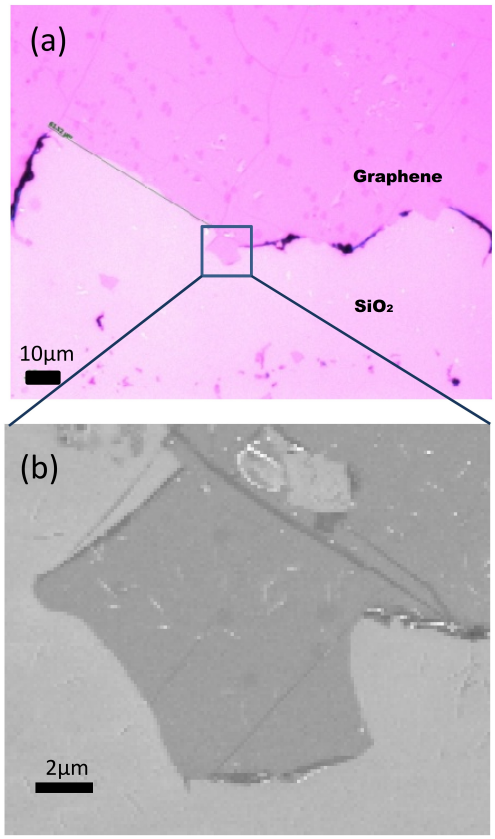

Figure 62: (a) Optical image of CVD graphene transferred on the substrate. (b) SEM picture of zoom in of the square part of (a) after grafting of TPyOs. No molecule cluster is visible at this scale.

Figure 62 (a) shows an optical image of graphene transferred on a 285 nm thick SiO_2/Si^{++} substrate. The continuous polycrystalline graphene layer covers most of the silicon surface, the edges can be easily observed due to our transfer process which induced defects at the border. Moreover, we observe ripples and small patches which represent bilayer or multilayer graphene growth at nucleation sites [25]. In the following, we focus on a small part of graphene located at the edge of the continuous layer, as shown in the square of Figure 62 (a). Thanks to its easily recognizable shape, we can always find it even after the grafting process. Figure 62 (b) shows the SEM image of TPyOs grafted graphene corresponding to the square part of Figure 62 (a). The overall structure is the same as before grafting indicating that the graphene structure is not strongly affected by the grafting process. To go further, spatially resolved Raman imaging was used to detect the presence of the grafted molecules on graphene.

Figure 63 shows G band intensity map before and after TPyOs grafting. We observe from the upper image that G band intensity is almost homogeneous except at edges and ripples where a higher inten-

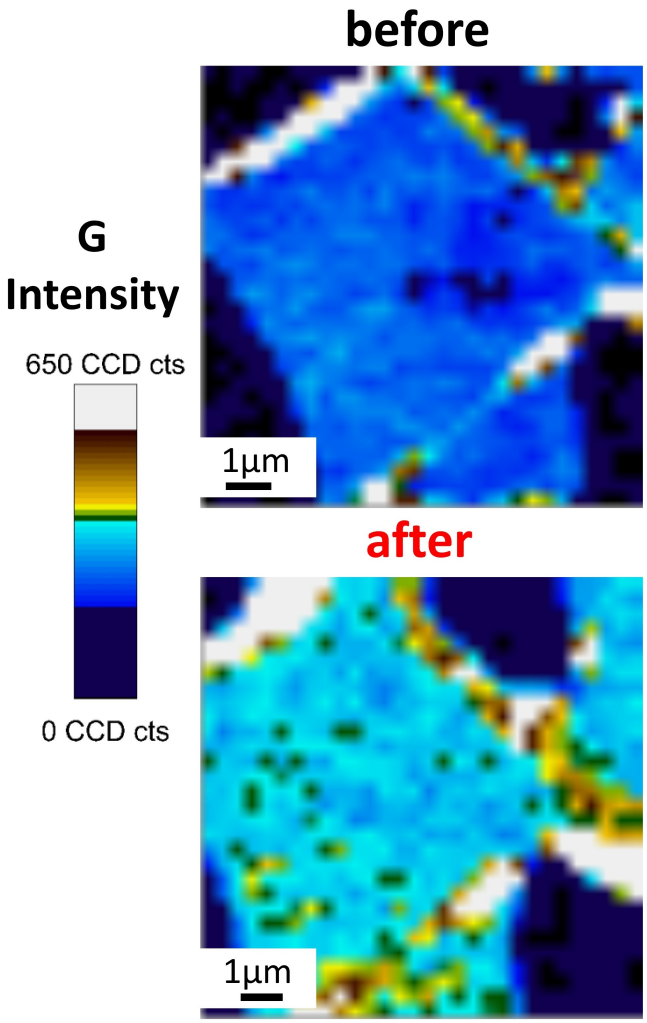

Figure 63: The Raman mapping of the G peak intensity of the graphene before and after grafting TPyOs.

sity is observed in agreement with previous studies [168]. The darker color areas on the map indicate a low G band intensity, compare to the main part (light blue), the intensity ratio I_{dark}/I_{main} is 0.54. The decrease of the intensity are probably due to PMMA residues from the transfer process. In fact, if residual PMMA covers part of graphene surface, it makes the Raman intensity decreased [169]. The bottom image of Figure 63 shows the G peak intensity mapping of graphene after grafting TPyOs. A global enhancement of the G peak intensity can be easily observed. On average, the intensity is increased by about 12%, due to a probable chemical enhancement process [167]. The origin of this enhancement is attributed to charge transfer between the molecule and the graphene surface [167, 170].

Figure 64 shows Raman spectra of graphene before (black) and after (blue) TPyOs grafting. First of all, we can observe a new peak around 1337 cm^{-1}. It can be fitted into two Lorentzien peaks at 1337

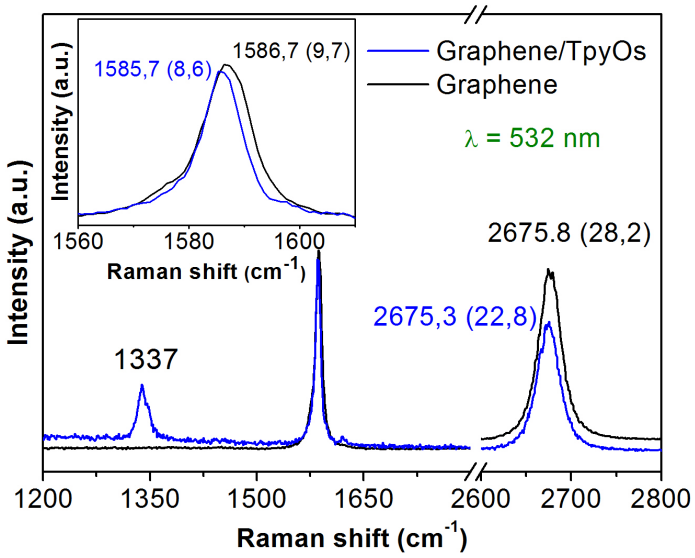

Figure 64: The Raman spectra of graphene before (in black) and after (in blue) grafting TPyOs (normallized by G mode). The inset is the zoom of the G band region.

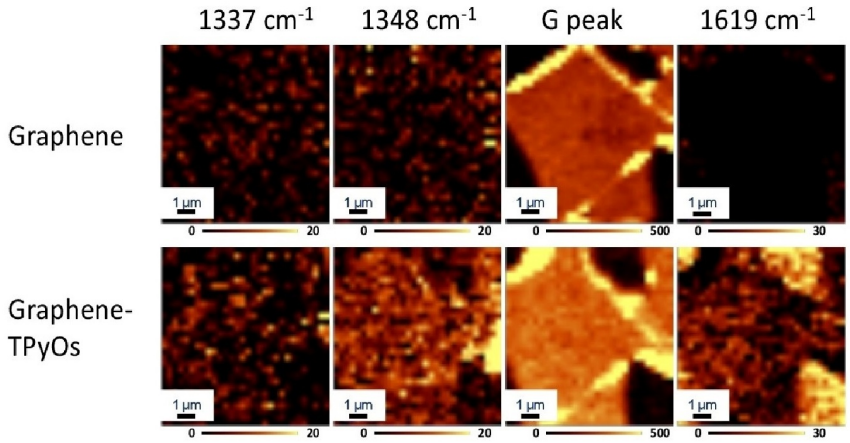

Figure 65

cm^{-1} and 1348 cm^{-1}. As we discussed before, the peak at 1348 cm^{-1} is from the molecule. Second, a small peak around 1619 cm^{-1} comes out after grafting TPyOs. In order to figure out the origin of these peaks, we obtained the Raman mapping of them, as it shown in Figure 65. It can be observed clearly that after grafting TPyOs, the peak at 1348 cm^{-1} and 1619 cm^{-1} can be observed not only on the graphene surface but also on the silicon substrate, which means that these two peaks are from TPyOs molecule. This result corresponding well with the Raman signature of TPyOs as it shown in Figure 61. From the Raman mapping, we also can observe that after grafting TPyOs, intensity of the peak at 1337 cm^{-1} does not change much, which means that the grafting method did not induced many defects in the graphene system. The inset of Figure 64 shows a downshift

and a shrinking of about $1cm^{-1}$ of the G mode with grafting. In the meanwhile, the 2D mode presents a small shift but its FWHM also narrowed about $5cm^{-1}$. We attribute these changes of G and 2D modes to charge transfer between TPyOs molecules and graphene which shifts the Fermi level and thus change the electron-phonon coupling . Different reasons leads to this assumption:

1. The terpyridine metal complex molecule can be an electron donner or acceptor [144] depending on the workfunction of the nanotubes. Previous experimental and theoretical works show that an efficient charge transfer process can occur between the complex and sp^2 carbon [166, 171].

2. The FWHM(2D) is narrowed after grafting which is a strong indication of a doping effect since a uniaxial strain effect will lead to a significant increase of 2D width [172] and a biaxial strain lead to a constant FWHM (2D) [173].

3. Moreover, the intensity ratio of G mode to 2D mode (I_G/I_{2D}) can also be used to monitor the charge transfer [174, 175]. In our case, I_G/I_{2D} changes from 1.2 to 1.6 indicating that graphene is doped by the TPyOs molecules.

4. As discussed in chapter 2, graphene is sensitive to changes in its direct environment, including surface charges. Charges can come from electrochemical doping, back or top gating or molecular charge transfer [167, 176, 177, 178]. It is well known that charge transfer induces stiffening or softening of graphene optical phonons frequencies depending on its initial electronic state (neutrality point or p or n doped point) [63]. Thus, the G band softening and shrinking observed in TPyOs grafted graphene (combined with a constant 2D band position but a narrow FWHM) is another strong indication of charge transfer. Finally, by comparing our results to Yan *et al.* [63] and Pisana *et al.* [65] works, we estimate that charge transfer between TPyOs molecules and graphene caused a Fermi level shift on graphene about $10-20$ meV , corresponding to a charge carrier density change around $10^{12}e^{-1}.cm^2$, approximately, 0.1 electron is transferred from one TPyOs molecule to graphene.

In order to investigate the doping level at different positions on the graphene sheet, the mapping of fitted G mode frequency and FWHM is presented in Figure 66. G mode frequency exhibits a global downshift, indicating that the doping effect is homogeneous over the graphene surface (which is about 100 μm^2).

In summary, non covalent functionalization of graphene with TPyOs molecules induced a charge transfer between them and a chemical enhancement is observed. Nevertheless, in this case, the enhancement is an exaltation of the graphene Raman signal. The only TPyOs signature is indirect: (1) TPyOs transfer charges to graphene with a

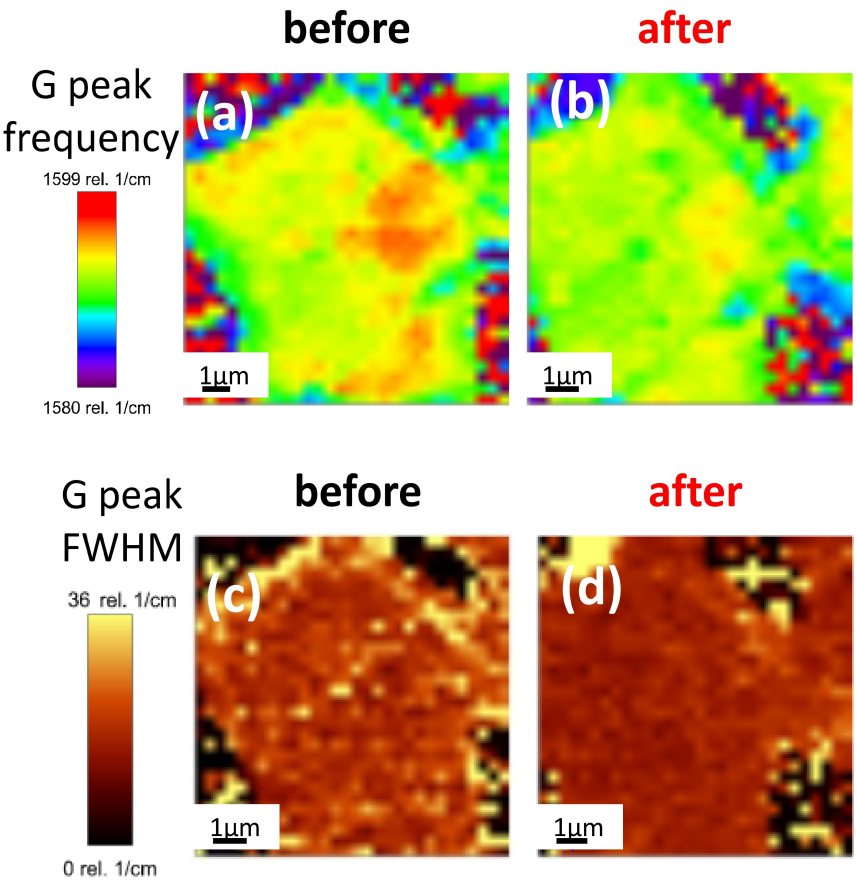

Figure 66: Raman mapping of graphene G peak frequency and FWHM before and after grafting TPyOs, wavelength: 532 nm, grating: 600 /mm

charge density about $10^{12} e/cm^2$ based on G mode frequency shift and (2) a shrink of the 2D mode FWMH. These effects are similar to those already measured by Lopes *et al.* on SMM-graphene hybrid [167].

3.1.3 *Complete assignment of an isolated DWNT FET*

The validation of a low charge transfer with a non covalent functionalization on 2D carbon material opens the way to probe same effect on 1D core-shell system like DWNT based transistors. Thus the same procedure has been applied in order to obtain functionalized DWNT based transistor.

Figure 67 shows the SEM image of a typical DWNT field effect transistor. From this image, we can clearly see a DWNT deposited onto SiO_2 substrate connected to drain and source electrodes. Most of the transistors used in this work have a 1 µm long inter electrode gap in order to be able to obtain Raman spectra without too much

luminescence from the metallic contacts. During this work, 42 DWNT based transistors were measured, only 4 of them present an inner and outer walls in resonance at the same laser energy.

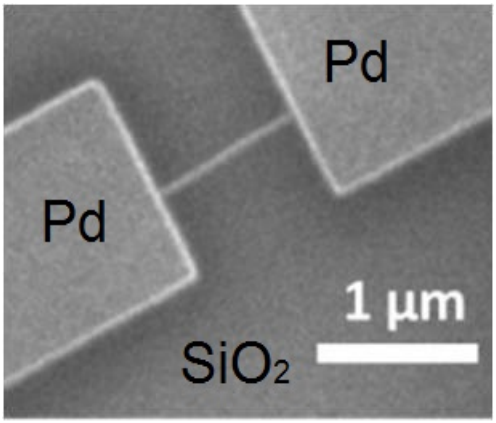

Figure 67: Typical SEM image of isolated DWNT field effect transistor.

In order to follow the changes induced by the functionalization with photoactive molecules, we need to fully characterize it. In other words to get structural information such as: is it a single tube? what about its diameters and electronic configuration? To reach this goal, we perform Raman and transport measurement.

3.1.3.1 *Optical phonons measurement of pristine DWNT transistor*

Figure 68 shows the Raman spectra featuring RBLM, G band and 2D band from a DWNT transistor measured at three different laser excitation wavelengths (488 nm, 514 nm and 532 nm respectively). The Raman spectra at 488nm show two RBLM modes at (162 cm^{-1} and 245 cm^{-1}) which means that both inner and outer tubes are resonant at this laser excitation energy. Moreover, the fitting parameters of the RBLM (see Figure 72) show a FWHM for both RBLM bands less than 8 cm^{-1}, which suggests that the DWNTs were dispersed at the single tube level [179]. The signal to noise ratio observed in these spectra vary strongly with laser excitation energy, indicating that resonance conditions for this nanotube are drastic even at G band range. Actually, from these spectra, we can extract an upper bound for RBLM resonance window about 130 meV which seems to be the same upper bound for 2D mode resonant conditions. This observation also leads us to suppose that this DWNT is an isolated one. Finally, we observe two peaks at 2D mode region, which are ω_{2D1} = 2657.5 (Γ_{2D1}=29.6) and ω_{2D2}= 2699.9 (Γ_{2D2}=33.3) cm^{-1}. According to the literature, for an isolated DWNT, the 2D peaks are different from the DWNT bundles [112] or bilayer graphene [180] which contains four peaks. 2D mode of an individual DWNT is composed of two peaks due to double resonance process occurring independently for each wall [133].

Thus, in order to extract diameters of both inner and outer tubes, we can estimate them thanks to the equation $\omega_{RBLM} = 218.8/d_t +$

$15.9 cm^{-1}$ [112], which is valid for individual DWNT on silicon substrate, as in our experiment. From this equation, we extract an inner tube diameter about 0.96 nm and an outer one about 1.50 nm with an inter-wall distance about 2.7 Å in agreement with previous DWNT Raman characterization studies [133, 112, 111]. Finally, a Kataura plot which was calculated considering environmental effects is used to determine metallic or semiconducting configurations of both inner and outer tube[49, 50, 133], as shown in Figure 69.

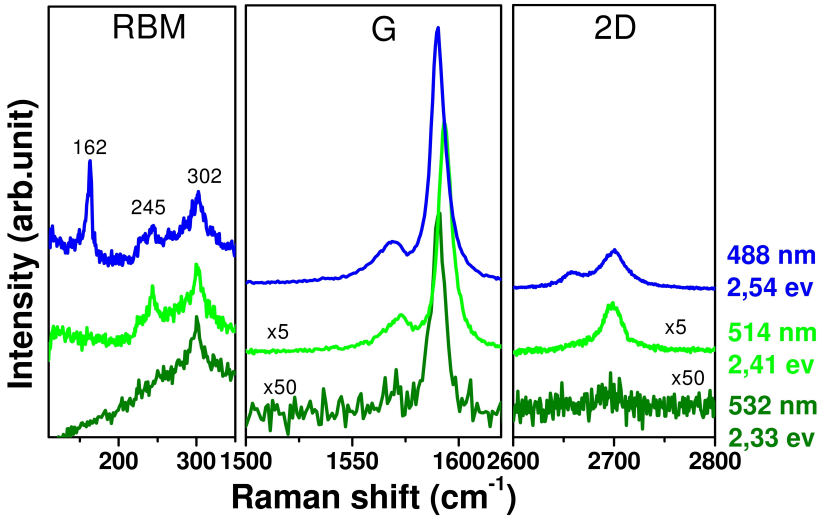

Figure 68: Raman spectra of DWNT sample A measured at three different laser wavelength (488 nm, 514 nm and 532 nm). The spectra were normalized by the silicon peak at 520.7 cm^{-1} and then the intensity of G peaks and 2D peaks were adjusted for comparison.

The two vertical lines in the Kataura plot (see Figure 69) indicate the diameters of both inner and outer wall. As observed in Figure 68, the inner wall is strongly excited at $E_{laser} = 2.41eV$ which corresponds in the Kataura plot to the $E_{11}M$ transition, whereas the outer tube is more resonant at $E_{laser} = 2.54eV$ corresponding to the $E_{33}S$ transition. Thus, optical phonons analysis suggests that this DWNT has an M@S configuration.

To be complete, we also try to assign the different G band components to outer and inner walls. By fitting the G band with 4 Lorentzian at $E_{laser} = 2.54eV$ (result is shown in Figure 72), we attribute the two highest peaks at 1589.9 and 1593.9 cm^{-1} to G^+ components of each walls, and the two lowest ones at 1565.3 and 1571.9 cm^{-1} to the G^- ones [14, 111, 112]. The same attribution has been done at $E_{laser} = 2.41eV$ and at $E_{laser} = 2.33eV$ (see Figure 72).

The fact that at $E_{laser} = 2.41eV$ (see Figure 68), we only observe one RBLM mode at 245 cm^{-1} meaning that only the inner tube is still in resonance at this laser excitation energy. If we now consider the intensity ratio between the G^+_{inner} and the G^+_{outer} measured at this excitation energy as $\eta_{2.41}$, and the one measured at E_{laser}= 2.54 eV as $\eta_{2.54}$, we find that $\eta_{2.41}$=0.70 is higher than $\eta_{2.54}$=0.19, which

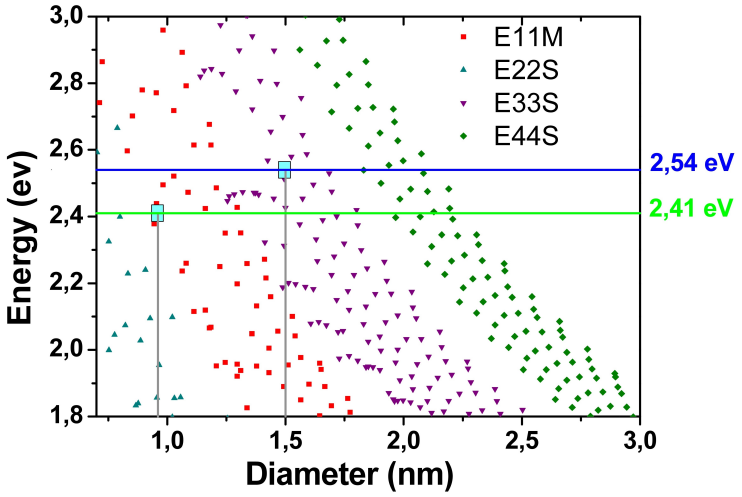

Figure 69: Comparison of the results from Raman spectra with the Kataura plot. The two horizontal lines stand for the two excitation laser energies (2.54 eV and 2.41 eV). The 2.54 eV laser excited the outer tube and the 2.41 eV laser excited the inner tube. The two vertical lines mark the diameter of the inner (0.96 nm) and outer tubes (1.50 nm), respectively. The two cyan rectangles stand for the positions of the outer and the inner tubes in the Kataura plot, the outer one falls into the $E_{22}S$ transition region and the inner one falls into the $E_{11}M$ transition region [49, 50].

indicates that E_{laser} =2.54 eV is closer to the resonant condition for the outer tube. This explanation correlates well with the RBLM signature as discussed before. This result also indicates that the assignment of each G peak component is reasonable. The results of the inter wall distance which is 2.7 Å as we discussed, lead us to consider the interwall mechanical coupling in this DWNT [81]. We also find that when $E_{laser} = 2.41eV$, the inner and outer tubes can be resonant at the same time, which prove that interwall coupling in this tube indeed exist. But since we didn't manage a complete tunable Raman experiment we are unable to extract the coupling strengh (see Section 3.3).

At this stage, Raman measurement of this DWNT transistor indicates an isolated M@S tube but we still need an electrical characterization in order to have the complete electronic picture of this device before molecular grafting and light illumination.

3.1.3.2 *Tranport measurements of pristine DWNT transistor*

Figure 70 presents the transfer characteristics of this pristine DWNT transistor at room temperature (black curve). We plot here the differential resistance (dV/dI) as a function of the gate voltage (V_g). In order to get rid of artifacts from gate hysteresis, all curves were acquired on the same measurement cycle while scanning from positive to negative bias. As we already know that in a metallic nanotube,

the conductance shows little dependence to V_g as expected from its band structure. On the contrary, a semiconducting nanotube shows a strong V_g dependence: (i) it has a high conductance when the Fermi level is located in the valence band (p-doped regime), (ii) its conductance decreases when the Fermi level falls within the band gap region and finally (iii) the conductance increases again when the Fermi level is in the conduction band (n-doped regime). In the case of this specific pristine DWNT transistor, Figure 70 shows ambipolar behavior with on-off ratio about 20. The Fermi neutral point of this transistor is around 22 V, which means that at around 22 V, the electrons filled the valence band. By comparing our statistics (see chapter 2) with this data, we determine that this DWNT has an M@S or S@M configuration in agreement with our Raman analysis on the same sample.

3.1.4 *Charge transfer on DWNT-terpyridine Osmium hybrids*

Let us now investigate the influence of TPyOs on this very nanotube. An electric field caused by charge density modification can stimulate the response of CNT based sensors by shifting the threshold voltage [152, 153, 154]. Therefore, by non covalently grafting TPyOs on this DWNT transistor (as for graphene see the last section), this molecule will act as an additional gate voltage giving rise to a visible shift equivalent to an effective electrostatic gating (which we can name as a molecular gating). The carbon nanotube itself can interact electronically through charge transfer processes with a broad range of molecules [181, 154, 182, 183, 184, 185, 186]. The Fermi level shift can be detected through the Fermi neutral point change in the probe test.

In fact, after grafting TPyOs molecules onto our DWNT transistor, the threshold voltage shifts by 5.5 V (from 25 to 19.5) towards the negative gate voltages. As Terpyridine complexes are known to be strong electron donors, we therefore demonstrate that the effective n doping process is caused by charge transfer from the TPyOs to DWNT.

The transferred charge carrier density can be calculated in a simplistic capacitive model through the formula

$$\Delta n = C_g \Delta V / e \tag{23}$$

[63, 187]

ΔV is the change of threshold voltage, C_g is the capacitance of the channel with respect to the back gate. C_g can be obtained by a cylinder/plane model of a capacitor from the geometry of the device

$$C_g = \frac{2\pi\varepsilon_{avg}\varepsilon_0}{\ln(2 + 4t_{ox}/d)} \tag{24}$$

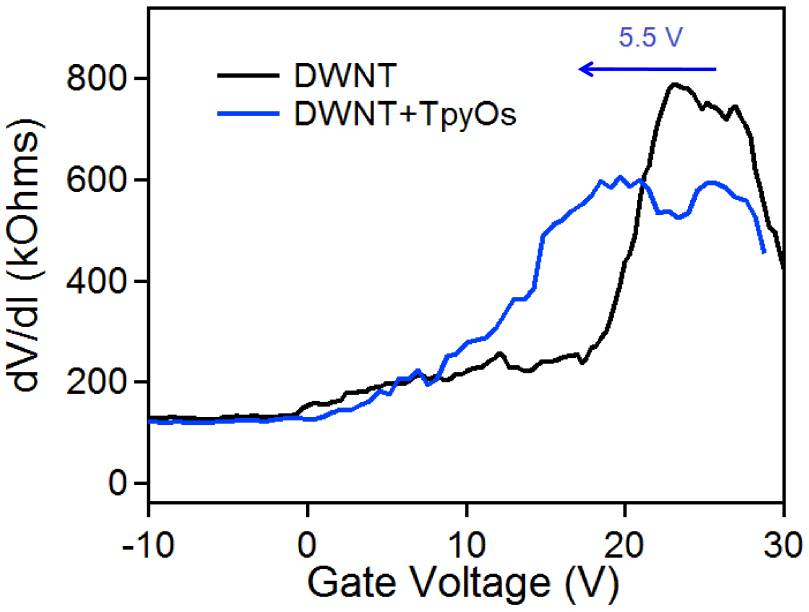

Figure 70: Transfer characteristics of DWNT sample A at V_{ds} = 50 mV before (black) and after (blue) grafting TPyOs.

[187, 188, 189]

Here, ε_{avg} is the average of the dielectric constant above $\varepsilon(air) = 1.0$ and below $\varepsilon(SiO_2) = 0.39$ the nanotube, t_{ox} is the silicon oxide thickness (285 nm) and d is the diameter of the nanotube (outer tube 1.50 nm). C_g has a value of 2.29×10^{-11}F/m giving $\Delta n = 0.76/nm$. The doping level is very similar to the functionalized SWNT with tetrathiafulvalene-based mediator system [187], which is also a non covalent functionalised system.

The charge transfer process can also be evaluated from the change of Raman peaks. Figure 71 shows the comparison between Raman spectra of sample A before (black) and after (blue) grafting TPyOs, for laser energy 2.54 eV, 2.41 eV and 2.33 eV. We observed several significant changes after the functionalization.

The most obvious change is in the RBLM region. In Figure 71 (a), for E_{laser} = 2.54 eV, RBLM modes disappeare after TPyOs grafting. In the meanwhile, the G band intensity decreases about 14 times indicating that resonant conditions for this tube at this laser excitation energy are not satisfied anymore [190]. This statement is confirmed by Figure 71(b), where the RBLM mode at 160 cm^{-1} appeared at E_{laser} = 2.41 eV. Even if this mode is slightly shifted (about 2 cm^{-1}), it still can be assigned to RBLM mode of outer wall.

Similarly, as can be observed in Figure 71 (c), at $E_{laser} = 2.33eV$, the peak at 244 cm^{-1} which is the RBLM peak of the inner wall comes out. The enhancement of the G peak can be observed at both exciting laser energies. The appearance and disappearance of RBLM mode compared to pristine DWNT (before grafting) can only be explained

by a shift of RBLM resonant window after TPyOs grafting. The resonance window described here is the Raman intensity as a function of laser excitation energy in the range where RBLM feature can be observed. It can be used to determine the electronic transition energy E_{ii}. The RBLM resonant window shift indicates the shift of E_{ii} electronic transition [190, 191, 192, 193]. Because of the limitation of our experiment facilities, we are not able to tune the laser wavelength continuously around these laser excitation energies for this DWNT. Later on, a complete picture of resonant Raman scattering process will be described on a different TPyOs-DWNT based transistor (see Section 3.3).

We also want to point out that not only the outer wall, which is considered to be directly in contact with the molecule, has dramatic change of its RBLM mode, but also the inner tube exhibits a resonance window shift even if it is supposed to be protected by the outer one. This result shows the possibility to transfer charges to inner wall and thus asks the question of the role of interaction between walls. Actually, in this case the DWNT is an M@S tube so if the Fermi level falls in the gap of the semiconducting tube, it is possible to imagine that both walls are doped by TPyOs.

From Figure 71, the G modes evolution of both the inner and outer tubes also suggests a doping effect of both walls. Clear upshifts of G^+ peaks can be observed after TPyOs functionalization . Under the 488 nm laser excitation (E_{laser}=2.54 eV), one of the G^+ peak position (FWHM) shifts from 1593.9 (8.3) to 1595.8 (12.3) cm^{-1}, the other one shifts from 1589.9 (6.8) to 1591.9 (6.7) cm^{-1}. Based on the literature, the G peak shift could be caused by different origins, such as defects [194], strain [195, 196, 197, 198], doping effect, temperature change [190]. In our case, the laser power was kept lower than 1 mW, and the Si substrate can be considered as a heat sink to absorb the thermal power from the laser. that laser heating is less important for individual DWNTs in contact with the substrate or connected to the metal electrode which are also efficient heat sinks [199]. The shift should then not be caused by the thermal effect. We did not induce any external force during the experimental process, so the strain effect should not be considered. No obvious D peak change is observed and the intensity ratio of the D peak to the G peak I_D/I_G is always below 0.04 no matter before or after grafting TPyOs, which indicates that the grafting process did not induced many defects. Thus, the G peak change is not caused by themal effect, nor by strain or defects, it is more likely originating from charge transfer from grafted TPyOs. There are also dramatic changes of 2D peak visible on the fitted data in Figure 72. $\Delta\omega$(488nm) for 2D mode is positive whereas at 532 nm is negative. At 488nm, TPyOs has an absorption band thus the Raman laser is invasive, TPyOs molecule is in an excited state and a doping occur, whereas at 532nm it's not the case and thus 2D mode shift back to its dark value of DWNT grafted with TPyOs in its intial state.

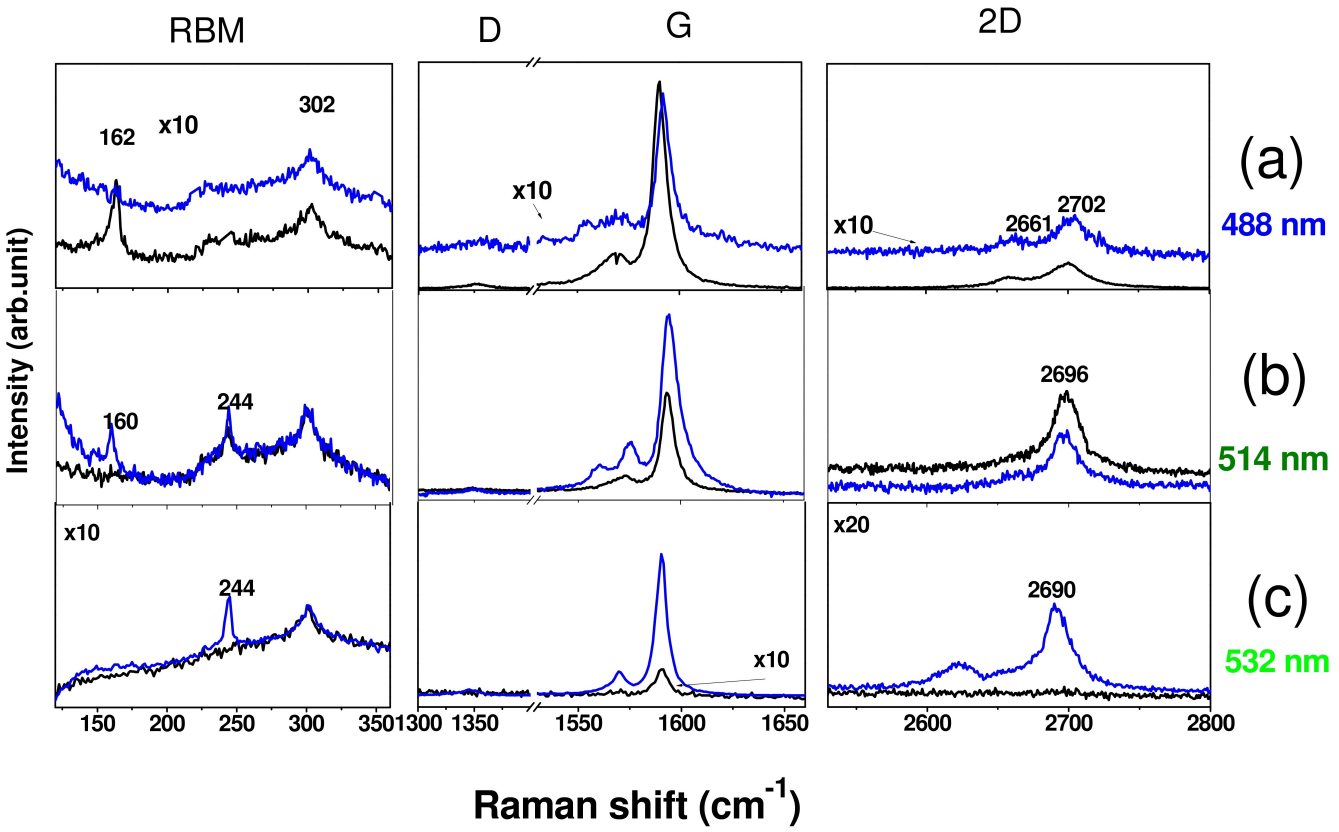

Figure 71: Raman spectra of DWNT sample A measured at three different laser wavelength (488 nm, 514 nm and 532 nm), before grafing(dark), after grafting (blue).

		RBM				G								2D			
		ωrbm1	Γrbm1	ωrbm2	Γrbm2	ωG1	ΓG1	ωG2	ΓG2	ωG3	ΓG3	ωG4	ΓG4	ω2D1	Γ2D1	ω2D2	Γ2D2
488 nm (2,54 ev)	before	162,3	7,2	244	5,8	1565,3	13	1571,9	6,4	1589,9	6,8	1593,9	8,3	2657,5	29,6	2699,9	33,3
	after	**	**	**	**	1563,6	14,5	1571,9	10,5	1591,9	6,7	1595,8	12,3	2657,7	53,8	2705,5	32,6
	Δω(after-before)	**	**	**	**	-1,7	1,5	0	4,1	2	-0,1	1,9	4	0,2	24,2	5,6	-0,7
514 nm (2,41 ev)	before	**	**	243,3	7,6	1565,8	11,2	1573,1	8,5	1592,9	5,6	1595	8,1	2697,8	27,6	**	**
	after	159,9	3,5	244,1	4,5	1560,8	12,3	1574,9	7,7	1594	7,3	1599,3	14,6	2696,3	34,2	**	**
	Δω(after-before)	**	**	0,8	-3,1	-4	1,1	1,8	-0,8	1,1	1,7	4,3	6,5	-1,5	6,6	**	**
532 nm (2,33 ev)	before	**	**	**	**	1568,3	9,2	**	**	1590,7	7,2	**	**	2646,2	32	2697,8	31
	after	**	**	244,1	4,9	1569,6	7	**	**	1590,3	6,2	**	**	2623,4	37,4	2691,3	24,2
	Δω(after-before)	**	**	**	**	1,3	-2,2	**	**	-0,4	-1	**	**	-22,8	5,4	-6,5	-6,8

Figure 72: Summary of the Raman peak fitting for DWNT before and after grafting TPyOs (sample A).

In the following paragraph, we will present the comparison with Raman spectra of another DWNT sample B before and after grafting TPyOs (Figure 73). This sample B present a broad G^- peak which is a signature of a metallic tube. Following the evolution of the metallic tube G^- peak can give us the information of charge transfer and electron phonon coupling [67, 129, 130, 131], as we discussed in Chapter 2. In the RBLM region, we observed the similar effect as for sample A. Two RBLM peaks can be observed, $\omega_{RBLM1} = 146cm^{-1}$ and $\omega_{RBLM2} = 200cm^{-1}$ before grafting TPyOs. After grafting, the two RBLM peaks can still be observed, but the intensity changes a lot. The intensity of the RBLM peak 1 I_{RBLM1} increases by 1.5 times and intensity of the RBLM peak 2 I_{RBLM2} decreases by 4.9 times. The changes of RBLM in this sample proves the repeatability of the experiment.

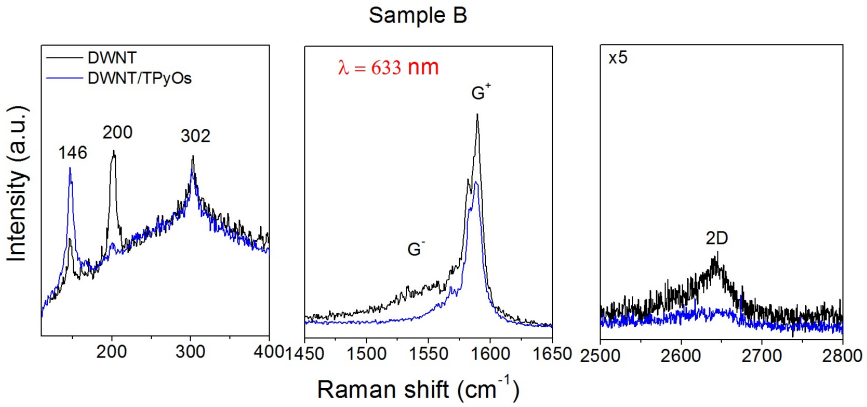

Figure 73: Raman spectra of sample B before and after grafting TPyOs, the laser wavelength is 633 nm

We can get more information through the analysis of the G band. The G band was fitted into four Lorentzian peaks Figure 74 (noted as peak 1, 2, 3 and 4). The fitting parameters are listed in Table 4. We can observed from Figure 74 and Table 4 that the position and FWHM of every peak changed after grafting. The most noticeable change occurs to peak 1 which is the broadest peak at 1543.7 cm^{-1} with a FWHM of 44.4 cm^{-1}. We assign this peak to the G^- peak of the inner metallic tube. After grafting, this peak shifts to 1568.3 cm^{-1} and the FWHM decreases by 19.6 cm^{-1}. Such a dramatic change was also observed in the liquid gating of metallic SWNTs [67, 129], back gate electrostatic gating of suspended metallic SWNTs [132] and it is also similar to the back gate tuned DWNT transistor that we observed and discussed in chapter 2. We then attribute the change of peak 1 to similar reasons as presented in the literature, that is, the electron-phonon coupling is modified by the shift of the Fermi level. A difference in this case is that the electrical field is caused by the molecular dipoles grafted onto the DWNT surface instead of by a liquid or back gate. In other words, the grafted TPyOs transfer charges to the DWNT which shifts the Fermi level of the system and brings it closer (or further) to the Fermi neutral point, making the electron-phonon coupling stronger or weaker. The decrease of the FWHM of peak 1 indicates that the electron-phonon coupling becomes weaker after grafting TPyOs: the

	ω_1	Γ_1	ω_2	Γ_2	ω_3	Γ_3	ω_4	Γ_4
Before	1543.7	44.4	1570.5	13.0	1582.6	7.5	1590.5	7.8
After	1568.3	19.6	1579.1	3.6	1583.6	5.5	1589.8	8.8
δ	25.6	-24.8	8.6	-9.4	1.0	-2.0	-0.7	1

Table 4: Fitting summary of Sample B : Raman G peak before and after grafting TPyOs

charge transfer induced doping of the DWNT shifts the Fermi energy further from the Fermi neutral point. To sum up, we investigated

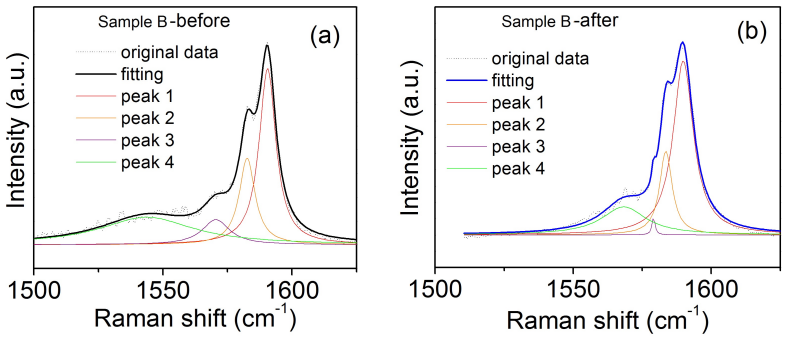

Figure 74: The Lorentzian fitting of the Raman G peak of sample B before and after grafting TPyOs

.

grafting effect of TPyOs onto DWNTs by combining Raman spectroscopy and transport measurements. The Raman G and 2D modes upshift with grafting whereas RBLM intensities change drastically before and after TPyOs functionalization. This optical phonons frequency shift is a direct probe of a modification in DWNT Fermi neutral point. Electrical characteristics confirm the Fermi neutral point downshift of this DWNT/TPyOs transistor and allow us to estimate a molecular transfer about 0.076 electrons/molecule to 1 carbon atom. Moreover, not only the outer tube is affected by charge transfer but also the inner one since a huge a modification in RBLM resonant condition for both tubes are observed. The doping caused the Fermi level to up shift further to the neutral point, implying a decrease of the electron-phonon coupling strength and thus a shrink on FWHM in the case of sample B which has an inner metallic tube. All these effects observed on DWNT/TPyOs hybrids are also observed in graphene-molecular devices for TPyOs but also with SMM molecules [167] indicating the universal behaviour of sp^2 carbon systems under charge transfer either by a back gate or a molecular charge transfer. Terpyridine are used here as a reference chromophore base on a light activated redox transition. Before investigating the optical properties of our hybrids, we will compare the terpyridin case with another family of molecules based on light-induced conformation changes.

3.1.5 *DHP chromophore DWNT based transistors*

In this section, we present a non covalently grafted DHP chromophore on DWNTs and we will show how the electronic and vibrational properties of our DWNT samples are changed by such a grafting. We will end up with a comparaison between TPyOs ans DHP in terms of grafting effects.

3.1.5.1 *Introduction to structural and electronic properties of the dimethyldihydropyrene chromophore*

Dimethyldihydropyrene (DHP, closed configuration) is a polycyclic π conjugated unit, which can be optically converted into a less π conjugated and colorless cyclophanediene (CPD, open configuration) isomer by opening one central bond. It is a multi-addressable system, that is, its property changes can be operated by at least two complementary input signals [200]. The open state (CPD) can be reversibly switched (both photochemically and thermally) into the colored and more stable closed isomer (DHP) by exposure to light with two different wavelengths (Figure 75(a)). Such systems are very useful for developing devices for complex logic operations [201]. Recent studies, mainly reported by Mitchell *et al.* [202], Nishihara *et al.*[203] and Royal *et al.* [204] clearly show that the DHP is a very promising candidate for the preparation of multi-functional materials. Especially, single-molecule conductance measurements have been done recently on the DHP/CPD isomer, which show a big change in the conductivity (ON/OFF ratio ($> 10^4$)) and an excellent reversibility of conductance switching of this molecule when its internal π conjugated structure is broken therefore such molecule has the required potential for molecular electronics. The polycyclic structure of this molecule is also a useful basis which can be adapted with different chemical functionalizations, so as to tune its properties. As a result, this material is very attractive for the creation of new molecular devices.

Figure 75 (b) shows the absorption spectra of DHP. There are two peaks in the UV light region and four peaks in the visible light region. It also shows time-dependent evolution (with 10 min intervals) of the UV/vis spectra of DHP with two pyridine rings, the blue line is the closed state and the red line is the open state. In the UV light region, the two absorption peaks were increasing while the the four peaks in the visible light region were decreasing during the light illumination process. These changes can be used to detect the photoconversion of the DHP closed state into its corresponding colorless open isomer. In that experiment, the switching process was taking place in solution. In our case, we want to check weather it is possible to convert the closed state for molecules deposited on a solid surfaces as a first step before envisioning devices. At first, macroscopic green crystals of DHP-pr were put inside the optical vacuum chamber, as shown in

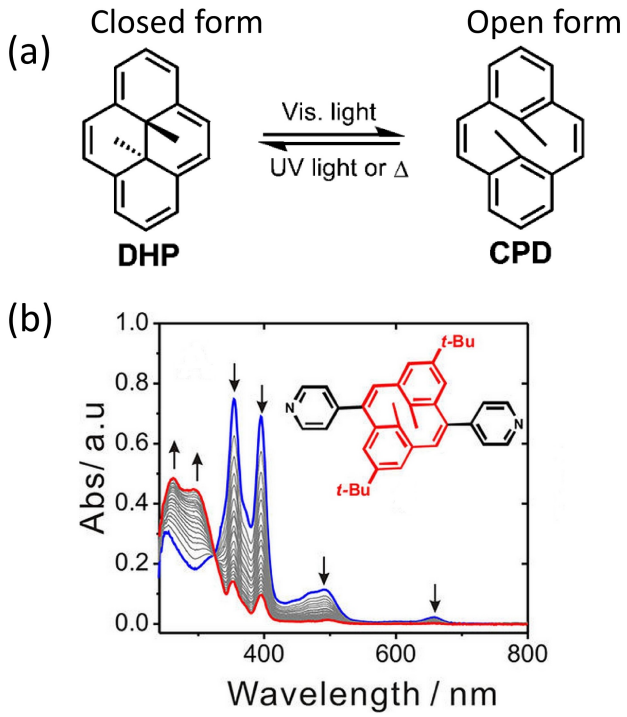

Figure 75: (a)Switch of DHP to its less stable conformational state CPD, (b) Time-dependent evolution (with 10 min intervals) of the UV/vis spectra of DHP with two pyridine rings (DHP-pr), the chemical sketch is shown in the inset figure [204].

Figure 76. We used a 405 nm wavelength laser to illuminate the crystals locally through the optical window of the chamber for 24 hours. We found that the illuminated crystals turned to white while the rest of them are still green. Figure 76 shows the photos of the white colour part and the green part taken through the microscope. It can be observed that the green part is still well crystallized and the white part shows more amorphous form. This result shows that the DHP-pr can be converted to its open form even in the solid state, which is the first step toward hybrid CNFETs.

Figure 77 shows the Raman spectra of the DHP-pr before and after the laser illumination (red light (600-700 nm), 100 W/m^2). It can be observed that before light illumination, there are a lot of sharp peaks with high intensity, but after the light illumination, some peaks become broader while other peaks disappeared. It indicates that the structure of the molecule changed a lot and the DHP group transforms to CPD.

3.1.5.2 *DHP grafting effect on DWNT based transistor*

We choose an alternatively functionalized DHP molecule (Figure 78) to decorate DWNTs (the deposition method was presented in chapter 2). This molecule is a good match for non-covalent functionalization onto CNTs, since its additional pyrene groups can be bound to the

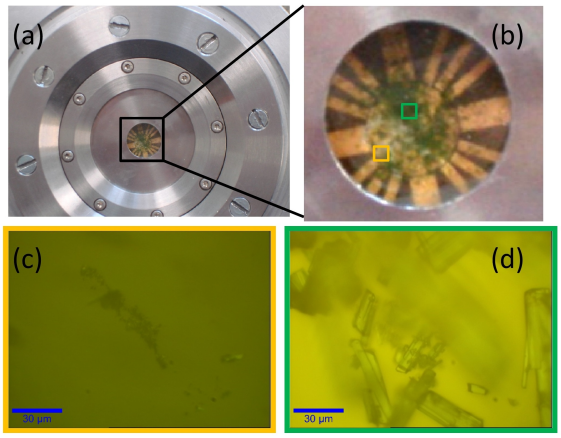

Figure 76: (a)The optical window of the optical cryostat with micro-crystals in vacuum inside, (b) the DHP crystals on the sample holder, the white part is the molecule after 405 nm laser illumination for 24 hours, (c) (d) are the microscope photos of the white part and the green part respectively.

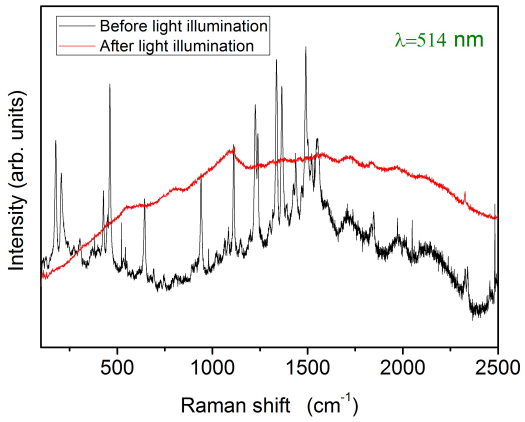

Figure 77: Raman spectra of DHP-pr before and after white light illumination,illumination time: 1 hour, power: 100 W/m^2.

surface of the CNTs by π-π stacking interactions, which can ensure a better charge-transfer mechanism during the optical gating process.

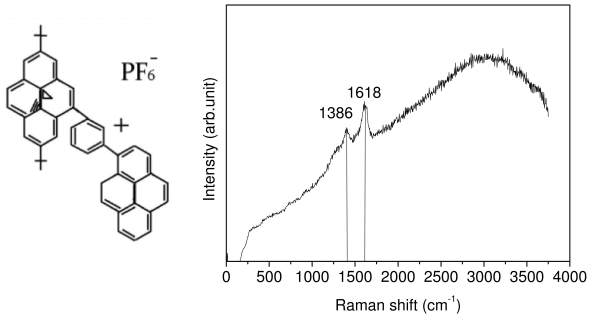

Figure 78: Left: chemical sketch of molecule DHP-ab73, right: Raman spectrum of DHP-ab73 (wavelength 532 nm).

Raman spectroscopy measurements were carried out, and different processes were studied. Spectra were taken before and after grafting the molecule. In fact, as visible from Figure 81, the general trend we observe is, with the grafting, the spectrum was modified: considering especially the G peak, we can see that its intensity is enhanced, in average, with functionalization.

From Figure 81, after grafting DHP-ab73 on DWNT, a global enhancement by a factor 2 of all the Raman peaks are observed. This is very similar to the chemical enhancement effect that many people have studied [205, 167]. Moreover, the 2D band, hardly visible before functionnalization, turns to be observed for the hybrid system. However, contrary to the TPyOs case, we observe no significant shift of any Raman peaks due to functionlaization. This seems to discard any charge transfer and would rather correspond to a change in the electrostatic environment of the nanotube only. Both charge transfer and dipolar effect leads to a modification of the Raman cross section and an enhancement of the nanotubes modes.

Here we showed the influence of grafting DHP on nanotubes is visible though weaker than for the TPyOs case. Let us now consider the effect of light on this DWNT-switch hybrid.

3.2 OPTICAL GATING ON DWNT-MOLECULE HYBRID TRANSISTORS

These new DWNT-molecular hybrid present now a huge photo-active potential for transducing a light excitation to an electrical one. Such excitation transfer can involve charge transfer from a redox photoactive molecule (terpyridine complex) to the inner wall, or a change in the electrostatic environment induced by the photo-excitation of chromophore molecule (DHP), which acts as an optical gate. We will now investigate each hybrid exposed to light in the absorption range of the molecule. Unfortunately our samples did not allow a complete characterization, so we will present only electrical characterization for the TPyOs hybrid and only Raman characterization for the DHP-hybrid.

3.2.1 *Light exitation of a redox switching molecule*

In order to illuminate the obtained TPyOs-DWNT based transistors, we use an X-Cite 120Q excitation light source. The illumination power applied to samples remains with a maximum value of about 100 W/m^2 for an illuminated surface of approximately 1 cm^2.

Figure 79 shows the compared transfer characteristics curves of DWNT-TPyOs hybrid transistor with and without light illumination. It can be clearly seen that the threshold voltage shifts towards positive direction, which is the opposite way of the grafting effect. So

this transistor undergoes an effective p-doping process under white light illumination, the shift of the Fermi neutral point is around 5 V, and the transferred charge carrier density is around 0.69/nm. Figure 80 shows the sketch of the p-doping process which is caused by the optical gating on the hybrid system. The black curve represents the density of state of a semiconducting carbon nanotube. The blue line represents the Fermi level of the hybrid system without light illumination; under light illumination, the Fermi level shifts to the position noted as E_F light on (red line). The Fermi level shift also caused the optical transition energy to change, which we will discuss in Section 3.3. The process is similar to the optical gating effect described by J. Borghetti *et al.* [105], and also similar to the DWNT coated TiO_2 [206] or ZnO [207]. White illumination causes a photoinduced positive charge transfer from the TPyOs to the DWNT.

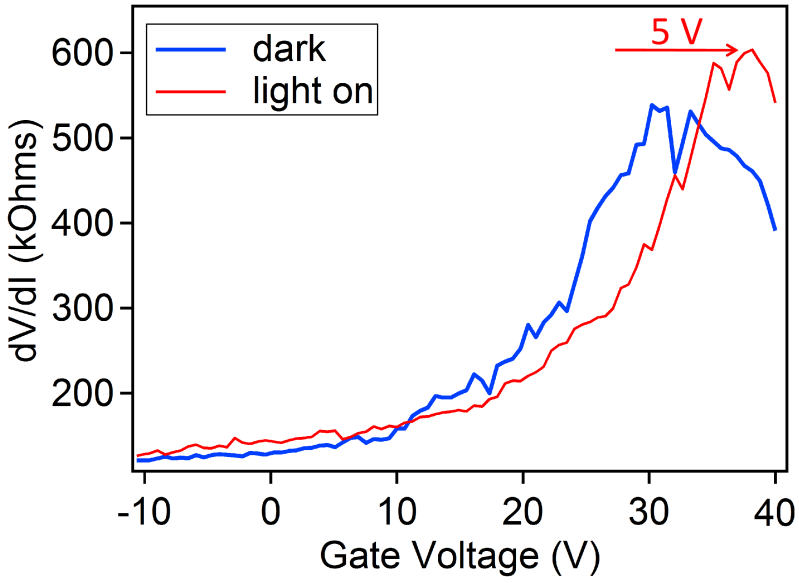

Figure 79: Transfer characteristics of sample A at V_{ds} = 50 mV measured in dark (blue) and under light illumination (red).

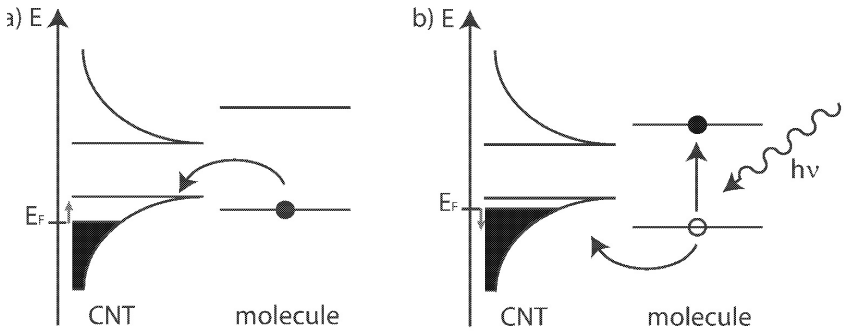

Figure 80: Sketch of the nanotube energy band structure showing the evolution of the Fermi level after grafting the molecule (left) and under light illumination (right).

	ω_{2D1} cm^{-1}	Γ_{2D1} cm^{-1}	I_{2D1}	ω_{2D2} cm^{-1}	Γ_{2D2} cm^{-1}	I_{2D2}
Dark	2670.7	28.9	1×10^{-3}	2702.6	23.6	1.2×10^{-3}
Light on	2669.3	34.4	2×10^{-3}	2704.3	36.2	2.1×10^{-3}
Light off	2665.0	32.7	1.2×10^{-3}	2704.2	34.3	2.4×10^{-3}

Table 5: Summary of the Lorentz fitting of the 2D peaks of sample DWNT/DHP-ab73

This result indicates that DWNT charge transport in DWNT-TPyOs hybrid can be modified upon illumination. Let us now turn to the DHP-based hybrid system as a comparison.

3.2.2 *Light excitation of a conformational switching molecule*

Illuminating the sample shows a clear increase of the 2D band (twice more intense) along with a higher signal to noise ratio, which is reversible when switching off the light (Table 5), the decrease of the intensity of RBLM peak evidences the Raman resonance window change. Therefore we can deduce that with the light illumination, the DHP converted to the opened state CPD, at the same time, the electronic structure of the molecule changes, which causes the change of the electronic structure of the hybrid system.

When the light is turned off, the increase of the intensity of the Raman RBLM and G peak is still visible, meaning that conformational change of molecule is stable beyond light exposure. The G peak intensity ratio of "light off" to "dark" is 2.4 and "light off" to "light on" is 1.7. One possibility is that the kinetic process through which the excited molecule changes its conformation had not come to an end when the spectra with illumination were acquired, and that the process continued throughout the "Off-state" (when the light stimulus was removed). The "Off-state" spectra were acquired approximately two hours after the light stimulus was imposed onto the system. In this case, two possible explanations can be given: either the kinetics of the molecule is long compared to the time which was waited before performing the experiments in the "Off-state". We know that heat might have a back-switching effect, even if UV light is not shone onto the sample. In the latter case, part of the DHP-ab73 might have undergone a conformational switch (from the closed-configuration to the open one) due to excitation given by the red light, and another part of it might have switched back due to the heat produced from the illumination, so that only when the light was turned off the kinetics of the conformational switch could be completed. In this case, the performed measurements might still not describe the final situation, but, in order to say this, further experiments need to be done, so as to study the kinetic characteristics of the molecular switches.

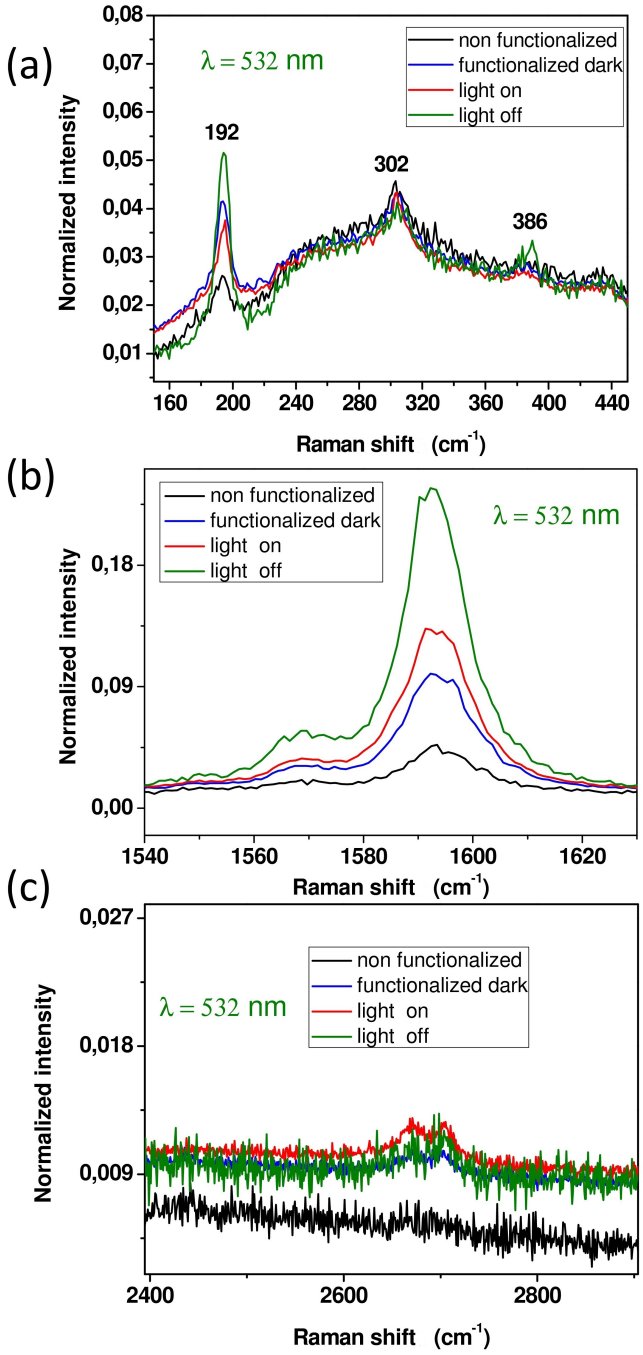

Figure 81: Raman spectra of DHP-ab73 functionalized DWNT before and after red light illumination (illumination time: 1 hour, power: 100 W/m^2, laser wavelength: 532 nm, grating: 1800/mm).

In summay, we introduced a new type of optical switch, which is DHP that can have conformational change by light illumination. The visible light can convert DHP to the open state CPD and it can go back to the closed state by heating or UV light. Our experiments indicate that even in the solid state, the DHP still can be converted to CPD if the illumination time is long and the power is high enough. The molecule DHP-ab73 is grafted onto individual DWNT and the Raman spectra at different conditions were carried out. The results indicate that the DHP-ab 73 can modify the resonance window of the

DWNT and can be stimulated by the visible light which is shown by the change of the Raman peaks. The DHP-ab 73 is suitable to functionalize DWNTs and make molecular electronic devices. Further experiments need to be done to study the kinetic characteristics of the DHP-ab 73 and DWNT hybrids.

As can be seen in these two systems (TPyOs , DHP), either we have charge transfer or a dipolar effect (respectively), but in both cases the first observed effect is an enhancement of optical phonons intensities indicating a strong electronic coupling between the molecule and the nanotube. the difference is the effective charge transfer in the case of TPyOs which leads to a frequency shift of optical phonons indicating a modification on the oscillator strength and interwall interaction as seen on RBLM features.

3.3 ROLE OF INTERWALL COUPLING ON OPTICAL GATING

Up to now we discussed dicrepancies between different molecule/DWNT hybrid based transistor, whatever the tube structure is. In the following, we want to emphasize the role of interwall coupling on the photo-induced light effect of the TPyOs/DWNT hybrid. From the last section, we know that TPyOs photo-active molecule can have an efficient charge transfer to DWNT. We proposed that the dramatic change of RBLM peak intensity of both walls is due to RBLM resonance window shift caused by the charge transfer from the TPyOs. To check our assumption, we performed tunable resonant Raman on the pristine DWNTs and the DWNT/TPyOs hybrids. This method has been used to determine quantitatively the RBLM resonance window of the isolated carbon nanotubes and nanotube hybrids.

Since the inner tube is protected from the environment by the outer tube [208], it is not in direct contact with a working electrode [114]: any charge effect must be mediated by charge transfer between the outer and inner tubes. A similar situation exists for the grafting of DWNTs when the dopant is located outside the DWNTs [209, 210]. These results lead us to emphasize the coupling between the two DWNT shells and investigate the inter-tube interaction due to a modification of its electronic environment.

The electronic transition energy determination E_{ii} can be obtained by analyzing the resonance window for each RBLM peak.

Figure 82 shows the RBLM region of the pristine and the grafted sample measured by tunable excitation laser energy from 750 nm to 820 nm. Two peaks appeared in this region, , one is very intense and the other one is hard to see since its intensity is very low. Nevertheless after TPyOS functionalization, the second RBLM peak is enhanced, which indicates a change in the inter wall interaction. Let's first discuss the pristine spectra at 790 nm, the high intensity peak at 262

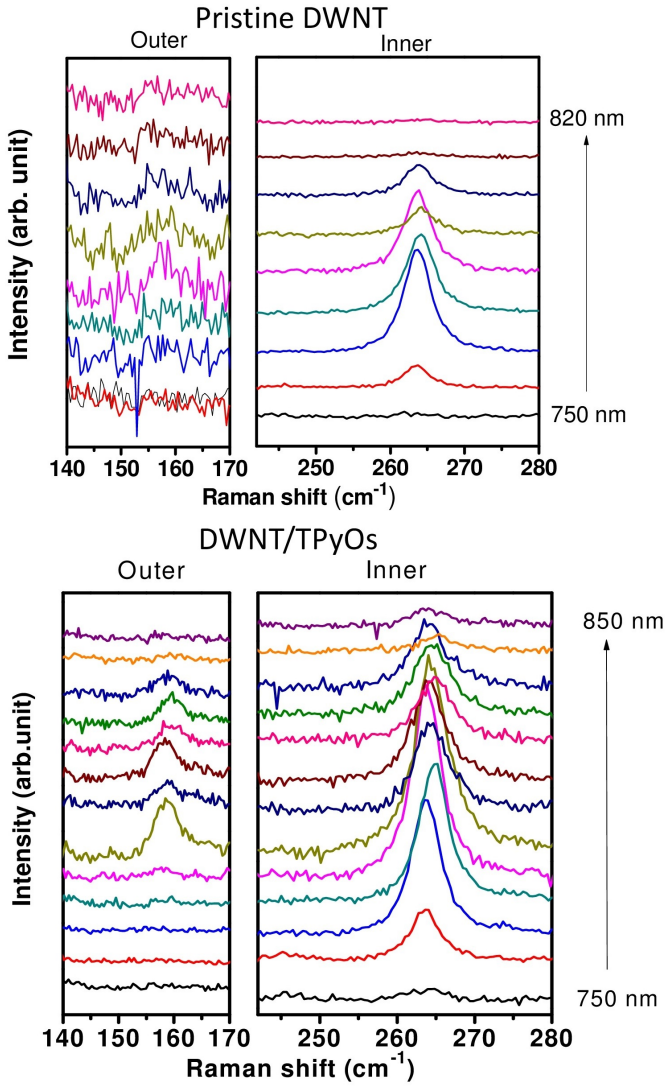

Figure 82: The RBLM region of sample C measured by tunable excitation laser energy in the 750-820 nm range.

cm^{-1} and the low intensity peak at 157 cm^{-1} can be observed. By using the equation $218.5/d_t + 15.9 = \omega_{RBLM}$ [133], which has been proven accurate to calculate the diameter of isolated double wall carbon nanotubes, we deduced the diameters of the walls to be 1.54 and 0.89 nm. The calculated inter-tube distance is 0.33 nm, which is slightly narrower than the graphite distance. So these two peaks can be assigned to outer and inner tube respectively. We compared the data of the corresponding E_{ii} to the ones in the Kataura plot and tried to find the chirality of the tube, but none of the plot matches the data that we measured for this sample, as shown in Figure 83.

We also tried other models which have been used in the literature previously for isolated DWNT, for example $228.8/d_t + 2.4 = \omega_{RBLM}$ [112] and the one considering weak inter tube coupling: $\omega_{RBLM,1} = 228/d_t$ (nm) $\omega_{RBLM,2} = 204/d_t + 27$ [82, 80, 211], none of those equations got a good match to the Kataura plot. This result is similar to the results from the Raman spectra of the DWNT with known structure

by Levshov *et al.* [82]. All these results, underline that this discrepencies is due to an intermediate or a strong interwall coupling regime between the two walls. Liu *et al.* [119] demonstrate that both RBLM modes have blue shifts compared to corresponding SWNTs. If we consider these blue shift, the inner tube has a possible chirality of (9,1), but there is still no data match for the outer tube in the Kataura plot. Liu and co-workers also investigate electronic interactions of both walls in this strong coupling regime. electronic interactions. They found that both coupled RBLM oscillations will be resonantly excited if an electronic transition of either wall matches the excitation photon energy. Turning to our results, we suppose that in the excitation laser energy range that we used (750 to 820 nm), only the electronic transition of inner wall matches the excitation photon energy, the RBLM peak of the outer tube is observed because of the coupled oscillations between the two walls. This hypothesis seems reasonnable since RBLM intensity of the outer wall ($\omega_{outer} = 157 cm^{-1}$) is much lower than the RBLM intensity of the inner one ($\omega_{inner} = 262 cm^{-1}$): the intensity ratio $I\omega_{inner}/I\omega_{outer}$ is about 25. Moreover, after grafting, the outer wall RBLM intensity increase by a factor 4 indicating an enhancement as describe in the previous section but also the ratio $I\omega_{inner}/I\omega_{outer}$ decrease drastically indicating a change on the electronic interaction due to a modification of the interwall interaction [119].

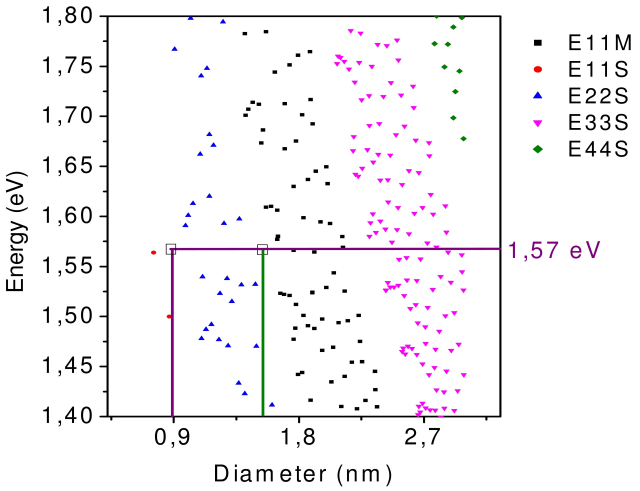

Figure 83: The Kataura plot calculated with the extended tight binding method, including many body corrections [49, 50]; the two rectangle is the transitions of the inner and the outer tube, the size of which are 0.07 nm × 0.01 eV; the horizontal line is the laser excitation energy of 1.57 eV.

A quantitavive analysis of resonance excitation profile will provide more insight on this modification of interwall interaction after grafting. Figure 84 shows the measured Raman scattered intensity as a function of laser excitation energy. The spectral location of the resonance excitation profiles yield information about the carbon nanotube electronic structure. The differential Raman scattering cross section

which can be used to quantify the strength of the measured Raman scattered signal was used to fit the curve [57, 212, 56]:

$$\frac{d\sigma}{d\Omega} = CN_{ph}|M_{e-ph}|^2 \left| \frac{1}{\sqrt{E_L - Eii - i\eta}} - \frac{1}{\sqrt{E_L - E_{ph} - Eii - i\eta}} \right|^2 \tag{25}$$

where C is a tube dependent constant which includes the photon energy independent parts of the optical matrix elements. E_L is the laser energy, E_{ph} is the phonon energy, η is the broadening factor of the curve and related to electronic transition relaxation time. M_{e-ph} is the e^--ph transition matrix element (we take it as a constant). $N_{ph} = n_{ph} + 1$ for Stockes scattering and $N_{ph} = n_{ph}$ for anti-Stockes scattering (Stockes scattering in our case), $n_{ph} = 1/(e^{|E_{ph}|/kT} - 1)$ is the phonon number. E_{ii} and η can be extracted from the fitting. From the fitting parameter, we noticed that the fitting E_{11} values of the outer wall and the inner wall just have 5 meV difference, whereas the $\Delta\eta_{outer}$(after-before) and the $\Delta\eta_{inner}$(after-before) are similar value but opposite in sign. Adding to this, the Intensity ratio : I_{outer}(before)/I_{outer}(after) (=0,26) versus I_{inner}(before)/I_{inner}(after) (=2) behave in opposite way also. All these observations strongly indicate that oscillation coupling between outer and inner tube takes place in this DWNT/TPyOs system. The RBLM peak of the outer wall is thus observed because of the inter tube coupling. This phenomenon could be explained by the energy transfer process, relying on a mechanical energy transfer between the two tubes as also describe and observed on SWNT small bundles [213].

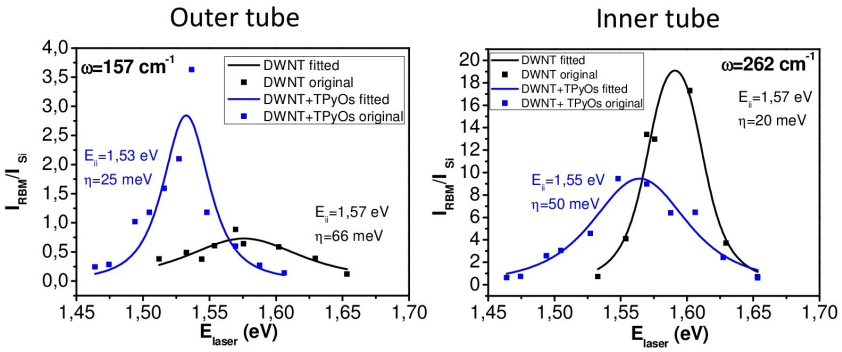

Figure 84: Resonance excitation profiles for the inner tube and the outer tube of isolated DWNT before (black) and after (blue) grafting TPyOs, which is fit using Equation 25, and E_{11} is extracted.

Finally, in Figure 84, we also observe a red shift of transition energy for both inner and outer tube. This transition energy of both the outer tube and the inner tube have red shifts. The transition energy shift can explain the RBLM intensity change of sample A and B that we discussed in the last subsection. From the transport measurement

comparison of the DWNT before and after grafting TPyOs, we concluded that the TPyOs transfer electrons to DWNT, making the Fermi energy of the DWNT down shift. We attribute the transition energy shift in Figure 84 to the electron transfer process. And because there is no direct contact between the TPyOs and the inner tube, the electron should transfer from the outer tube to the inner tube. Based on these results, a schematic electronic structure of the two tubes and the Fermi level change caused by the grafting effect is deduced in Figure 85.

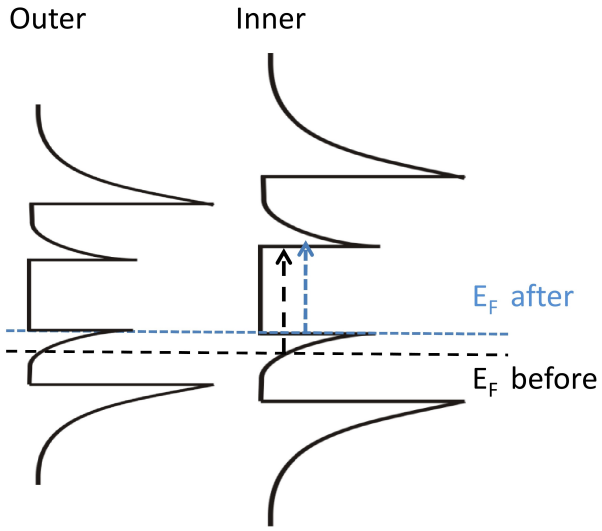

Figure 85: Schematic electronic structure of the inner and the outer tubes, the Fermi level upshift, the blue dash line shows where the charge transfer from the outer tube to the inner tube may occur. (Figure deduced from [214])

Figure 87 shows the resonance excitation profiles of sample C and TPyOs hybrids with and without light illumination. The curves are fitted by Equation 25.

We can observe that under white light illumination, the measured transition energy of the outer tube shifts from 1.53 eV to 1.61 eV ($\Delta E_{outer} = 80$ meV) , and the one of the inner tube shifts from 1.55 eV to 1.59 eV ($\Delta E_{outer} = 40$ meV). We already know from the transport measurements that the light induces an effective p-doping process to the hybrid system. The Fermi level shift direction observed from the resonance Raman spectroscopy correlated well with the transport measurement of the optical gating process.

Another important change is that, for the best excitation condition, the RBLM peak intensity of both the inner and the outer tubes increased over 8 times under the light illumination. Because under the light illumination, the TPyOs molecule is excited, thus the energy transfer process should be involved. The mechanical and the electronic coupling between the two walls of the DWNT allows the inter

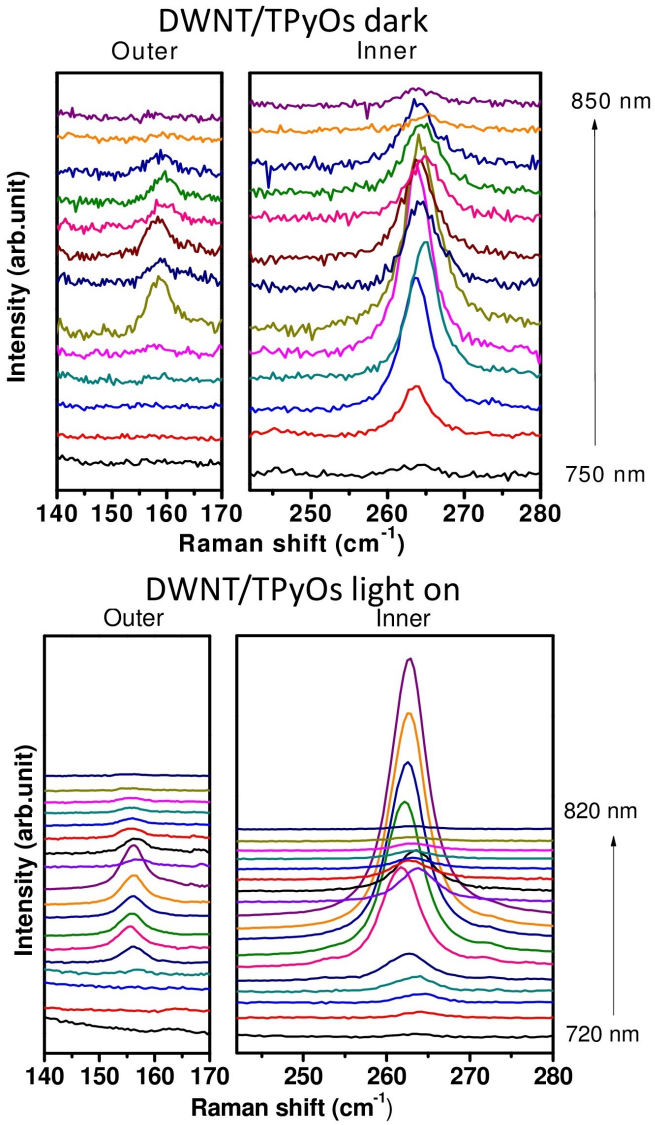

Figure 86: RBLM peaks of sample C and TPyOs hybrids with (bottom) and without (top) white light illumination.

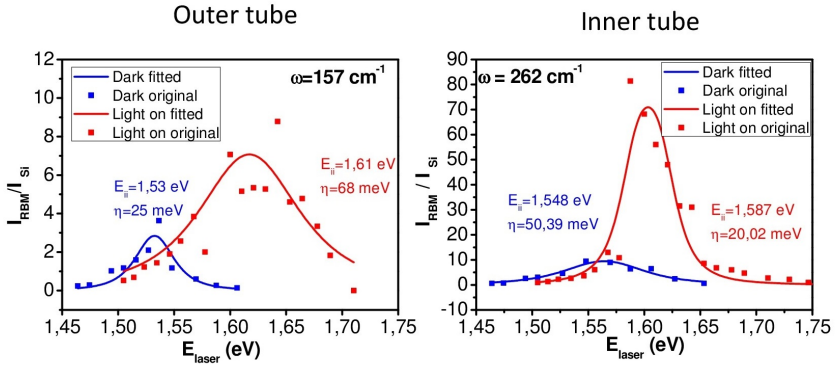

Figure 87: Resonance excitation profiles for the inner tube and the outer tube of sample C and TPyOs hybrids with (red) and without (blue) white light illumination.

tube energy transfer [213, 215, 216, 119]. So the intensity enhancement happens to both of outer and inner tubes.

To sum up, we present results of a tunable resonant Raman spectroscopy on an individual DWNT and DWNT TPyOs hybrids with and without light illumination

1. We revealed the important role of mechanical and electronic coupling between the two carbon nanotube shells.

2. Based on the analysis of the so called RBLM resonant window, the information of the excitation transition energy is extracted. After grafting TPyOs, the excitation transition energy have a red shift, indicating that TPyOs transfer electrons to DWNT. Moreover, for the first time, we show that electrons not only can be transferred to outer wall, but to the inner one.

3. Under light illumination, the excitation transition energy of the DWNT is blue shifted. Transport measurements indicate that light induced an effective p doping transfer to the DWNT and optical phonons measurement indicate an energy transfer from the molecule to DWNT. Actually, both measurements are in agreement with an effective charge transfer, since transport measurement give only information about the fermi level shift and can not give the information of energy transfer.

3.4 CONCLUSION

In conclusion, we showed that both kinds of chromophores induce significant signal when coupled to a DWNT. Their light excitation is therefore detected by both walls of the DWNTs. Moreover, we show that the signal is strongly dependent on the nature of the DWNT and more precisely on the coupling strength between its two walls. This opens the possibility to use hybrid DWNTFETs as optoelectronic transducers. Because the oxidation states of TPyOs is relatively stable, it is difficult to switch it back when turning off the light. Thus, in the next chapter, we will present our work on chromophore-porphyrin, which is supposed to be more switchable when it functionlized onto nanotubes.

4

REVERSIBLE OPTICAL GATING ON REDOX MOLECULE/GRAPHENE AND/OR DWNT HYBRIDS

In the previous chapter, we showed charge transfer between a redox chromophore and DWNT FET is efficient. In order to gain a specific wavelength dependence and reversibility of the signal, we now turn to a Zinc(II) metalloporphyrin (TPPZn)/ DWNT hybrids. Optical properties of TPPZn molecule have been studied widely. It has sharp and narrow absorption peaks in the blue light range, which can limit the light trigger in a very narrow range in order to meet specific requirements. We will more discuss light effect and memory effect on DWNT/TPPZn hybrid FETs in this chapter.

4.1 INTRODUCTION TO THE TPPZN METALLOPORPHYRIN

Porphyrins are a group of ring structure macrocycle organic compounds, composed of four modified pyrrole subunits interconnected at their α carbon atoms via methine bridges (= CH−). These molecules allow trapping a single metallic ions in their center, the latter being weakly bonded and thus exhibiting its ionic properties. Many fundamental processes in nature rely on exchange with the metallic core of metalloporphyrins such as , for example, chlorophyll for photosynthesis and heme (the pigment in red blood cells) for oxygen storage. Porphyrins provide an extremely versatile synthetic base for variety of materials applications [217]. The exploration of metalloporphyrin assemblies as building blocks for tailored materials properties has grown rapidly during the past decade. Recent applications of porphyrins for dye-sensitized solar cells have shown high conversion efficiencies [218]. The nonlinear optical properties of porphyrins are very interesting for the energy transfer with molecular control [219, 220, 221, 110, 109] and for the potential applications in optical communications, data storage and electro optical signal processing [222].

Porphyrins and metalloporphyrins have broad applications as field responsive materials, particularly for optoelectronic applications. For example, Zinc(II) metalloporphyrin was used to coat a SWNT network field effect transistor device in order to initiate an electron transfer for light harvesting [104]. Our group reported porphyrin coated silicon nanowire FETs display a large and reproducible conductance increase upon illumination [106]. As far as we know, SWNT networks, fullerene and graphene have been functionalized with porphyrin for

optoelectronic applications, but there is no report on porphyrin functionalized individual nanotubes, especially on DWNTs.

Figure 88(a) shows the structure of the studied porphyrin which has a single Zn atom in the center of the porphyrin ring. We characterized TPPZn by using both UV-visible absorption spectroscopy and Raman spectroscopy. The UV-visible absorption spectrum shown in Figure 88(b) is measured in $5.89 \times 10^{-4} mol.L^{-1}$ TPPZn in Tetrahydrofuran (THF) solution.

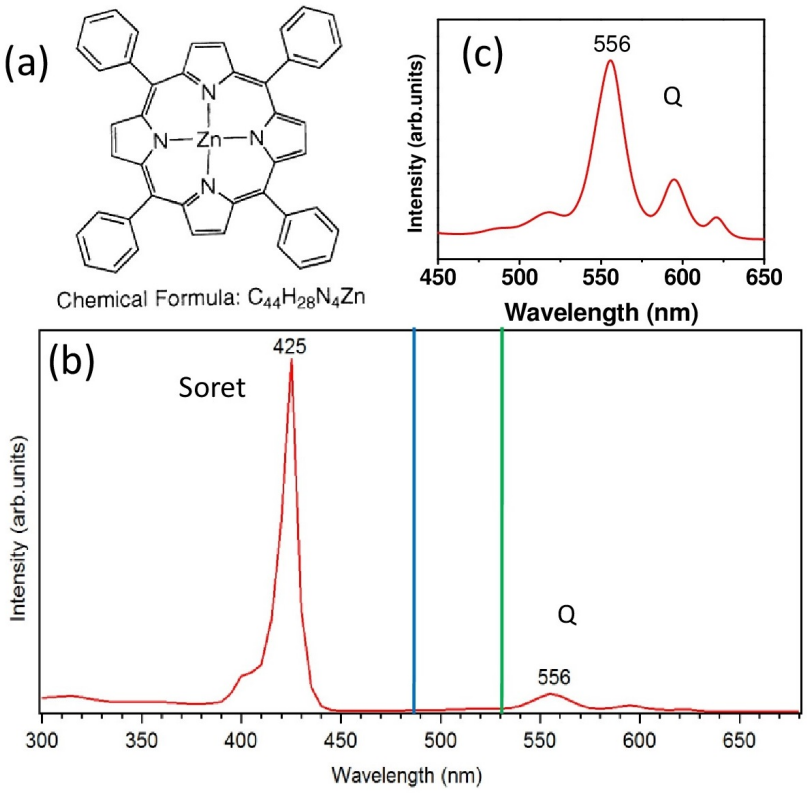

Figure 88: (a) Chemical structure of the zinc(II) metalloporphyrin derivative(TPPZn) [223], (b) UV-visible absorption spectra of TPPZn,(c) zoom in of the absorption spectrum of TPPZn from 450 to 650 nm.

The highest peak at 425 nm is the so called Soret band [224], while the other small peaks around 556 nm which can also be observed are the Q bands. Such absorption spectrum is typical for porphyrins [224, 225, 226].

Figure 89 shows the Raman spectra of TPPZn powder measured at 488 nm (a) and 532 nm (b). In Figure 89(a), two main peaks at 1356 cm^{-1} and 1547 cm^{-1} can be observed. Figure 89 (a) shows the atom labeling scheme for a metalloporphyrin, we note the vibration between atom α and β as $\nu(C_\alpha C_\beta)$, the peak at 1356 cm^{-1} comes from $\nu(C_\alpha C_\beta)+\nu(NC_\alpha)$ and the peak at 1547 cm^{-1} comes from $\nu(C_\alpha C_m)+\nu(C_\beta C_\beta)$ [227, 223, 227]. There is no sharp peak observed in Figure 89 (b), the whole spectrum shows a convex line shape, a broad peak around 3000 cm^{-1} can be observed. Since the

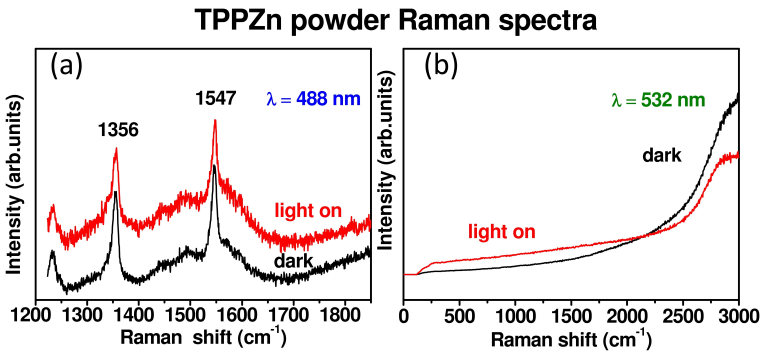

Figure 89: Raman spectrum of TPPZn powder with and without extra light illumination. The Raman spectra are measured at excitation wavelength of 488 nm (a) and 532 nm (b) respectively

sample was measured at the 532 nm laser wavelength in the Stockes process range, the position of the broad peak is $532nm - 3000cm^{-1} \approx 633nm$. We deduce that this broad peak is caused by the fluorescence of TPPZn for the following reasons: firstly, we know from [228], that the Zinc porphyrin shows fluorescence peaks at 610 nm and 650 nm, which are close to the position of the broad peak; secondly, from the UV-visible absorption spectrum (Figure 88), in the Q band region, there is a small peak at 621 nm, which corresponds to the position of the observed broad peak. Therefore, we conclude that when the sample was measured by the laser wavelength at 532 nm, the Raman signal is washed out because of the strong fluorescence signal. Under white light illumination, there is no obvious shift of the peaks as expected from the fluorescence background.

In this section, we gave a brief introduction to TPPZn metalloporphyrins and also presented its UV-visible absorption and Raman characterization, which provide the fingerprint of this molecule. It will provide a reference for us to study the properties of the graphene or DWNT/TPPZn hybrids.

4.2 MOLECULAR DOPING ASSOCIATED WITH THE TPPZN FUNCTIONALIZATION OF DWNT/GRAPHENE

In the last section, we described the UV-Visible and Raman fingerprints of TPPZn, which is helpful for studying the more complex graphene or carbon nanotube/TPPZn system. In this section, we will investigate the physical properties of the hybrid systems. As we discussed in the previous chapter, graphene was first used to investigate the influence of functionalization in order to get the best experiment conditions and the doping criteria, then we performed the same experiment protocol onto DWNTs (see chapter 2 for the deposition method). Such experiment plan also allows to compare the differences in the doping effect of 2D to the 1D hybrids.

4.2.1 *Charge transfer in 2D hybrids*

As we already discussed in chapter 2, the graphene transistor was made by directly by evaporating Ti/Au electrodes through a stencil mask. We characterized the devices electrically by measuring the dV/dI as a function of the gate voltage (V_g).

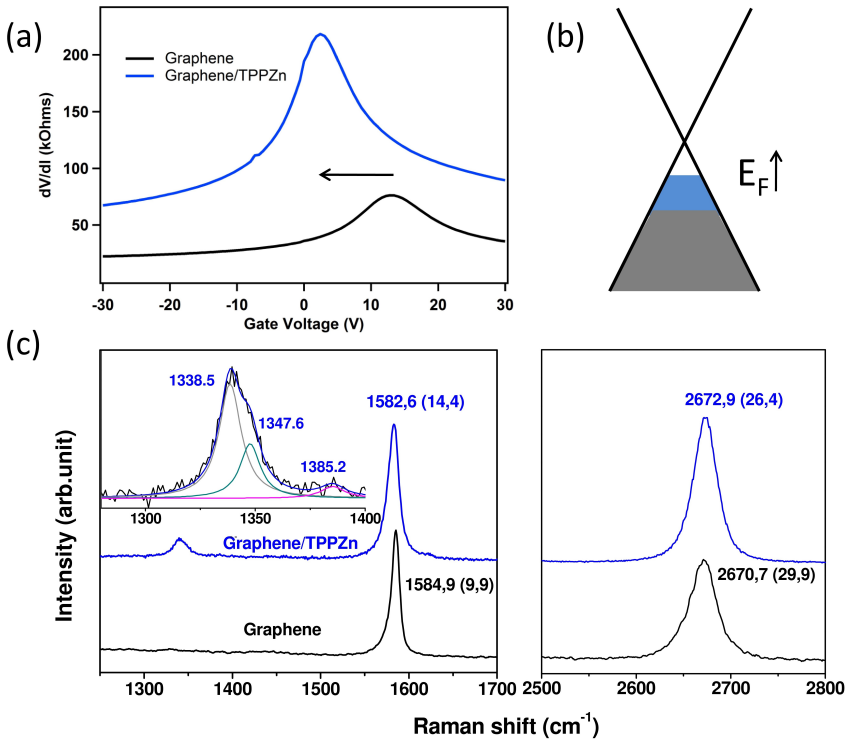

Figure 90: Comparison of the field effect and Raman spectra of graphene to graphene/TPPZn hybrids, (a) transfer characteristics of graphene before (black) and after (blue) coating TPPZn, (b) schematic representation of the Fermi level shift after TPPZn coating, (c) Raman spectra of graphene and graphene/TPPZn hybrids, the inset is the fitting of the D peak of graphene/TPPZn

Figure 90 (a) shows the transfer characteristic curves of graphene before and after TPPZn functionalization, which show that the charge neutrality point shifts from 12.5 V (hole doping) to 2.4 V, which points out an n-doping upon functionalization. The n-type doping of graphene suggests an electron transfer from TPPZn to graphene due to functionalization the charge transfer can be attributed to the energy level alignment of graphene and TPPZn [229, 230]. Because the chemical potential of TPPZn (-4.5 eV) is higher than that of graphene (lower than -4.6 eV) [231, 232], the chemical potential of TPPZn is lowered when the two materials are brought into contact and the electrons tend to transfer from TPPZn to graphene. The charge transfer consequently causes both n-type doping in graphene and a positively charged region near the interface at TPPZn side [107]. Moreover, the positively charged region results in a built-in electric field at the interface that points toward graphene. According to ref. [63], the two

following equations are used to calculate the decrease of charge carrier density and the Fermi level shift.

$$\Delta n = C_g \Delta V / e \tag{26}$$

where n is the charge density, C_g is the capacitance per unit surface between graphene and the substrate,

$$C_g = \frac{\varepsilon_0 \varepsilon_r}{d} \tag{27}$$

where $d = 285nm$ in our case so as to get optimized optical contrast for graphene [233]

$$C_g = 115aF/\mu m^2 \text{ and } \Delta n = 7.8 \times 10^{11} \text{ cm}^{-2}.$$

$$E_F(n) = -sgn(n)\hbar v_F \sqrt{(\pi |n|)} \tag{28}$$

where $v_F = 10^6$ m.s^{-1} is the Fermi velocity. We obtain the charge carrier density change is $7.8 \times 10^{11} cm^{-2}$ and the Fermi level shift is 54.3 meV. The amount of charge transfer is of the same order of magnitude and even a little higher than the Pt-porphyrin coated graphene system measured by Li *et al*. [234]. It indicates that the drop cast method for functionalizing zinc porphyrins onto graphene is efficient and can be extended to carbon nanotubes.

The Raman signature of graphene hybrids was also investigated. As shown in Figure 90 (c), the G and 2D peaks can be easily observed. These two peaks were fitted into two single Lorenztian peaks, indicating that the sample is monolayer graphene [235]. After TPPZn coating, several changes are visible on the Raman spectra. The first one is that several small peaks appear in the D band region, as shown in the inset of Figure 90 (c). We assign these peaks to a mixed signal from the molecule peaks and the DWNT D peak. Still the D peak is not very high: the intensity ratio of D peak to G peak is 0.14, which means that only a small amount of defects are induced in the functionalization process. The G peak shifts from 1582.6 to 1584.9 cm^{-1}, and the FWHM increases from 9.9 to 14.4 cm^{-1}, which are the Raman signatures of doping in graphene [167]. Here, the doping comes from the molecule grafting, we can estimate the doping level by comparing the Raman G peak shift with the electrostatic doped graphene, as shown in Figure 92. The black and blue lines stand for the G peak position of pristine graphene and graphene/TPPZn hybrids respectively. The molecule doping induced Fermi level shift in graphene is about 40±20 meV, which correlates well with the electrical transport measurements estimation of 54.3 meV as we discussed in the last paragraph. One possible effect on the Raman shifts of the mode could also

be the influence of pressure induced by the molecules onto graphene. Lee *et al*. have shown that it is somehow possible to disentangle the respective influence of doping and induced strain by looking at the evolution of the G and 2D modes frequencies [236, 237]. Their interpretation relies on the fact that these two modes are highly sensitive to the influence of doping and strain through the Grüneisen parameters. For a constant doping (resp. strain) in graphene, one expects a linear dependence of the 2D to G frequency ratio according to:

$$(\frac{\Delta\omega_{2D}}{\Delta\omega_G})_{doping} = 0.36 \pm 0.05 \tag{29}$$

$$(\frac{\Delta\omega_{2D}}{\Delta\omega_G})_{strain} = 2.2 \pm 0.20 \tag{30}$$

This provides a new reference system based on strain and doping, as shown on Figure 91.

If we translate the shifts measured on Figure 90 c) spectra in this new reference system, we obtain:

$$\frac{\Delta\omega_{2D}}{\Delta\omega_G} = -1,045 \tag{31}$$

which corresponds to a shift of -3.95 unit vectors along the direction of doping at constant strain and 1.65 unit vectors along the strain at constant doping one. This means that functionalization drives the graphene in a less p-doped region along with higher compressive strain, as expected from such molecular decoration.

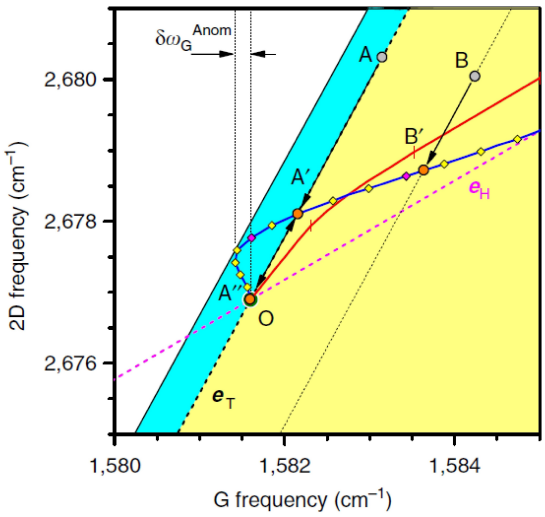

Figure 91: The effects of hole carriers with varying density n on (ω_G, ω_{2D}) of graphene, figure taken from [236].

To sum up, in this section, we discussed the charge transfer in the graphene/TPPZn hybrid FETs by the cross study of optical phonons and transfer properties of pristine monolayer graphene and

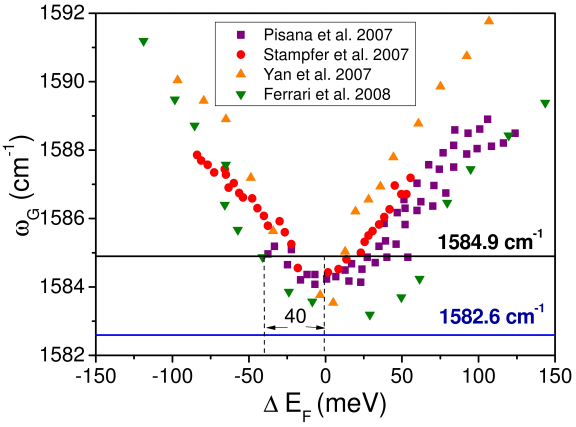

Figure 92: Comparison of the field effect and Raman spectra of graphene to graphene/TPPZn hybrids

graphene/TPPZn hybrid FETs. By a simple drop cast method, TPPZn can be coated onto the graphene surface and also transfer charges to graphene, about $7.8 \times 10^{11} cm^{-2}$ charges transfer from TPPZn to graphene, which induced 54.3 meV increase of graphene Fermi energy. The drop cast method for functionalizing Zinc porphyrins to graphene is efficient, we can extend the method to carbon nanotube functionalization. In the next section, we will use the same method to study the charge transfer between DWNTs and TPPZn.

4.2.2 *Charge transfer in 1D hybrids*

Since we already confirm charge transfer between TPPZn and graphene, we thus expect that there should be similar charge transfer effect between TPPZn and DWNTs. We then functionalize the isolated DWNT FETs with TPPZn and investigate the charge transfer in the hybrid system.

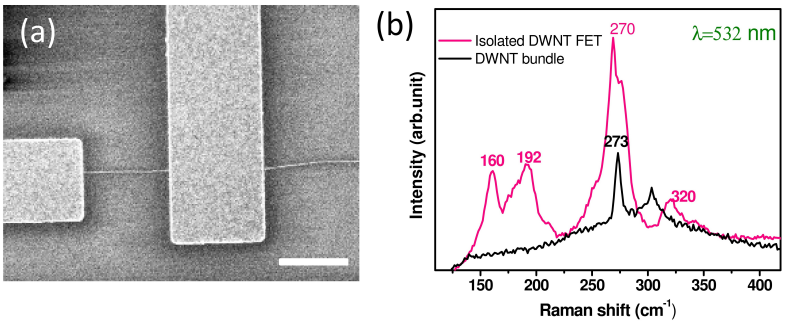

Figure 93: (a) SEM image of TPPZn grafted isolated DWNT transistors, the scale bar is 1 μm, (b) Raman spectra of the DWNT bundle and isolated DWNT transistor.

Figure 93 (a) shows a SEM image of the functionalized isolated DWNT with TPPZn molecules. This is a typical DWNT FET that we made, the length of which is around 1 μm. The molecule is not observed in this image, indicating that the thickness of the molecule deposit is very small. Figure 93 (b) shows the Raman spectra of DWNT bundles from the DWNT powder before dispersion (pink) and the bare DWNT transistor before molecule deposition (black), measured using a 532 nm excitation wavelength. From the pink line, two groups of peaks can be observed in the RBLM region (100 to 400 cm^{-1}). The first group contains two main peaks at 160 cm^{-1} and 192 cm^{-1}, and the second group contains two main peaks at 270 cm^{-1} and 320 cm^{-1}. The diameter of the inner and the outer walls of the pristine DWNT bundles can be estimated by the equations mentioned in [114]. The corresponding two main outer wall diameters are 1.53 nm (159 cm^{-1}) and 1.22 nm (191 cm^{-1}), the two main inner wall diameters are 0.89 nm (270 cm^{-1}) and 0.73 nm (320 cm^{-1}). For the bare DWNT transistor (black), two peaks can be observed in the RBLM range. We assign the peak at 302 cm^{-1} to the silicon substrate, and the peak at 273 cm^{-1} to a RBLM peak from the DWNT transistor. Here we want to emphasize that because most of the measured DWNTs are individual ones, it is very difficult to observe the RBLM peaks, since it has much less opportunity to be resonated by the laser with single wavelength. For the TPPZn functionalized DWNT, the RBLM peak could be observed only in 10% of the samples. After the chemical functionalization process, around half of the transistors were of infinite resistance. We will now focus on the sample of Figure 93 as it exhibits both the vibrational (RBLM peak) and the electrical signal. The combination of Raman and transport measurements provides more comprehensive information on the DWNT and the hybrid transistors. From the RBLM peak position, we estimate the diameter of this excited nanotube to be about 0.9 nm. Compared with the source DWNT bundles, we assign this RBLM peak to the inner wall of the isolated DWNT. We used Lorentzian equation to fit this peak, the full width at half maximum (FWHM) of the RBLM is only 4.7 cm^{-1} (close to the instrumental function of our spectrometer). Usually, the linewidths of the RBLM peak obtained from DWNT bundles are larger (from 11 to 27 cm^{-1}). Considering the other reported isolated single wall carbon nanotube and individual DWNT dispersed onto a silicon substrate which have FWHM of RBLMs larger than 7 cm^{-1} [133], the RBLM linewidth we measured on this tube is much smaller. This indicates that this RBLM peak comes from a single inner tube. Since the smallest RBLM linewidth values (the natural linewidths) occur under the strongest resonance conditions where $E_{laser} - E_{ii} \approx 0$, for both isolated metallic and semiconducting SWNTs [194, 14], such a small linewidth indicates that this sample meets the strong resonance requirement at 532 nm.

By placing the tube diameter and the excitation laser energy E_{laser} on the Kataura plot, the inner tube falls into the $E_{22}S$ region, indicating it is a semiconducting one. Moreover, in the G peak region,

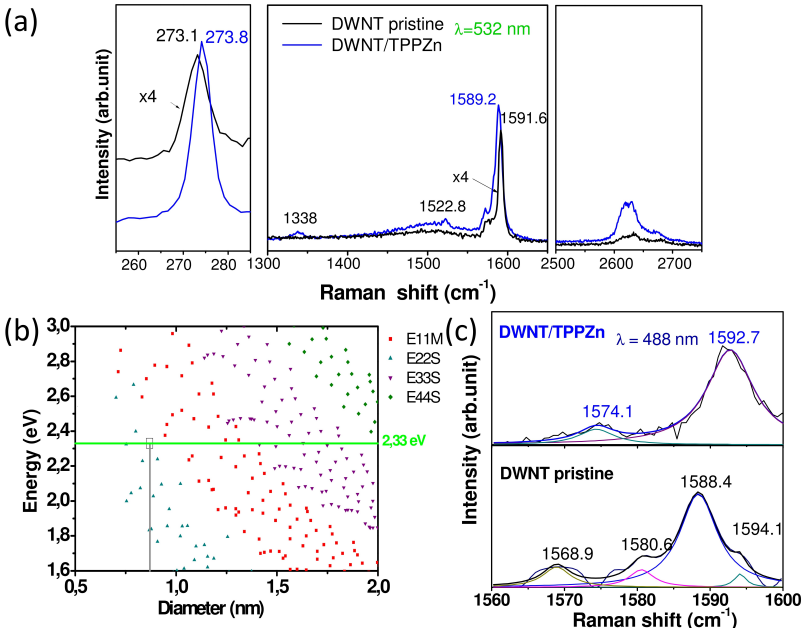

Figure 94: (a),(b) Raman spectra of isolated DWNT before(black) and after(blue) grafting TPPZn, measured at 532 nm, (c) the position of the inner tube in the Kataura plot, (d) Raman spectra of isolated DWNT before(black) and after(blue) grafting TPPZn, measured at 488 nm.

as shown in Figure 94 (a), a metallic like BWF shoulder appears. Thus there is a metallic tube in the DWNT transistor, which can only be the outer tube. Therefore, this tube has a S @ M configuration.

At first, we investigated the Raman spectra of the isolated DWNT before and after grafting TPPZn, as shown in Figure 94. For ease of comparison, Raman spectra have been normalized to the intensity of the Si peak at 520.7 cm^{-1}, and the intensity was expanded by a factor of 4 for the bare DWNT transistor for the sake of visibility. Because a BWF line shape is observed, the G peak region was fitted into 3 Lorenztian peaks and one Fano-like peak. The fitting parameters are shown in Table 6.

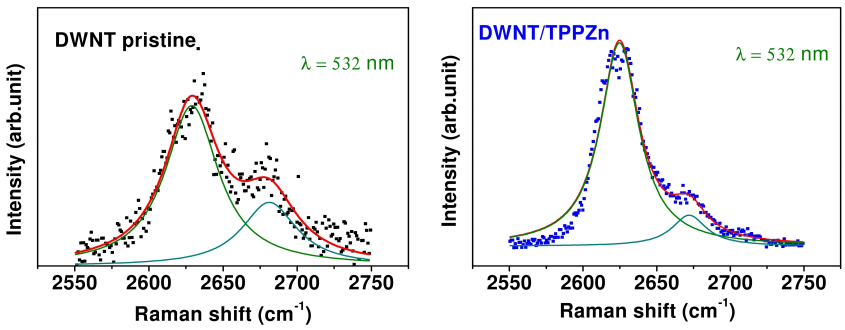

Figure 95: Fitting of 2D peak of pristine DWNT and DWNT/TPPZn.

	DWNT	DWNT/TPPZn dark	DWNT/TPPZn light on	DWNT/TPPZn light off
ω_{G1} (cm^{-1})	1591.6	1589.2	1589.8	1589.5
Γ_{G1} (cm^{-1})	6.4	9.0	8.9	8.7
ω_{G2} (cm^{-1})	1580.9	1582.0	1580.1	1580.2
Γ_{G2} (cm^{-1})	4.2	4.4	3.1	3.8
ω_{G3} (cm^{-1})	1574.2	1571.8	1571.9	1571.1
Γ_{G3} (cm^{-1})	9.0	8.0	8.0	10.6
ω_{Fano} (cm^{-1})	1527.6	1521.5	1515.8	1513.2
Γ_{Fano} (cm^{-1})	99.3	106.1	64.2	81.7
Q	-2.3	-3.9	-3.8	-5.4
ω_{RBLM} (cm^{-1})	273.1	273.8	274.0	274.0
Γ_{RBLM} (cm^{-1})	4.7	3.2	3.9	3.9
I_{RBLM}	0.03	0.21	0.13	0.15
I_{G1}	0.035	0.20	0.10	0.13
ω_{2D1} (cm^{-1})	2628.9	2624.8	2621.7	2622.2
Γ_{2D1} (cm^{-1})	43.5	31.7	32.2	32.2
ω_{2D2} (cm^{-1})	2681.1	2672.1	2668.9	2669.2
Γ_{2D2} (cm^{-1})	45.2	28.3	36.7	31.7

Table 6: Peak fit summary for the spectra measured at 532 nm.

The Raman spectra showing several evidences for the charge transfer effect:

1. Fluorescence quench: the Raman spectrum of TPPZn powder measured by 532 nm laser shows no visible Raman peaks due to the high fluorescence background. But once the molecule is grafted onto DWNT, the fluorescence signal is not observed at all, on the contrary, the Raman signature of the TPPZn appears. The fluorescence quenching of organic molecule or DNA by carbon nanotube or graphene were observed by many groups [238, 239, 240, 241, 242], which is explained by the charge transfer between the nanotube or graphene and the molecules. So, in our case, the fluorescence quenching is also attributed to the charge transfer between the DWNT and the TPPZn .

2. Shift of G peak: the pristine spectrum shows four peaks, the two highest are assigned to G^+ components of each two walls and the two lowest to the G^- ones. After doping with TPPZn, ω_{G1} shifts from 1591.6 to 1589.2 cm^{-1} ($\delta = -2.4 cm^{-1}$), ω_{G2} shifts from 1574.2 to 1571.8 cm^{-1} ($\delta = -2.4 cm^{-1}$). Comparing with the G mode shift for molecule-induced doping of SWNTs [60, 243] and graphene [167], we infer that the outer wall of DWNT was n-doped, because the G peaks down shift. TPPZn transfer charges to DWNT, which caused the shift of Fermi level.

To roughly estimate the shift of Fermi energy, we compare the G peaks' shift to the electrostatically induced doping, as shown in Figure 96. We can clearly see that the Fermi energy change is 20 meV to 43 meV. If we use the equation

$$\Delta E_F = \frac{\hbar}{2} V_F \Delta n \tag{32}$$

to calculate the increase of charge carrier density, we get Δn is 61 to 132 $e^- / \mu m$.

3. Shift of RBLM peak: the RBLM peak shifted from 273.10 cm^{-1} to 273.78 cm^{-1} ($\delta = 0.68 cm^{-1}$), which can be also caused by the charge transfer. H. Farat *et al.*detected the RBLM peak shift with the gate voltage and Fermi level change in electrochemically doped metallic SWNTs [244]. In our case, the RBLM peak has a slight upshift: the Fermi level is moving away from the neutral point, meaning the tube is doped. From ref. [245] and our own data of resonance Raman spectra of TPyOs/DWNT hybrids (see chapter 3), we know that the doping from the molecule can cause the shift of RBLM resonance window. The experimental resonant window range of RBLM peaks of SWNTs is typically ranging from 40 to 63 meV [246]. The reported resonant window of RBLM peak for isolated DWNT is even as low as 30 to 40 meV [133]. Furthermore, the RBLM resonance window that we measured for a inner tube is around 21 meV, and since we still can observe the RBLM peak after the coating of TPPZn, the resonant window of this RBLM peak did not shift a lot. So the doping level is less than 40 meV, which is in accordance with the doping level analysis from the shift of G peaks as we discussed previously. It is moreover noteworthy that the RBLM shifts due to doping though it corresponds to the inner tube with a metallic shell as the outer wall. This points to the fact that it is possible to probe the doping from a weakly coupled molecule (since not covalently bound) to another shell. In the case we show here, only one RBLM is visible, meaning the mechanical coupling between the walls is weak, while charge transfer is still visible between the walls. Last but not least, metallic walls are expected to screen the electrostatic environment of the inner wall, but since the latter is doped, it transfers the environment change towards the inner wall.

4. A global enhancement of the intensity can be observed. The G peak intensity ratio of DWNT before and after coating TPPZn $I^+_{Gbefore}/I^+_{Gafter}$ reaches 5.71, which is another evidence of the shift of Raman resonance window induced by the charge transfer between TPPZn and DWNT.

5. Figure 95 shows the Lorenztian fitting of the Raman 2D peak of pristine DWNT and DWNT/TPPZn transistor. Each curve can be fitted into two peaks, which originate from the two walls of

the DWNT [133]. We can observe that the intensity ratio of the first to the second peak I_{2D1}/I_{2D2} increases a bit, from 2.5 to 6.5, which also can be explained by the Raman resonance window shift caused by the doping from the molecule. In the case of graphene, we analyzed the peak shifts in terms of strain and doping. Such analysis would be highly promising for nanotubes. However our situation is rather complex since we can hardly attribute each mode to a specific wall and more investigation would be required to check whether analogue analysis could be implemented on nanotubes.

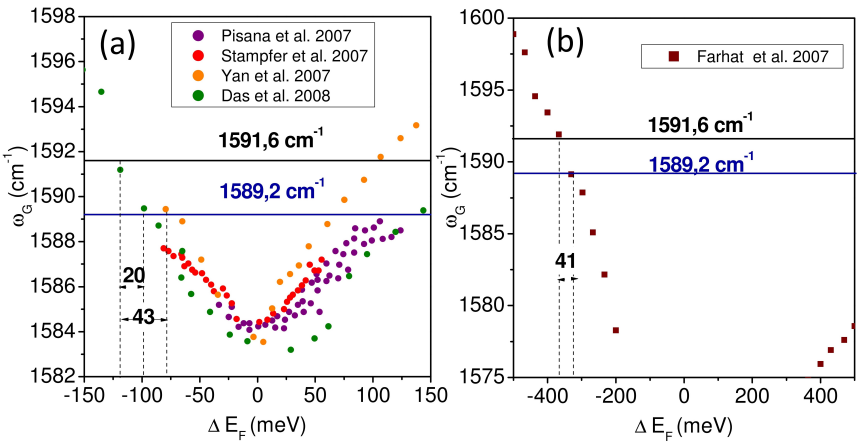

Figure 96: Estimation of the TPPZn doping induced Fermi energy change of DWNT. The black and blue lines stand for the G^+ peak position before and after coating TPPZn respectively, the colorful dots are extracted from ref. [65, 64, 63, 62, 67], which are the G peak frequency VS. Fermi level shift in the electrostatically doped graphene (a) and SWNT (b).

Over all, the Raman spectra of DWNT/TPPZn show the direct evidence of charge transfer from TPPZn to DWNT, which induced 20 to 43 meV increase of Fermi energy of DWNT, in other words, the charge carrier density change is 61 to 132 μm^{-1}. Next, we will further demonstrate the charge transfer process from another point of view, which is the electrical transport measurement.

Figure 97 shows the transfer characteristics curves of isolated DWNT (black) and DWNT/TPPZn hybrid (blue) FETs. The bare DWNT FET exhibits p-type field effect characteristics from doping with air exposure. The DWNT FET has a relatively low resistance at the off state (63 kΩ) and the on/off ratio is about 6.8. Cabana *et al.* demonstrated that transfer characteristics show features from the contribution of both walls [247]. Based on the method of Cabana *et al.*, we dedicate that this tube is a mixture of metallic and semiconductor nanotubes, which is in agreement with the result of Raman spectra. After porphyrin coating, the DWNT exhibits a conductance drop of 80%, which could be the result of the addition of charge scattering sites distributed randomly along the nanotube [104]. The second change is an increase of the on to off ratio from 7 to 65, which may be attributed to

the fact that porphyrins reduce conduction along the metallic outer wall which reveals the semiconducting behaviour of the inner one. An increase of 4% in the hysteresis width is also observed. Ong et al. have shown direct evidence that the charge injection around CNT is responsible for the hysteretic behavior of CNT FETs using SiO_2 as the gate dielectric [248]. So the increase of the hysteresis can be attributed to the phorphyrin coating acting as additional charge traps in the DWNT vicinity. We also observe that the addition of porphyrins introduces a 4.5 V shift in the threshold voltage towards negative gate voltage. The direction of the shift is in agreement with the results of Hecht *et al*. [104]: in SWNT hybrid devices, changes in threshold voltage are attributed to charge transfer of the functionalized donor to the acceptor molecule [249, 250]. The electron-donating molecule leads to a shift towards negative gate voltages. In our case, the shift caused by the charge transfer from TPPZn to DWNT correlates well with the Raman spectra in Figure 94, and also with the graphene/TPPZn system, as we discussed in the last section.

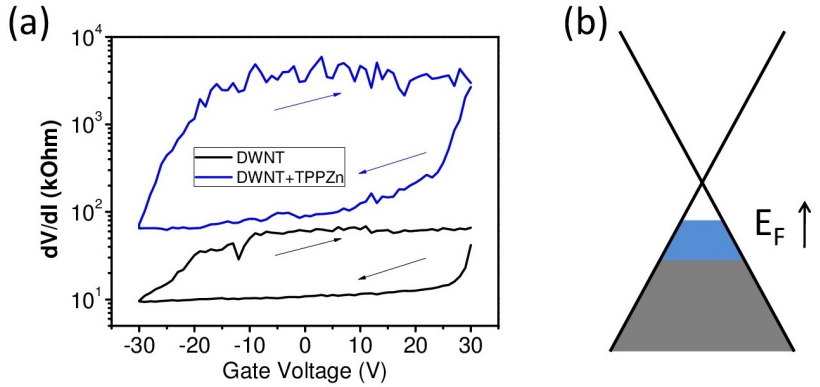

Figure 97: left: transfer characteristics of isolated DWNT (black) and TPPZn grafted DWNT (blue) FETs, right: the schematic representation of the Fermi level shift after grafting TPPZn.

From the cross comparison of electron transport and vibrational characteristics, we can conclude that deposited TPPZn transferred 61 to 132 μm^{-1} charge to the connected DWNT, the DWNT Fermi level shift is around 20 to 43 meV.

The charge tranfer can be more easily monitored at low temperature where the Coulomb blockade effect takes place and the transfer of charge becomes discrete (which can be observed from the transfer characteristic curve). This effect can be implemented for single electron memories as proposed in ref. [94]: as shown in Figure 98, which shows the principle of a single electron flash memory. This geometry is widely used in its classical non quantized version. In the vicinity of the conduction channel of a field effect transistor is a floating island used as a memory point. The charge injection in this island is controlled by a local electrostatic gate. The electric field induced by this gate controls the transfer of electrons between the channel and the memory point, which allows one to store information in the memory cell. In the case of the single electron memory, information is encoded

by the transfer of a single electron in the floating island the low capacity of which induces selectivity on the number of charge carriers by Coulomb blockade. In ref. [94], the gold nano particle is used to trap the charges; in our case, we expect the TPPZn molecule instead of gold induces the transfer of charges as a real molecular dot.

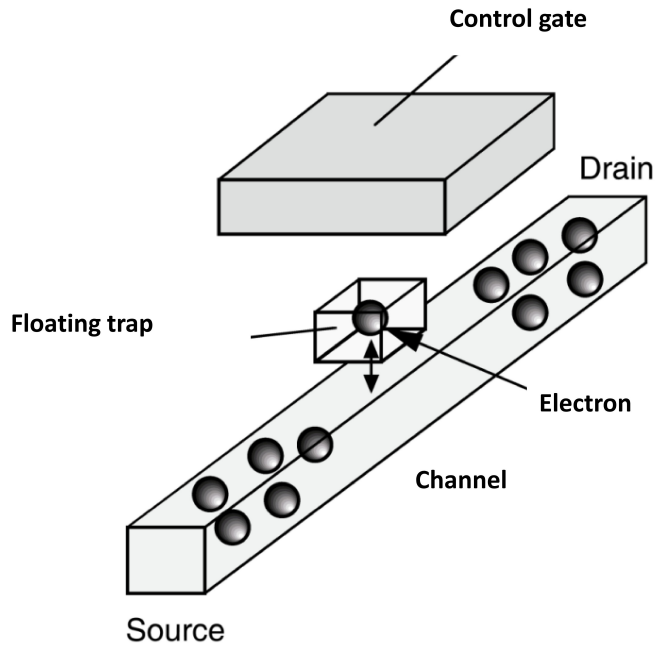

Figure 98: Principle of the single electron flash memory, figure reproduced from [251].

The sample was cooled down to 10 K in a He^4 circulation cryostat. Figure 99 (a) shows the transfer characteristics of the DWNT and TPPZn hybrid FET in dark. The characteristics curve exhibits similar field effect as at room temperature along with additional features visible as reproducible conductance steps which are regularly spaced in V_g and log dependent in dI/dV directions with a hysteretic behaviour. The regular field effect we observe indicates that the nanotube still behaves as a classical field effect transistor while the observed steps superimposed on it are signatures of single electron transfer from a trap in the Coulomb blockade regime. Such steps are usually not observed for non-functionalized nanotubes and we attribute them to signature of single charge transfer between the nanotube and one well-coupled charge trap [251]. The transfer characteristics was differentiated so as to extract the exact position of the steps. We observe double peaks in the derivative of each step which are plotted on Figure 99 (c) for each branch of the hysteresis (noted as forward and backward). The gate dependence of these peaks is linear, $\Delta V_g = 0.64 \pm 0.04$ V, as expected for a conductance channel coupled to a trap. These regularly steps are not from the Coulomb blockade of DWNT because the conductance in the step appearance region is still high, with no range of blocked current, which further illustrates that the steps come from the Coulomb blockade behavior of the trap. Fur-

thermore, these steps are regularly spaced in gate voltage meaning there is no confinement energy involved but only classical Coulomb blockade from charge repulsion: the gate voltage spacing refers only to the charging energy of the island. This excludes that the trap is realized by a single molecule which would exhibit a more complex electronic level structure. The exact nature of the trap is difficult to infer, but it could be a cluster of TPPZn molecules as the ones observed in AFM (Figure 100). Furthermore, the steps are also of same height in semi-log scale: they originate from sharp offsets of the field effect of the transistor since, in the threshold region, the CNFET has an exponential response. For this reason, quantized charging of the trap seems to be the origin of these steps.

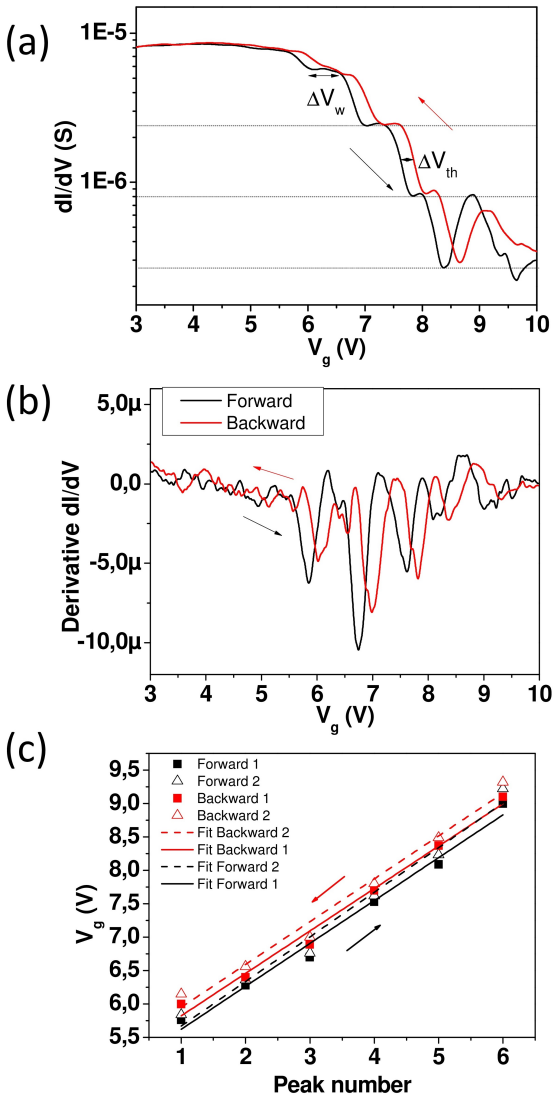

Figure 99: The conductivity of DWNT/TPPZn hybrids versus gate voltage at 10 K. The curve is plotted at V_{ds} = 1 mV (AC) for opposite gate sweeps of ± 0.1 V/s, (b) shows the derivative curve of (a), (c) shows the position of each step along with the associated linear fit.

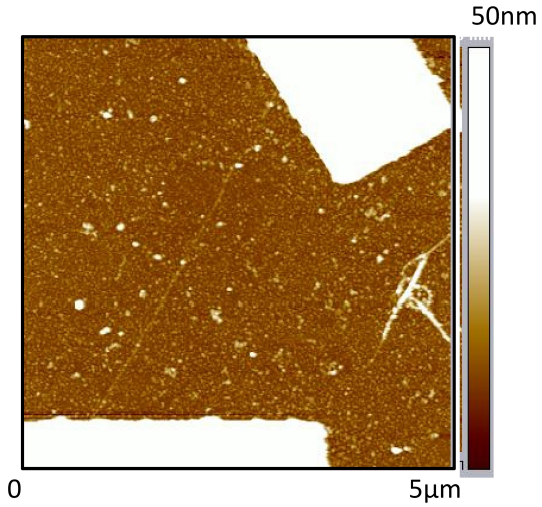

Figure 100: AFM image of one TPPZn coated DWNT FET.

A simplified model was used to explain the charge transfer process: a capacitive equivalent circuit is shown in (Figure 101). The molecule can be seen as a complex series of tunnel junctions referred to as multiple tunnel junction (MTJ) [252] with the capacitance of C_M.

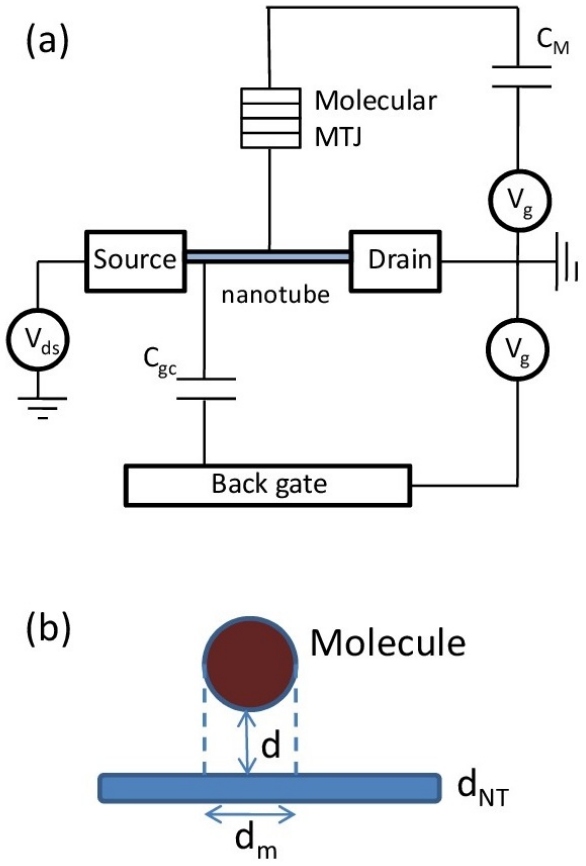

Figure 101: Capacitive model of the hybrid FET at low temperature, (a) circuit of multiple tunnel junction (MTJ), (b) sketch of molecule/-nanotube hybrid.

C_{gc} stands for the coupling between the back gate and the DWNT. In Figure 99 (a), the step parameters ΔV_w give the information of charge quantity, which will be discussed in the following paragraph.

ΔV_w is controlled by the back gate and refers to the steps appearing for each quantized charge transfer, if we assume that the single tunnelling region was achieved at 10 K, then

$$C_M \Delta V_w = e \tag{33}$$

from Figure 99, we can obtain that $\Delta V_w = 1.56V$, therefore, $C_M = 0.3aF$.

C_M can also be calculated through a simplified two panel model, as it shown in Figure 101,

$$C_M = \frac{\varepsilon_0 \varepsilon_r d_{NT} d_m}{d} \tag{34}$$

Through this formula, we can get $d_m \approx 10nm$, which correlated well with the AFM image.

In the other hand, if we calculate the charge energy through the following equation,

$$E_c = \frac{e^2}{2C_\Sigma} \tag{35}$$

where C_Σ is the self-capacitance of molecule,

$$C_\Sigma = 4\pi\varepsilon_0\varepsilon_r r = 1.7aF \tag{36}$$

$E_c = 50meV$, the thermal fluctuation energy $E_{thermal} = K_B T = 0.86meV$, with T = 10K. Therefore, $E_c > E_{thermal}$, which also supports our assumption of single electron tunneling in our system. In a word, the result of electrical transport measurement is consistent with a model of classical Coulomb blockade (without quantum confinement).

To sum up, we did the transport measurement of DWNT and TPPZn hybrids in low temperature (lower than 10K). The regularly spaced steps are observed along the typical transfer characteristic curve of DWNT which can be measured in room temperature. The stairs are the signature of the Coulomb blockade of a trap coupled to carbon nanotube. Quantized electron transfer happens between trap and the DWNT. Because what we are using here is a chromophore, we expect it can be controlled optically instead of electrically. In ad-

dition, as we discussed in the last chapter, with the help of light, the optical sensitive molecule can induce the optical gating effect in both graphene and CNTs. In the next section, we will study the optical gating effect of TPPZn and nano carbon hybrid FETs.

4.3 OPTOELECTRONIC RESPONSE OF THE HYBRID FETS

In the last chapter, we realized optical gating on the DWNT/TPyOs hybrid transistors; in this section, we not only use the same method to study the optical gating on the graphene/TPPZn and DWNT/TPPZn FETs, but also to perform wavelength dependent experiment, taking advantage of the molecular light absorption spectrum. Furthermore, as it has already been probed in the last section, the DWNT/TPPZn can be used for single electron transfer controlled by the back gate. In this section, we will use the optical gate instead of the electrical one to study the single electron transfer.

4.3.1 *Optical gating of graphene/TPPZn hybrids*

We use the same graphene/TPPZn sample from the last section, the transfer characteristic curves of pristine graphene and graphene/TPPZn hybrid FETs were shown in Figure 90. We demonstrate that TPPZn induces n-type doping to graphene. The equipment that we used for optical gating is described in Figure 42 (b) (see chapter 2): in the Desert Cryogenics probe station, light is shone on the sample through an optical window of the probe station.

Figure 102 shows the transfer characteristics of graphene/TPPZn hybrid FET measured in dark (blue), under white light (100 W/m^2) illumination (red) and after switching again the light off (green). All data are taken in vacuum at room temperature and at a constant drain-source voltage of 50 mV. It is obvious that under light illumination, the Fermi neutral point shifts from 6.7 V to 12.2 V, thus, the sample exhibits a large p-type photodoping effect. One has to note that we work in a wavelength range outside the absorption band of silicon to avoid the creation of free carriers in the substrate. By using Equation 26 and Equation 28, we estimate the photo induced carrier concentration in this sample is $4.2 \times 10^{11} cm^{-2}$, and the graphene Fermi level shift is 29.5 meV. After turning off the light, the Fermi neutral point shifts back slowly (in about 24 hours, green curve), revealing a reversible photoresponse process. The inset of Figure 102 shows the Fermi level change when turning on and off the light. The shift directions are the same as for graphene-chlorophyll hybrids [107], and also the same as for porphyrin coated SWNT films [104].

We also examined the photoresponse dynamics revealed by the time dependent measurement of the current. Figure 102 (b) shows

the bias current change of the sample for a sequence of on and off periods of irradiation. In the hole conduction regime (V_g = 0 V), the device exhibits a positive gain in current with photoexcitation and goes back to the previous state after the illumination shuts off. The time constant for the rise of the conductance under light illumination is about 1 hour and the time for the decay of the current is about 24 hours for this sample. This is much longer than other reported graphene hybrids which usually exhibit few milliseconds timescales [107]. There are several possible reasons. Firstly, this graphene sample is of millimeter size, which is very large compared to the usually micrometric reported graphene samples. A lot of charges can be trapped on the large graphene surface or by the molecule on top of graphene. Secondly, the SiO_2 substrate might trap a lot of charges, causing the long charge separation time, as proposed in ref [105] and [253]. In addition, it could be caused by the weak interaction between the graphene and the TPPZn molecule, considering the π-π stacking of TPPZn and graphene instead of the covalently interaction. Such weak coupling would lead to large molecule/nanotube capacitances and slow relaxation.

We propose a charge transfer mechanism in this graphene and porphyrin hybrids. At first, the TPPZn is excited by shining light which creates electron-hole pairs. Holes can be transferred to graphene which leads to the observed p-doping upon light illumination. The molecules trap the negative charges which are then slowly relaxing after light illumination is switched off. As we discussed before, the charge carrier density change is $4.2 \times 10^{11} cm^{-2}$.

The photo-induced charge transfer can also be detected through Raman spectroscopy. Figure 103(a) shows Raman spectra of graphene/TPPZn measured with and without external white light illumination. The graphene G peak and 2D peak can be easily observed. Peaks are fitted by the Lorentz function. Before light illumination, the graphene G peak is observed at 1582.6 cm^{-1} with the FWHM = 14.4 cm^{-1} and the 2D peak at 2672.9 with the FWHM = 26.4 cm^{-1}. After light illumination, both the G and the 2D peaks are broadened and upshifted. The G peak shifts to 1583.5 cm^{-1}, the FWHM is 15.9 cm^{-1}; the 2D peak shifts to 2674.8 cm^{-1}, the FWHM is 25.2 cm^{-1}. The upshift and the broadening of the G and the 2D peak are caused by the charge transfer [176, 62, 254, 255], which in this case, originates from the light induced charges in the hybrid system. By comparing the Raman G peak shift to the electrostatically doped graphene, we estimate that the Fermi level shift of graphene is 25$\pm$10 meV, which correlates well with the electrical transport measurements.

We observe that the Raman response change of the TPPZn molecule is much stronger during light illumination and furthermore evolves in time. As shown in Figure 103 (b), during the white light illumination, a series of Raman spectra are captured at different light illumination duration: the black, red, blue, and olive curves are the

	5s		29s		53s		54s	
	ω (cm^{-1})	Γ (cm^{-1})	ω (cm^{-1})	Γ (cm^{-1})	ω (cm^{-1})	Γ (cm^{-1})	ω (cm^{-1})	Γ (cm^{-1})
D mode	1344.7	20.0	1344.2	18.2	1342.4	15.8	1344.1	17.2
TPPZn	–	–	1350.7	21.1	1351.8	17.0	1354.1	19.9
	–	–	1520.7	18.5	1459.2	54.8	1457.5	27.7
	–	–	1549.2	17.3	1487.7	21.2	1492.5	23.1
G mode	1583.3	13.9	1583.7	13.6	1583.6	14.9	1584.5	12.3

Table 7: Summary of Lorentzian fitting of Raman spectra in Figure 103

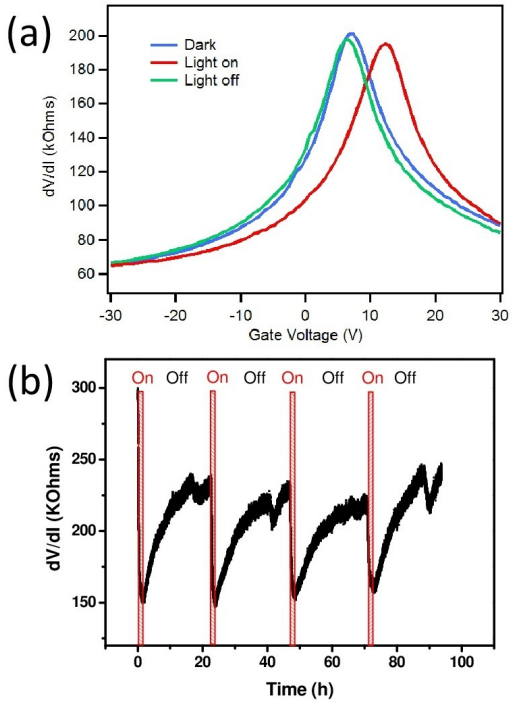

Figure 102: (a) Transfer characteristics of graphene and TPPZn hybrid FET measured in dark (blue), under white light (power: 100 W/m^2) illumination (red) and light off (green), the sample is measured by a lock-in system (b) source-drain current record of a graphene and TPPZn hybrids FET at V_{ds} = 50 mV, V_g =0 V. Upon illumination (red shaded periods) the conductance of the device is largely and reproducibly enhanced.

spectra measured after 5, 29, 53 and 54 seconds' illumination, respectively. As far as the accumulation time is only 1 second, the signal to noise ratio is much lower than for usual Raman spectra. The charge transfer dynamics can be observed from the change of the G peak and the molecule peaks. The curves in Figure 103 (b) are fitted by the Lorenztian function, the summary of the fitting results is presented in Table 7. There are several peaks from 1300 to 1560 cm^{-1} that can be assigned to the molecule peaks [227]. The fitted G and molecules' peaks frequencies are plotted in Figure 104. First, the G peak shifts from 1583.3 cm^{-1} after 5s to 1584.5 cm^{-1} after 54s light illumination. Meanwhile, at the fifth second, no peak can yet be observed in the molecule peak range. At the 29th second, the peaks at 1520.7 and 1549.2 cm^{-1} appear and at the 54th second, two more peaks appear at 1457.5 and 1492.5 cm^{-1}. Based on reference [227], the peak at 1457.5 cm^{-1} comes from $\nu(C_mC_\alpha)_{sym}$ and 1492.5 cm^{-1} comes from $\nu(C_\alpha C_m) + \nu(C_\beta C_\beta)$ vibrational modes of TPPZn (see Figure 88 for the position of the atoms), meaning that the molecule modes become progressively visible upon light exposure. The dramatic enhancement and shifts of the Raman peaks of the molecule can be caused by the charge transfer between the molecule and graphene, or by the conformational change of the molecule. Because the molecule shift (over than 56.0 cm^{-1}) is much bigger than the G peak shift (1.2 cm^{-1}),

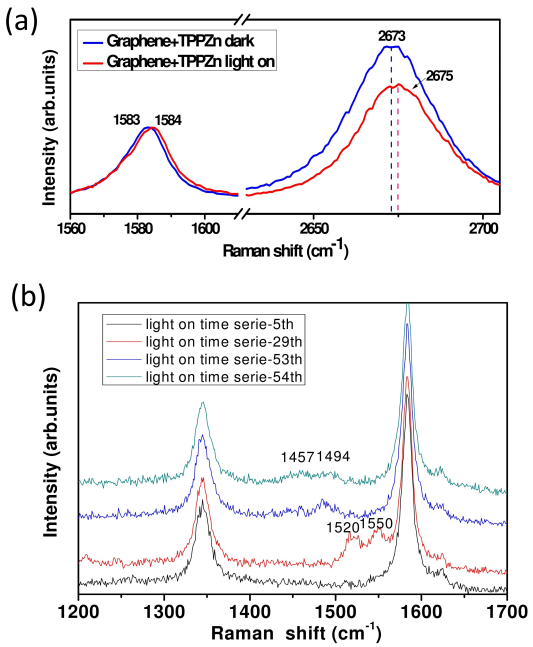

Figure 103: (a) Raman spectra of graphene and TPPZn measured with (red) and with out (blue) external white light illumination, excitation laser wavelength is 532 nm. (b) series Raman spectra measured at different light illumination time, the black, red, blue, olive curves are the spectra measured at the 5th, 29th, 53th and 54th second, respectively, during the white light illumination, the accumulation time is 1s, the grating is 1800/mm

we suppose that the molecule is undergoing conformational change rather than charge transfer during the light illumination. We also noticed that the dramatic peak shift happens only in the first minute of the light illumination, therefore, we deduced that after 1 minute, the system achieves an equilibrium state.

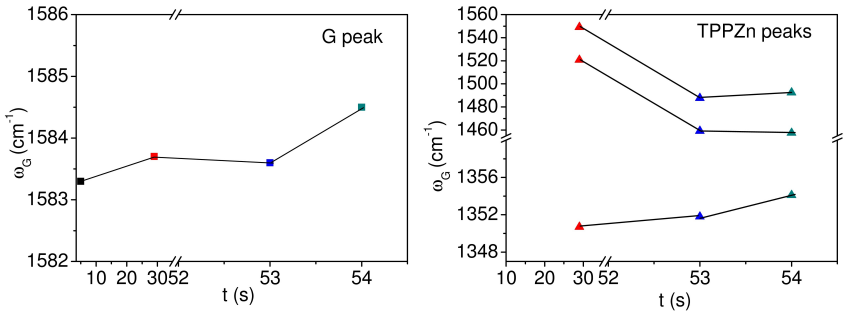

Figure 104: Raman peak evolution with time during white light illumination, left: graphene G peak, right: TPPZn peaks

To sum up, we investigated the photo response in the graphene and TPPZn hybrids, the results shows that there is efficient light induced changer transfer happened between the graphene and TPPZn molecule, giving rise to the Fermi level down shift of the graphene and the increase of the bias current. The charge transfer is reversible, after tuning off the light, the hybrids went back to the original state.

The charge transfer process was further proved by the Raman spectra of the hybrids under the white light illumination through tracking the graphene and TPPZn Raman peaks' shift. From the transfer characterisation, we obtained the graphene Fermi level shift is 29.5 meV, which correlates well with the result of Raman spectroscopy.

4.3.2 *Optical gating and memory effect of DWNT/TPPZn*

4.3.2.1 *Light effect on DWNT/TPPZn FETs at room temperature*

In the last section, we investigated the light induced charge transfer in the graphene/TPPZn hybrid FETs, in this section, we use the same method to study the light effect on DWNT/TPPZn hybrids. At first, we investigated the light induced threshold voltage shift during the white light illumination on 16 semiconducting DWNT/TPPZn hybrid FETs. The statistics of threshold voltage shift ΔV_{th} are shown in Figure 105, among which, 13 FETs (81.3%) show positive shifts. This means most of the DWNT transistors undergo p-doping under white light illumination. In order to generalize our findings, we also made the functionalized DWNT FETs with H_2TPP, which is another kind of porphyrin molecule without metal ion inside. 9 among 11 FETs (81.8%) show a positive shift of the threshold voltage, similar to the DWNT with TPPZn molecule, indicating that the porphyrin group more than the metal ion in TPPZn plays an important role in the light induced charge transfer process.

Next, we used the laser at two different wavelengths, 457 nm and 555 nm to check the wavelength dependence of the threshold voltage shifts.

Figure 106 (c) shows the transfer characteristic curves of DWNT and TPPZn hybrid transistor with and without 555 nm laser illumination. A shift of threshold voltage can be clearly observed. In the mean time, the shift of Fermi neutral point (V_n) can also be observed because this tube shows an ambipolar behaviour. The V_n has 1.3 V up shift, from 23.4 V to 24.7 V which means we realize the optical gating effect on the hybrid transistors. But if we change the laser wavelength to 488 nm, which is not in the absorption range of the molecule, the change of threshold voltage can hardly be observed (<0.2 V), as shown in Figure 106 (c). This indicates that the optical gating effect is related to the absorption peak of the molecule. It gives the direct evidence that the molecule instead of the nanotube is excited and transfers the charges to the DWNT, which leads to the optical gating. TPPZn acts as a wavelength dependent optical gate.

Since the device is very sensitive to light at 555 nm wavelength, we observed "'fast changes"' (in the 100s range) of the resistance when shining the light at V_g = 22 V, as shown in Figure 107(b): the con-

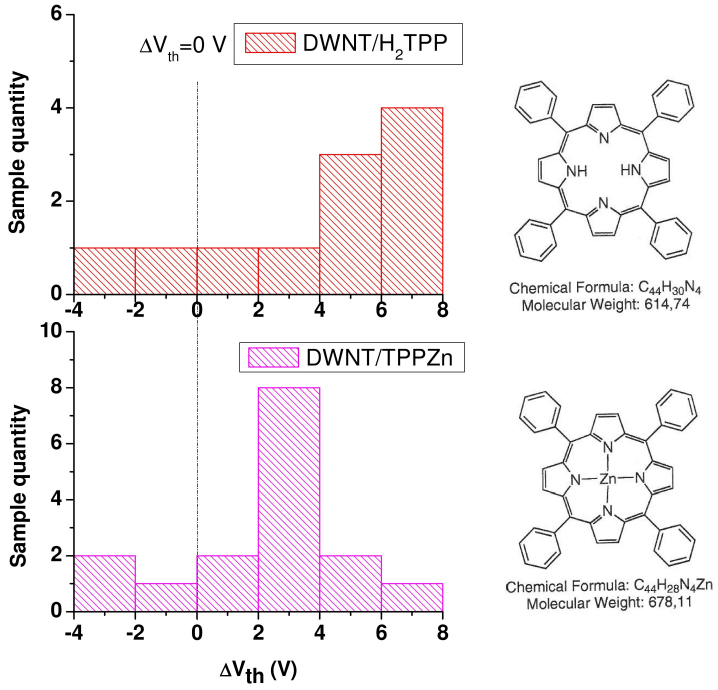

Figure 105: Statistics of the shift of threshold voltage in the DWNT/H_2TPP and DWNT/TPPZn hybrid FETs during white light illumination.

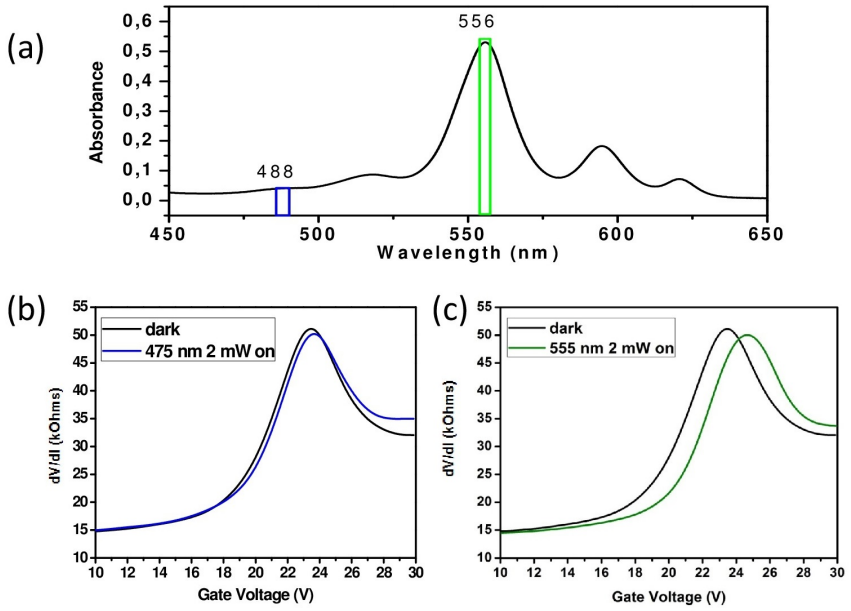

Figure 106: (a) Q bands of the absorption spectra of TPPZn, measured in TPPZn/THF solution: the blue and green colors point out the two wavelengths that were used for the optical gating experiments; transfer characteristic curves of DWNT and TPPZn hybrid transistor measured in vacuum at 300 K in dark and under 475 nm (b) and 555 nm (c) laser illumination, the laser power is 2 mW.

ductance did not completely return to its initial value when turning off the light. We tested over 20 samples, and only one of them went

back to the previous state after 2 days in ambient condition. This semi-permanent charged state is a metastable state [256], which is caused by deeply trapped electrons in organic materials [257, 258]. Unlike single-crystalline inorganic semiconductors, organic materials usually exist in an amorphous state, which inherently creates a large number of trap sites. This effect can be used to make memory as long as we find a way to "erase" it [259]. Actually, we are performing an 'optical writing' process to make the molecule trap the charges. It is though difficult to detrap them optically. It is described in ref. [257, 105] that a strong external electrical field is needed to do such an "erase step". This means we need to make an electrical erase step to make the system go back to the initial state. Figure 107 (a) shows the several steps necessary for the electrical erasing. A full write-erase cycle sets as follows: at first, we measure the resistance in dark when applying a 22 V back gate, which is around 20 kΩ (black). Then the light is turned on, after a few seconds, the resistance decreases to 17 kΩ, the optical writing step is complete (green), when the light turned off, the resistance does not change. Next, -40 V back gate is applied for adding a large electrical field, this step last about 150 seconds (purple). In order to avoid the influence of the hysteresis, we then apply 30 V back gate voltage (blue). At last, the back gate is tuned from 30 V to 22 V, the resistance goes to 22 KΩ which is slightly higher than before. We consider that the system goes back to the previous state, the electrical erasing step is finished. Figure 107 (b) also shows that the 'optical write' and the 'electrical erase' step is reversible, the process is repeated many times. We noted that the resistance change is higher and higher. Here, we have two explanations:

1. Firstly, because of the contaminants on the silicon substrate or other charge impurities around the DWNT/TPPZn devices, the devices is not originally in the ground state. When we apply a back gate of -40 V, under the drive induced by the external electrical field, the charges induced by the light illumination and the intrinsic charge impurities can both be removed. Because of the hysteresis of the back gate induced electrical field, one needs to apply several cycles to settle all the charge impurities. We expect that at one point the traps are saturated and the resistance change between the ground state and the excited stated becomes constant.

2. Secondly, as discussed in ref. [258], the density of deep traps can be amplified due to a lattice distortion in an organic layer. And from Figure 103, we observed a dramatic change of the TPPZn Raman features, which may be caused by the conformational change of TPPZn induced by light illumination. Therefore, the conformational change of TPPZn could affect the structure and induce the lattice distortion, which then can store more deep traps, causing the higher and higher resistance difference.

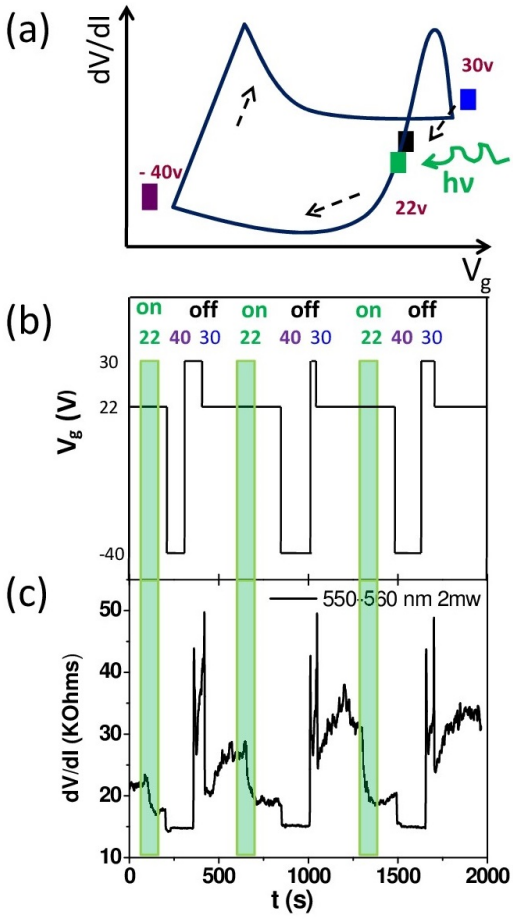

Figure 107: (a) Sketch of the transfer characteristic curve with the hysteresis, the arrows mark the direction of the back gate change, the black, green, purple, blue squares mark the V_g position of several steps to manipulate the memory effect shown in (b) which is the resistance change at different operation steps (see the explanation in the main text).

For better understanding the light effect, we did a detailed investigation of the Raman spectroscopy of the DWNT and TPPZn hybrid under white light illumination by using both 488 nm and 532 nm laser excitations. These two wavelengths were chosen because they are not in the absorption range of TPPZn, as shown in Figure 88. Figure 108 (a) shows the Raman spectra measured using 488 nm laser excitation for TPPZn coated DWNT before and after shining light. Neither the inner nor the outer tube were resonant at these excitation wavelengths, the Raman signals are very weak with no peak in the RBLM range. We can only observe the G peaks. A sum of Lorentzians was used to fit each spectrum Figure 109. The peak summary at 488 nm is presented in Table 8. While illuminating the device, the G mode region exhibits dramatic changes as shown by the red spectrum in Figure 108 (a). Two large peaks are visible at 1586 and 1594 cm^{-1}, none of which matching the values obtained for the G modes before illumination (dark). Different interpretations for this double peak can be proposed:

1. The DWNT is not fully covered with molecules and some parts of it sense the molecule excitation. This would lead to a spectrum featuring superimposed peaks from the two portions, coupled and not to the molecules. In such case we would have expected to also observe such superimposed features from the charge transfer associated with grafting in the dark and off states which is not the case. We then discard this possibility;

2. One could also consider that excitation energy of the molecule could be transferred to the DWNT and allow the enhancement of the intrinsic G mode of the nanotube, as for the energy transfer effect observed by F. Vialla *et al.* through photoluminescence [109].

3. In a previous chapter, we discussed the resonance window shift of the DWNT and TPyOs hybrid under the light illumination. The Raman resonance window shift also could happen on the DWNT and TPPZn hybrids and lead to intensity increase.

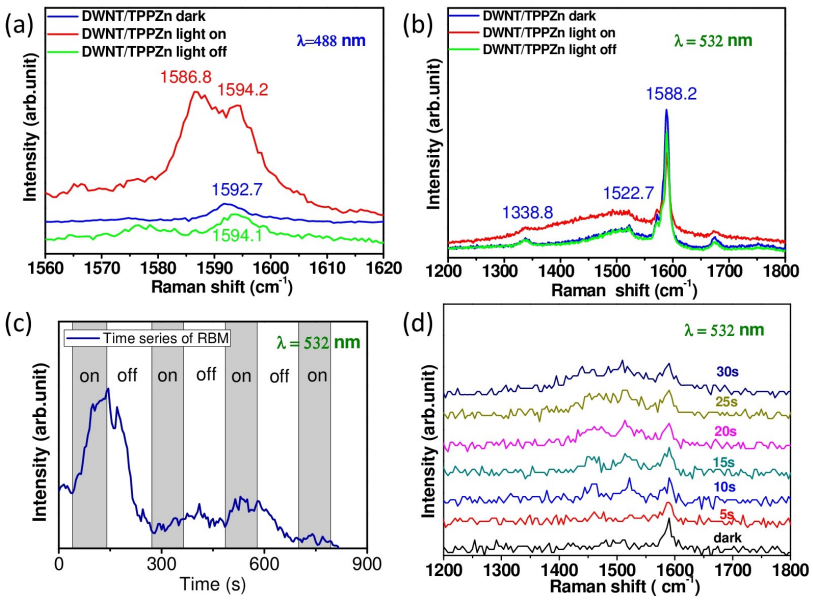

Figure 108: Raman spectra of DWNT/TPPZn under white light illumination, (a) measured at 488 nm, (b) measured at 532 nm, (c) the evolution of the RBLM peak under alternative light illumination (d) the change of molecule peaks during the light illumination in the first 30 seconds.

In order to get more information, we get the Raman spectra of the same sample measure using 532 nm laser excitation. The peak fit summary is presented in Table 6. We obtain that ω_{G1} shifts from 1589.2 to 1589.8 (δ= 0.6 cm^{-1}). The intensity ratio of peak G_1 to peak G_2 I_{G1}/I_{G2} decrease from 2.0 to 1.8, and I_{G1}/I_{G3} decrease from 3.40 to 2.19. These results lead us to consider more about the assumption of the resonance window shift caused by the light induced charge transfer from DWNT to TPPZn.The RBLM peak intensity was also

recorded and shown in Figure 108(c). There is a clear increase of the RBLM intensity (x2) when switching the light on, with a constant time of about 50s, followed by a decrease at the switching off to a lower value than in the dark state (-25%) with a constant time of about 60s. However, no significant change is observed for the subsequent cycles of light switching. We can discard any damage of the hybrid since the same effect can be recovered after an overnight relaxation. Similar measurements were performed for non functionalized devices which showed no effect at all. Two different phenomena come into play to explain these results. First a relatively fast process with a constant time of 50s involves the light excitation of the molecule leading to the creation of excitons. These excitons are broken providing free carriers transferred to the nanotube and leading to the observed enhancement. Doping induced by the charges shifts the resonance window of the RBLM which gives rise to the intensity increase under light exposure. The 50s characteristic time involved in this process reveals the low capacitive coupling between the nanotube and the molecules. Another process involves long characteristics time of up to hours. Indeed, the light effect cannot be reproduced before a relaxation time of hours corresponding to the relaxation time of charges trapped around the nanotube. It seems that charges get also trapped, either in the substrate or in molecules around and remain after light exposure, acting as a local gate but not directly injected in the nanotube anymore.

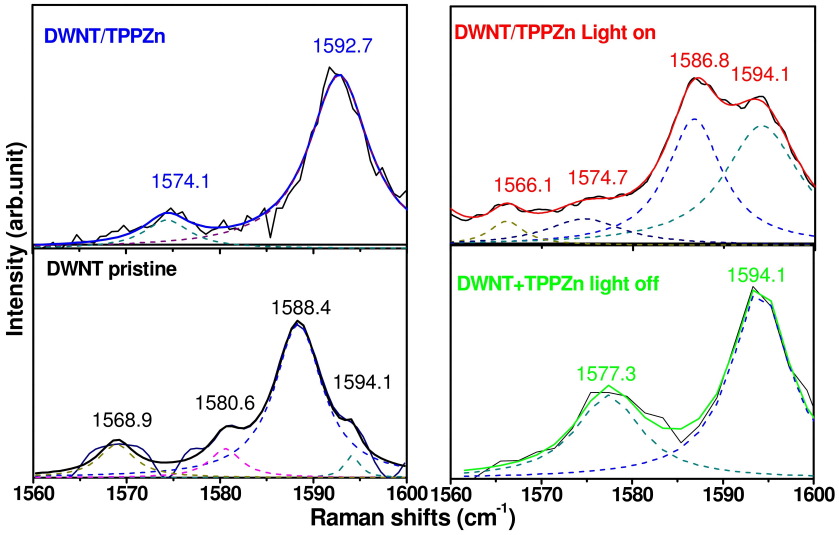

Figure 109: Lorentz fit of the Raman spectra of pristine DWNT (a), DWNT and TPPZn measured in dark (b), light on (c) and light off (d).

Another feature that appeared after the light illumination is the broadening of the G^- peak and an increase of the back ground. At this stage, it is difficult to assign the origin of the broadening and the back ground. It may be attributed to the fluorescence of the sample or some component from the TPPZn peaks, as we discussed previously, there are several TPPZn peaks in the range of 1350 to 1550 cm^{-1} (see Figure 89). For better understanding the origin of this peak, burst mode Raman spectroscopy was performed which is shown in Fig-

	ω_{G1}	Γ_{G1}	ω_{G2}	Γ_{G2}	ω_{G3}	Γ_{G3}	ω_{G4}	Γ_{G4}
DWNT pristine	1594.1	3.8	1588.4	6.2	1580.6	4.1	1568.9	4.6
DWNT+TPPZn dark	1592.7	7.3	–	–	1574.1	4.9	–	–
DWNT+TPPZn light on	1594.2	10.1	1586.8	7.4	1574.7	10.4	1566.1	4.7
DWNT+TPPZn light off	1594.1	7.9	–	–	1577.3	9.6	–	–

Table 8: The summary of Lorentz fit of the spectra measured by 488 nm excitation laser, the units are cm^{-1}.

ure 108(d). A very short accumulation time (1s) was used so as to record one spectrum every five second. In order to get the signal of both G and RBLM peaks, a 600 mm^{-1} grating was used. After ten seconds of illumination, two new peaks at 1521.7 cm^{-1} and 1459.7 cm^{-1} came out. We assign these two peaks to features of TPPZn . Normally, the TPPZn is not resonant at this excitation energy (2.33 eV), for which we did not see any Raman peak of TPPZn powder (see Figure 89). At the 20th second, the background began to rise, and the intensity of the molecule peaks becomes higher and higher. We then deduce that around 20th second, the DWNT and TPPZn begin to have strong interaction and the charges begin to accumulate to the molecule and nanotube interface, then affect the intensity of the metallic BWF peak. This effect is very similar to the back gated doped metallic nanotube, the position, the FWHM and also the intensity of Fano peak change with the change of doping carrier density [67, 121, 132]. Therefore the strong and broad peak comes from the mixture of the broadening of the Fano peak and several molecule peaks. These results correlate well with the light effect on graphene/TPPZn hybrids, as we already discussed in the last section (see Figure 104), after 29 seconds of light illumination, the peaks of TPPZn are observed, which indicate a charge transfer process happening.

From the Raman spectroscopy, we observe a remarkable change of the DWNT/TPPZn spectra under the white light illumination, which is not observed for graphene/TPPZn. It indicates that the DWNT/TPPZn system is more sensitive than the graphene/ TPPZn. As we discussed before, the optical gating and the memory effect on DWNT/TPPZn make it a system to make optically controlled memory. Considering the memory effect, we found that the DWNT/TPPZn shows another advantage. Here, we used the resistance difference to distinguish the memory "0" and "1" state. The state before the light illumination is "0", during the light illumination, the resistance decrease, the system is processing the "write" step. After turning off the light, the system should go to a stable state in order to store the information. But for graphene/TPPZn, when the light is off, the resistance slowly increases, it needs a long time to achieve a stable state. And for DWNT/TPPZn, as we discussed before, the system goes to a metastable state very quickly. We extracted the resistance change

with time of graphene/TPPZn and DWNT/TPPZn after turning off the light and fitted the curves by the equation

$$dV/dI = R_1 e^{-t/\tau} + R_0 \tag{37}$$

For graphene/TPPZn $\tau_{gr} = 10.08 \pm 0.03$ and for DWNT/TPPZn, $\tau_{DW} = 0.07 \pm 0.02$, so $\tau_{DW} \ll \tau_{gr}$, which means DWNT/TPPZn needs much shorter time to achieve the "1" state. Another advantage of DWNT/TPPZn is that because the DWNT has 1 D structure, single electron transfer can take place at the low temperature, which provides more sensitivity to the molecule and to charge detection. In the next subsection, we will discuss the light effect of DWNT/TPPZn at low temperature.

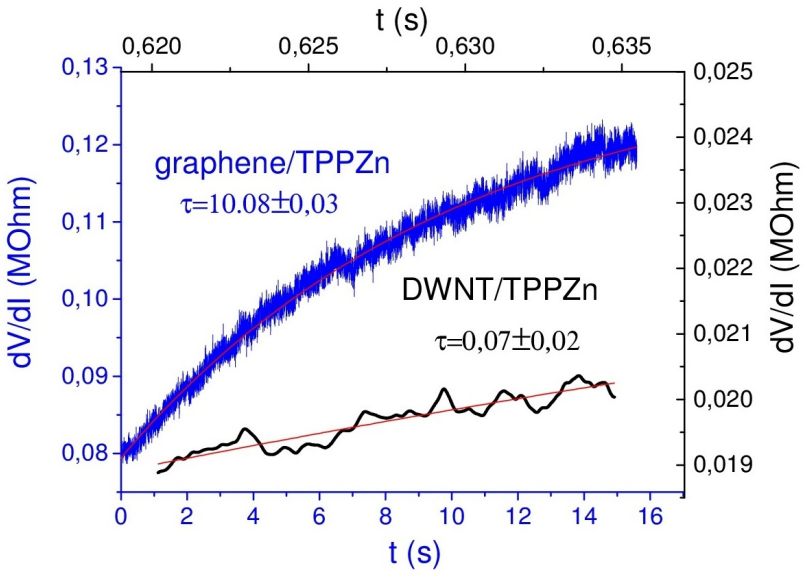

Figure 110: Time evolution of the differential resistance change with time for graphene/TPPZn and DWNT/TPPZn after turning off the light; the curves are extracted from Figure 102 and Figure 107 respectively.

4.3.2.2 *Light induced charge transfer in the single charge regime*

In the next paragraph, we will discuss the behaviour of the optically induced charge transfer at low temperature. The white light source (X-cite 120Q) was put on top of the optical window of the optical cryostat, which we introduced in chapter 2, with a distance of about 20 cm with no focusing to reduce the light surface power density and prevent any heat effect. Two filters were used for getting the light in (blue) and out (red) of the absorption range of TPPZn. Figure 111 shows the spectra of the white light source with a red and a blue filter superimposed on the absorption spectrum of TPPZn. Since the spectrum with the red filter is not in the absorption range of TPPZn, the electrical transport properties of the TPPZn and DWNT with and without shining the red light should be the same.

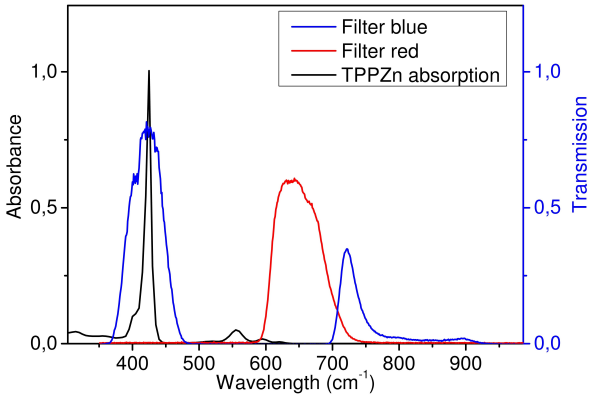

Figure 111: The spectra of the light source with the red and the blue filters, the black curve is the absorption spectrum of TPPZn.

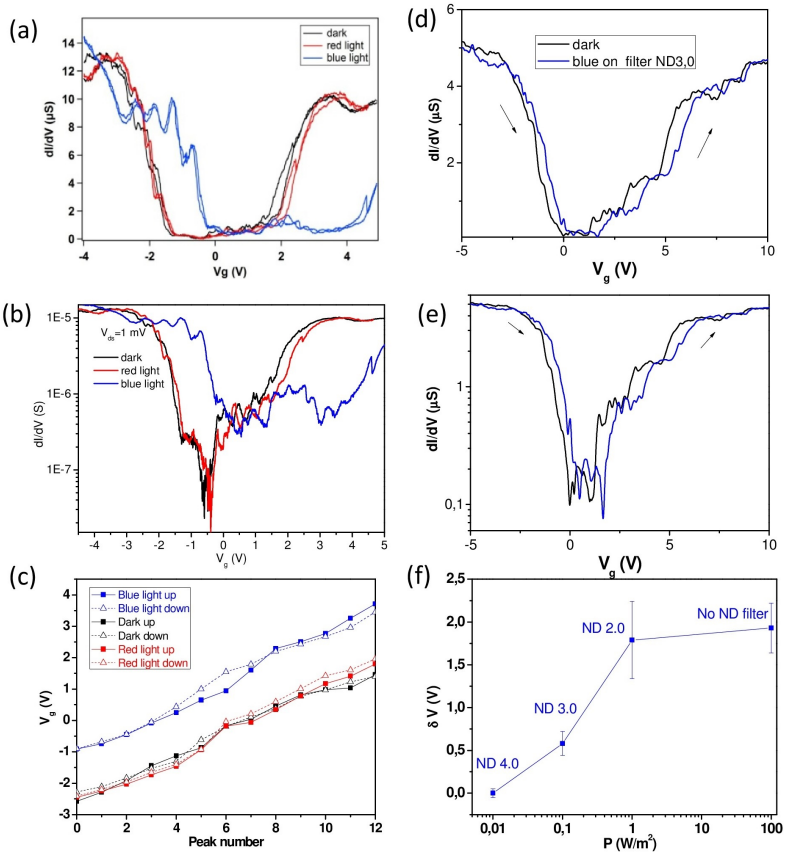

Figure 112: (a) Transfer characteristic curves of DWNT/TPPZn hybrid transistor measured in dark (black curve), under illumination with red light (red curve) and blue light (blue curve), (c) the plot is the position of the steps shown in (a), (d) comparison of the transfer characteristic curves measured in dark and under the blue light with ND3.0 filter, (f) average characteristic curve of the steps as a function of light power, (b) and (e) are the same curve of (a) and (d) plot in the log scale for better observation of the steps.

Figure 112 (a) shows the transfer characteristic curves of a DWNT and TPPZn hybrid transistor measured in dark (black curve), under red light (red curve) and blue light (blue curve) illumination. As we

discussed in the charge transfer section, the characteristic curve exhibits similar field effect as at room temperature along with additional features visible as reproducible conductance steps. At first, let us discuss the main field effect curve: the hole doping and the electron doping part can be easily distinguished. If we focus on the hole doping part, which is approximately ranging from -4 V to 0 V, we find that there is almost no change of the threshold voltage while shining the red light. Inversely, there is significant change while shining the blue light. Firstly, the threshold voltage shifts of about 1.52 V, this behaviour is very similar to the samples measured at room temperature. The transfer characteristic curve shifts towards the positive side, which means the DWNT gets positive charges from the molecule when shining the blue light. In addition, the curve is stable: we did many measurement cycles of changing the back gate from -4 to 5 V back and forth while keeping shining the blue light at the same power, the curve is stable. The only explanation is that the system achieves the equilibrium state.

Secondly, if we focus on the additional steps which we attribute to the Coulomb blockade features of a nearby trap as we discussed in the last section, we found that these steps are following the very same trend. For better comparison, we plot the position of every step (Figure 112 (c)). The gate dependence of these steps is also linear and has the same slope as the ones measured in dark and measured under the red light. Thus the steps are indeed due to the discrete additional charges traps from the same trap, with no change of its charging energy considering the constant slope observed at any wavelength. Still, the hysteresis is reduced and the shape of the steps look sharper. This effect is strongly power dependent. The position of the steps can be controlled by changing the power of the light, as shown in Figure 112 (d), (e) and (f). We used neutral density filters to decrease the power of the light. The ND n.0 filter means only 10^{-n} times of the whole light power can pass through the filter. Figure 112 (c) shows the dI/dV-Vg curve for the sample measured in dark and under blue light with the ND 3.0 neutral density filter. We can observe that the shift of steps is much smaller than the blue curve presented in Figure Figure 112 (a). The average shift of the steps for the sample measured by the ND 3.0 filter is 0.58 ± 0.14V , and the one for the sample measured by the ND 2.0 filter is 1.79 ± 0.45V, and the one without using filter is 1.93 ± 0.29V (Figure 112 (f)). Comparing with the V_{th} that we measured in the last section, which is 0.23 V, the observed shift is one order of magnitude larger than at room temperature, we thus observe the device is far more sensitive to light stimulus. This is promising in terms of using the light induced photo gating effect at very low temperature for detecting and trapping single charge. This result is very interesting because it indicates that the optical gate can be substituted to the electrostatic gate for making the single electron devices. Indeed sharp peaks are expected for a single electron memory with efficient tunnel rates. On the contrary, less transparent MTJ can lead to lower rates and step like features [252, 260]. One has to note that the step

features are not smoothed by light exposure which allows to discard any heating from the light.

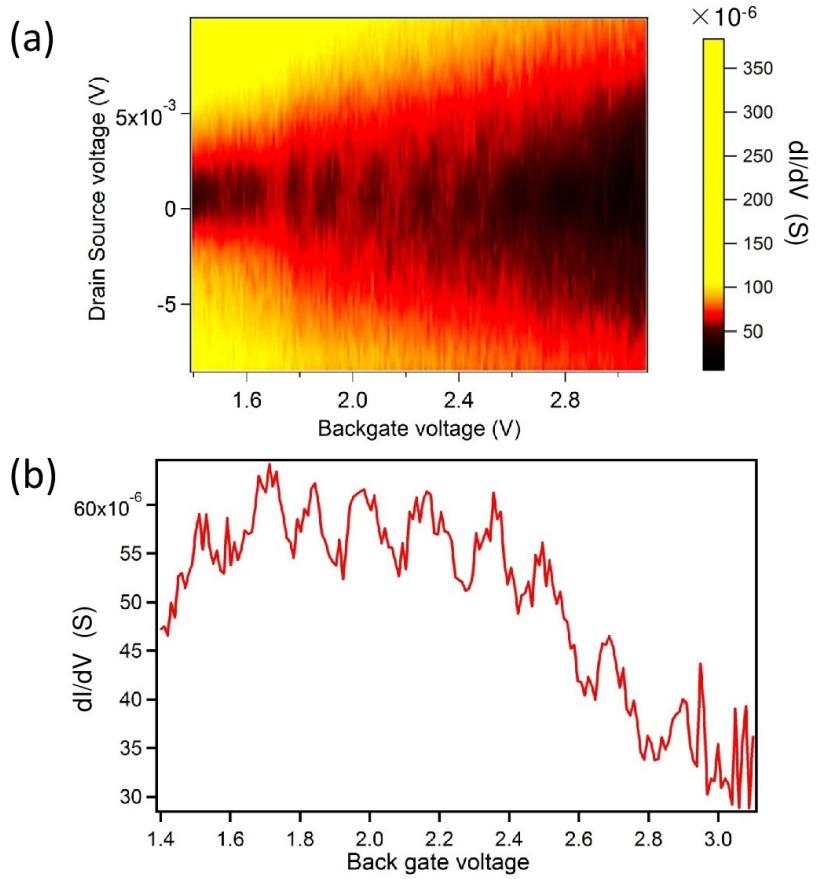

Figure 113: Mapping of light induced peaks shows the Coulomb diamond (a), (b) is the data from the cutting line of (a).

Figure 113 presents a mapping of the light induced peaks. We record the dI/dV when sweeping both the bias voltage and the back gate voltage. The map looks quite similar to the Coulomb diamond but with a background related to the field effect. When applying proper amount of energy, one electron can escape from the trap and jump to the channel, which shows an increase of conductivity. The cross section of the map Figure 113 (b) shows an oscillation. One striking feature of this map is that we manage to detect up to seven steps in the conductivity which also superimpose to the field effect of the transistor. This shows the robustness of the transfer process over a large range of electric field. The capacitive model can still be used to explain these changes. As shown in Figure 101, without light illumination, charge transfer at low temperature is driven through a multiple tunnel junction between the trap and DWNT, noted as (C_{mc}, R_t). Since most efficient effect is observed only for blue light, this points to the fact the MTJ is governed by TPPZn molecules coupling the trap and the nanotube. Under light exposure, photons absorbed by the molecules allow the lowering of the MTJ barriers which eases the tunneling of the trapped charges towards the nanotube. The MTJ, which is the building block element of the single electron memory,

turns out to be photo-activated with the wavelength selectivity of the chosen molecule as in ref [261, 262]. With light activation (see Figure 114), the tunneling rate increases and the faster kinetics is visible as sharp peaks on the transfer characteristics while for reduced excitation (dark or low power or out of absorption light), the low transfer rate compared to the gate sweep induces slow response visible as quantized steps. As a result, the sharp peaks instead of the steps come out during the light illumination.

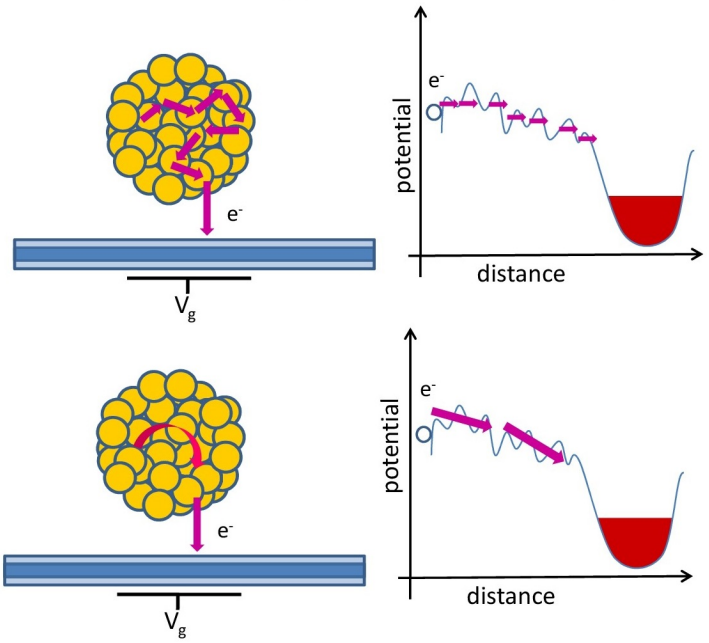

Figure 114: Sketch for the explanation of charge transfer kinetics, up: with out light illumination, down: with blue light illumination.

In this subsection, we investigated light effect on DWNT/TPPZn hybrid FETs at 10K. We already know from the last section that the charge transfer becomes discrete at 10K, which shows regular steps superimposed on the transfer characteristic curve of DWNT transistor. With the illumination of blue light, there is a global shift of transfer characteristic curve, which is the same optical gating effect that measured in room temperature. Beyond that, additional peaks with regular steps are observed, which are the signature of quantized charge transfer. The next step to overcome would be to prepare the device in the vicinity of such a step and detect the activation of the transfer with light.

4.4 CONCLUSION

To sum up, we firstly did the electrical transport and Raman measurement on monolayer graphene/TPPZn and on individual DWNT/TPPZn hybrid transistors. The two kind of hybrids show the similar behavior. The shift of threshold voltage and Raman modes indicate that there is efficient charge transfer between sp^2 carbon and TPPZn

interface. Then the optical gating and the memory effect on the two systems are realized. There is remarkable change of Raman spectra of DWNT/TPPZn hybrids, the mechanism of which is still unclear, several explanations were proposed, the light induced energy or change transfer process might be involved. It indicates that the DWNT/TPPZn is much more sensitive to light exitation than graphene/TPPZn hybrid. The charge transfer and the optical gating effects are also investigated at low temperature, where the transfer of charge becomes discrete. Under light illumination, transport of charges in DWNT/TPPZn shows Coulomb blockade behavior, which was explained by a capacitive model. The DWNT/TPPZn FETs can be used to make single electron memory, which can be controlled by a given light excitation energy. In the next step, we want to further improve the hybrid system by using the covalent grafting methods in order to make the hybrids more stable.

5

TOWARDS COVALENTLY GRAFTED HYBRIDS

As we discussed in chapter 1, there are two approaches for the functionalization of carbon nanotubes. One way is to use noncovalent functionalization and the other is covalent functionalization methods. Thus different functionalization methods have their own benefits and limitations, and the choice of these methods is dictated by the applications required from the generated nanocomposite materials. In the previous chapters, we studied the functionalization by the noncovalent methods. In this chapter, we will use the covalent method to functionalize the individual double wall carbon nanotube transistors. Covalent functionalization of carbon nanotubes has significantly expanded the utility of the nanotube structure. But it may produce defects in the wall structure of the nanotubes by breaking the sp^2 lattice. Our study will be focused on the inner wall properties change while covalently functionalizing the outer wall.

Finally, we show that this process could be a solution to preserve exceptional electrical properties of inner tube on an operating photoactive DWNT-molecule device.

The Raman mapping and single Raman spectrum were obtained on both pristine and fuctionalized DWNT transistors. The excitation laser wavelength were 532 and 633 nm. The probe test was performed on a probe station with two tungsten probe in ambient condition. A YOKOGAWA 7651 DC source was used to provide the back gate voltage, a KEITHLY 2400 source meter was used to apply the bias voltage and measure the bias current.

For covalently grafting 4-bromobenzene diazonium tetrafluoroborate to the individual DWNT transistors (chapter 5), the deoxygenated ultrapure water was needed to perform the experiment. The sodium hydroxide was put into the 25 mL ultrapure water to adjust the PH to around 9. The nitrogen was continuously flowing in the reaction vessel to get rid of the oxygen in the solvent. Then, the 54.9 mg 4-bromobenzene diazonium tetrafluoroborate was dissolved to make the 0.8 mM solvent. Put the substrate with as prepared double wall carbon nanotube transistor (see chapter 2) into the solvent for 10 minutes. At last, the substrate taken out and washed in distilled water and IPA.

8 transistors were measured in total. After the functionalization, 2 of them have no conductivity left, which may be caused by the chemical reaction process. In order to figure out what happened to the disconnected transitors, we took SEM pictures and compared them with the pristine DWNT transistors (Figure 115). The orange and red circles mark two transitors. After the functionalization, one end of DWNT was disconnected from the electrode. The DWNT was broken by external force which may comes from liquid flow.

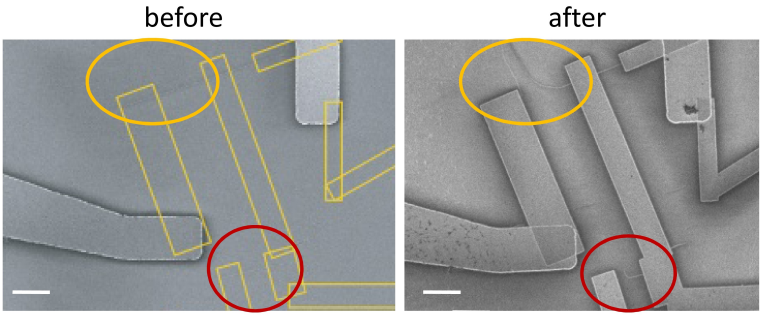

Figure 115: SEM picture of two dammaged samples of DWNT before lithography of the contacts (in yellow) (left) and after (right) covalent reaction.

Anyway, the 75% success rate proves that this method is reliable for grafting the diazonium salt to the individual DWNT transistor. As discussed by Villalpando-Paez *et al.* [133] double wall carbon nanotubes have 4 kinds of metallic and semiconducting configurations: M@S, S@S, M@M, M@S respectively. Bouilly *et al.* distinguish the configurations by comparing transfer characteristics before and after covalent functionalization of DWNT transistor [111]. We combine Raman spectroscopy and transfer characteristics to study the inner tube's behavior after covalently breaking the C=C bond of the outer wall. The samples that we measured can be divided into 3 categories, the M@S, S@S and M@S DWNTs. We will present the results of the combing Raman and probe test in the following paragraphs.

Figure 116 (a) and (b) present the SEM image and Raman mapping of the G peak of the same tube. At the nanotube position, the G peak can be easily observed. After the functionalization, there are two main differences: one is that the surface of the substrates is more rough than before, small particles can be observed (Figure 116), the appearance of nano particles may be due to the residual of 4-bromobenzene diazonium tetrafluoroborate which was used in the experimental process; the other one is that the G peak can not be observed anymore from the Raman map, this is caused by the breaking of the C=C bond of the outer wall by the covalent reaction process. In order to study into more details, we perform the probe test and Raman spectrum on the same tube.

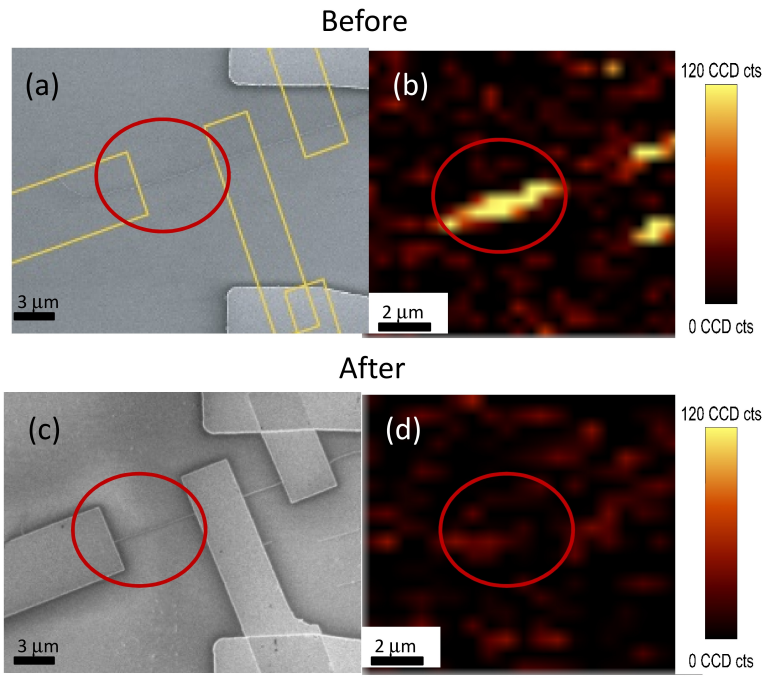

Figure 116: Comparison of SEM images ((a),(c)) and the Raman mapping ((b),(d)) of the same DWNT transistor before ((a),(b)) and after ((c),(d)) covalent functionalization. The excitation wavelength for Raman mapping is 532 nm

Figure 118 shows the transfer characteristics of the sample before (black) and after (red) functionalization, the drain-source voltage is 10 mV. The black curve indicates that before functionalization, the pristine DWNT shows an unambiguous semiconducting behavior, because it shows clearly the field effect and with on/off current ratio around 4. Like wise, after the functionalization, the drain source current I_{ds} is almost constant (about 20 nA), therefore the tube has a metallic behavior. Considering the current measured for the functionalized DWNT is due to the contribution of the inner wall [111], the red curve indicates the presence of a metallic inner wall. Furthermore, the I_{ds} of the red curve is very close to the off current of the black curve (about 15nA). So we assign this tube has a M@S configuration.

Figure 119 shows the Raman spectra of the same M@S sample before (black) and after (red) functionalization. (a),(b) and (c) are the RBLM, G and 2D modes measured by laser wavelength at 532 nm; (d),(e) and (f) are the RBLM, G and 2D mode measured by laser wavelength at 633 nm. Let us discuss the RBLM band at first. As shown in Figure 119 (a), except the peak at $302cm^{-1}$ (Si peak), the other peak at $127cm^{-1}$ is observed. In order to calculate the diameter, we use the following equation which was presented in [112]

$$\omega_{RBLM} = 228.8/d_t + 2.4cm^{-1} \tag{38}$$

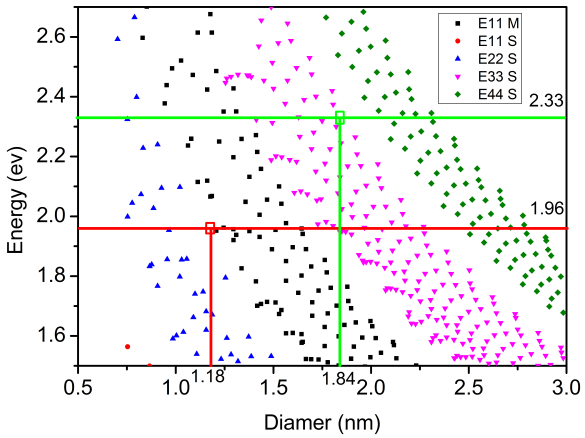

Figure 117: The Kataura plot calculated within the extended tight binding method, including many body corrections, the red and green squares represent the inner and outer tube in our case, horizontal lines stand for the laser excitation energies used in this work [50]

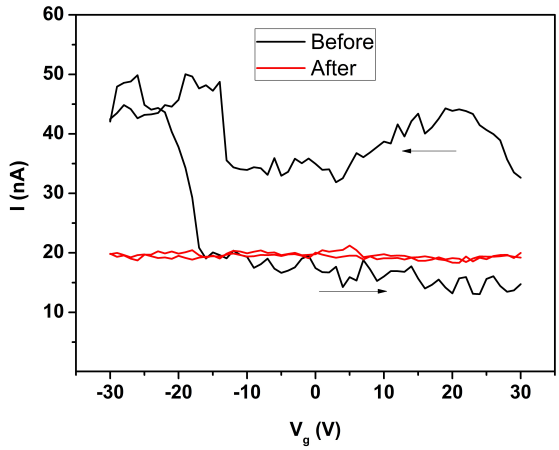

Figure 118: Transfer characteristic of the M@S DWNT before (black) and after (red) functionalization (V_{ds} = 10 mV).

for $\omega_{RBLM1} = 127cm^{-1}$, the tube diameter is 1.83 nm. In Figure 119 (d), the other RBLM peak at $196cm^{-1}$ is observed when the excitation laser length is 633 nm. $\omega_{RBLM2} = 196cm^{-1}$ corresponding to $d_{t2} = 1.18nm$. $\Delta d_t = d_{t1} - d_{t2}$ has a result of 0.66 nm. Comparing diameters to the ones of the DWNT bundles that we measured in (chapter 2), we assign the RBLM1 at $127cm^{-1}$ to the outer tube, and the RBLM2 at $196cm^{-1}$ to the inner tube. The tube-tube distance is 0.33 nm which is close to the graphite inter layer distance and other reported DWNT inner and outer tube distances [112]. We compare the data to the Kataura plot of optical transition energy versus the tube diameter. The Kataura plot was calculated within the extended tight binding method, including many body corrections, and fitted to the resonance Raman scattering data from sodium dodecyl sulfate wrapped high pressure CO conversion SWNTs[50, 49]. In our case, the Kataura plot is represented in Figure 117, the transition energies

for the third semiconducting transition of the corresponding outer tube and the first metallic transition for the inner tube are denoted by the green and red squares, respectively. From the Kataura plot, we also can see that the inner tube is metallic tube and the outer one is a semiconducting one, which is in agreement with the electrical transport measurement.

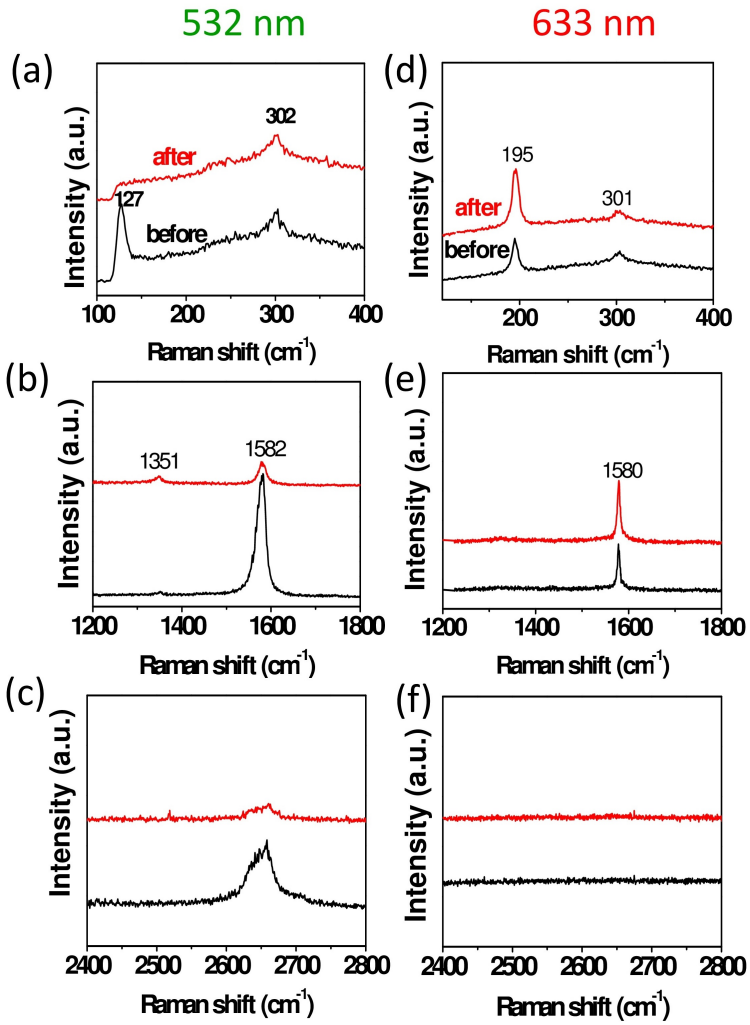

Figure 119: Raman spectra of M@S sample before (black) and after (red) functionalization. Two excitation wavelengths were used 532 nm ((a)(b)(c)) and 633 nm((d)(e)(f))

The process presented in this part is therefore an efficient way to identify the metallic and semiconducting configuration of the DWNT. In the next paragraph, we will present the data for an individual DWNT with other metallic and semiconducting configurations.

Electrical measurement as a function of gate voltage of sample 2 before and after functionalization is presented in Figure 120. Current modulation upon gate voltage variation is very strong for the pristine device (by several orders of magnitude) as well as functionalized device. Considering that the current measured for a functionalized DWNT is due to inner wall, the field effect of functionalized DWNT indicates the presence of a semiconducting inner wall. More

over, since both before and after functionalization states show strong modulation, the outer wall must also be semiconducting. We thus assign this DWNT to a S@S configuration.

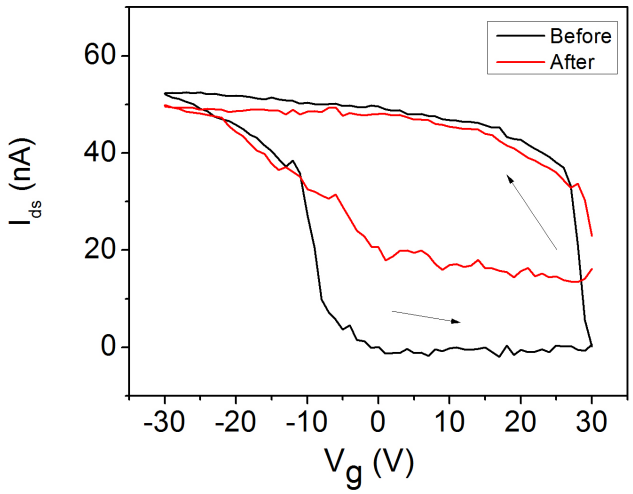

Figure 120: Transfer characteristic of the S@S DWNT before (black) and after (red) functionalization (V_{ds} = 10 mV).

On the other hand, Raman spectra of S@S sample is presented in Figure 121. In Figure 121(a), a small peak at 314 cm^{-1} can be observed, which means a tube (diameter 0.73 nm) is excited at 532 nm. Likewise, in Figure 121(d), another peak at 181 cm^{-1} is observed, the tube diameter is around 1.28 nm (calculated by Equation 38). We assign the peak at 314 cm^{-1} and 181 cm^{-1} to the RBLM peak of inner and outer tube, respectively. The G mode is very useful to assign the DWNT configurations, because at the individual DWNT level, the shape of the G band is dominated by the S or M nature of the layer that is in strongest resonance with E_{laser} [133]. The peak at 1557 and 1582 cm^{-1} in Figure 121 (b) corresponding to the G band of the inner tube (G_{inner}) since the 532 nm laser excited the inner tube. The G_{inner} has the semiconducting line shape [14], indicating that the inner tube is semiconducting. Similarly, when E_{laser} = 633nm, the outer tube is excited, the line shape of the G band should dominated by S or M nature of outer tube. From Figure 121 (e), we can observe that the G_{outer} shows a semiconducting lineshape. Therefore, we assign the outer tube to a semiconducting one. Thus from the Raman spectra, we can get that this DWNT has a S@S configuration.

The Raman spectra are correlated well with the transfer characteristics. Both of these two methods indicate that the sample has a S@S configuration. By using the same method, we can find a DWNT with a M@M configuration. As it shown in Figure 122. The third sample shows no current modulation either before or after functionalization. The absence of modulation after functionalization indicates presence of a metallic inner wall. Bouilly et al. assigned this signature to either a metallic core inside a semiconducting wall or a combination of two

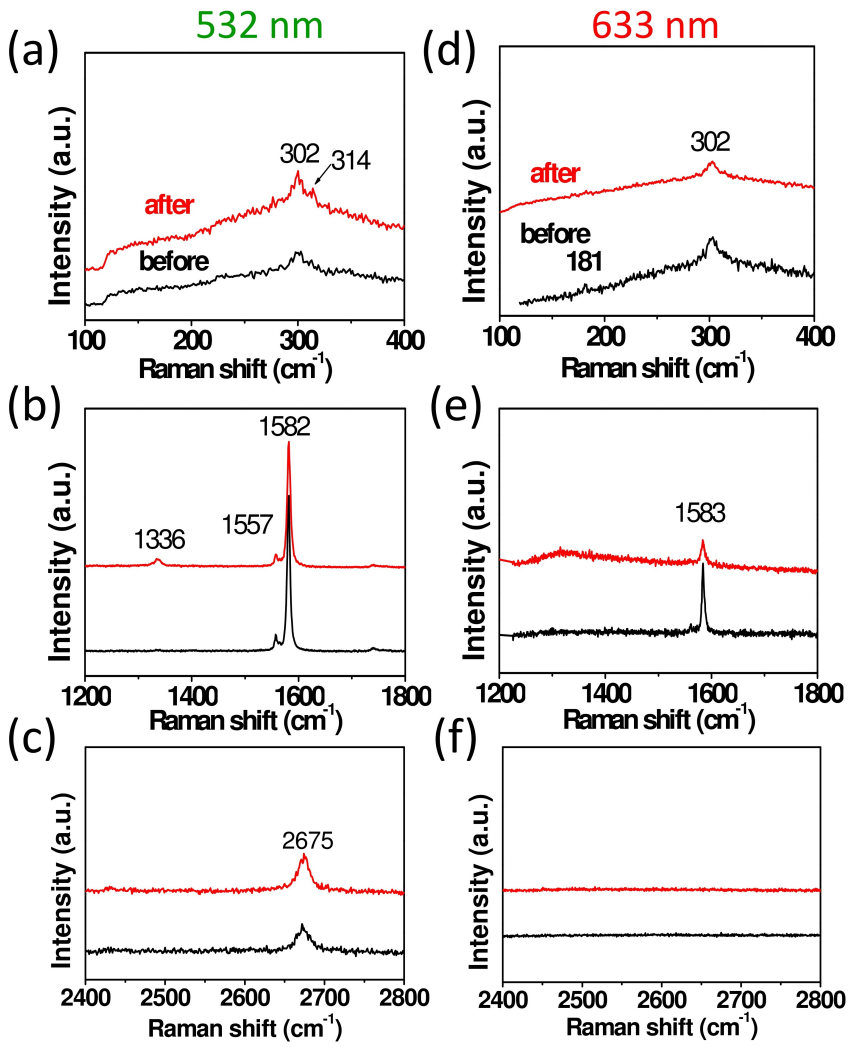

Figure 121: Raman spectra of sample S@S before (black) and after (red) functionalization. Two excitation wavelengths were used 532 nm ((a)(b)(c)) and 633 nm((d)(e)(f)).

metallic walls. In our case, we assign this signature to a M@M tube directly. Because if the outer wall is semiconducting, the modulation of the current upon the back gate should be observed, which is not the case on this sample. Unfortunately, we did not get the Raman spectra of this tube to confirm our assignment. Neither the inner wall nor the outer wall transition energy match two laser energies that we used here.

In summary, by covalent grafting method, Raman and the electrical transport measurements, we can assign different metallic and semiconducting configurations of double wall carbon nanotubes. In the following, we will investigate the effect of the covalent grating process onto the inner tube.

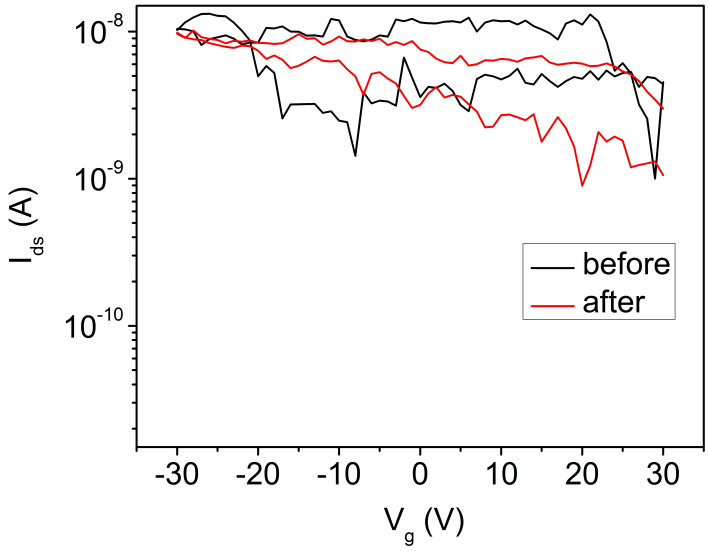

Figure 122: Transfer characteristic of the M@M DWNT before (black) and after (red) functionalization (V_{ds} = 10 mV).

5.2 INNER WALL PHONONS MODIFIED BY COVALENT GRAFTING

As we discussed in Section 5.1, for pristine M@S tube, the RBLM modes of inner wall and outer wall are observed. For the inner metallic tube, the closest dot in the Kataura plot is corresponding to the (13,4) SWNT ($d_t = 1.21nm$) with the transition energy of 1.94 eV. And for the closest dot to outer semiconducting tube is the (21,4) SWNT ($d_t = 1.82nm$) with transition energy 2.30 eV. Comparing to excitation laser energy that we used for the inner tube (1.96 eV) and the outer tube (2.33 eV), the transition energy shift is 10 meV for the inner tube and -30 meV for the outer tube. Another important result is that ω_{RBLM} of the inner tube has about 3.4 cm^{-1} blue shift compared to the expected SWNT with the chirality of (13,4), the ω_{RBLM} of the outer tube has 0.6 cm^{-1} red shift comparing to the (21,4) SWNT. We also notice that the diameter difference of the two SWNTs is 0.61 nm, if there is no interaction between the two tubes, the tube distance should be 0.305 nm, which is smaller than the layer distance of the graphite and also the tube distance of this DWNT (0.34 nm). So in this case, these two RBLM modes are highly coupled in this DWNT. Because of the inter-wall coupling, the inner tube here is suppressed, and outer tube is expanded. As a result, the RBLM peak of the inner tube and the outer tube has blue shift and red shift, respectively [263, 264].

After functionalization, there are several changes of both inner tube and outer tube:

1. The RBLM "outer mode" has disappeared, while the response of the inner wall is still observed. In the mean time, the relative intensity ratio of G peak to the Si peak I_G/I_{Si} decreases 79% (from 3.35 to 0.70), indicating that the G component con-

	Inner	SWNT 1 (13,4)	outer	SWNT 2 (21,4)
$E_{ii}(eV)$	1.96	1.95	2.30	2.33
$\omega_{RBLM}(cm^{-1})$	195.2	191.8	127.4	128.0

Table 9: The comparison of the transition energy E_{ii}, RBLM frequencyω_{RBLM} of the inner tube and outer tube of DWNT with the corresponding SWNTs.

	ω_{RBLM}	Γ_{RBLM}	ω_G	Γ_G	I_G/I_{Si}	I_D/I_G
Inner before	195.2	6.8	1578.5	6.6	0.59	0.03
Inner after	196.0	8.2	1579.0	8.3	0.74	0.03
Outer before	127.4	11.8	1577.5	24.3	3.35	0.08
Outer after	–	–	1580.1	22.4	0.70	0.34

Table 10: Summary of the Raman RBLM and G peaks before and after functionalization of sample M@S (see Figure 119).

tribution of the outer wall reduced dramatically. Further more, for the outer wall, the intensity ratio of the D peak to the G peak I_D/I_G, which is usually used to evaluate the defect concentration in the system, increased from 0.08 to 0.34. But for inner wall, it has no obvious change, indicating that the structure of the inner wall is not strongly affected by the functionalization process. According to the above results, we can confirm that the functionalization process only affected the outer wall, the inner wall structure can be preserved. This conclusion is well correlated well with other works reported in the literatures [111, 265, 266, 267].

2. As it presented in Table 10, the RBLM frequency ω_{RBLM} of the inner tube shifts from 195.2 to 196.0 cm^{-1} and the FWHM Γ_{RBLM} increases from 6.8 to 8.2 cm^{-1}. The functionalization process increase the disorder of the system, thus providing more scattering mechanism, resulting to a peak broadening.

3. The intensity of RBLM peak and G peak of inner tube increased. One explanation could be a shift of the transition energy. Bouilly *et al.* got the absorption spectra of the DWNT film in pristine, functionalized and defunctionalized states [111]. From that spectra, a shift of the E_{11} transition energy can be observed. The shift of the transition energy causes a shift of resonant window, thus affecting the intensity of the RBLM and the G peak intensity [190].

From the Raman analysis of DWNTs before and after covalent grafting, we can obtain that the RBLM and the G peak have slight shift after the functionalization, which is due to the interaction between the inner and outer wall. In summary, from this study, we found that the functionalization process mostly affects the outer tube, the electrical and optical properties of inner wall are preserved. Af-

ter functionalization, field effect can be measured on the inner tube despite the damage of the outer wall. This a a prof of the concept of core-shell system. Our next step will be to grafting an optical switch to realise optoelectronics system.

5.3 CONCLUSION

The covalent process presented here is an efficient way to identify the electrical combination of walls forming a DWNT. The covalent functionalization is revealed as a powerful technique to explore fundamental electronic phenomena in DWNTs, such as interwall couplings, current repartition between walls or velocity saturation of carriers. The diazonium salt can be used as a bridge to graft other functional molecules, such as the optical switch [92], the molecule magnets [268, 269], protein [270, 271] *et al.*. This method can be considered as the first step for more complex DWNT functionalization process. The result presented here gives us a very important information, that is: the diazonium covalent functional process only affect the outer wall, the electrical and optical properties of inner wall is protected. Thus, the outer wall can be used as a platform to graft photo-active groups like DHP, TPyOs, TPPZn... These covalently grafted photo-active molecules, will allow a more efficient light transduction to an electrical excitation than non covalently grafted ones. We expected a better efficiency thanks to a faster excitation exchange between molecule and nanotube interface.

CONCLUSION AND PERSPECTIVES

CONCLUSIONS

In this thesis, we have demonstrated isolated double wall carbon nanotube and chromophore hybrid field effect transistors, from the synthesis, characterization of pristine transistor, the investigation of inter-wall coupling in isolated DWNT, the study of vibrational and electrical properties of DWNT/chromophore hybrids, to the non covalently functionalized molecule doping effect on DWNT, the optical gating effect on the hybrid transistors. At last, we realized the single electron memory based on the hybrids at 10 K with some optical response. We then started investigating the case of covalent grafting.

The fabrication techniques were introduced in chapter 2. By combining different probes, chirality and metallic or semiconducting nature of both inner and the outer wall were determined. Strong or weak mechanical coupling of individual DWNT can be distinguished through the optical phonon measurement. Moreover, electron-phonon coupling in individual DWNT is investigated, to the best of our knowledge, this is the first experimental study of EPC in the complex DWNT system.

In chapter 3, the optical gating effect is achieved in DWNT (with strongly coupled walls) and TPyOs hybrid transistors. We demonstrated that the optically induced charge carriers not only can be transferred to the outer tube, but also can affect the vibrational and electrical properties of the inner tube, which caused change of transition energy E_{ii} and the RBLM resonant condition. This shows that the optical excitation of the molecule can indeed be sensed by the inner tube.

Since TPyOs has relatively more stable oxidation state than porphyrin molecules, the DWNT/TPPZn hybrid transistors were investigated in order to get a reversible optical gating. The color dependent memory effect was achieved in the 1D system. At helium temperature, the charge transport in DWNT/TPPZn shows Coulomb blockade behavior and can be tuned optically in certain extend. We investigated the hybrid DWNT/chromophore transistors in a new regime where single electron process take place.

PERSPECTIVES

Inter wall interaction in 1D core-shell systems

In this thesis, we probe inter wall interaction in a S@M individual DWNT thanks to molecular grafting. In the near future, the coupling in DWNT which have different configuration will be possible using tunable Raman spectroscopy with an electrostatic or a molecule gate. This study will be interesting to compare with the study of interlayer coupling in the bilayer graphene system, for example to address the influence of curvature and commensurability. Furthermore, it will be also interesting to use the same method to study other 1D core-shell systems, for example, the BN nanotubes, WS_2 tubes*etc.*

Light induced energy/charge transfer, and the role of excitons

In DWNT/TPPZn system, we found that there is remarkable change of the Raman modes during illumination, the mechanism of which is still unclear. Several explanations were proposed: the most possible one is light induced energy transfer. The role of exciton is very important to understand more about the excitation transfer process. For studying this, one would require other techniques, for instance, photoluminescence spectroscopy or ultrafast spectroscopy to capture the exciton behavior.

Covalent functionalization of individual DWNT FETs.

Covalently grafting methods allow us to graft a variety of molecules. In this thesis, we show the influence of diazonium salts, which can be used as a bridge to link the molecule and individual DWNT FETs, on RBLM peaks. For the next step, we want to realise the covalently functionnalized devices in order to make different kind of sensors or switches, for example, we can funtionalize the DWNT covalently by molecules with DHP groups. By taking advantage of the conformational change of the DHP, more stable optical switches or memory devices can be made.

Electron phonon coupling in low dimensional hybrids

The mechanism of single electron charge transfer could be investigated more deeply by Raman spectroscopy together with transport measurement at low temperature. The modification of the vibrational properties of DWNTS by the single electron transfer will be also valuable to study the sensitivity of the inner tube and the inter-tube interaction.

The functionalization of individual DWNTs have promising potential on the application to the photoelectric transducer with single electron sensitivity.

BIBLIOGRAPHY

[1] K.S. Novoselov, Andre K. Geim, S.V. Morozov, D. Jiang, M.I. Katsnelson, I.V. Grigorieva, S.V. Dubonos, and A.A. Firsov. Two-dimensional gas of massless dirac fermions in graphene. *Nature*, 438(7065):197–200, 2005.

[2] A. Geim and K. Novoselov. The rise of graphene. *Nature Materials*, 6(3):183–191, 2007.

[3] Jae-Ung Lee, Duhee Yoon, and Hyeonsik Cheong. Estimation of young's modulus of graphene by raman spectroscopy. *Nano Letters*, 12(9):4444–4448, 2012.

[4] P.J. Zomer, S.P. Dash, N. Tombros, and B.J. Van Wees. A transfer technique for high mobility graphene devices on commercially available hexagonal boron nitride. *Applied Physics Letters*, 99(23): 232104, 2011.

[5] Meisam Rahmani, Razali Ismail, Mohammad Taghi Ahmadi, Mohammad Javad Kiani, Mehdi Saeidmanesh, FA Karimi, Elnaz Akbari, and Komeil Rahmani. The effect of bilayer graphene nanoribbon geometry on schottky-barrier diode performance. *Journal of Nanomaterials*, 2013:3, 2013.

[6] Taisuke Ohta, Aaron Bostwick, Thomas Seyller, Karsten Horn, and Eli Rotenberg. Controlling the electronic structure of bilayer graphene. *Science*, 313(5789):951–954, 2006.

[7] Yuanbo Zhang, Tsung-Ta Tang, Caglar Girit, Zhao Hao, Michael C Martin, Alex Zettl, Michael F Crommie, Y Ron Shen, and Feng Wang. Direct observation of a widely tunable bandgap in bilayer graphene. *Nature*, 459(7248):820–823, 2009.

[8] K.S. Novoselov, Edward McCann, S.V. Morozov, Vladimir I. Fal'ko, M.I. Katsnelson, U. Zeitler, D. Jiang, F. Schedin, and A.K. Geim. Unconventional quantum hall effect and berry's phase of 2π in bilayer graphene. *Nature Physics*, 2(3):177–180, 2006.

[9] Kin Fai Mak, Chun Hung Lui, Jie Shan, and Tony F. Heinz. Observation of an electric-field-induced band gap in bilayer graphene by infrared spectroscopy. *Physical Review Letters*, 102 (25):256405, 2009.

[10] Li Yang, Jack Deslippe, Cheol-Hwan Park, Marvin L. Cohen, and Steven G. Louie. Excitonic effects on the optical response of graphene and bilayer graphene. *Physical Review Letters*, 103 (18):186802, 2009.

[11] Angela Kou, Benjamin Ezekiel Feldman, Andrei Joseph Levin, Bertrand I Halperin, Kenji Watanabe, Takashi Taniguchi, and Amir Yacoby. Electron-hole asymmetric integer and fractional quantum hall effect in bilayer graphene. *Science*, 345(6192):55–57, 2014.

[12] H. S. Wong, C. Durkan, and N. Chandrasekhar. Tailoring the local interaction between graphene layers in graphite at the atomic scale and above using scanning tunneling microscopy. *ACS Nano*, 3(11):3455–3462, 2009.

[13] K. Schouteden, A. Volodin, Z. Li, and C. Van Haesendonck. Atomically resolved moiré type superstructures in double-walled carbon nanotubes. *Carbon*, 61(0):379 – 385, 2013. ISSN 0008-6223.

[14] M.S. Dresselhaus, G. Dresselhaus, R. Saito, and A. Jorio. Raman spectroscopy of carbon nanotubes. *Physics Reports*, 409(2):47–99, 2005.

[15] K. Novoselov, A. Geim, S.V. Morozov, D. Jiang, Y. Zhang, S.V. Dubonos, I.V. Grigorieva, and A.A. Firsov. Electric field effect in atomically thin carbon films. *Science*, 306(5696):666–669, 2004.

[16] L. Wang, I. Meric, P.Y. Huang, Q. Gao, Y. Gao, H. Tran, T. Taniguchi, K. Watanabe, L.M. Campos, D.A. Muller, et al. One-dimensional electrical contact to a two-dimensional material. *Science*, 342(6158):614–617, 2013.

[17] Cristina Vallés, Carlos Drummond, Hassan Saadaoui, Clascidia A Furtado, Maoshuai He, Olivier Roubeau, Luca Ortolani, Marc Monthioux, and Alain Pénicaud. Solutions of negatively charged graphene sheets and ribbons. *Journal of the American Chemical Society*, 130(47):15802–15804, 2008.

[18] Amélie Catheline, Cristina Vallés, Carlos Drummond, Luca Ortolani, Vittorio Morandi, Massimo Marcaccio, Matteo Iurlo, Francesco Paolucci, and Alain Pénicaud. Graphene solutions. *Chemical Communications*, 47(19):5470–5472, 2011.

[19] Claire Berger, Zhimin Song, Tianbo Li, Xuebin Li, Asmerom Y Ogbazghi, Rui Feng, Zhenting Dai, Alexei N Marchenkov, Edward H Conrad, Phillip N First, et al. Ultrathin epitaxial graphite: 2d electron gas properties and a route toward graphene-based nanoelectronics. *The Journal of Physical Chemistry B*, 108(52):19912–19916, 2004.

[20] Claire Berger, Zhimin Song, Xuebin Li, Xiaosong Wu, Nate Brown, Cécile Naud, Didier Mayou, Tianbo Li, Joanna Hass, Alexei N. Marchenkov, et al. Electronic confinement and coherence in patterned epitaxial graphene. *Science*, 312(5777):1191–1196, 2006.

[21] Keun Soo Kim, Yue Zhao, Houk Jang, Sang Yoon Lee, Jong Min Kim, Kwang S Kim, Jong-Hyun Ahn, Philip Kim, Jae-Young Choi, and Byung Hee Hong. Large-scale pattern growth of graphene films for stretchable transparent electrodes. *Nature*, 457(7230):706–710, 2009.

[22] Johann Coraux, Alpha T. N'Diaye, Carsten Busse, and Thomas Michely. Structural coherency of graphene on ir (111). *Nano Letters*, 8(2):565–570, 2008.

[23] Alfonso Reina, Xiaoting Jia, John Ho, Daniel Nezich, Hyungbin Son, Vladimir Bulovic, Mildred S Dresselhaus, and Jing Kong. Layer area, few-layer graphene films on arbitrary substrates by chemical vapor deposition. *Nano Letters*, 9(8):3087–3087, 2009.

[24] Xuesong Li, Weiwei Cai, Jinho An, Seyoung Kim, Junghyo Nah, Dongxing Yang, Richard Piner, Aruna Velamakanni, Inhwa Jung, Emanuel Tutuc, et al. Large-area synthesis of high-quality and uniform graphene films on copper foils. *Science*, 324(5932):1312–1314, 2009.

[25] Zheng Han, Amina Kimouche, Dipankar Kalita, Adrien Allain, Hadi Arjmandi-Tash, Antoine Reserbat-Plantey, Laëtitia Marty, Sébastien Pairis, Valérie Reita, Nedjma Bendiab, et al. Homogeneous optical and electronic properties of graphene due to the suppression of multilayer patches during cvd on copper foils. *Advanced Functional Materials*, 24(7):964–970, 2014.

[26] Y Zhang, H Gu, and S Iijima. Single-wall carbon nanotubes synthesized by laser ablation in a nitrogen atmosphere. *Applied physics letters*, 73(26):3827–3829, 1998.

[27] C Journet, WK Maser, P Bernier, A Loiseau, M Lamy de La Chapelle, de la S Lefrant, P Deniard, R Lee, and JE Fischer. Large-scale production of single-walled carbon nanotubes by the electric-arc technique. *nature*, 388(6644):756–758, 1997.

[28] T. Yamada, T. Namai, K. Hata, D. Futaba, K. Mizuno, J. Fan, M. Yudasaka, M. Yumura, and S. Iijima. Size-selective growth of double-walled carbon nanotube forests from engineered iron catalysts. *Nature Nanotechnology*, 1(2):131–136, 2006.

[29] M. Endo, H. Muramatsu, T. Hayashi, Y.A. Kim, M. Terrones, and M.S. Dresselhaus. Nanotechnology: Buckypaper from coaxial nanotubes. *Nature*, 433(7025):476–476, 2005.

[30] B. Smith, M. Monthioux, and D. Luzzi. Encapsulated c60 in carbon nanotubes. *Nature*, 396:323–324, 1998.

[31] B. Smith, M. Monthioux, and D. Luzzi. Carbon nanotube encapsulated fullerenes: a unique class of hybrid materials. *Chemical Physics Letters*, 315(1):31–36, 1999.

[32] Emmanuel Flahaut, Revathi Bacsa, Alain Peigney, and Christophe Laurent. Gram-scale ccvd synthesis of double-walled carbon nanotubes. *Chemical Communications*, pages 1442–1443, 2003.

[33] P. R. Wallace. The band theory of graphite. *Phys. Rev.*, 71:622–634, 1947.

[34] M. Pashangpour and V. Ghaffari. Investigation of structural and electronic transport properties of graphene and graphane using maximally localized wannier functions. *Journal of Theoretical and Applied Physics*, 7(1):1–8, 2013.

[35] J.C. Slonczewski and P.R. Weiss. Band structure of graphite. *Physical Review*, 109(2):272, 1958.

[36] A. Castro Neto, F. Guinea, N. Peres, K. Novoselov, and A. Geim. The electronic properties of graphene. *Reviews of Modern Physics*, 81(1):109, 2009.

[37] R. Saito, G. Dresselhaus, M.S. Dresselhaus, et al. *Physical properties of carbon nanotubes*, volume 4. World Scientific, 1998.

[38] G. Samsonidze, A. Saito, D. Jorio, E. Pimenta, F. Souza, F. Grüneis, G. Dresselhaus, and M.S. Dresselhaus. The concept of cutting lines in carbon nanotube science. *Journal of Nanoscience and Nanotechnology*, 3(6):431–458, 2003.

[39] Z.M. Li, Z.K. Tang, H.J. Liu, N. Wang, C.T. Chan, R. Saito, S. Okada, G.D. Li, J.S. Chen, N. Nagasawa, et al. Polarized absorption spectra of single-walled 4 å carbon nanotubes aligned in channels of an alpo 4- 5 single crystal. *Physical Review Letters*, 87(12):127401, 2001.

[40] R. Saito, G. Dresselhaus, and M.S. Dresselhaus. Electronic structure of double-layer graphene tubules. *Journal of Applied Physics*, 73(2):494–500, 1993.

[41] S.D. Liang. Intrinsic properties of electronic structure in commensurate double-wall carbon nanotubes. *Physica B: Condensed Matter*, 352(1):305–311, 2004.

[42] V. Zólyomi, J. Koltai, Á. Rusznyák, J. Kürti, Á. Gali, F. Simon, H. Kuzmany, A. Szabados, and P.R. Surján. Intershell interaction in double walled carbon nanotubes: Charge transfer and orbital mixing. *Physical Review B*, 77(24):245403, 2008.

[43] W. Song, M. Ni, J. Lu, Z. Gao, S. Nagase, D. Yu, H. Ye, and X. Zhang. Electronic structures of semiconducting double-walled carbon nanotubes: Important effect of interlay interaction. *Chemical Physics Letters*, 414(4):429–433, 2005.

[44] G.W. Ho, Y.H. Ho, T.S. Li, C.P. Chang, and M.F. Lin. Band structure and absorption spectrum of double-walled zigzag carbon nanotubes in an electric field. *Carbon*, 44(11):2323–2329, 2006.

[45] Cristina E. Giusca, Yann Tison, Vlad Stolojan, Ewa Borowiak-Palen, and S Ravi P. Silva. Inner-tube chirality determination for double-walled carbon nanotubes by scanning tunneling microscopy. *Nano Letters*, 7(5):1232–1239, 2007.

[46] Andrea C. Ferrari and Denis M. Basko. Raman spectroscopy as a versatile tool for studying the properties of graphene. *Nature Nanotechnology*, 8(4):235–246, 2013.

[47] Stephanie Reich, Christian Thomsen, and Janina Maultzsch. *Carbon nanotubes: basic concepts and physical properties*. John Wiley & Sons, 2008.

[48] Kentaro Sato, Ahmad RT Nugraha, and Riichiro Saito. Excitonic effects on raman intensity of single wall carbon nanotubes. *e-Journal of Surface Science and Nanotechnology*, 8:358–361, 2010.

[49] A.R.T. Nugraha, R. Saito, K. Sato, P.T. Araujo, A. Jorio, and M.S. Dresselhaus. Dielectric constant model for environmental effects on the exciton energies of single wall carbon nanotubes. *Applied Physics Letters*, 97(9):091905, 2010.

[50] K. Sato, R. Saito, J. Jiang, G. Dresselhaus, and M.S. Dresselhaus. Discontinuity in the family pattern of single-wall carbon nanotubes. *Physical Review B*, 76(19):195446, 2007.

[51] Mildred S. Dresselhaus, Ado Jorio, Mario Hofmann, Gene Dresselhaus, and Riichiro Saito. Perspectives on carbon nanotubes and graphene raman spectroscopy. *Nano Letters*, 10(3):751–758, 2010.

[52] F Tuinstra and J Lo Koenig. Raman spectrum of graphite. *The Journal of Chemical Physics*, 53(3):1126–1130, 1970.

[53] Y.S. Lim, A. Nugraha, S.J. Cho, M.Y. Noh, E.J. Yoon, H. Liu, J.H. Kim, H. Telg, E. Haroz, G.D Sanders, et al. Ultrafast generation of fundamental and multiple-order phonon excitations in highly enriched (6,5) single-wall carbon nanotubes. *Nano Letters*, 14(3):1426–1432, 2014.

[54] Matthias Müller. *Electronic properties of functionalized carbon nanotubes*. Berlin, Techn. Univ., Diss., 2010, 2010.

[55] Hagen Telg. *Raman studies on individual nanotubes and nanotube ensembles vibrational properties and scattering efficiencies*. PhD thesis, Dissertation TU Berlin, 2009.

[56] Y. Yin, A.N. Vamivakas, A.G. Walsh, S.B. Cronin, M.S. Ünlü, B.B. Goldberg, and A.K. Swan. Optical determination of electron-phonon coupling in carbon nanotubes. *Physical Review Letters*, 98(3):037404, 2007.

[57] R.M. Martin and L.M. Falicov. Resonant raman scattering. In *Light scattering in Solids I*, pages 79–145. Springer, 1983.

[58] V.N. Popov and L. Henrard. Breathinglike phonon modes of multiwalled carbon nanotubes. *Physical Review B*, 65(23):235415, 2002.

[59] A. Jorio, A.G. Souza Filho, G. Dresselhaus, M.S. Dresselhaus, A.K. Swan, M.S. Ünlü, B.B. Goldberg, M..A Pimenta, J.H. Hafner, C.M. Lieber, et al. G-band resonant raman study of 62 isolated single-wall carbon nanotubes. *Physical Review B*, 65 (15):155412, 2002.

[60] Am M. Rao, P.C. Eklund, Shunji Bandow, A. Thess, and Richard E. Smalley. Evidence for charge transfer in doped carbon nanotube bundles from raman scattering. *Nature*, 388(6639): 257–259, 1997.

[61] Takashi Koretsune and Susumu Saito. Electronic structure of boron-doped carbon nanotubes. *Physical Review B*, 77(16): 165417, 2008.

[62] A. Das, S. Pisana, B. Chakraborty, S. Piscanec, S.K. Saha, U.V. Waghmare, K.S. Novoselov, H.R. Krishnamurthy, A.K. Geim, A.C. Ferrari, et al. Monitoring dopants by raman scattering in an electrochemically top-gated graphene transistor. *Nature Nanotechnology*, 3(4):210–215, 2008.

[63] Jun Yan, Yuanbo Zhang, Philip Kim, and Aron Pinczuk. Electric field effect tuning of electron-phonon coupling in graphene. *Physical Review Letters*, 98(16):166802, 2007.

[64] C. Stampfer, F. Molitor, D. Graf, K. Ensslin, A. Jungen, C. Hierold, and L. Wirtz. Raman imaging of doping domains in graphene on sio2. *Applied Physics Letters*, 91(24):241907, 2007.

[65] Simone Pisana, Michele Lazzeri, Cinzia Casiraghi, Kostya S Novoselov, Andre K Geim, Andrea C Ferrari, and Francesco Mauri. Breakdown of the adiabatic born–oppenheimer approximation in graphene. *Nature Materials*, 6(3):198–201, 2007.

[66] Anindya Das, A.K. Sood, Achutharao Govindaraj, A. Marco Saitta, Michele Lazzeri, Francesco Mauri, and C.N.R. Rao. Doping in carbon nanotubes probed by raman and transport measurements. *Physical Review Letters*, 99(13):136803, 2007.

[67] H. Farhat, H. Son, G. Samsonidze, S. Reich, M.S. Dresselhaus, and J. Kong. Phonon softening in individual metallic carbon nanotubes due to the kohn anomaly. *Physical Review Letters*, 99 (14):145506, 2007.

[68] Peter M. Rafailov, Janina Maultzsch, Christian Thomsen, Urszula Dettlaff-Weglikowska, and Siegmar Roth. Kohn anomaly and electron- phonon interaction at the k-derived point of the brillouin zone of metallic nanotubes. *Nano Letters*, 9(9):3343–3348, 2009.

[69] Adam W. Bushmaker, Vikram V. Deshpande, Scott Hsieh, Marc W. Bockrath, and Stephen B. Cronin. Direct observation of born-oppenheimer approximation breakdown in carbon nanotubes. *Nano Letters*, 9(2):607–611, 2009.

[70] Antoine Reserbat-Plantey. *Nanosystèmes graphitiques: cavités optiques ajustables et détection spectrale des contraintes dans un nanorésonateur mécanique*. PhD thesis, Université de Grenoble, 2012.

[71] Nicolas Caudal, A. Marco Saitta, Michele Lazzeri, and Francesco Mauri. Kohn anomalies and nonadiabaticity in doped carbon nanotubes. *Physical Review B*, 75(11):115423, 2007.

[72] Stefano Piscanec, Michele Lazzeri, John Robertson, Andrea C Ferrari, and Francesco Mauri. Optical phonons in carbon nanotubes: Kohn anomalies, peierls distortions, and dynamic effects. *Physical Review B*, 75(3):035427, 2007.

[73] S. Piscanec, M. Lazzeri, Francesco Mauri, A.C. Ferrari, and J. Robertson. Kohn anomalies and electron-phonon interactions in graphite. *Physical Review Letters*, 93(18):185503, 2004.

[74] L. Ci, Z. Zhou, X. Yan, D. Liu, H. Yuan, L. Song, J. Wang, Y. Gao, J. Zhou, W. Zhou, et al. Raman characterization and tunable growth of double-wall carbon nanotubes. *The Journal of Physical Chemistry B*, 107(34):8760–8764, 2003.

[75] Jinquan Wei, Bin Jiang, Xianfeng Zhang, Hongwei Zhu, and Dehai Wu. Raman study on double-walled carbon nanotubes. *Chemical Physics Letters*, 376(5):753–757, 2003.

[76] S. Bandow, G. Chen, G.U. Sumanasekera, R. Gupta, M. Yudasaka, S. Iijima, and P.C. Eklund. Diameter-selective resonant raman scattering in double-wall carbon nanotubes. *Physical Review B*, 66(7):075416, 2002.

[77] Shunji Bandow, Tatsuki Hiraoka, Takashi Yumura, Kaori Hirahara, Hisanori Shinohara, and Sumio Iijima. Raman scattering study on fullerene derived intermediates formed within single-wall carbon nanotube: From peapod to double-wall carbon nanotube. *Chemical Physics Letters*, 384(4):320–325, 2004.

[78] R. Pfeiffer, F. Simon, H. Kuzmany, V.N. Popov, V. Zolyomi, and J. Kürti. Tube–tube interaction in double-wall carbon nanotubes. *Physica Status Solidi B*, 243(13):3268–3272, 2006.

[79] R. Pfeiffer, F. Simon, H. Kuzmany, and V.N. Popov. Fine structure of the radial breathing mode of double-wall carbon nanotubes. *Physical Review B*, 72(16):161404, 2005.

[80] Kaihui Liu, Wenlong Wang, Muhong Wu, Fajun Xiao, Xiaoping Hong, Shaul Aloni, Xuedong Bai, Enge Wang, and Feng Wang. Intrinsic radial breathing oscillation in suspended single-walled carbon nanotubes. *Physical Review B*, 83(11):113404, 2011.

[81] Dmitry I. Levshov, Thierry Michel, Raul Arenal, Huy-Nam Tran, T.X. Than, Matthieu Paillet, Yu I. Yuzyuk, and J.-L. Sauvajol. Interlayer dependence of g-modes in semiconducting double-walled carbon nanotubes. *The Journal of Physical Chemistry C*, 119(40):23196–23202, 2015.

[82] D. Levshov, T. X. Than, R. Arenal, V. N. Popov, R. Parret, M. Paillet, V. Jourdain, A. A. Zahab, T. Michel, Yu. I. Yuzyuk, and J.-L. Sauvajol. Experimental evidence of a mechanical coupling between layers in an individual double-walled carbon nanotube. *Nano Letters*, 11(11):4800–4804, 2011.

[83] AG Souza Filho, N Kobayashi, J Jiang, A Grüneis, R Saito, SB Cronin, J Mendes Filho, Ge G Samsonidze, G Dresselhaus, and MS Dresselhaus. Strain-induced interference effects on the resonance raman cross section of carbon nanotubes. *Physical review letters*, 95(21):217403, 2005.

[84] S. Tans, A. Verschueren, and C. Dekker. Room-temperature transistor based on a single carbon nanotube. *Nature*, 393(6680): 49–52, 1998.

[85] R. Martel, T. Schmidt, H.R. Shea, T. Hertel, and Ph. Avouris. Single-and multi-wall carbon nanotube field-effect transistors. *Applied Physics Letters*, 73(17):2447–2449, 1998.

[86] Jean-Christophe Charlier, Xavier Blase, and Stephan Roche. Electronic and transport properties of nanotubes. *Rev. Mod. Phys.*, 79:677–732, May 2007.

[87] S. Heinze, J. Tersoff, R. Martel, V. Derycke, J. Appenzeller, and Ph. Avouris. Carbon nanotubes as schottky barrier transistors. *Physical Review Letters*, 89(10):106801, 2002.

[88] Zhihong Chen, Joerg Appenzeller, Joachim Knoch, Yu-ming Lin, and Phaedon Avouris. The role of metal-nanotube contact in the performance of carbon nanotube field-effect transistors. *Nano Letters*, 5(7):1497–1502, 2005.

[89] Thomas Rueckes, Kyoungha Kim, Ernesto Joselevich, Greg Y. Tseng, Chin-Li Cheung, and Charles M. Lieber. Carbon nanotube-based nonvolatile random access memory for molecular computing. *Science*, 289(5476):94–97, 2000.

[90] Max M. Shulaker, Gage Hills, Nishant Patil, Hai Wei, Hong-Yu Chen, H-S Philip Wong, and Subhasish Mitra. Carbon nanotube computer. *Nature*, 501(7468):526–530, 2013.

[91] Qing Cao, Shu-Jen Han, Jerry Tersoff, Aaron D Franklin, Yu Zhu, Zhen Zhang, George S Tulevski, Jianshi Tang, and Wilfried Haensch. End-bonded contacts for carbon nanotube transistors with low, size-independent resistance. *Science*, 350(6256): 68–72, 2015.

[92] Xuefeng Guo, Joshua P Small, Jennifer E Klare, Yiliang Wang, Meninder S Purewal, Iris W Tam, Byung Hee Hong, Robert Caldwell, Limin Huang, Stephen O'Brien, et al. Covalently bridging gaps in single-walled carbon nanotubes with conducting molecules. *Science*, 311(5759):356–359, 2006.

[93] C. Y. Sorgenfrei, S.and Chiu, Ruben L. Gonzalez Jr., Y.J. Yu, P. Kim, C. Nuckolls, and K. Shepard. Label-free single-molecule detection of dna-hybridization kinetics with a carbon nanotube field-effect transistor. *Nature Nanotechnology*, 6(2):126–132, 2011.

[94] Laëtitia Marty, Anne-Marie Bonnot, Aurore Bonhomme, Antonio Iaia, Cécile Naud, Emmanuel André, and Vincent Bouchiat. Self-assembly of carbon-nanotube-based single-electron memories. *Small*, 2(1):110–115, 2006.

[95] Marc A Kastner. The single-electron transistor. *Reviews of Modern Physics*, 64(3):849, 1992.

[96] Hermann Grabert and Michel H. Devoret. *Single charge tunneling: Coulomb blockade phenomena in nanostructures*, volume 294. Springer Science & Business Media, 2013.

[97] Günter Schmid. *Nanoparticles: from theory to application*. John Wiley & Sons, 2011.

[98] Subhadeep Datta. *Propriétés de transport électronique de nanotubes de carbone remplis de particules magnétiques*. PhD thesis, Grenoble, 2011.

[99] Leo P. Kouwenhoven, Charles M. Marcus, Paul L. McEuen, Seigo Tarucha, Robert M. Westervelt, and Ned S. Wingreen. Electron transport in quantum dots. In *Mesoscopic electron transport*, pages 105–214. Springer, 1997.

[100] Andreas Hirsch. Functionalization of single-walled carbon nanotubes. *Angewandte Chemie*, 41(11):1853–1859, 2002.

[101] Sharon Bahena-Garrido, Norihiro Shimoi, Daisuke Abe, Toshimasa Hojo, Yasumitsu Tanaka, and Kazuyuki Tohji. Plannar light source using a phosphor screen with single-walled carbon nanotubes as field emitters. *Review of Scientific Instruments*, 85 (10):104704, 2014.

[102] Michael S Arnold, Jeramy D Zimmerman, Christopher K Renshaw, Xin Xu, Richard R Lunt, Christine M Austin, and Stephen R Forrest. Broad spectral response using carbon nanotube/organic semiconductor/c60 photodetectors. *Nano letters*, 9(9):3354–3358, 2009.

[103] S Bhattacharyya, E Kymakis, and GAJ Amaratunga. Photovoltaic properties of dye functionalized single-wall carbon nanotube/conjugated polymer devices. *Chemistry of materials*, 16 (23):4819–4823, 2004.

[104] David S. Hecht, Robert J.A. Ramirez, Mikhail Briman, Erika Artukovic, Kelly S. Chichak, J. Fraser Stoddart, and George Grüner. Bioinspired detection of light using a porphyrin-sensitized single-wall nanotube field effect transistor. *Nano Letters*, 6(9):2031–2036, 2006.

[105] Julien Borghetti, Vincent Derycke, Stephane Lenfant, Pascale Chenevier, Arianna Filoramo, Marcelo Goffman, Dominique Vuillaume, and Jean-Philippe Bourgoin. Optoelectronic switch and memory devices based on polymer-functionalized carbon nanotube transistors. *Advanced Materials*, 18(19):2535, 2006.

[106] Clemens B. Winkelmann, Irina Ionica, Xavier Chevalier, Guy Royal, Christophe Bucher, and Vincent Bouchiat. Optical switching of porphyrin-coated silicon nanowire field effect transistors. *Nano Letters*, 7(6):1454–1458, 2007.

[107] Shao-Yu Chen, Yi-Ying Lu, Fu-Yu Shih, Po-Hsun Ho, Yang-Fang Chen, Chun-Wei Chen, Yit-Tsong Chen, and Wei-Hua Wang. Biologically inspired graphene-chlorophyll phototransistors with high gain. *Carbon*, 63:23–29, 2013.

[108] Raghu Chitta. Studies on self-assembled porphyrin-fullerene and porphyrin-carbon nanotube donor-acceptor conjugates. *PhD thesis*, 2007.

[109] Fabien Vialla, Cyrielle Roquelet, Benjamin Langlois, Géraud Delport, Silvia Morim Santos, Emmanuelle Deleporte, Philippe Roussignol, Claude Delalande, Christophe Voisin, and Jean-Sébastien Lauret. Chirality dependence of the absorption cross section of carbon nanotubes. *Physical Review Letters*, 111(13): 137402, 2013.

[110] Cyrielle Roquelet, Fabien Vialla, Carole Diederichs, Philippe Roussignol, Claude Delalande, Emmanuelle Deleporte, Jean-Sébastien Lauret, and Christophe Voisin. Local field effects in the energy transfer between a chromophore and a carbon nanotube: A single-nanocompound investigation. *ACS Nano*, 6(10): 8796–8802, 2012.

[111] Delphine Bouilly, Janie Cabana, Franc?ois Meunier, Maxime Desjardins-Carriere, François Lapointe, Philippe Gagnon, Francis L Larouche, Elyse Adam, Matthieu Paillet, and Richard Martel. Wall-selective probing of double-walled carbon nanotubes using covalent functionalization. *ACS Nano*, 5(6):4927–4934, 2011.

[112] F. Villalpando-Paez, L.G. Moura, C. Fantini, H. Muramatsu, T. Hayashi, Y.A. Kim, M. Endo, M. Terrones, M.A. Pimenta, and M.S. Dresselhaus. Tunable raman spectroscopy study of cvd and peapod-derived bundled and individual double-wall carbon nanotubes. *Physical Review B*, 82(15):155416, 2010.

[113] Morinobu Endo, Yoong Ahm Kim, Takuya Hayashi, Hiroyuki Muramatsu, Mauricio Terrones, Riichiro Saito, Federico Villalpando-Paez, Shin Grace Chou, and Mildred S. Dresselhaus. Nanotube coalescence-inducing mode: A novel vibrational mode in carbon systems. *Small*, 2(8-9):1031–1036, 2006.

[114] Julien Cambedouzou, J.-L. Sauvajol, Abdelali Rahmani, Emmanuel Flahaut, Alain Peigney, and Christophe Laurent. Raman spectroscopy of iodine-doped double-walled carbon nanotubes. *Physical Review B*, 69(23):235422, 2004.

[115] Wei Wu, Luis A Jauregui, Zhihua Su, Zhihong Liu, Jiming Bao, Yong P Chen, and Qingkai Yu. Growth of single crystal graphene arrays by locally controlling nucleation on polycrystalline cu using chemical vapor deposition. *Advanced Materials*, 23(42):4898–4903, 2011.

[116] Yu-Chuan Lin, Wenjing Zhang, Jing-Kai Huang, Keng-Ku Liu, Yi-Hsien Lee, Chi-Te Liang, Chih-Wei Chu, and Lain-Jong Li. Wafer-scale mos 2 thin layers prepared by moo 3 sulfurization. *Nanoscale*, 4(20):6637–6641, 2012.

[117] Yung-Chang Lin, Chun-Chieh Lu, Chao-Huei Yeh, Chuanhong Jin, Kazu Suenaga, and Po-Wen Chiu. Graphene annealing: how clean can it be? *Nano Letters*, 12(1):414–419, 2011.

[118] Adrien Allain, Zheng Han, and Vincent Bouchiat. Electrical control of the superconducting-to-insulating transition in graphene–metal hybrids. *Nature Materials*, 11(7):590–594, 2012.

[119] Kaihui Liu, Xiaoping Hong, Muhong Wu, Fajun Xiao, Wenlong Wang, Xuedong Bai, Joel W. Ager, Shaul Aloni, Alex Zettl, Enge Wang, et al. Quantum-coupled radial-breathing oscillations in double-walled carbon nanotubes. *Nature Communications*, 4: 1375, 2013.

[120] Merijntje S. Bronsgeest, Nedjma Bendiab, Shashank Mathur, Amina Kimouche, Harley T. Johnson, Johann Coraux, and Pascal Pochet. Strain relaxation in cvd graphene: wrinkling with shear lag. *Nano Letters*, 15(8):5098–5104, 2015.

[121] SDM Brown, A Jorio, P Corio, MS Dresselhaus, G Dresselhaus, R Saito, and K Kneipp. Origin of the breit-wigner-fano lineshape of the tangential g-band feature of metallic carbon nanotubes. *Physical Review B*, 63(15):155414, 2001.

[122] Walter Kohn. Theory of bloch electrons in a magnetic field: The effective hamiltonian. *Phys. Rev.*, 115:1460–1478, Sep 1959.

[123] Ali Javey, Jing Guo, Magnus Paulsson, Qian Wang, David Mann, Mark Lundstrom, and Hongjie Dai. High-field quasiballistic transport in short carbon nanotubes. *Physical Review Letters*, 92 (10):106804, 2004.

[124] Ji-Yong Park, Sami Rosenblatt, Yuval Yaish, Vera Sazonova, Hande Üstünel, Stephan Braig, TA Arias, Piet W Brouwer, and Paul L McEuen. Electron-phonon scattering in metallic single-walled carbon nanotubes. *Nano Letters*, 4(3):517–520, 2004.

[125] Eric Pop, David Mann, Jien Cao, Qian Wang, Kenneth Goodson, and Hongjie Dai. Negative differential conductance and hot phonons in suspended nanotube molecular wires. *Physical Review Letters*, 95(15):155505, 2005.

[126] S. Sapmaz, P. Jarillo-Herrero, Y.M. Blanter, C. Dekker, and H.S;J. Van Der Zant. Tunneling in suspended carbon nanotubes assisted by longitudinal phonons. *Physical Review Letters*, 96(2): 026801, 2006.

[127] Yuhei Miyauchi and Shigeo Maruyama. Identification of an excitonic phonon sideband by photoluminescence spectroscopy of single-walled carbon-13 nanotubes. *Physical Review B*, 74(3): 035415, 2006.

[128] Flávio Plentz, Henrique B. Ribeiro, Ado Jorio, Michael S. Strano, and Marcos A. Pimenta. Direct experimental evidence of exciton-phonon bound states in carbon nanotubes. *Physical Review Letters*, 95(24):247401, 2005.

[129] Hagen Telg, Erik H Hároz, Juan G Duque, Xiaomin Tu, Constantine Y Khripin, Jeffrey A Fagan, Ming Zheng, Junichiro Kono, and Stephen K Doorn. Diameter dependence of to phonon frequencies and the kohn anomaly in armchair single-wall carbon nanotubes. *Physical Review B*, 90(24):245422, 2014.

[130] J.C. Tsang, M. Freitag, V. Perebeinos, J. Liu, and Ph. Avouris. Doping and phonon renormalization in carbon nanotubes. *Nature Nanotechnology*, 2(11):725–730, 2007.

[131] Benjamin Hatting, Sebastian Heeg, Kenichi Ataka, Joachim Heberle, Frank Hennrich, Manfred M Kappes, Ralph Krupke, and Stephanie Reich. Fermi energy shift in deposited metallic nanotubes: A raman scattering study. *Physical Review B*, 87(16): 165442, 2013.

[132] Yang Wu, Janina Maultzsch, Ernst Knoesel, Bhupesh Chandra, Mingyuan Huang, Matthew Y. Sfeir, Louis E. Brus, J. Hone, and Tony F. Heinz. Variable electron-phonon coupling in isolated metallic carbon nanotubes observed by raman scattering. *Physical Review Letters*, 99(2):027402, 2007.

[133] F. Villalpando-Paez, H. Son, D. Nezich, Y. Hsieh, J. Kong, Y.A. Kim, D. Shimamoto, H; Muramatsu, T. Hayashi, M. Endo, et al. Raman spectroscopy study of isolated double-walled carbon nanotubes with different metallic and semiconducting configurations. *Nano Letters*, 8(11):3879–3886, 2008.

[134] E.B. Barros, H. Son, Ge. G. Samsonidze, A.G. Souza Filho, R. Saito, Y.A. Kim, H. Muramatsu, T. Hayashi, M. Endo, J. Kong, et al. Raman spectroscopy of double-walled carbon nanotubes treated with h_2so_4. *Physical Review B*, 76(4):045425, 2007.

[135] Shaoning Yuan, Qing Zhang, Yumeng You, Ze-Xiang Shen, Daisuke Shimamoto, and Morinobu Endo. Correlation between in situ raman scattering and electrical conductance for an individual double-walled carbon nanotube. *Nano Letters*, 9(1):383–387, 2008.

[136] A. Mohite, S. Chakraborty, P. Gopinath, G.U. Sumanasekera, and B.W. Alphenaar. Displacement current detection of photoconduction in carbon nanotubes. *Applied Physics Letters*, 86(6): 061114, 2005.

[137] Qingsheng Zeng, Sheng Wang, Leijing Yang, Zhenxing Wang, Tian Pei, Zhiyong Zhang, Lian-Mao Peng, Weiwei Zhou, Jie Liu, Weiya Zhou, et al. Carbon nanotube arrays based high-performance infrared photodetector [invited]. *Optical Materials Express*, 2(6):839–848, 2012.

[138] Paul W. Barone, Seunghyun Baik, Daniel A. Heller, and Michael S. Strano. Near-infrared optical sensors based on single-walled carbon nanotubes. *Nature Materials*, 4(1):86–92, 2005.

[139] Hongzhi Chen, Ning Xi, King WC Lai, Carmen KM Fung, and Ruiguo Yang. Development of infrared detectors using single carbon-nanotube-based field-effect transistors. *Nanotechnology, IEEE Transactions on*, 9(5):582–589, 2010.

[140] Leijing Yang, Sheng Wang, Qingsheng Zeng, Zhiyong Zhang, and Lian-Mao Peng. Carbon nanotube photoelectronic and photovoltaic devices and their applications in infrared detection. *Small*, 9(8):1225–1236, 2013.

[141] Sébastien Nanot, Aron W Cummings, Cary L Pint, Akira Ikeuchi, Takafumi Akiho, Kazuhisa Sueoka, Robert H Hauge, François Léonard, and Junichiro Kono. Broadband, polarization-sensitive photodetector based on optically-thick films of macroscopically long, dense, and aligned carbon nanotubes. *Scientific Reports*, 3, 2013.

[142] Dominick J. Bindl, Meng-Yin Wu, Frederick C. Prehn, and Michael S. Arnold. Efficiently harvesting excitons from electronic type-controlled semiconducting carbon nanotube films. *Nano Letters*, 11(2):455–460, 2010.

[143] Mingjie Yang, Jia-Lin Zhu, Wei Liu, and Jia-Lin Sun. Novel photodetectors based on double-walled carbon nanotube film/tio2 nanotube array heterodimensional contacts. *Nano Research*, 4(9): 901–907, 2011.

[144] Jean Pierre Sauvage, Jean Paul Collin, Jean Claude Chambron, Stephane Guillerez, Christophe Coudret, Vincenzo Balzani, Francesco Barigelletti, Luisa De Cola, and Lucia Flamigni. Ruthenium (ii) and osmium (ii) bis (terpyridine) complexes in covalently-linked multicomponent systems: synthesis, electrochemical behavior, absorption spectra, and photochemical and photophysical properties. *Chemical Reviews*, 94(4):993–1019, 1994.

[145] Mauro Maestri, Nicola Armaroli, Vincenzo Balzani, Edwin C. Constable, and Alexander M.W. Cargill Thompson. Complexes of the ruthenium (ii)-2, 2′: 6′, 2″-terpyridine family. effect of electron-accepting and-donating substituents on the photophysical and electrochemical properties. *Inorganic Chemistry*, 34 (10):2759–2767, 1995.

[146] Ulrich S. Schubert, Harald Hofmeier, and George R. Newkome. *Modern terpyridine chemistry*. John Wiley & Sons, 2006.

[147] Abdelkrim El-Ghayoury, Albertus P.H.J. Schenning, Paul A. van Hal, Christian H. Weidl, Joost L.J. van Dongen, René A.J. Janssen, Ulrich S. Schubert, and E.W. Meijer. Metallosupramolecular oligo (p-phenylene vinylene)/[60] fullerene architectures: towards functional materials. *Thin Solid Films*, 403: 97–101, 2002.

[148] Davide Bonifazi, Olivier Enger, and François Diederich. Supramolecular [60] fullerene chemistry on surfaces. *Chemical Society Reviews*, 36(2):390–414, 2007.

[149] Shungang Song, Yuhua Xue, Lianfang Feng, Hany Elbatal, Pingshan Wang, Charles N. Moorefield, George R. Newkome, and Liming Dai. Reversible self-assembly of terpyridine-functionalized graphene oxide for energy conversion. *Angewandte Chemie*, 53(5):1415–1419, 2014.

[150] G.D. Sharma, D. Daphnomili, K.S.V. Gupta, T. Gayathri, S.P. Singh, P.A. Angaridis, T.N. Kitsopoulos, D. Tasis, and A.G. Coutsolelos. Enhancement of power conversion efficiency of dye-sensitized solar cells by co-sensitization of zinc-porphyrin and thiocyanate-free ruthenium (ii)-terpyridine dyes and graphene modified tio 2 photoanode. *RSC Advances*, 3(44): 22412–22420, 2013.

[151] M.A. Kamyabi, O. Narimani, and H. Hosseini Monfared. Electrocatalytic oxidation of hydrazine using glassy carbon electrode modified with carbon nanotube and terpyridine manganese (ii) complex. *Journal of Electroanalytical Chemistry*, 644 (1):67–73, 2010.

[152] MS Fuhrer, BM Kim, T Dürkop, and T Brintlinger. High-mobility nanotube transistor memory. *Nano Letters*, 2(7):755–759, 2002.

[153] Jia Chen, Christian Klinke, Ali Afzali, and Phaedon Avouris. Self-aligned carbon nanotube transistors with charge transfer doping. *Applied Physics Letters*, 86(12):123108, 2005.

[154] Mark E. Roberts, Melburne C. LeMieux, and Zhenan Bao. Sorted and aligned single-walled carbon nanotube networks for transistor-based aqueous chemical sensors. *Acs Nano*, 3(10): 3287–3293, 2009.

[155] Francesco Barigelletti, Lucia Flamigni, Vincenzo Balzani, Jean-Paul Collin, Jean-Pierre Sauvage, Angelique Sour, Edwin C. Constable, and Alexander MW Cargill Thompson. Rigid rod-like dinuclear ru (ii)/os (ii) terpyridine-type complexes. electrochemical behavior, absorption spectra, luminescence properties, and electronic energy transfer through phenylene bridges. *Journal of the American Chemical Society*, 116(17):7692–7699, 1994.

[156] Jiwoong Park, Abhay N. Pasupathy, Jonas I. Goldsmith, Connie Chang, Yuval Yaish, Jason R. Petta, Marie Rinkoski, James P. Sethna, Héctor D. Abruña, Paul L. McEuen, et al. Coulomb blockade and the kondo effect in single-atom transistors. *Nature*, 417(6890):722–725, 2002.

[157] Marc Beley, Jean-Paul Collin, Jean-Pierre Sauvage, Hideki Sugihara, Francine Heisel, and Albert Miehé. Photophysical and photochemical properties of ruthenium and osmium complexes with substituted terpyridines. *Journal of the Chemical Society, Dalton Transactions*, 11:3157–3159, 1991.

[158] Gabriella Albano, Vincenzo Balzani, Edwin C Constable, Mauro Maestri, and Diane R Smith. Photoinduced processes in 4′-(9-anthryl)-2, 2′: 6′, 2 ″-terpyridine, its protonated forms and zn (ii), ru (ii) and os (ii) complexes. *Inorganica Chimica Acta*, 277(2): 225–231, 1998.

[159] Andrew C. Benniston, Anthony Harriman, Peiyi Li, and Craig A. Sams. Temperature-induced switching of the mechanism for intramolecular energy transfer in a 2, 2′: 6′, 2″-terpyridine-based ru (ii)-os (ii) trinuclear array. *Journal of the American Chemical Society*, 127(8):2553–2564, 2005.

[160] Edwin C. Constable, Robyn W. Handel, Catherine E. Housecroft, Angeles Farràn Morales, Lucia Flamigni, and Francesco Barigelletti. Fine tuning of the photoinduced energy transfer rate in trinuclear ru/os 2, 2′: 6′, 2 ″-terpyridine complexes through structural modification of the periphery. *Dalton Transactions*, 7:1220–1222, 2003.

[161] Ronald Siebert, Andreas Winter, Ulrich S Schubert, Benjamin Dietzek, and Jürgen Popp. The molecular mechanism of dual emission in terpyridine transition metal complexes-ultrafast investigations of photoinduced dynamics. *Physical Chemistry Chemical Physics*, 13(4):1606–1617, 2011.

[162] Etienne Baranoff, Jean-Paul Collin, Lucia Flamigni, and Jean-Pierre Sauvage. From ruthenium (ii) to iridium (iii): 15 years of triads based on bis-terpyridine complexes. *Chemical Society Reviews*, 33(3):147–155, 2004.

[163] Dong-Cheol Jeong, Jiyoung Lee, Yunmi Lee, Chinnadurai Satheeshkumar, and Changsik Song. Enhancement of photoinduced electron transfer in self-assembled polymer films using mixed metal–terpyridine complexes. *Macromolecules*, 48(6): 1621–1626, 2015.

[164] Chi Ho Li, Alan Man Ching Ng, Chris SK Mak, Aleksandra B. Djuris?ic?, and Wai Kin Chan. Ruthenium complex containing block copolymer for the enhancement of carbon nanotube photoconductivity. *ACS Applied Materials & Interfaces*, 4(1):74–80, 2011.

[165] Yoonmi Lee, Hyun Jae Song, Hyeon Suk Shin, Hyun Joon Shin, and Hee Cheul Choi. Spontaneous formation of transition-metal nanoparticles on single-walled carbon nanotubes anchored with conjugated molecules. *Small*, 1(10):975–979, 2005.

[166] Lian C.T. Shoute and Glen R. Loppnow. Excited-state metal-to-ligand charge transfer dynamics of a ruthenium (ii) dye in solution and adsorbed on tio2 nanoparticles from resonance raman spectroscopy. *Journal of the American Chemical Society*, 125 (50):15636–15646, 2003.

[167] Manuel Lopes, Andrea Candini, Matias Urdampilleta, Antoine Reserbat-Plantey, Valerio Bellini, Svetlana Klyatskaya, Laëtitia Marty, Mario Ruben, Marco Affronte, Wolfgang Wernsdorfer, et al. Surface-enhanced raman signal for terbium single-molecule magnets grafted on graphene. *ACS Nano*, 4(12):7531–7537, 2010.

[168] Qingkai Yu, Luis A Jauregui, Wei Wu, Robert Colby, Jifa Tian, Zhihua Su, Helin Cao, Zhihong Liu, Deepak Pandey, Dongguang Wei, et al. Control and characterization of individual grains and grain boundaries in graphene grown by chemical vapour deposition. *Nature Materials*, 10(6):443–449, 2011.

[169] Zheng Han. *Graphène pour la nanoélectronique: de la croissance CVD jusqu'à la supraconductivité de proximité à deux dimensions*. PhD thesis, Grenoble, 2013.

[170] Hua Xu, Yabin Chen, Weigao Xu, Haoli Zhang, Jing Kong, Mildred S. Dresselhaus, and Jin Zhang. Modulating the charge-transfer enhancement in gers using an electrical field under vacuum and an n/p-doping atmosphere. *Small*, 7(20):2945–2952, 2011.

[171] Hany Elbatal. *Terpyridine-based metallo-supramolecular architectures: From structure to function*. PhD thesis, University of Akron, 2013.

[172] H.-C. Chiu, G.L. Klimchitskaya, V.N. Marachevsky, V.M. Mostepanenko, and U. Mohideen. Demonstration of the asymmetric lateral casimir force between corrugated surfaces in the nonadditive regime. *Physical Review B*, 80(12):121402, 2009.

[173] Jakob Zabel, Rahul R. Nair, Anna Ott, Thanasis Georgiou, Andre K. Geim, Kostya S. Novoselov, and Cinzia Casiraghi. Raman spectroscopy of graphene and bilayer under biaxial strain: bubbles and balloons. *Nano Letters*, 12(2):617–621, 2012.

[174] C. Casiraghi, S. Pisana, K.S. Novoselov, A.K. Geim, and A.C. Ferrari. Raman fingerprint of charged impurities in graphene. *Applied Physics Letters*, 91(23):233108, 2007.

[175] D.M. Basko, S. Piscanec, and A.C. Ferrari. Electron-electron interactions and doping dependence of the two-phonon raman intensity in graphene. *Physical Review B*, 80(16):165413, 2009.

[176] Rakesh Voggu, Barun Das, Chandra Sekhar Rout, and C.N.R. Rao. Effects of charge transfer interaction of graphene with electron donor and acceptor molecules examined using raman spectroscopy and cognate techniques. *Journal of Physics: Condensed Matter*, 20(47):472204, 2008.

[177] Henry Medina, Yung-Chang Lin, Dirk Obergfell, and Po-Wen Chiu. Tuning of charge densities in graphene by molecule doping. *Advanced Functional Materials*, 21(14):2687–2692, 2011.

[178] Shengxi Huang, Xi Ling, Liangbo Liang, Yi Song, Wenjing Fang, Jin Zhang, Jing Kong, Vincent Meunier, and Mildred S. Dresselhaus. Molecular selectivity of graphene-enhanced raman scattering. *Nano Letters*, 15(5):2892–2901, 2015.

[179] M.S. Dresselhaus, G. Dresselhaus, and A. Jorio Filho. Raman spectroscopy on isolated single wall carbon nanotubes. *Carbon*, 40:2043–2061, 2002.

[180] Felix Herziger, Matteo Calandra, Paola Gava, Patrick May, Michele Lazzeri, Francesco Mauri, and Janina Maultzsch. Two-dimensional analysis of the double-resonant 2d raman mode in bilayer graphene. *Physical Review Letters*, 113(18):187401, 2014.

[181] Jing Kong, Nathan R. Franklin, Chongwu Zhou, Michael G. Chapline, Shu Peng, Kyeongjae Cho, and Hongjie Dai. Nanotube molecular wires as chemical sensors. *Science*, 287(5453): 622–625, 2000.

[182] Marc Bockrath, J. Hone, A. Zettl, Paul L; McEuen, Andrew G. Rinzler, and Richard E; Smalley. Chemical doping of individual semiconducting carbon-nanotube ropes. *Physical Review B*, 61 (16):R10606, 2000.

[183] Keith Bradley, Mikhail Briman, Alexander Star, and George Grüner. Charge transfer from adsorbed proteins. *Nano Letters*, 4(2):253–256, 2004.

[184] Christian Klinke, Jia Chen, Ali Afzali, and Phaedon Avouris. Charge transfer induced polarity switching in carbon nanotube transistors. *Nano Letters*, 5(3):555–558, 2005.

[185] Bo Ram Kang, Woo Jong Yu, Ki Kang Kim, Hyeon Ki Park, Soo Min Kim, Yongjin Park, Gunn Kim, Hyeon-Jin Shin, Un Jeong Kim, Eun-Hong Lee, et al. Restorable type conversion of carbon nanotube transistor using pyrolytically controlled antioxidizing photosynthesis coenzyme. *Advanced Functional Materials*, 19(16):2553–2559, 2009.

[186] Christian Klinke, Ali Afzali, and Phaedon Avouris. Interaction of solid organic acids with carbon nanotube field effect transistors. *Chemical Physics Letters*, 430(1):75–79, 2006.

[187] Annette Wurl, Sebastian Goossen, David Canevet, Marc Salle, Emilio M Perez, Nazario Martin, and Christian Klinke. Supramolecular interaction of single-walled carbon nanotubes with a functional ttf-based mediator probed by field-effect transistor devices. *The Journal of Physical Chemistry C*, 116(37):20062–20066, 2012.

[188] Yu-Ming Lin, Joerg Appenzeller, Zhihong Chen, Zhi-Gang Chen, Hui-Ming Cheng, and Phaedon Avouris. High-performance dual-gate carbon nanotube fets with 40-nm gate length. *Electron Device Letters, IEEE*, 26(11):823–825, 2005.

[189] Shahal Ilani, Luke AK Donev, Mark Kindermann, and Paul L McEuen. Measurement of the quantum capacitance of interacting electrons in carbon nanotubes. *Nature Physics*, 2(10):687–691, 2006.

[190] C. Fantini, A. Jorio, M. Souza, M.S. Strano, M.S. Dresselhaus, and M.A. Pimenta. Optical transition energies for carbon nanotubes from resonant raman spectroscopy: Environment and temperature effects. *Physical Review Letters*, 93(14):147406, 2004.

[191] M.S. Dresselhaus, G. Dresselhaus, A. Jorio, A.G. Souza Filho, and R. Saito. Raman spectroscopy on isolated single wall carbon nanotubes. *Carbon*, 40(12):2043–2061, 2002.

[192] A. Jorio, A.G. Souza Filho, G. Dresselhaus, M.S. Dresselhaus, R. Saito, J.H. Hafner, C.M. Lieber, F.M. Matinaga, M.S.S. Dantas, and M.A. Pimenta. Joint density of electronic states for one isolated single-wall carbon nanotube studied by resonant raman scattering. *Physical Review B*, 63(24):245416, 2001.

[193] C. Fantini, A. Jorio, A.P. Santos, V.S.T. Peressinotto, and M.A. Pimenta. Characterization of dna-wrapped carbon nanotubes by resonance raman and optical absorption spectroscopies. *Chemical Physics Letters*, 439(1):138–142, 2007.

[194] A. Jorio, M.A. Pimenta, A.G. Souza Filho, R; Saito, G; Dresselhaus, and M.S. Dresselhaus. Characterizing carbon nanotube samples with resonance raman scattering. *New Journal of Physics*, 5(1):139, 2003.

[195] S.B. Cronin, A.K. Swan, M.S. Ünlü, B.B. Goldberg, M.S. Dresselhaus, and M. Tinkham. Measuring the uniaxial strain of individual single-wall carbon nanotubes: resonance raman spectra of atomic-force-microscope modified single-wall nanotubes. *Physical Review Letters*, 93(16):167401, 2004.

[196] M.D. Frogley, Q. Zhao, and H.D. Wagner. Polarized resonance raman spectroscopy of single-wall carbon nanotubes within a polymer under strain. *Physical review B*, 65(11):113413, 2002.

[197] Rajay Kumar and Stephen B Cronin. Raman scattering of carbon nanotube bundles under axial strain and strain-induced debundling. *Physical Review B*, 75(15):155421, 2007.

[198] U.D. Venkateswaran, A.M. Rao, E. Richter, M. Menon, A. Rinzler, R.E. Smalley, and P.C. Eklund. Probing the single-wall carbon nanotube bundle: Raman scattering under high pressure. *Physical Review B*, 59(16):10928, 1999.

[199] Pascal Puech, Sebastien Nanot, Bertrand Raquet, Jean-Marc Broto, Marius Millot, Abdul Waheed Anwar, Emmanuel Flahaut, and Wolfgang Bacsa. Comparative raman spectroscopy of individual and bundled double wall carbon nanotubes. *Physica Status Solidi (b)*, 248(4):974–979, 2011.

[200] Vincenzo Balzani, Alberto Credi, and Margherita Venturi. Molecular devices and machines. *Nano Today*, 2(2):18–25, 2007.

[201] Joakim Andréasson, Stephen D. Straight, Subhajit Bandyopadhyay, Reginald H. Mitchell, Thomas A. Moore, Ana L. Moore, and Devens Gust. A molecule-based 1: 2 digital demultiplexer. *The Journal of Physical Chemistry C*, 111(38):14274–14278, 2007.

[202] Reginald H. Mitchell, Rui Zhang, David J. Berg, Brendan Twamley, and Richard Vaughan Williams. Measuring aromaticity with the dimethyldihydropyrene ring current probe. experimental and computational studies of the fulvenes and the strongly antiaromatic cyclopentadienone reveal large mills-nixon-type bond localization effects. synthesis of fulvene-fused dihydropyrenes. *Journal of the American Chemical Society*, 131(1): 189–199, 2008.

[203] Satoshi Muratsugu, Shoko Kume, and Hiroshi Nishihara. Redox-assisted ring closing reaction of the photogenerated cyclophanediene form of bis (ferrocenyl) dimethyldihydropyrene with interferrocene electronic communication switching. *Journal of the American Chemical Society*, 130(23):7204–7205, 2008.

[204] Diego Roldan, Veerabhadrarao Kaliginedi, Saioa Cobo, Viliam Kolivoska, Christophe Bucher, Wenjing Hong, Guy Royal, and Thomas Wandlowski. Charge transport in photoswitchable dimethyldihydropyrene-type single-molecule junctions. *Journal of the American Chemical Society*, 135(16):5974–5977, 2013.

[205] Hua Xu, Yabin Chen, Weigao Xu, Haoli Zhang, Jing Kong, Mildred S. Dresselhaus, and Jin Zhang. Modulating the charge-transfer enhancement in GERS using an electrical field under vacuum and an n/p-doping atmosphere. *Small*, 7(20):2945–2952, 2011. ISSN 16136810.

[206] Mengning Ding, Dan C Sorescu, and Alexander Star. Photoinduced charge transfer and acetone sensitivity of single-walled carbon nanotube–titanium dioxide hybrids. *Journal of the American Chemical Society*, 135(24):9015–9022, 2013.

[207] Alina Chanaewa, Beatriz H Juárez, Horst Weller, and Christian Klinke. Oxygen and light sensitive field-effect transistors based on zno nanoparticles attached to individual double-walled carbon nanotubes. *Nanoscale*, 4(1):251–256, 2012.

[208] Konstantin Iakoubovskii, Nobutsugu Minami, Taro Ueno, Said Kazaoui, and Hiromichi Kataura. Optical characterization of double-wall carbon nanotubes: Evidence for inner tube shielding. *The Journal of Physical Chemistry C*, 112(30):11194–11198, 2008.

[209] Gugang Chen, S. Bandow, E.R. Margine, C. Nisoli, A.N. Kolmogorov, Vincent H. Crespi, R. Gupta, G.U. Sumanasekera, S. Iijima, and P.C. Eklund. Chemically doped double-walled carbon nanotubes: cylindrical molecular capacitors. *Physical Review Letters*, 90(25):257403, 2003.

[210] H. Rauf, T. Pichler, R. Pfeiffer, F. Simon, H. Kuzmany, and V.N. Popov. Detailed analysis of the raman response of n-doped double-wall carbon nanotubes. *Physical Review B*, 74(23):235419, 2006.

[211] Jannik C. Meyer, Matthieu Paillet, Thierry Michel, Alain Moréac, Anita Neumann, Georg S. Duesberg, Siegmar Roth, and Jean-Louis Sauvajol. Raman modes of index-identified free-standing single-walled carbon nanotubes. *Physical Review Letters*, 95(21):217401, 2005.

[212] M. Canonico, G.B. Adams, C. Poweleit, J. Menendez, J.B. Page, Gari Harris, H.P. van der Meulen, J.M. Calleja, and J. Rubio. Characterization of carbon nanotubes using raman excitation profiles. *Physical Review B*, 65(20):201402, 2002.

[213] Anne Débarre, Mathias Kobylko, Anne-Marie Bonnot, A. Richard, V.N. Popov, Luc Henrard, and Mathieu Kociak. Electronic and mechanical coupling of carbon nanotubes:

A tunable resonant raman study of systems with known structures. *Physical Review Letters*, 101(19):197403, 2008.

[214] Martin Kalbac, Alexander A. Green, Mark C. Hersam, and Ladislav Kavan. Probing charge transfer between shells of double-walled carbon nanotubes sorted by outer-wall electronic type. *Chemistry-A European Journal*, 17(35):9806–9815, 2011.

[215] O.N. Torrens, D.E. Milkie, M. Zheng, and J.M. Kikkawa. Photoluminescence from intertube carrier migration in single-walled carbon nanotube bundles. *Nano Letters*, 6(12):2864–2867, 2006.

[216] Takeshi Koyama, Yuki Asada, Naoki Hikosaka, Yasumitsu Miyata, Hisanori Shinohara, and Arao Nakamura. Ultrafast exciton energy transfer between nanoscale coaxial cylinders: Intertube transfer and luminescence quenching in double-walled carbon nanotubes. *ACS Nano*, 5(7):5881–5887, 2011.

[217] Karl M. Kadish. *The porphyrin handbook*. Elsevier, 1999.

[218] Aswani Yella, Hsuan-Wei Lee, Hoi Nok Tsao, Chenyi Yi, Aravind Kumar Chandiran, Md Khaja Nazeeruddin, Eric Wei-Guang Diau, Chen-Yu Yeh, Shaik M. Zakeeruddin, and Michael Grätzel. Porphyrin-sensitized solar cells with cobalt (ii/iii)–based redox electrolyte exceed 12 percent efficiency. *Science*, 334(6056):629–634, 2011.

[219] Cyrielle Roquelet, Damien Garrot, Jean-Sébastien Lauret, Christophe Voisin, Valérie Alain-Rizzo, Ph. Roussignol, J.A. Delaire, and Emmanuelle Deleporte. Quantum efficiency of energy transfer in noncovalent carbon nanotube/porphyrin compounds. *Applied Physics Letters*, 97(14):141918, 2010.

[220] Gurvan Magadur, Jean-Sébastien Lauret, Valérie Alain-Rizzo, Christophe Voisin, Philippe Roussignol, Emmanuelle Deleporte, and Jacques A. Delaire. Excitation transfer in functionalized carbon nanotubes. *ChemPhysChem*, 9(9):1250–1253, 2008.

[221] Damien Garrot, Benjamin Langlois, Cyrielle Roquelet, Thierry Michel, Philippe Roussignol, Claude Delalande, Emmanuelle Deleporte, Jean-Sébastien Lauret, and Christophe Voisin. Time-resolved investigation of excitation energy transfer in carbon nanotube–porphyrin compounds. *The Journal of Physical Chemistry C*, 115(47):23283–23292, 2011.

[222] K. S. Suslick, N. A. Rakow, M. E. Kosal, and J. H. Chou. The materials chemistry of porphyrins and metalloporphyrins. *Journal of Porphyrins and Phthalocyanines*, 4(4):407–413, 2000. ISSN 10884246.

[223] Xiao Yuan Li, Roman S. Czernuszewicz, James R. Kincaid, Y. Oliver Su, and Thomas G. Spiro. Consistent porphyrin force field. 1. normal-mode analysis for nickel porphine and nickel

tetraphenylporphine from resonance raman and infrared spectra and isotope shifts. *Journal of Physical Chemistry*, 94(1):31–47, 1990.

[224] Martin Gouterman. Spectra of porphyrins. *Journal of Molecular Spectroscopy*, 6:138–163, 1961.

[225] Diane Marsh and Larry Mink. Microscale synthesis and electronic absorption spectroscopy of tetraphenylporphyrin h2 (tpp) and metalloporphyrins znii (tpp) and niii (tpp). *Journal of Chemical Education*, 73(12):1188, 1996.

[226] Anthony Harriman. Luminescence of porphyrins and metalloporphyrins. part 1.¡ a zinc (ii), nickel (ii) and manganese (ii) porphyrins. *Journal of the Chemical Society, Faraday Transactions 1: Physical Chemistry in Condensed Phases*, 76:1978–1985, 1980.

[227] Dae Hong Jeong, Min-Chul Yoon, Sung Moon Jang, Dongho Kim, Dae Won Cho, Naoya Yoshida, Naoki Aratani, and Atsuhiro Osuka. Resonance raman spectroscopic investigation of directly linked zinc (ii) porphyrin linear arrays. *The Journal of Physical Chemistry A*, 106(10):2359–2368, 2002.

[228] Boris Minaev and Mikael Lindgren. Vibration and fluorescence spectra of porphyrin-coredbis (methylol)-propionic acid dendrimers. *Sensors*, 9(3):1937–1966, 2009.

[229] Hisao Ishii, Kiyoshi Sugiyama, Eisuke Ito, and Kazuhiko Seki. Energy level alignment and interfacial electronic structures at organic/metal and organic/organic interfaces. *Advanced Materials*, 11(8):605–625, 1999.

[230] Georg Heimel, Lorenz Romaner, Egbert Zojer, and Jean-Luc Brédas. Toward control of the metal-organic interfacial electronic structure in molecular electronics: A first-principles study on self-assembled monolayers of π-conjugated molecules on noble metals. *Nano Letters*, 7(4):932–940, 2007.

[231] S. Narioka, H. Ishii, D. Yoshimura, M. Sei, Y. Ouchi, K. Seki, S. Hasegawa, T. Miyazaki, Y. Harima, and K. Yamashita. The electronic structure and energy level alignment of porphyrin/metal interfaces studied by ultraviolet photoelectron spectroscopy. *Applied Physics Letters*, 67(13):1899–1901, 1995.

[232] Young-Jun Yu, Yue Zhao, Sunmin Ryu, Louis E. Brus, Kwang S. Kim, and Philip Kim. Tuning the graphene work function by electric field effect. *Nano Letters*, 9(10):3430–3434, 2009.

[233] P. Blake, E. W. Hill, A. H. Castro Neto, K. S. Novoselov, D. Jiang, R. Yang, T. J. Booth, and A. K. Geim. Making graphene visible. *Applied Physics Letters*, 91(6):063124, 2007. ISSN 00036951.

[234] Chuan Li, Katsuyoshi Komatsu, G Clave, S Campidelli, A Filoramo, S Gueron, and H Bouchiat. Unipolar supercurrent

through graphene grafted with pt-porphyrins: signature of gate-tunable magnetism. *arXiv preprint arXiv:1304.7089*, 2013.

[235] LM Malard, MA Pimenta, G Dresselhaus, and MS Dresselhaus. Raman spectroscopy in graphene. *Physics Reports*, 473(5):51–87, 2009.

[236] Ji Eun Lee, Gwanghyun Ahn, Jihye Shim, Young Sik Lee, and Sunmin Ryu. Optical separation of mechanical strain from charge doping in graphene. *Nature Communications*, 3:1024, 2012.

[237] Fei Ding, Hengxing Ji, Yonghai Chen, Andreas Herklotz, Kathrin Dörr, Yongfeng Mei, Armando Rastelli, and Oliver G Schmidt. Stretchable graphene: a close look at fundamental parameters through biaxial straining. *Nano Letters*, 10(9):3453–3458, 2010.

[238] H.S.S. Ramakrishna Matte, K.S. Subrahmanyam, K. Venkata Rao, Subi J. George, and CNR Rao. Quenching of fluorescence of aromatic molecules by graphene due to electron transfer. *Chemical Physics Letters*, 506(4):260–264, 2011.

[239] Ronghua Yang, Jianyu Jin, Yan Chen, Na Shao, Huaizhi Kang, Zeyu Xiao, Zhiwen Tang, Yanrong Wu, Zhi Zhu, and Weihong Tan. Carbon nanotube-quenched fluorescent oligonucleotides: probes that fluoresce upon hybridization. *Journal of the American Chemical Society*, 130(26):8351–8358, 2008.

[240] Libing Zhang, Tao Li, Bingling Li, Jing Li, and Erkang Wang. Carbon nanotube–dna hybrid fluorescent sensor for sensitive and selective detection of mercury (ii) ion. *Chem. Comm.*, 46(9): 1476–1478, 2010.

[241] Nozomi Nakayama-Ratchford, Sarunya Bangsaruntip, Xiaoming Sun, Kevin Welsher, and Hongjie Dai. Noncovalent functionalization of carbon nanotubes by fluorescein-polyethylene glycol: supramolecular conjugates with ph-dependent absorbance and fluorescence. *Journal of the American Chemical Society*, 129(9):2448–2449, 2007.

[242] B.C. Satishkumar, Leif O. Brown, Yuan Gao, Chun-Chih Wang, Hsing-Lin Wang, and Stephen K. Doorn. Reversible fluorescence quenching in carbon nanotubes for biomolecular sensing. *Nature Nanotechnology*, 2(9):560–564, 2007.

[243] Moonsub Shim, Taner Ozel, Anshu Gaur, and Congjun Wang. Insights on charge transfer doping and intrinsic phonon line shape of carbon nanotubes by simple polymer adsorption. *Journal of the American Chemical Society*, 128(23):7522–7530, 2006.

[244] Hootan Farhat, Ken-ichi Sasaki, Martin Kalbac, Mario Hofmann, Riichiro Saito, Mildred S. Dresselhaus, and Jing Kong. Softening of the radial breathing mode in metallic carbon nanotubes. *Physical Review Letters*, 102(12):126804, 2009.

[245] M. Muller, J. Maultzsch, D. Wunderlich, A. Hirsch, and C. Thomsen. Raman spectroscopy on chemically functionalized carbon nanotubes. *Physica Status Solidi B*, 244(11):4056–4059, 2007.

[246] J.S. Park, Y. Oyama, R. Saito, W. Izumida, J. Jiang, K. Sato, C. Fantini, A. Jorio, G. Dresselhaus, and M.S. Dresselhaus. Raman resonance window of single-wall carbon nanotubes. *Physical Review B*, 74(16):165414, 2006.

[247] Janie Cabana and Richard Martel. Probing the reversibility of sidewall functionalization using carbon nanotube transistors. *Journal of the American Chemical Society*, 129(8):2244–2245, 2007.

[248] Hock Guan Ong, Jun Wei Cheah, Lang Chen, Hosea TangTang, Yanping Xu, Bing Li, Hua Zhang, Lain-Jong Li, and Junling Wang. Charge injection at carbon nanotube-sio$_2$ interface. *Applied Physics Letters*, 93(9):093509, 2008.

[249] Keith Bradley, Jean-Christophe P. Gabriel, Mikhail Briman, Alexander Star, and George Grüner. Charge transfer from ammonia physisorbed on nanotubes. *Physical Review Letters*, 91 (21):218301, 2003.

[250] Liangbing Hu, Yanli Zhao, Koungmin Ryu, Chongwu Zhou, J Fraser Stoddart, and George Grüner. Light-induced charge transfer in pyrene/cdse-swnt hybrids. *Adv. Mat.*, 20:939, 2008.

[251] Laëtitia Marty. *Effet de champ et électronique à un électron dans des nanotubes de carbone auto-assemblés par CVD assisté d'un filament chaud*. PhD thesis, Grenoble 1, 2004.

[252] K. Nakazato, R.J. Blaikie, and H. Ahmed. Single-electron memory. *Journal of Applied Physics*, 75(10):5123–5134, 1994.

[253] Yumeng Shi, Xiaochen Dong, Hosea Tantang, Cheng-Hui Weng, Fuming Chen, Chunwei Lee, Keke Zhang, Yuan Chen, Junling Wang, and Lain-Jong Li. Photoconductivity from carbon nanotube transistors activated by photosensitive polymers. *The Journal of Physical Chemistry C*, 112(46):18201–18206, 2008.

[254] Xi Ling, L.G. Moura, Marcos A. Pimenta, and Jin Zhang. Charge-transfer mechanism in graphene-enhanced raman scattering. *The Journal of Physical Chemistry C*, 116(47):25112–25118, 2012.

[255] Xi Ling, Liming Xie, Yuan Fang, Hua Xu, Haoli Zhang, Jing Kong, Mildred S. Dresselhaus, Jin Zhang, and Zhongfan Liu. Can graphene be used as a substrate for raman enhancement? *Nano Letters*, 10(2):553–561, 2009.

[256] V.I. Arkhipov, Paul Heremans, E.V. Emelianova, and Heinz Baessler. Effect of doping on the density-of-states distribution and carrier hopping in disordered organic semiconductors. *Physical Review B*, 71(4):045214, 2005.

[257] Soumya Dutta and K.S. Narayan. Gate-voltage control of optically-induced charges and memory effects in polymer field-effect transistors. *Advanced Materials*, 16(23-24):2151–2155, 2004.

[258] Myeong-Lok Seol, Sung-Jin Choi, Ji-Min Choi, Jae-Hyuk Ahn, and Yang-Kyu Choi. Hybrid porphyrin–silicon nanowire field-effect transistor by opto-electrical excitation. *ACS Nano*, 6(9): 7885–7892, 2012.

[259] M Radosavljevic, M Freitag, KV Thadani, and AT Johnson. Nonvolatile molecular memory elements based on ambipolar nanotube field effect transistors. *Nano Letters*, 2(7):761–764, 2002.

[260] Gregory W Holloway, Yipu Song, Chris M Haapamaki, Ray R LaPierre, and Jonathan Baugh. Trapped charge dynamics in inas nanowires. *Journal of Applied Physics*, 113(2):024511, 2013.

[261] Qiliang Li, Shyam Surthi, Guru Mathur, Srivardhan Gowda, Qian Zhao, Thomas A Sorenson, Robert C Tenent, Kannan Muthukumaran, Jonathan S Lindsey, and Veena Misra. Multiple-bit storage properties of porphyrin monolayers on sio2. *Applied Physics Letters*, 85(10):1829–1831, 2004.

[262] Qiliang Li, Shyam Surthi, Guru Mathur, Srivardhan Gowda, Veena Misra, Thomas A Sorenson, Robert C Tenent, Werner G Kuhr, Shun-ichi Tamaru, Jonathan S Lindsey, et al. Electrical characterization of redox-active molecular monolayers on sio2 for memory applications. *Applied Physics Letters*, 83(1):198–200, 2003.

[263] A.L. Aguiar, E.B. Barros, R.B. Capaz, A.G. Souza Filho, P.T.C. Freire, J. Mendes Filho, D. Machon, C. Caillier, Y.A. Kim, H; Muramatsu, et al. Pressure-induced collapse in double-walled carbon nanotubes: chemical and mechanical screening effects. *The Journal of Physical Chemistry C*, 115(13):5378–5384, 2011.

[264] D. Christofilos, J. Arvanitidis, G.A. Kourouklis, S. Ves, T. Takenobu, Y. Iwasa, and H. Kataura. Identification of inner and outer shells of double-wall carbon nanotubes using high-pressure raman spectroscopy. *Physical Review B*, 76(11):113402, 2007.

[265] Jia Huang, Allen L Ng, Yanmei Piao, Chien-Fu Chen, Alexander A Green, Chuan-Fu Sun, Mark C Hersam, Cheng S Lee, and YuHuang Wang. Covalently functionalized double-walled carbon nanotubes combine high sensitivity and selectivity in the electrical detection of small molecules. *Journal of the American Chemical Society*, 135(6):2306–2312, 2013.

[266] Shunliu Deng, Yanmei Piao, Alexandra H Brozena, and YuHuang Wang. Outerwall selective alkylcarboxylation and enrichment of double-walled carbon nanotubes. *Journal of Materials Chemistry*, 21(46):18568–18574, 2011.

[267] Yanmei Piao, Chien-Fu Chen, Alexander A Green, Hyejin Kwon, Mark C Hersam, Cheng S Lee, George C Schatz, and YuHuang Wang. Optical and electrical properties of inner tubes in outer wall-selectively functionalized double-wall carbon nanotubes. *The Journal of Physical Chemistry Letters*, 2(13):1577–1582, 2011.

[268] Subhadeep Datta, Laëtitia Marty, Jean-Pierre Cleuziou, Carmen Tilmaciu, Brigitte Soula, Emmanuel Flahaut, and Wolfgang Wernsdorfer. Magneto-coulomb effect in carbon nanotube quantum dots filled with magnetic nanoparticles. *Physical Review Letters*, 107(18):186804, 2011.

[269] Stefan Thiele, Franck Balestro, Rafik Ballou, Svetlana Klyatskaya, Mario Ruben, and Wolfgang Wernsdorfer. Electrically driven nuclear spin resonance in single-molecule magnets. *Science*, 344(6188):1135–1138, 2014.

[270] Robert J. Chen, Hee Cheul Choi, Sarunya Bangsaruntip, Erhan Yenilmez, Xiaowu Tang, Qian Wang, Ying-Lan Chang, and Hongjie Dai. An investigation of the mechanisms of electronic sensing of protein adsorption on carbon nanotube devices. *Journal of the American Chemical Society*, 126(5):1563–1568, 2004.

[271] Nadine Wong Shi Kam, Zhuang Liu, and Hongjie Dai. Functionalization of carbon nanotubes via cleavable disulfide bonds for efficient intracellular delivery of sirna and potent gene silencing. *Journal of the American Chemical Society*, 127(36):12492–12493, 2005.